# Optimal Design of 245kV $SF_6$ Bushing by Using Genetic Algorithm

Von der Fakultät für Maschinenbau, Elektrotechnik und Wirtschaftsingenieurwesen der Brandenburgischen Technischen Universität Cottbus zur Erlangung des akademischen Grades eines Doktors der Ingenieurwissenschaften

genehmigte Dissertation

vorgelegt von

Master of Science

Han Bao

geboren am 04. Augst 1986 in Shanghai, China

Vorsitzender: Prof. Dr.-Ing. Christian Heinrich

Gutachter: Prof. Dr.-Ing. Dr. h. c. Heinz-Helmut Schramm

Gutachter: Prof. Dr.-Ing. Harald Schwarz

Tag der Mündlichen Prüfung: 07. August 2014

# Abstrakt

In Schaltanlagen bis zur Spannungsebene 245 kV werden grob gesteuerte Durchführungen verwendet. Derzeit konzentrieren sich immer mehr Entwicklungen solcher Durchführungen auf eine einfache Gestaltung, kompakten Aufbau und geringes Gewicht. Obwohl im Allgemeinen $SF_6$-gefüllte Durchführungen die gestellten Anforderungen erfüllen, gibt es weitere Möglichkeiten, die $SF_6$-gefüllte Durchführung im Betrieb und Design zu verbessern.

Geringere Dimensionen könnten die elektrische Feldstärke an Schwachstellen der Durchführung verstärken und dadurch Teilentladungen und Überschläge verursachen, die zur Zerstörung der Durchführung führen. Darüber hinaus hängt die elektrische Feldstärke von der Gestaltung der Oberfläche und vom Grad der Verschmutzung ab.

Diese Dissertation stellt vor Allem die Optimierung der Strukturen einer $SF_6$-gefüllten Durchführung mittels genetischem Algorithmus vor.

Zunächst wurde ein Modell der $SF_6$-gefüllten Durchführung entwickelt und für den Theorie-Zweck simuliert. Danach werden potentielle Probleme identifiziert und näher erläutert. Anschließend folgt eine Einführung in die Methode des genetischen Algorithmus zur Optimierung des Kontourdesigns. Die Ausführungseffizienz wird durch den Zugriff auf die Fitnesswerte während des Optimierungs-verfahrens verbessert. Die Validierung des genetischen Algorithmus wird durch Minimieren der elektrischen Feldstärke an den Schwachstellen verifiziert. Damit ist die Gestaltung der Schwachpunkte optimiert worden. Verschiedene neue Strukturen der Erdelektrode wurden vorgeschlagen und durch Anwenden des genetischen Algorithmus optimiert. Durch Verwenden einer neuen Kurve aus kubischen Splines wurde die Kontur der Kopfelektrode so gestaltet, dass der Einfluss von Tripelpunkten vermieden wurde. Die elektrische Feldstärke an der Oberfläche der Kopfelektrode ist durch Anwenden des genetischen Algorithmus minimiert worden. Die Potentialverteilung entlang der Oberfläche des Isolierkörpers wurde durch eine neue Struktur optimiert. Die Enden der Rippen des Silikon-Verbundisolators sind ebenfalls mit Hilfe des genetischen Algorithmus für das Verhalten bei Befeuchtung gestaltet worden.

Unter Verwendung des genetischen Algorithmus sind eine gleichmäßigere Potentialverteilung entlang der Gehäuseoberfläche und minimale Werte der elektrischen Feldstärke an Schwachstellen erreicht worden. Die Dimensionen der so optimierten $SF_6$-Durchführung sind geringer als die der ursprünglichen Durchführung.

Abstract

**Schlagwörter:** Optimale Gestaltung, $SF_6$ Durchführung, α Prozess, Streamer Theorie, Genetischer Algorithmus, Ansoft Maxwell, Kubische Spline, Bézier Kurve.

# Abstract

Currently more and more researches of high voltage bushings are focused on the requirements for a simple structure, compactness and light-weight. The general operation of $SF_6$ gas-filled bushings ($SF_6$ bushings) is satisfying the requirements, but in the operation and design of $SF_6$ bushings still many improvements may be possible. The minimizing of dimension might enhance the electric field strength (E) on the crucial points of bushings, which may lead to partial discharge, flashover and even break down. Electric field distribution along the surface mainly depends on contour design, besides the effect of contamination. This dissertation mainly describes the optimization of the bushings design by genetic algorithm.

First, a model of $SF_6$ bushings was developed and simulated for the theory purpose. Then, the potential breakdown problems were defined and the mechanisms of the potential breakdown were explained. Afterwards, the dissertation proposes an approach, i.e. genetic algorithm to optimize the contour design of $SF_6$ bushings. The approach improved the execution efficiency by accessing the fitness values of searched solutions during the optimization process. To verify the effectiveness of the genetic algorithm, it has been applied to minimize the electric field strength at the critical positions. Furthermore, the critical points of $SF_6$ bushings were optimized. Several new structures of the ground electrode were proposed and optimized desperately by genetic algorithm. A new curve, i.e. cubic spline was applied to the contour of the top flange to avoid the influence of the triple points. By optimization E on the surface of top flange was minimized. The potential distribution on the surface of insulator was optimized by a new structure. By the genetic algorithm the contour of composite weather sheds (WS) was optimized as water-drop form.

In summary, a more uniform electric field strength distribution along the surface of weather sheds and minimal values at critical points can be derived effectively by genetic algorithm. In addition, a smaller dimension of $SF_6$ bushings was obtained in comparison with presently available ones.

**Index Terms: O**ptimal Dimension, Optimized contour design, $SF_6$ bushing, α process, Streamer theory, Genetic algorithm, Ansoft Maxwell, Cubic spline, Bézier curve.

# Acknowledgments

I would like to acknowledge many people who have provided me with the assistances, encouragements and inspirations.

First of all, I express my sincere gratitude to Professor Heinz-H. Schramm for guiding me through my most important three years in my life at BTU Cottbus. I appreciate his expert guidance, insightful discussions, valuable suggestions and enormous supports in persisting me to solve the difficulties encountered during my study. His broad knowledge, experience, enthusiasm as well as the understanding of the problems inspire and lead me to face this challenging and dissertation work.

I am grateful for the generous supports and assistances from Siemens experts, Dr. Edelhard Kynast and Dr. Volker.Bergmann, for spending their valuable time to discuss with me and for their constructive advices.

I would also like the thank Prof. Harald Schwarz for participating in my dissertation committee, taking time to review my dissertation draft and giving me his helpful suggestions.

Last but not least, I also owe the special thanks to my parents, who are the source of inspiration and spiritual support in completing my doctor degree. For the education and love I received from them, I owe my achievement to them. This dissertation is also dedicated to them.

Cottbus

2014-02-25

Han Bao

# Contents

# 1 Introduction

## 1.1 Motivation and introduction

High voltage bushings are a critical component of all power networks, as the chief role of bushings is to insulate conductors, which carry high-voltage current through a grounded enclosure. Sometimes in the power system it is regarded as nothing more than a hollow piece of porcelain or composite housing a conductor. However, the task of insulation makes great demands on bushings, as the dimension of bushings is relatively small compared with the equipment that connects by bushings. Besides that, the manufacturing, design and operation of bushings should exceed the requirements of its applications during the lifetime. It is a challenge to complete such a task without flashover or partial discharges. Therefore, it plays a very important role in the power system reliability and their performance influences the whole power system.

The bushings suffer from wide variety of stresses including electrical, mechanical and environmental. Depending on the structure, application and installation location of bushings, the character and magnitude of such stresses will be totally different. From the electrical point of view, the steady state stress, i.e. the operating voltage is imposed on the bushings, and the transient stress is imposed by the lightning and switch impulse voltage. Besides that, dielectric losses have to be taken into account. While dielectric losses can be ignored at low voltages, they become substantially at high voltage. From the mechanical point of view, tensile and vibration stress can be anticipated in the operation of bushings. A wide range of environmental effects, such as temperature variation, altitude, moisture, contamination, ice shedding and ultra-violet radiation from sunlight, also have to be considered.

The design of bushings is related with achievement of precision manufacturing, insulation technologies and computer simulation technologies. With the development of manufacturing technologies, it enables the new structure of bushings to be possible. By new computer simulation-technologies, stresses e.g. voltage distribution in the axial and radial directions, mechanical stress and thermal current can be analyzed and optimized [1][2][3][4]. And nowadays, due to more and more attentions on greenhouse gas, i.e. $SF_6$ and economic benefits, designers are forcing on compact structure and light-weight of bushings. However, in the process of construction the mechanical or electrical requirements may conflict with dimension and structure of bushings. Therefore, the bushings have to be designed to take all factors into account.

This introductory chapter provides general information of $SF_6$ bushings, starting with designs, technologies and structures of $SF_6$ bushings. The object of this dissertation is also discussed. Then, a literature survey regarding of optimization of bushings is presented. The structure of this dissertation is discussed in the final section.

## 1.2 Present designs and technologies of $SF_6$ bushings

In any domain of industry, the prerequisite of a new successful technology is to develop a better product offering advantages over the previous one. In the power system industry, this statement is even stronger. Not even the advantages have to be confirmed, but the reliability is seen as essential requirement. As far as structure of bushings is concerned, it can be classified into two types: condenser and electrode type. The condenser bushings consists of resin bonded paper insulation or oil impregnated paper insulation with interspersed conducting layers. This type of bushings usually consists of equal capacitance layers between the center conductor and ground flange. These capacitance layers provide equal voltage steps, which makes a uniform voltage gradient. This dissertation concentrates on the electrode type bushing.

During the late 1950s, sulphurhexafluoride ($SF_6$) gas found application in high voltage circuit breakers [6]. Ever since, the application of $SF_6$ gas has been spread widely in power systems. In the meantime, $SF_6$ gas as insulating media was applied for the gas-filled bushings, which was named $SF_6$ gas-filled bushings. In comparison with condenser bushings, the structure of $SF_6$ bushings is relative simple.

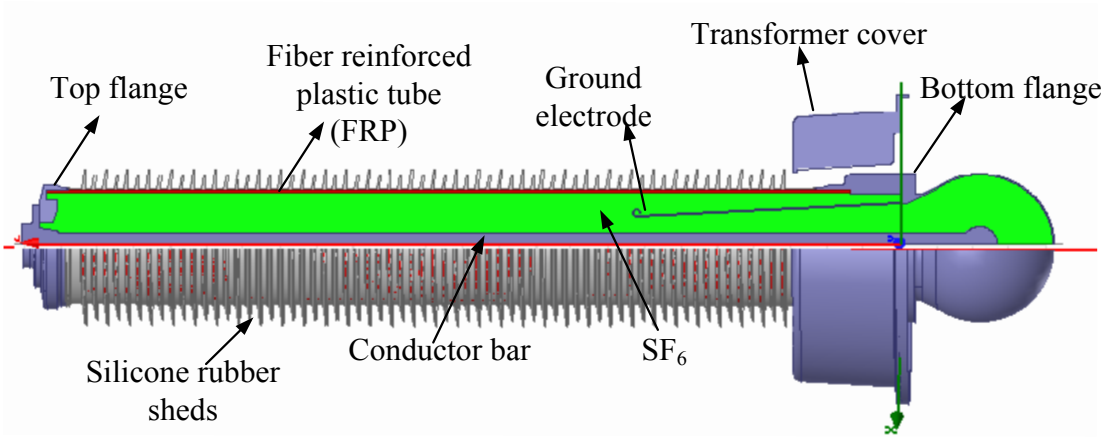


*Figure 1: Legend of GIS $SF_6$ bushing*

Figure 1 shows a typical design of GIS $SF_6$ bushing. It consists of a central conductor bar, which carries current through the bushing. $SF_6$ is used as insulating gas since it is non-toxic, non-ageing, non-flammable and non-explosive besides being chemically inert and thermally stable. It has good dielectric property, arc-quenching as well. As the molecular mass of $SF_6$ gas is quite high (146), it has a high density. Because of high density the charge carriers have a short mean free path. This property and the property of electron attachment make $SF_6$ a gas of electro-negativity and high ionization energy, which results in high dielectric strength of $SF_6$ gas [6]. The ground electrode is designed for the purpose of reduction the electric field strength at the bottom flange. A fiber reinforced plastic (FRP) tube is the mechanical support for the insulator, which is designed for requirements regarding internal pressure, bending and traction. The bottom and top flange are made of galvanized iron or high strength aluminum alloy. The insulator can be either ceramic or polymeric. Ceramic has a long history and currently is dominant in the power system industry, but over the last decades polymeric has increased their market share, which is constantly increasing due to their important advantages. First of all, polymeric is an organic material, which has weaker electrostatic bonds resulting in a lower surface free energy [7][8]. Therefore, insulators made of that material are not wetted easily, which is called hydrophobicity in technical terms. It increases the surface resistance of the insulator under the wet and contaminated condition and suppresses leakage current, which can result in flashover. Second, because of the characteristic of polymer, insulators made of polymeric are less fragile compared to porcelain insulators. As a consequence, polymeric insulators will not explode like porcelain insulators in case of installation-, manufacturing-defects or failures. And the structure of the FRP tube of polymeric prevents damaged parts from bursting away. Besides, lighter weight of polymeric insulators is a third advantage over porcelain insulators, which makes the transportation and

installation much easier. On the one hand, the industry is exploring improved safety, mechanical, electrical, seismic withstand and contamination performance of bushings. On the other hand, reductions of overall costs and weights are also of great concern. It is likely that the dominant role of porcelain will diminish and more and more people prefer polymeric over porcelain material. Polymeric material can be divided into three classes: epoxy resins, ethylene-propylene rubbers and silicone rubbers [9]. The silicone rubbers have proven to be the most reliable polymeric materials for the outdoor insulation. There are three different types in the silicone rubbers, i.e. room temperature vulcanized (RTV), high temperature vulcanized (HTV) and liquid silicone rubbers (LSR) [9]. Unlike other polymeric materials, silicone rubbers have the capability to maintain the hydrophobicity for a long-term. Nowadays, the trend is toward using silicone rubber for housing the polymeric bushings.

## 1.3 Aim and assumptions for $SF_6$ bushing

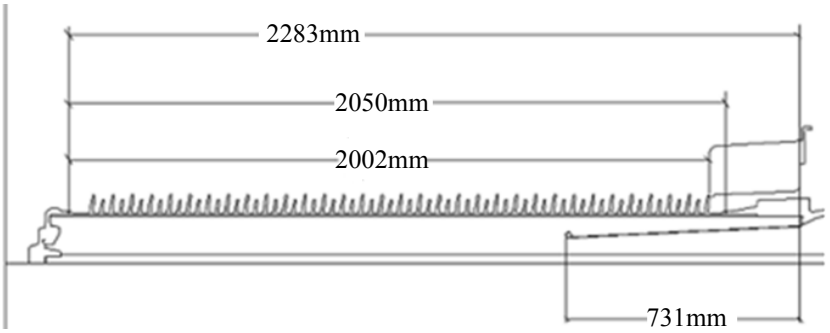


*Figure 2: Overall dimension of original bushings*

This dissertation will concentrate on theoretical explanations and proposals for the optimization of a $SF_6$ gas filled bushing. It points out the procedures of optimizations i.e. genetic algorithm for a bushing with regarding of electric field strength, design and dimension. Genetic algorithm is applied to optimize two curves Bézier curve and cubic natural spline. This bushing [23] is used as reference structure for the construction of the model as shown in Figure 2. For the comparison to the subsequent structures this reference structure is considered as original structure.

The basic structure is shown in Figure 1. In the middle of bushing there is a conductor bar for carrying current through. $SF_6$ is used as insulating gas. The ground electrode is designed at the bottom part. The insulator is made of fiber reinforced plastic (FRP). For housing and increasing the creepage the weather shed is designed, which is made by silicon rubber.

Based on the previous introduction and for the further optimization and investigation the research object, i.e. $SF_6$ bushing is based on the following assumptions:

- Rated AC voltage: 245kV
- Bushing filled with $SF_6$ at the pressure of 0.7Mpa
- Only electrode designs are considered
- Material: FRP for insulator and silicon rubber for weather shed.
- The continuous current carrying capacity and short-circuit current withstand are not taken into account.

## 1.4 Literature review

The reasons for the increased usage of $SF_6$ bushings include the relatively simple structure of bushings, increasingly favorable service experience and cost advantage over conventional condenser bushings. However, electric field strength (E) on the critical positions and non-uniform E and potential distribution on the surface of silicone rubber sheds are the great challenges, which may affect adversely the reliability and long-term performance of $SF_6$ bushings in service. In this section, a literature review of the research in this area is presented. It includes the following aspects,, i.e. break-down mechanism in $SF_6$ gas, flash-over mechanism of silicone rubbers, streamer theory of silicone rubber surface, calculation of electric field strength by simulation software and genetic algorithm for optimization purposes.

Studies of break-down mechanism in $SF_6$ gas have been investigated in [10][11][12]. Niemeyer *et al*. [10] investigated the leader break-down of electronegative gas $SF_6$ in non-uniform field gaps and under fast-rising voltage waveforms. The basic physical processes were explained, which involved streamer corona, the transformation from streamers into leader step and the propagation

of leader through the gap. Two leader inception mechanisms were discussed, namely the stem and precursor mechanisms. From this study, the conclusion can be drawn that the leader break-down process can be predicted in dependence of the experimental parameters, i.e. applied voltage, gas pressure and gap geometry. Seeger *et al*.[11] studied the break-down mechanism of $SF_6$ under uniform and weakly non-uniform field with small electrode protrusions, such as particles or surface roughness. The physical process can be explained also by two types of leader break-down associated with the stem and precursor mechanisms. They also yielded the parameters of leader propagation, which include applied fields, protrusion, gas pressure, polarity and temperatures. Chen *et al*.[12] summarized the physical process and break-down mechanism of $SF_6$ and derived the discharge models under different mechanisms, i.e. the stem and precursor mechanisms. In the meanwhile they explained the scope of applications for different break-down mechanisms.

Karady *et al*. issued two pieces of papers regarding with flash-over mechanism of silicone rubbers [13][14]. Experimental results in the first paper showed that the contamination performance of silicone rubber composite insulators is better than porcelain insulators. It was attributed to the hydrophobicity of the silicone rubber. This paper explained the process of flash-over, i.e. contamination build-up, diffusion of low molecular weight (LMW) polymer chains, surface wetting, ohmic heating, electric field causing interactions between droplets, generation of conductive regions and filaments, field intensification causing spot discharge and the ultimate flashover of silicone rubber along wetted filaments. In the second research the effects of different ohmic heating (resistive contamination layer), water droplets and electric field intensification were investigated. The studies resulted in the descriptions of a new flashover mechanism compared with porcelain and glass, which provides a better understanding of the superior performance of silicone rubber outdoor insulators.

The streamer development on silicone rubber insulator surfaces has also been investigated by N.L. Allen *et al*. [15][16]. The experiments for streamer properties have been performed in air, along the surface of a smooth cylindrical silicone rubber insulator and along a cylindrical silicone rubber insulator with a single shed. It was demonstrated that the threshold fields for propagation were minimum in air and greatest for the shedded insulator. From the comparison of propagation fields and variations in velocities it was clarified that energy was lost from formative avalanches by attachment of electrons to the surface of the material. The relative permittivity of the material was considered to be significant in restricting the branching and lateral diffusion of streamers close to the surface. It was shown that the shed increases the minimum stress needed for streamer propagation. Therefore, the overall stress needed for breakdown was also increased.

Rokunohe, T *et al.* presented a project on the optimization of 800kV $SF_6$ gas-filled bushings by conventional experimental method [18]. In the research in order to reduce the electric field strength on the surface of a ground electrode different structures of ground electrodes were investigated. The ground electrode was coated by epoxy with the silica-filler to withstand the peak value of electric field strength.

Researchers Murugan, N *et al.*[19] and Monga, S *et al.*[20] made design optimizations of $SF_6$ bushings and insulator by using electric field computation. Based on the finite elements method the electric field distributions were analyzed, the position and magnitude of maximum electric field strength were found and optimized, which results in the enhancement of performance of bushings and insulator.

Some researchers have focused on the optimal contour design of electrical equipment by a certain algorithm. Bhattacharya K *et al.*[21] optimized the contour design of a support insulator by artificial neutral network (ANN), which relates electric field distribution (as input data) with the insulator contour (as output data). Wen-Shiush Chen *et al.*[22] presented a study on contour optimization of suspension insulators by using genetic algorithms. In this paper, the approach of the charge simulation method (CSM) was integrated into the genetic algorithm. The results showed that a more uniform electric field distribution on the surface of an insulator can be obtained through the proposed approach in comparison with the original structure.

The above surveys indicate that in spite of extensive research on flash-over and break down mechanism on the surface of silicone rubber a complete understanding and physical model of break down processes have still not been obtained yet. However, it is clear that the structure of bushings is one of the most important factors affecting insulation performance.

## 1.5 Organization of this dissertation

Considerable work has been done in the last several decades to clarify the break-down mechanism in $SF_6$ gas and flash-over along the silicone rubber surface. However, the literature review indicates that general processes of break down and flash-over have been analyzed qualitatively. In the meantime the external (experimental) parameters, which influence the basic physical processes, have been yielded. Very little information is available on quantitative analysis of physical processes and model and quantitative mathematical calculations. Besides that, with

the development of computer aided design (CAD) technology more and more researchers are focusing on contour design of high voltage electrical devices resulting in an increase of onset voltage for surface flash-over and significant savings for the economic purpose. Therefore, this dissertation will concentrate on the optimizations of bushings by a new algorithm, i.e. genetic algorithm.

After the introduction and the brief description of $SF_6$ bushing in chapter 2, the simulation setup and procedures used for electric field calculation are discussed. The detailed configurations and model of $SF_6$ bushings are presented in the subchapter 2.1. The results of simulations under alternating current (AC) voltage and lightning impulse voltage (LIV) are presented in the subchapter 2.3.

According to the simulation criteria and results from chapter 2 the critical positions of the peak values of electric field strength are defined. Chapter 3 proposes a hypothesis of break down mechanism. In the subchapter 3.1 break down mechanisms between the conductor bar and ground electrode are analyzed qualitatively. The flash-over mechanism on the surface of silicon rubber is discussed in the following subchapters 3.2 and 3.3.

Chapter 4 states the method for optimization of $SF_6$ bushings, i.e. genetic algorithm. The basic concepts and genetic algorithm are introduced in subchapter 4.1. The detailed information of parameters for genetic algorithm is shown in subchapter 4.2. Simultaneously, the flowchart for the optimizations is also given.

Results and discussions on optimizations of $SF_6$ bushings are illustrated in chapter 5. Four new structures of ground electrode are presented in subchapter 5.1. An optimal design of a ground electrode is given in 5.1.7. The reduction of diameter of fiber-reinforced plastic tube is discussed in subchapter 5.2. Afterwards, the optimization of top flange is described in subchapter 5.3. In subchapters 5.5 and 5.6 the methods for optimizations of potential deviation on the surface of silicone rubber insulator and of electric field strength at the weather shed's end are proposed.

Finally, the overall conclusions and recommendations for further work are presented in chapter 6.

# 2 Simulation setups and procedures

## 2.1 Construction of bushings by Ansoft Maxwell 2D

In the realistic situation, the rated 245kV $SF_6$ bushing operates under $\frac{245kV}{\sqrt{3}}$ line to ground AC voltage and before operation it tested under short duration of 460kV AC voltage (1 min) and 1050kV lightning impulse voltage (LIV). Therefore, the modeling of a $SF_6$ bushing is constructed under two different circumstances, i.e. under AC voltage and LIV. The simulation is performed by the software Ansoft Maxwell (AM) 2D. AM is a leading electromagnetic field simulation software for researchers and engineers oriented to design and analyze 3D and 2D electromagnetic and electromechanical devices, including motors, insulators, transformers, sensors, coils etc. The basic principle of Maxwell is the finite element method (FEM), which can solve static, frequency-domain, and time-varying electromagnetic and electric fields. Besides that, Maxwell can generate an appropriate, efficient and accurate mesh for solving the problem, which removes complexity from the analysis process and benefits from a highly efficient, easy-to-use design flow. The chapter describes detailed configurations of simulation procedures and the results of the simulation.

### 2.1.1 Solution type

Lightning impulse is a transient procedure. However, transient procedure is not available in the AM 2D. A compromise method should be considered. Taking into account the rise time of LIV 1.2μs, the distance ( $D_{LI}$ ) traveled by the LIV during its rise time can be calculated as following,

$$D_{LI} = 1.2\mu s \cdot c = 1.2 \cdot 10^{-6} s \cdot 3 \cdot 10^{8} m / s = 360m \qquad Eq.\ 1$$

Obviously, the distance traveled by LIV is much larger than the dimension of bushing. Therefore, the electric field produced by LIV can be approximately considered as a steady-state situation and analyzed by electrostatic. For the AC voltage the model is simulated under the solution type of "AC Conduction". The configurations of solution type are shown in Figure 3.

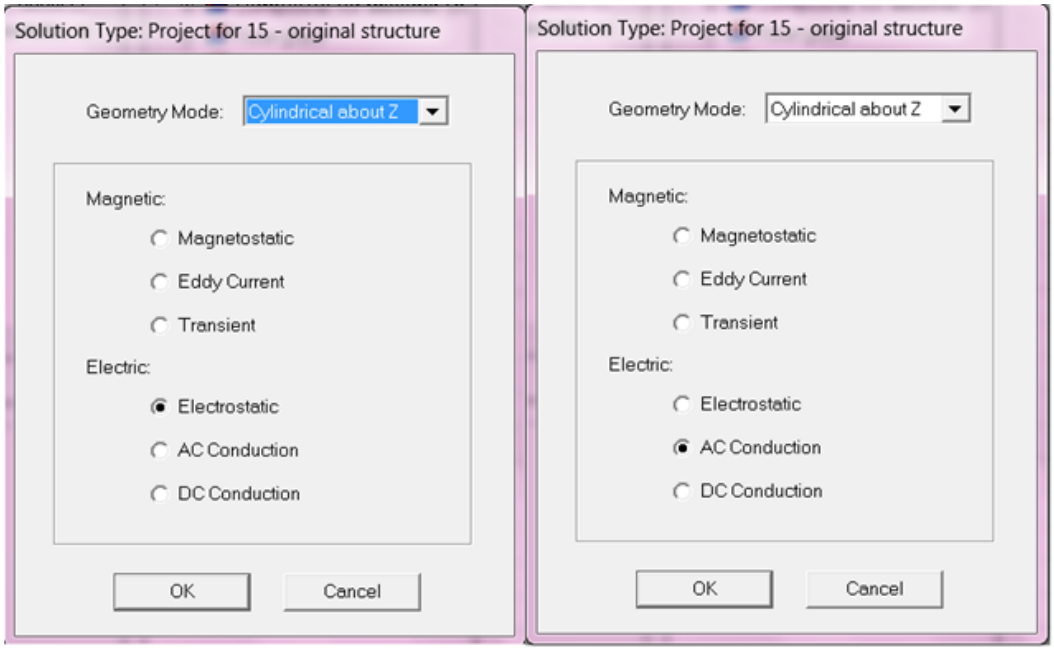


LI Voltage AC Voltage

*Figure 3: Solution types for LIV and AC voltage*

Apparently, the bushing is a cylindrical structure and has an axis Z of rotational symmetry. Consequently, geometry mode “cylindrical about Z” is set, which assumes that the bushing model sweeps 360° around the z-axis of a cylindrical coordinate system.

### 2.1.2 Boundary conditions and modeling of bushings

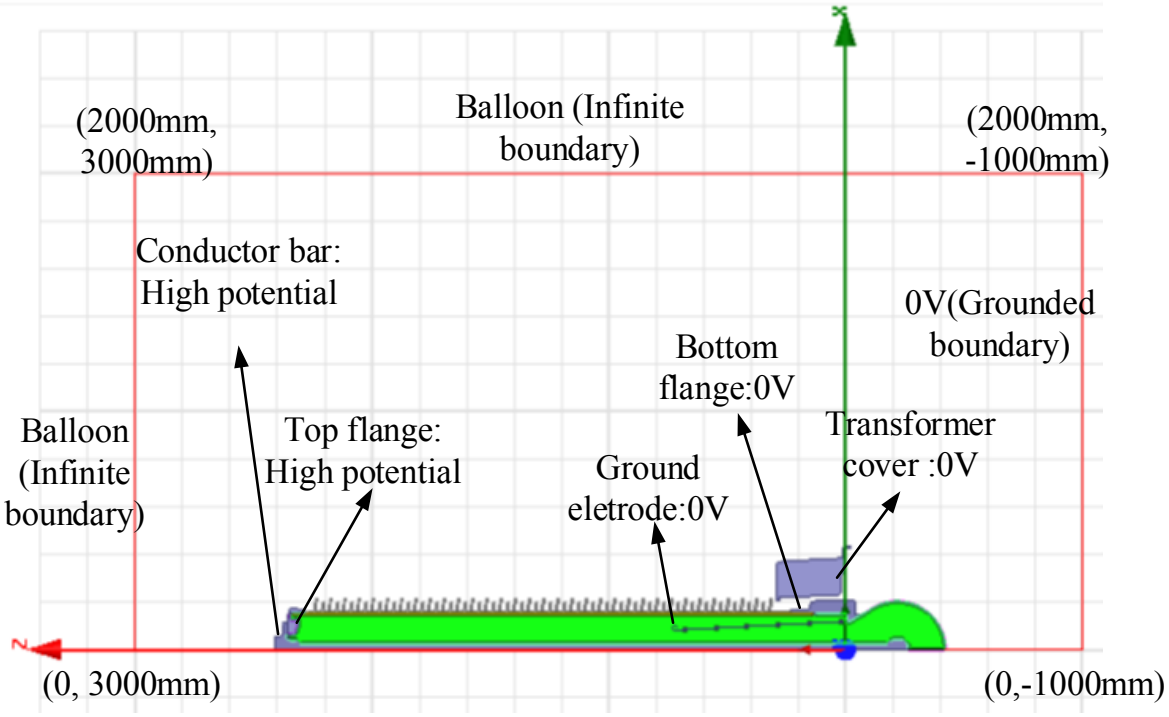


*Figure 4: Modeling and boundary conditions of bushings under LIV 1050kV and under AC voltage* $\frac{245kV}{\sqrt{3}}$

Figure 4 illustrates the model and boundary conditions of the reference bushing. Taking into account the cylindrical symmetrical structure only half of the bushing is constructed. Different components of bushings are arranged as corresponding materials. The only difference of excitation between LIV, and AC voltage is that the conductor bar and top flange are energized by 1050kV under LIV and under AC voltage the conductor bar and top flange are energized by the high potential i.e. 50Hz AC voltage $\frac{245kV}{\sqrt{3}}$. In the reality of type test, the ground electrode, bottom flange and transformer cover are grounded. The boundary at the bottom is grounded as well. Therefore, the simulation is adopted the same configurations. The $SF_6$ bushing in the test should not be impacted by another sources of current or magnetic fields. So, the boundaries at the top and right side are assigned as “Balloon” boundary, which simulates the region outside the background as being nearly “infinitely” large and isolates the model from other sources of current or magnetic fields. The width of boundary is assumed as “w” in Figure 4. It indicates that different dimension of boundary has almost no effect on the simulation results (see Figure 5). For

this reason, it is unnecessary to enlarge the background space several times larger than the bushing. The coordinates of appropriate boundaries are located at (0, -1000mm), (2000mm, -1000mm), (2000mm, 3000mm) and (0, 3000mm).

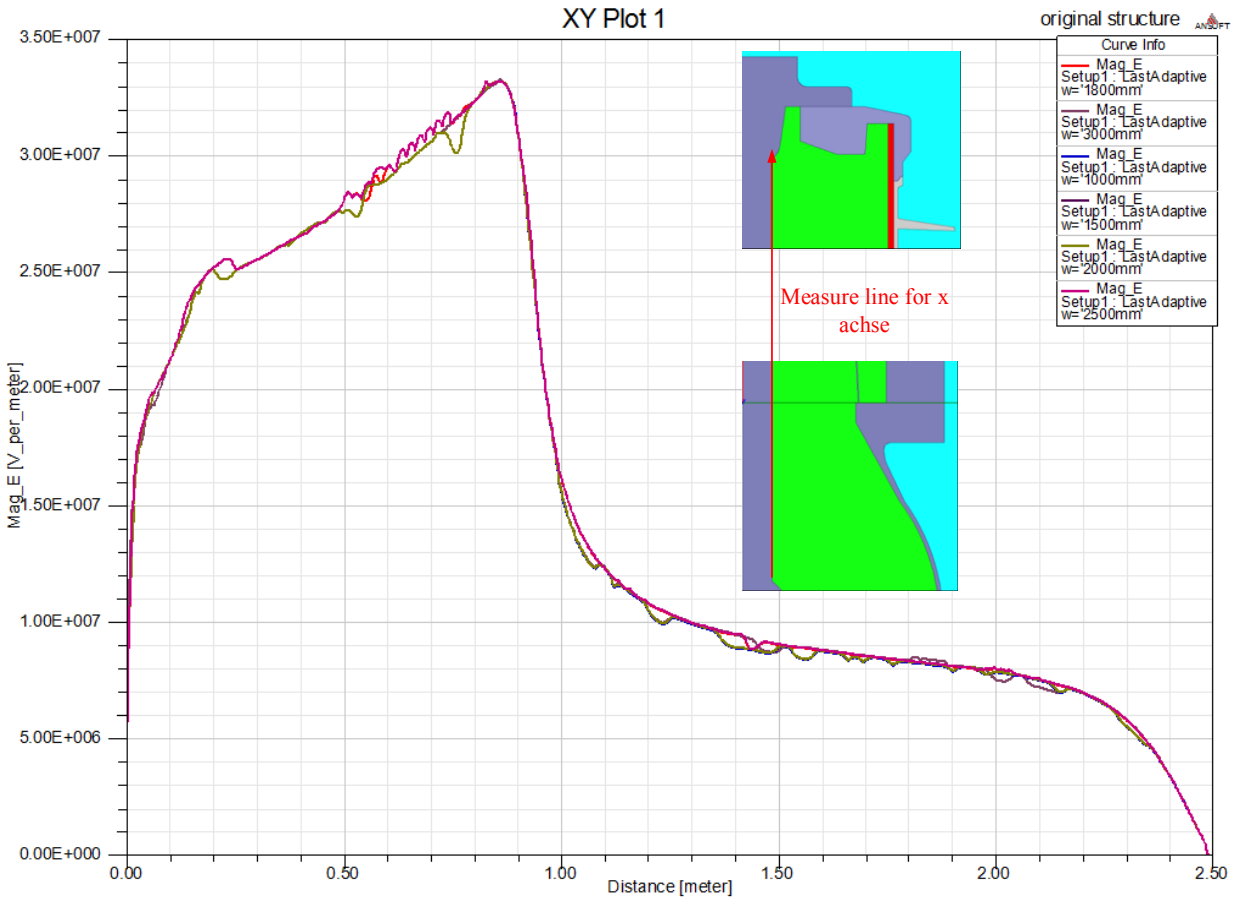


*Figure 5: E along the surface of conductor bar with different "w" width of boundary*

### 2.1.3 Mesh generation

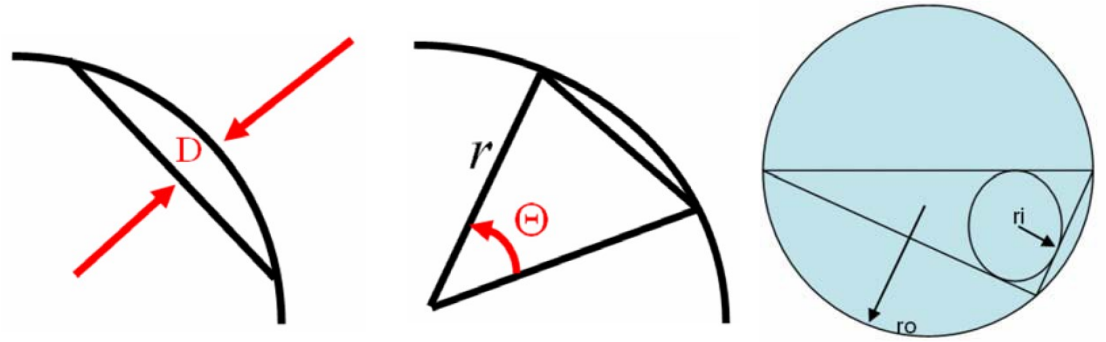


a: Maximum surface deviation D b: Maximum surface normal deviation Θ c: Maximum aspect ratio R

*Figure 6: The definitions of maximum surface deviation D, maximum surface normal deviation Θ and maximum aspect ratio R*

First of all, different mesh types in AM 2D are introduced. AM 2D provides 3 different mesh constructions [24][25]. They are "On Selection", "Inside Selection" and "Surface Approximation". When a mesh "On Selection" is defined, the length of tetrahedral elements on the surface will be refined below a specified value. Compared to tetrahedral elements on the surface the length of tetrahedral elements inside is getting larger and larger. An example of mesh type of "On Selection" on insulating gas $SF_6$ is taken. It shows the high mesh density on the interface of ground electrode and $SF_6$ and lower mesh density on where the tetrahedral elements far away from the ground electrode (see Figure 7). Similarly "Inside Selection" will refine the length of all tetrahedral elements within a specified value. It shows the mesh density of $SF_6$ is in the same degree (see Figure 8). "Surface Approximation" is mainly refined under the some circumstances of a bend object. For planar surfaces, the triangles lie exactly on the model faces; there is no difference in the location of the true surface and the meshed surface. When dealing with bend-surfaces, the faceted triangle faces lie a small distance from the object's true surface. In our simulation, this distance is called the surface deviation resulting in finial deviation of electric field strength on the bend-surface. Therefore by mesh generation "Surface Approximation" the maximum surface deviation D and maximum surface normal deviation Θ could be manipulated to reduce the finial deviation. Figure 6 illustrates maximum surface deviation D and maximum surface normal deviation Θ. It assumes that the bend part is divided into many small parts of grids composed of triangles. Maximum surface deviation D is defined by the maximum chord length of this triangle inside the circle (bend part). Maximum surface normal deviation Θ is defined by angle towards the maximum chord. By manipulation of maximum aspect ratio R the shape of triangle can be modified. According to illustration in Figure 6 the maximum aspect ratio R can be

defined as $R = \frac{r_0}{2r_i}$. In the following, different mesh grids of the ground electrode and $SF_6$ have been configured to investigate, whether the mesh grids have effect on the accuracy of calculations for electric field strength.

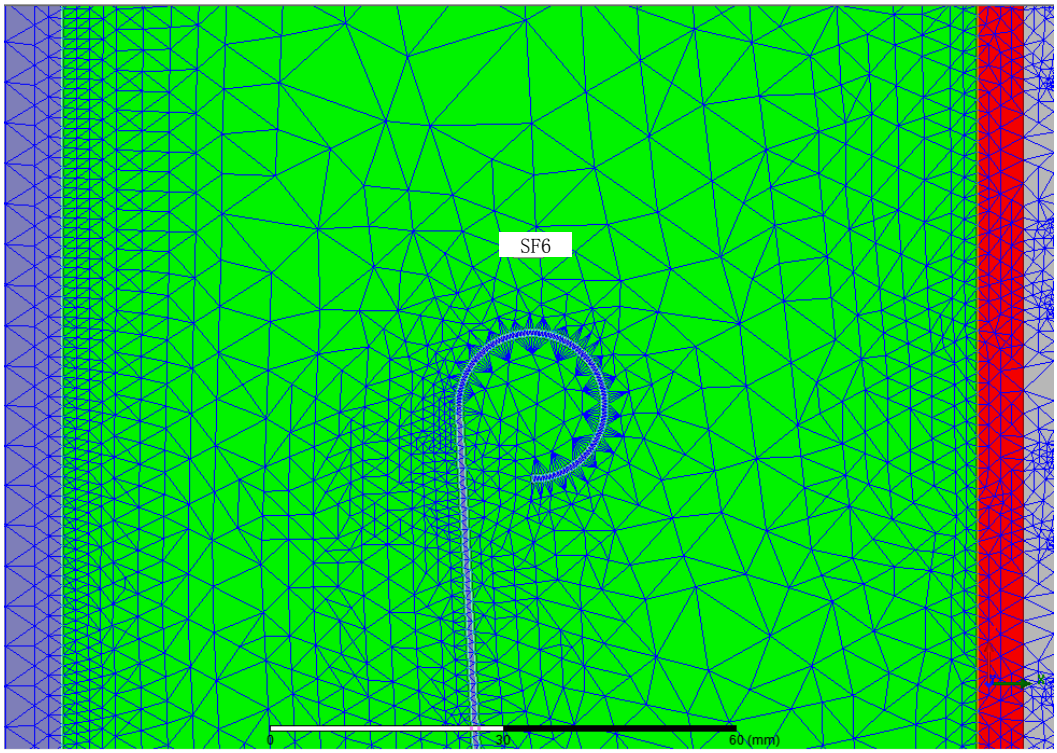


*Figure 7: Mesh generation "On Selection" on insulating gas and "Surface Approximation" on ground electrode*

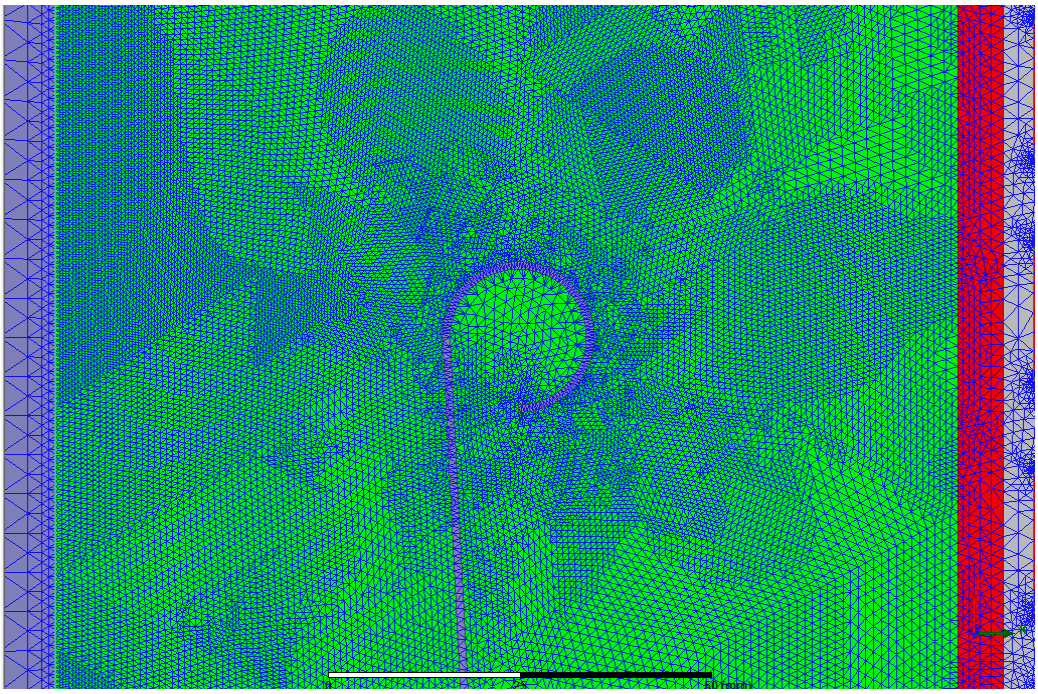

*Figure 8: Mesh generations "Inside Selection" on insulating gas and "Surface Approximation" on ground electrode*

Figure 7 and Figure 8 specify different mesh generations individually. The bend part, i.e. the ground electrode is refined by "Surface Approximation" in both figures. In the meanwhile $SF_6$ is refined by "On Selection" in Figure 7 and by "Inside Selection" in Figure 8. For $SF_6$ the maximum length of elements in "On Selection" and "Inside Selection" are both restricted at 2mm. The maximum surface deviation D is restricted at 0.01mm. a too small angle of Θ makes the sharp of element triangles narrow and long. The maximum surface normal deviation Θ is restricted to no more than 15º.

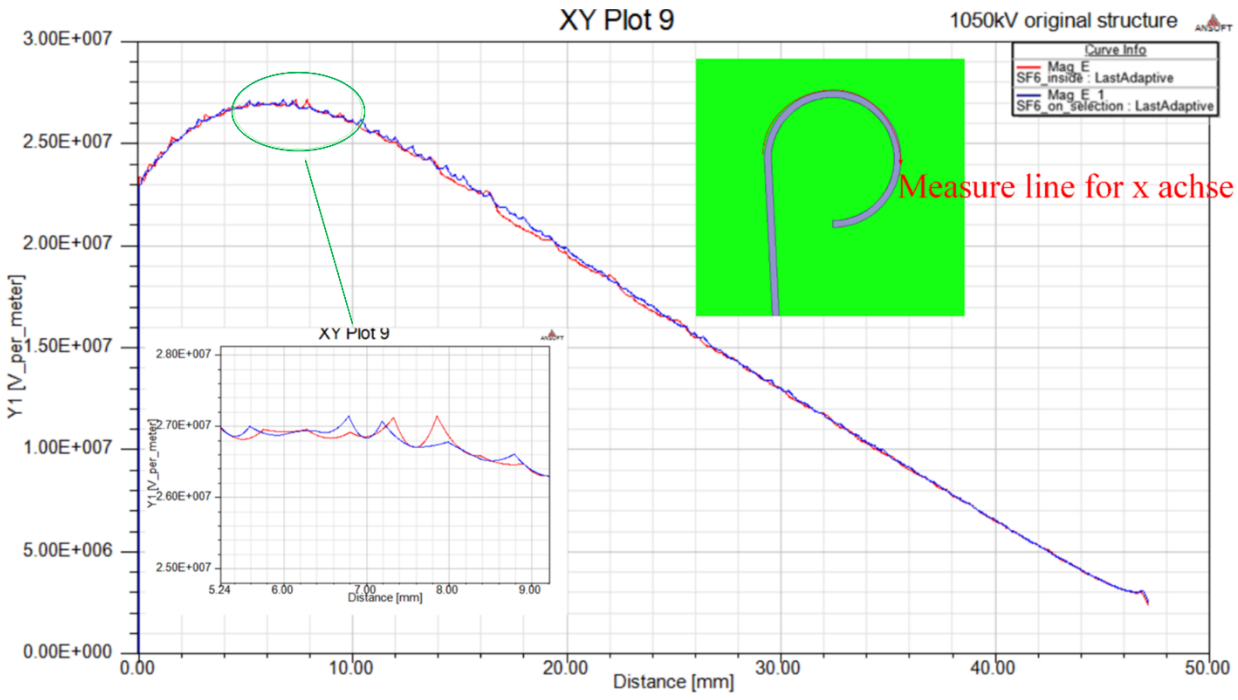


*Figure 9: E curve of ground electrode by two different mesh generations*

Figure 9 depicts the electric field strength distribution of the ground electrode by two different mesh grid generations. The two curves are basically identical and overlap together, which demonstrates that this configuration for mesh type “On Selection” has a good fit for the simulation of bushing and dimension of mesh grid is sufficient to meet the accuracy. As a consequence, this configuration of mesh generations can be used for modeling in AM 2D and the following optimization.

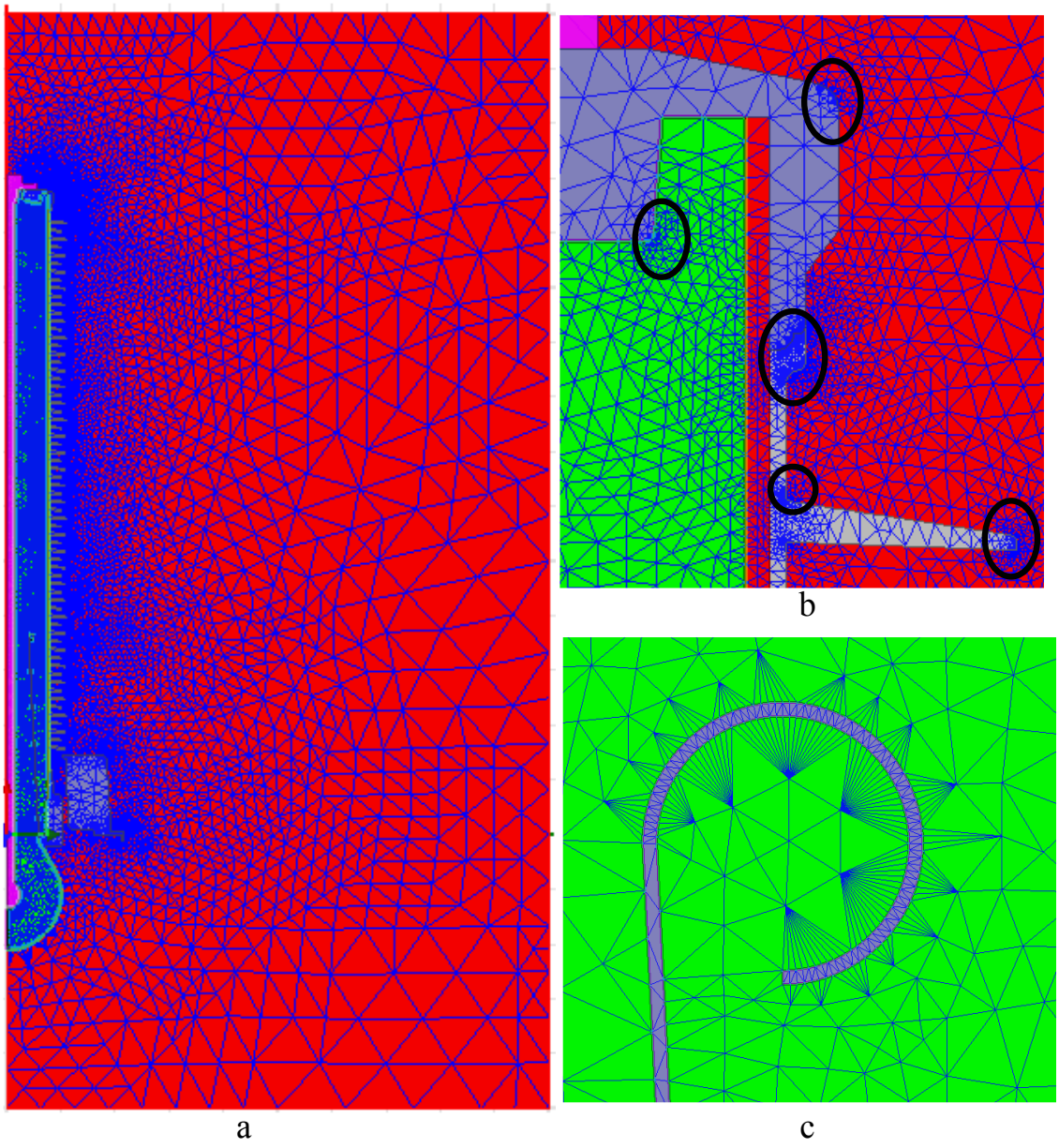


*Figure 10: Mesh generations of bushing with original structure (a: whole distribution of mesh grid b: local mesh grid refinement c: local mesh grid of ground electrode)*

Figure 10 delineates mesh generations of the bushing with the original structure. The non-bend components of the bushing are configured by the mesh type of "On Selection". The mesh grids concentrate on the bushing and present divergent distribution. At the positions of edge, bend, transition and connection part the mesh grids are refined. An additional attention should be taken on the mesh generation of the ground electrode due to bend structure and the peak value of electric field strength. The mesh grids of the ground electrode are generated by "Surface Approximation" manually.

## 2.2 Criteria for simulation results

For the practical purposes, it is necessary to determine the withstand electric field strength of $SF_6$ under different pressure for different electrode configurations. This withstand electric field strength (E) can be obtained by 2 methods, i.e. statistic method and empirical method.

**Method A:** statistic method

According to the Bin LI's statistic and experimental investigation [26], under the condition of lightning impulse voltage, statistic equation of the 50% breakdown voltage of $SF_6$ could be expressed as follow

$$E_{50\%} = 63(p + 0.1) + 2.4 \qquad \textit{Eq. 2}$$

where in the equation $E_{50\%}$ kV/mm and p in MPa.

The withstand voltage $E_B$ can be expressed as follow

$$E_B = E_{50\%}(1 - 3\sigma) \qquad \textit{Eq. 3}$$

Where σ is standard deviation and equal to 0.05

In the analysis and simulation the withstand voltage should keep the safety margin in order to guarantee non breakdown of $SF_6$. The factor $k_1$ of safety margin is introduced,

$$E_1 = k_1 \cdot E_B \qquad \textit{Eq. 4}$$

Where $E_1$ is the withstand E of $SF_6$ for design and $k_1$=0.85 [26]. The withstand E of $SF_6$ for different pressure is summarized as follow,

| Pressure of $SF_6$ (MPa) / E (kV/mm) | 0.3 | 0.4 | 0.5 | 0.6 | 0.7 |
|---|---|---|---|---|---|
| $E_{50\%}$ | 27.6 | 33.9 | 40.2 | 46.5 | 52.8 |
| $E_B$ | 23.6 | 28.8 | 34.2 | 40 | 44.8 |
| $E_1$ | 20 | 24 | 29 | 33 | 38 |

*Table. 1: The allowed $E_1$ for design (roughness of surface $R_a$=6.3μm) under lightning impulse voltage for coaxial cylinder configuration*

**Method B:** empirical method

Based on the Ravindra Arora's statement [6], the practical electric field strength ($E_{bt}$) of $SF_6$ is dependent on the type of applied voltage and satisfies the following nonlinear exponential curve

$$E_{bt} = (\frac{E_b}{p})t \cdot (10p)^z \qquad \textit{Eq. 5}$$

Where $E_{bt}$ in kV/mm and p in MPa at 20°C. The factor z represents the slop of the curve for different types of voltages. It is determined by the lowest experimental measured values of $E_{bt}$ at different gas pressure. From such curves measured at normal temperature, the values of $E_{bt}$, described as technical term $\left(\frac{E_b}{p}\right)t$ and z for different type of voltage sources are given together in Table. 2.

| Type of voltage | Polarity | $\left(\frac{E_b}{p}\right) t\ in \frac{kV}{mm \cdot MPa}$ | Factor z |
|---|---|---|---|
| AC | | 65 | 0.73 |
| DC | + | 70 | 0.76 |
| Switching impulse (250/2500μs) | + | 73 | 0.76 |
| | - | 68 | 0.73 |
| Lightning impulse (1.2/50μs) | + | 80 | 0.80 |
| | - | 75 | 0.75 |

*Table. 2: Practical electric field strength $E_{bt}$ in $SF_6$ by experiment [6]*

Therefore, according to Table. 1 and Table. 2, the practical withstand electric field strength of $SF_6$ under different voltage types for design can be summarized in following table.

| kV/mm | Method | Polarity | Pressure (MPa) | | | | |
|---|---|---|---|---|---|---|---|
| | | | 0.3 | 0.4 | 0.5 | 0.6 | 0.7 |
| $E_1$ | A | | 20 | 24 | 29 | 33 | 38 |
| $E_{bt}$ under AC | B | | 14.5 | 17.9 | 21 | 24 | 27 |
| $E_{bt}$ under switch impulse voltage | B | - | 15 | 18.7 | 22 | 25.1 | 28.1 |
| | | + | 16.8 | 20.9 | 24.8 | 28.5 | 32.0 |
| $E_{bt}$ under lightning impulse voltage | B | - | 17.1 | 21.2 | 25 | 28.7 | 32.3 |
| | | + | 19.3 | 24.3 | 29 | 33.5 | 37.9 |

*Table. 3: Summary of two different methods under different pressure of $SF_6$ (0.3-0.7MPa)*

The allowed $E_1$ for design by method A conforms to practical electric field strength under positive lightning impulse voltage by method B. However, for the design purpose the lowest withstand electric field strength should be taken into account. For this reason, electric field strength under negative lightning impulse voltage should be considered as criterion. According to the requirement the withstand electric field strength of $SF_6$ for design purpose should be no more than 32.3kV/mm at the pressure 0.7 MPa.

## 2.3 Simulation results of original $SF_6$ bushing

This section begins with the simulation results of the original $SF_6$ bushing. The goal of these simulations is to measure the electric field strength (E) in the different positions along the surface of components and to orientate the positions of peak values of electric field strength ($E_{peak}$). Figure 11 to Figure 15 show the E on the surface of different components under LIV 1050kV and AC $\frac{245kV}{\sqrt{3}}$. Later on, 2D plot electric field distribution of original structure is presented. By this means $E_{peak}$ is impressed directly. Additionally, a table of E on the critical positions is summarized at the last part, which aims to provide a better understanding of E.

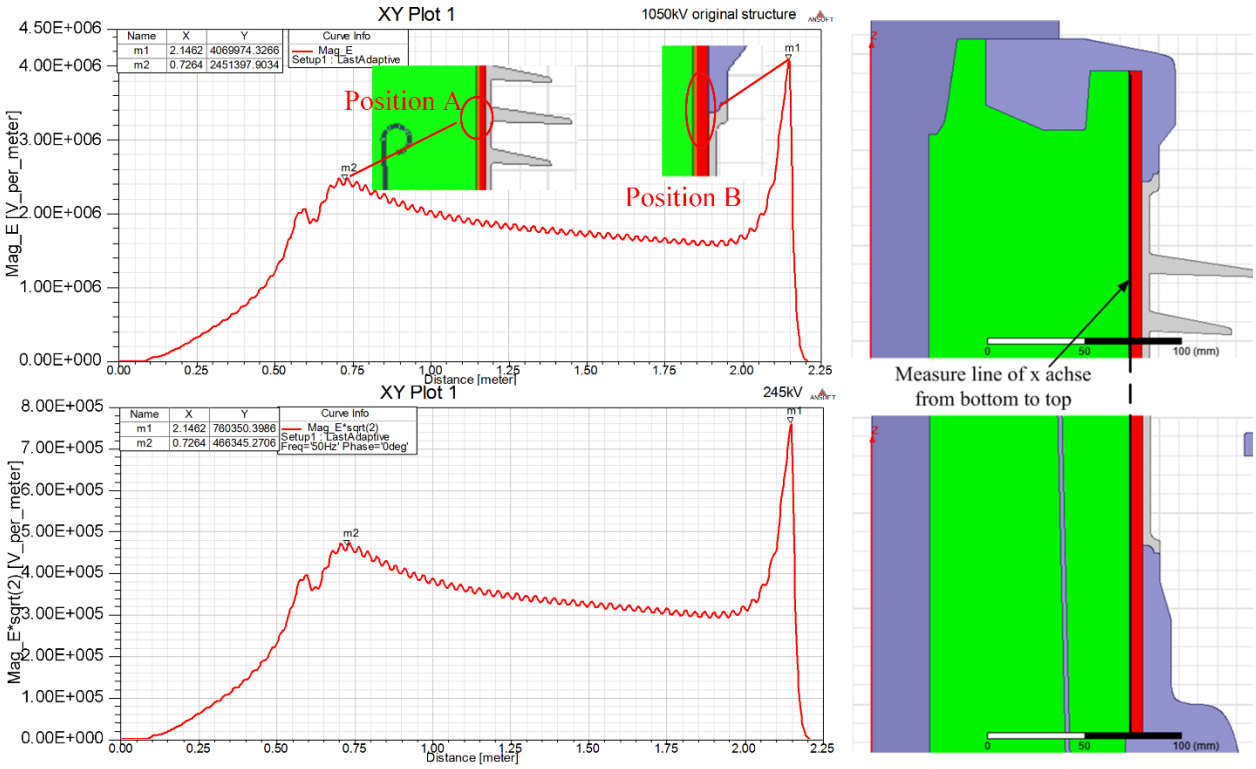


*Figure 11: E along the fiber-reinforced plastic (FRP) tube inside under LIV 1050kV and AC* $\frac{245kV}{\sqrt{3}}$

As seen from Figure 11, the results show E along the inside surface of the FRP tube under LIV 1050kV and AC $\frac{245kV}{\sqrt{3}}$. The shape of the two curves and the position of the peak values under LIV 1050kV and AC $\frac{245kV}{\sqrt{3}}$ are identical. The only difference between these two circumstances is the magnitude of E. This characteristic is also shown in the Figure 12, Figure 13, Figure 14 and Figure 15. Therefore, the identical shape of curves under LIV 1050kV and AC $\frac{245kV}{\sqrt{3}}$ are not shown in the following figures. Two peak values are shown in the curve under LIV 1050kV. The first $E_{peak}$ is 2.45kV/mm and occurs at the distance of approximate 720mm, where locates at the vicinity of the top of ground electrode (position A). The second $E_{peak}$ is 4kV/mm and occurs at the tail of the curve (2150mm), where locates near the interface between the top flange and silicon rubber insulator (position B). The positions of $E_{peak}$ in the curve under AC $\frac{245kV}{\sqrt{3}}$ voltage are

identical. The magnitude of first and second $E_{peak}$ reaches 0.46kV/mm and 0.76kV/mm respectively.

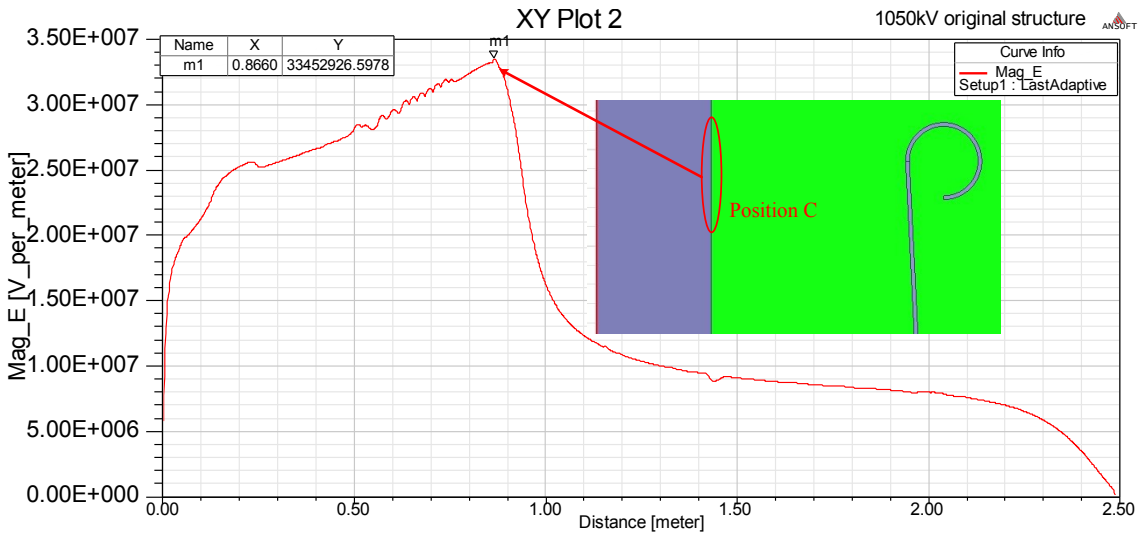


*Figure 12: E along the surface of conductor bar under LIV 1050kV (Measure line see Figure 5)*

The simulation results show E along the surface of conductor bar under LIV 1050kV in Figure 12. A peak value is shown in the curve under LIV 1050kV. The $E_{peak}$ is 33.4kV/mm and occurs at the distance of approximate 860mm, where locates at the vicinity of the top of ground electrode (position C). Under the AC $\frac{245kV}{\sqrt{3}}$ voltage, the $E_{peak}$ reaches at 6.3kV/mm.

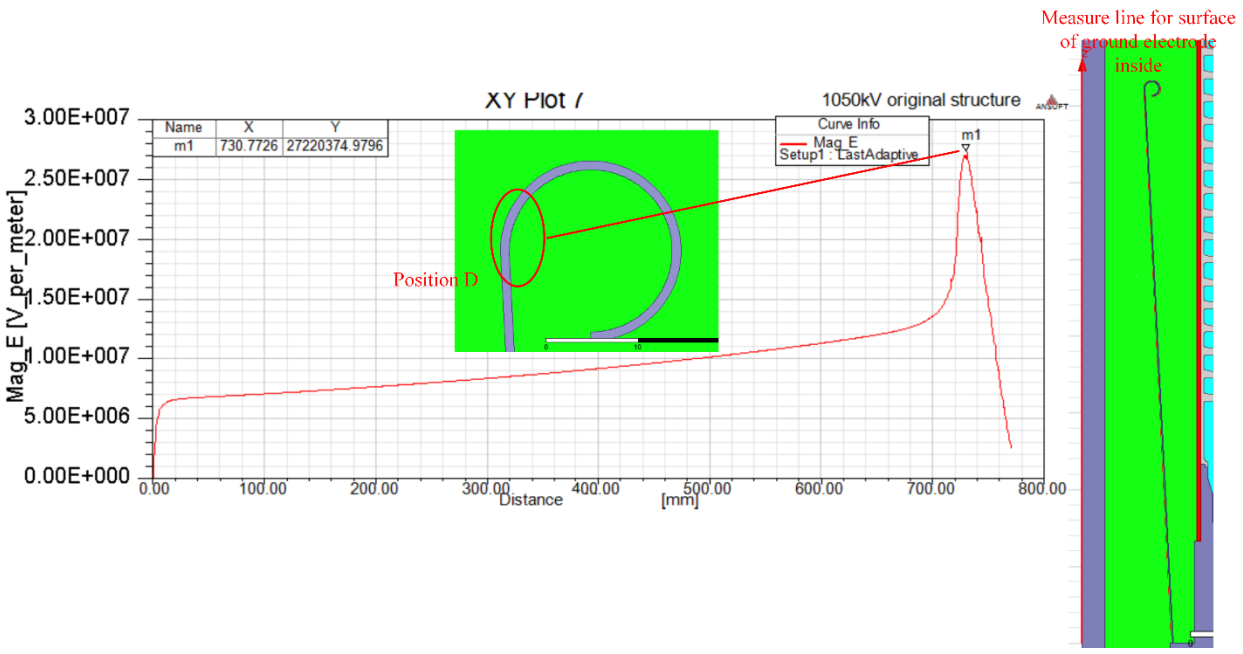


*Figure 13: E along the surface of ground electrode under LIV 1050kV*

The E along the surface of ground electrode under LIV 1050kV is investigated in Figure 13. As the results show, a peak value is shown in the curve under LIV 1050kV. The $E_{peak}$ is 27.2kV/mm and occurs at the distance of approximate 730mm. It is located at the bend part of the ground electrode (position D). Under the AC $\frac{245kV}{\sqrt{3}}$, the $E_{peak}$ reaches at 5.1kV/mm.

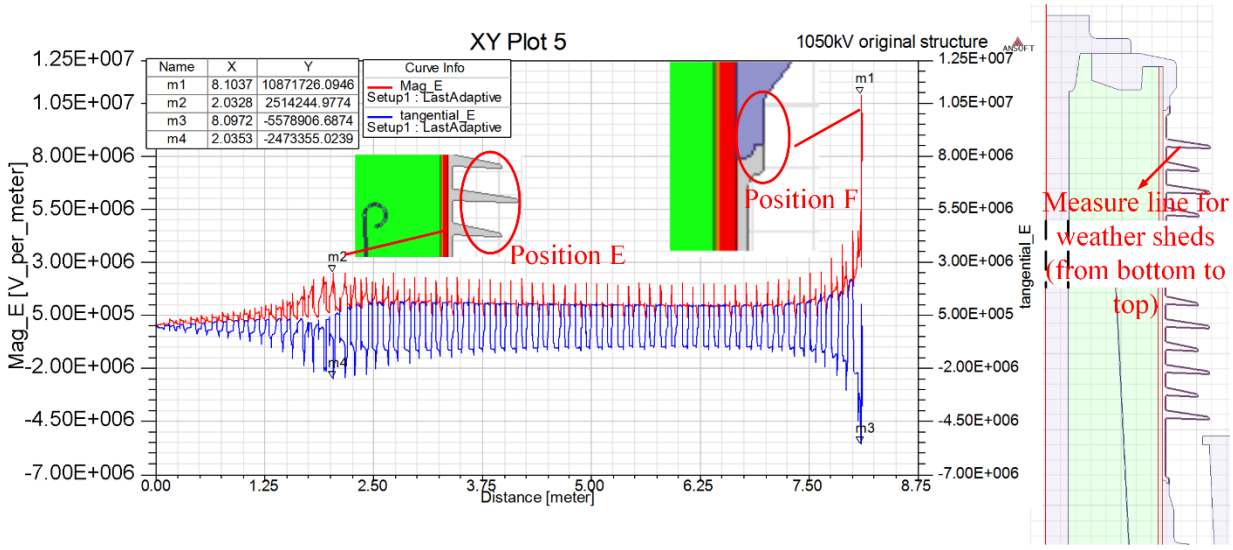


*Figure 14: E along the surface of silicon rubber sheds under LIV 1050kV*

Figure 14 shows the E curve along the surface of silicon rubber sheds under LIV 1050kV. As seen from figure, the electric field distribution is not homogenous and $E_{max}$ is located at the triple point (position F). It is significantly higher than in other positions. $E_{max}$ reaches 10.8kV/mm under LIV 1050kV and 2kV/mm under AC $\frac{245kV}{\sqrt{3}}$. Another peak value occurs at the weather shed closing to ground electrode (position E). The magnitude of this $E_{peak}$ is 2.5kV/mm under LIV 1050kV and 0.48kV/mm under AC $\frac{245kV}{\sqrt{3}}$. Due to the flash-over on the surface of silicon rubber insulator, tangential components of electric field strength ($E_{tan}$) are considered to be measured as well. The results show that $E_{tan,max}$ at the triple point is 5.5kV/mm under LIV 1050kV and 1kV/mm under AC $\frac{245kV}{\sqrt{3}}$. $E_{tan,peak}$ near the ground electrode is 2.4kV/mm under LIV 1050kV and 0.47kV/mm under AC $\frac{245kV}{\sqrt{3}}$.

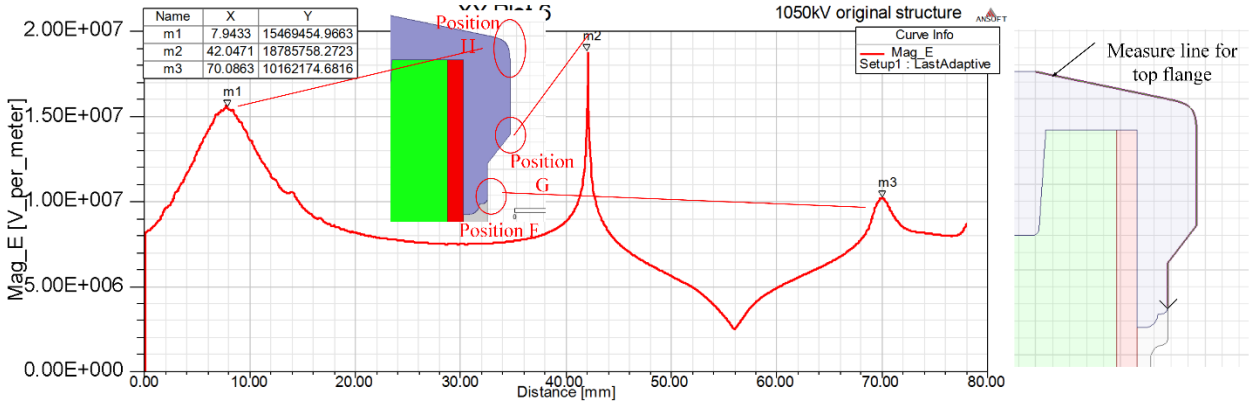


*Figure 15: E along the surface of top flange under LIV 1050kV*

The E curve along the surface of top flange under LIV 1050kV is shown in Figure 15. From the figure it can be seen that the $E_{max}$ occurs at the protrusion of the top flange (position G), which reaches at 18.7kV/mm under LIV 1050kV. $E_{max}$ reaches 3.4kV/mm under AC $\frac{245kV}{\sqrt{3}}$. Another $E_{peak}$ occurs at the bend part of top flange, which is 15.4kV/mm under LIV 1050kV and 2.8kV/mm under AC $\frac{245kV}{\sqrt{3}}$ (position H). In the following, a direct impression of E magnitude is

given by a 2D plot electric field distribution. Table. 4 summarizes all the $E_{peak}$ we mentioned above.

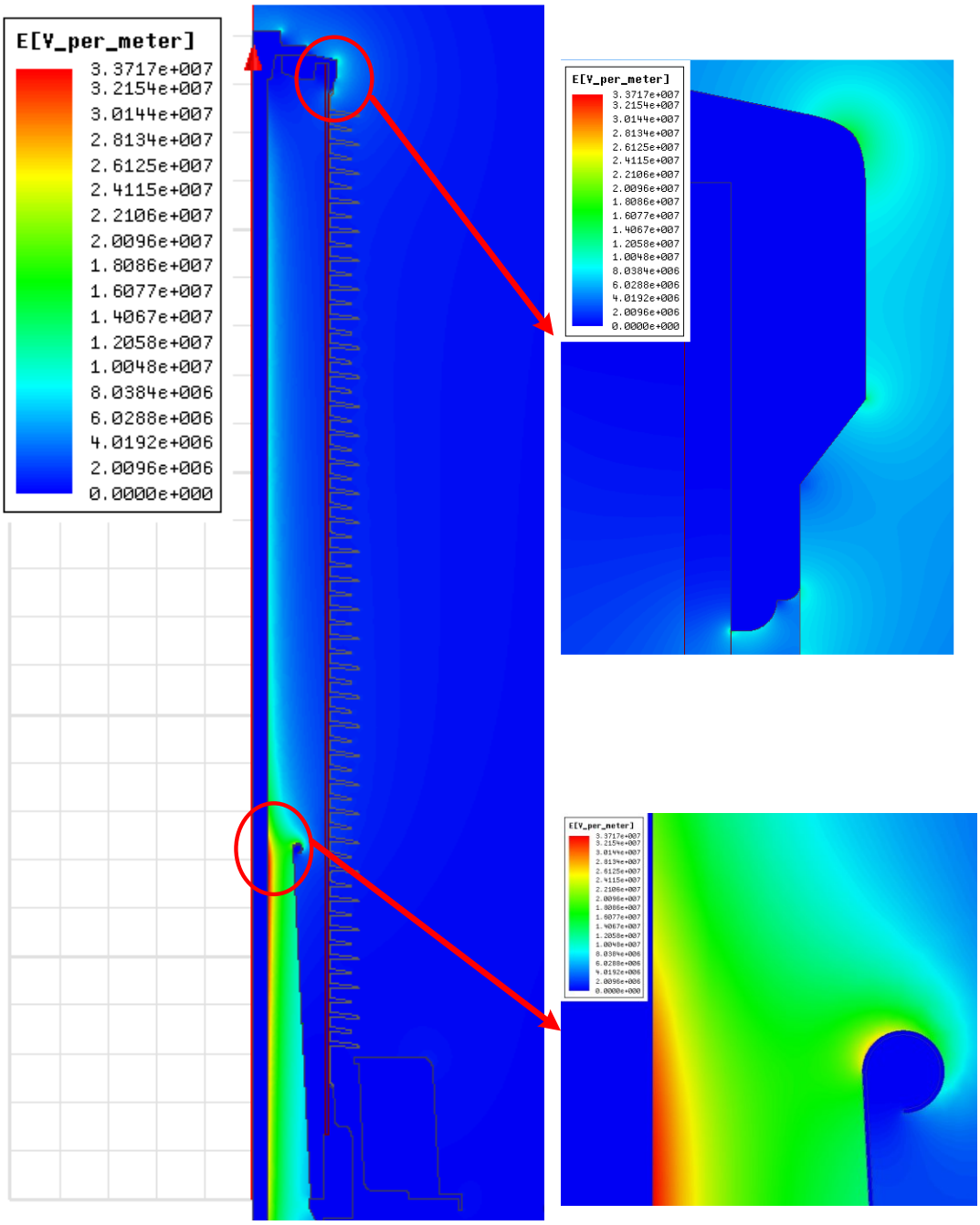


*Figure 16: 2D plot electric field distribution of original structure*

| Positions | $E_{max}$ (kV/mm)<br>$E_{tan,\,max}/E_{tan,\,peak}$ (kV/mm) | |
|---|---|---|
| | LIV 1050kV | AC $\frac{245kV}{\sqrt{3}}$ |
| Conductor bar | 33.4 | 6.3 |
| Surface of ground electrode | 27.2 | 5.1 |
| Inside of FRP | 4 | 0.76 |
| Inside of FRP (close to ground electrode) | 2.45 | 0.46 |
| Top flange | 18.7 | 3.4 |
| Surface of silicon weather sheds | 10.8<br>5.5 | 2<br>1 |
| Surface of silicon weather sheds (close to ground electrode) | 2.5<br>2.4 | 0.48<br>0.47 |

*Table. 4: Summaries of the simulation results with original structure under LIV 1050kV and AC* $\frac{245kV}{\sqrt{3}}$

## 2.4 Summary

This chapter describes the simulation procedures, criteria and results of the original $SF_6$ bushing by means of Ansoft Maxwell 2D. In the section 2.1detailed simulation procedures, i.e. solution type, boundary conditions and mesh generation were discussed. The simulation results were presented in section 2.3. The results show the electric field distribution on the surface of different components. The positions of $E_{max}$ were figured out.

# 3 Hypothesis of break-down mechanisms

The electric field distributions along the surfaces of different bushing components are investigated in the previous chapter. Considering the criteria of $SF_6$ withstand electric field strength in 2.2 and the inappropriate design of the bushing and multi-dielectric interface, it gives an electric field enhancement in the several positions (see Figure 11 to Figure 15). Considering the positions of the electric field enhancement, there are three possibilities of the discharge development, i.e. break-down between the conductor bar and ground electrode (1), partial discharge at the top flange (2), flash-over along surface of the silicon rubber sheds (3). The detailed paths are shown in the Figure 17. In the following sections the mechanisms will be discussed respectively.

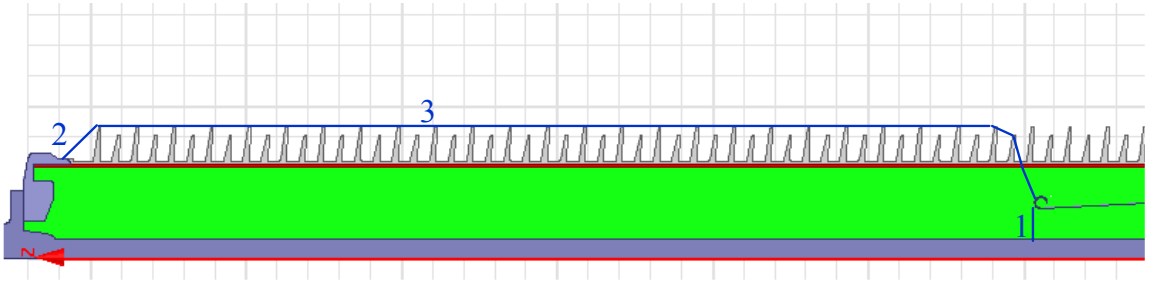


*Figure 17: Three possible break-down paths*

## 3.1 Break-down mechanisms between the conductor bar and ground electrode (Path.1 in Figure 17)

### 3.1.1 α process and streamer theory

It is known that more than 80% of the polarity of lightning in nature is negative. For this reason, the explanation of a break-down process is based on the negative polarity lightning impulse voltage. The break-down between the conductor bar and the ground electrode could be explained by the α process and streamer theory briefly.

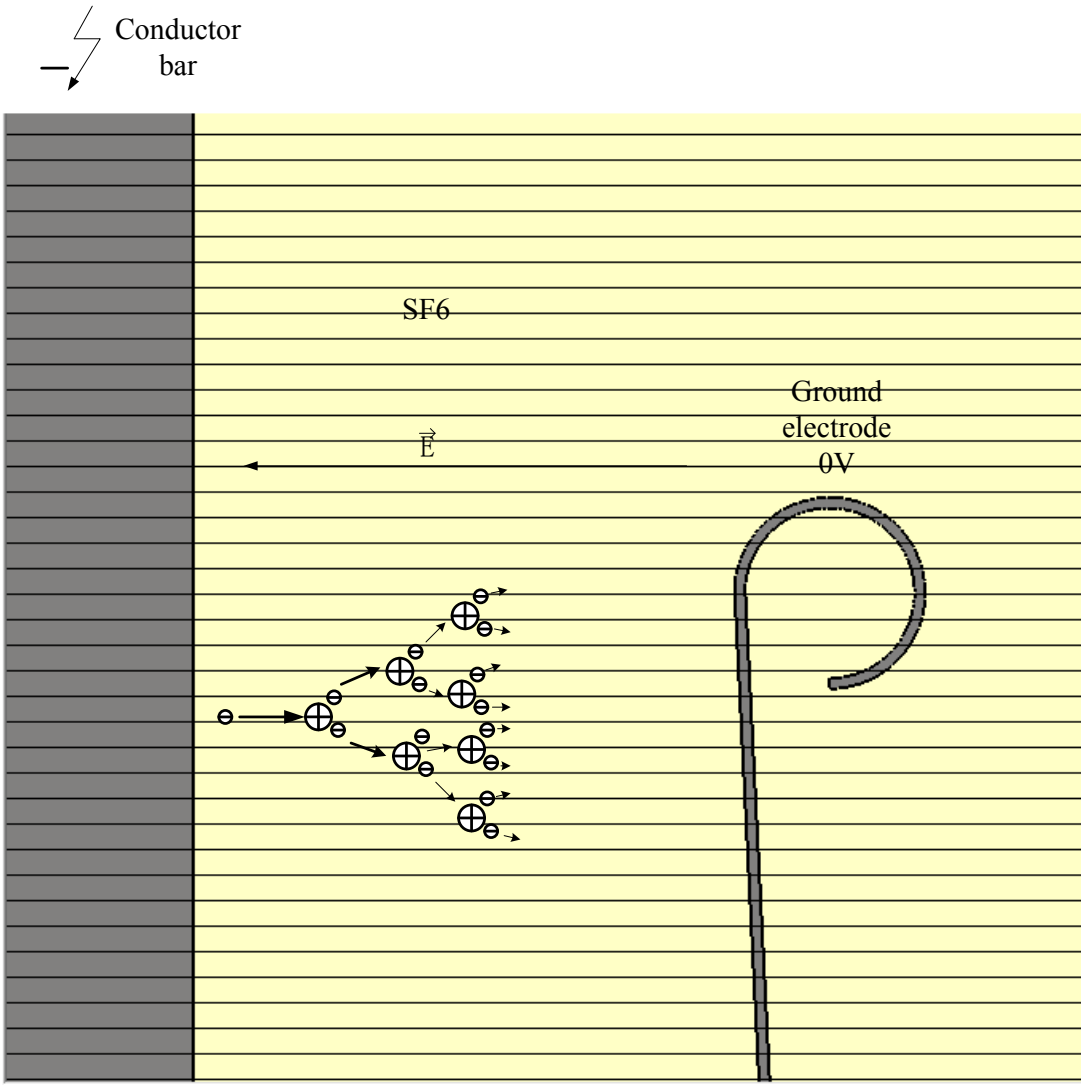


*Figure 18: Development of α process (electron avalanche) between the conductor bar and ground electrode*

The α process is the development of electron avalanches. When the conductor bar is energized by the negative lightning impulse voltage, the initial effective electron, which later develops into an electron avalanche, is originated either by desorption from negative ion $SF_6^-$ or by ionization of $SF_6$ molecules near the conductor bar. The electron originated by desorption is based on following expression:

$$SF^-_6+SF_6 \rightarrow SF_6+SF_6+e \qquad \textit{Eq. 6}$$

Under the effect of the electric field the generated electrons accelerate towards the ground electrode, and gain the kinetic energy. The kinetic energy will become so high that on the

collision with $SF_6$ molecules the electrons may ionize them. For the ionization the $SF_6$ molecule will be separated into two electrons and a positive ion. Since the mass of a $SF_6$ positive ion is much heavier than the electron so that it drifts much more slowly than the electron, and compared to the drift velocity of electrons the positive ions stay in its position and makes no effect on the ionization process. On the opposite side, in the collision process the initial electron loses its kinetic energy and turns into ionization energy. Now the previous electron and freshly originated electron accelerate together and repeat this process. In the first collision a fresh electron will be originated, which means one electron will turn into two electrons, two will turn into four electrons. The number of electrons increases exponentially ($n=e^{\alpha x}$). More and more electrons will be released from the $SF_6$ molecules by collision and ionization processes. An 'avalanche' of electrons ultimately develops towards to the ground electrode as shown in Figure 18.

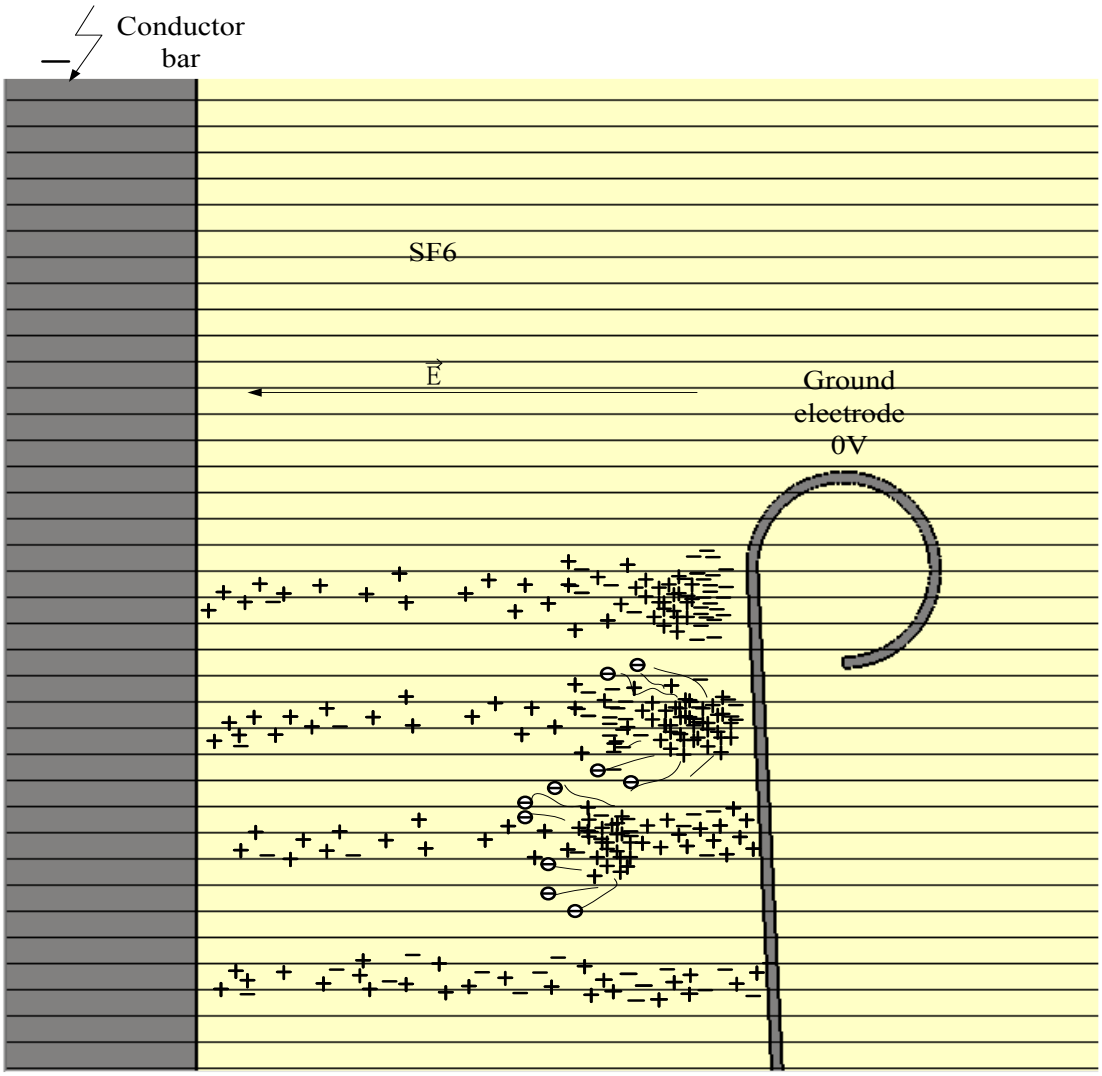


*Figure 19: The development of streamer between the conductor bar and ground electrode*

The further development of the breakdown process refers to the streamer theory shown in Figure 19. Due to the exponential increase of electron numbers most of the fresh electrons are originated at the very last moment. Most of the positive ions accumulate at the head of electron avalanche. Taking into account the movement of electron the electrons are located in front of positive ion. Under this circumstance the distribution of positive ions and electrons enhances the inhomogeneous distribution of the electric field and causes more distortion of the electric field at avalanche head. When the primary electron avalanche develops its critical length (i.e. the number of electron approaches its critical number, the degree of distortion exceeds its limit), the photo-ionizations will occur at the head of avalanche. In this condition the secondary avalanches are formed from the fresh electrons, which are originated by the photo-ionizations in the vicinity of

the primary avalanche head. Because of the electric field and accumulation of positive ions in the vicinity of the ground electrode, the fresh electrons move towards the ground electrode once again. The remaining positive ions increase the space charges effect. This process develops very fast until the positive ions extend to the conductor bar rapidly resulting in the formation of plasma streamer. The gap between the ground electrode and conductor bar is totally broken down.

From the explanation of the mechanism we can notice that the critical number of electrons, i.e. critical length of electron avalanche plays an important role in development of the breakdown process. In the following part the parameters, which influence the critical number of electrons, will be investigated.

$SF_6$ is an electronegative gas. In the development of avalanche processes (i.e. the process of splitting $SF_6$ molecules into positive ions and electrons) the absorption of electrons occurs simultaneously. The electron attachment of $SF_6$ should be taken into account. Similar to the ionization coefficient α in the α process, the attachment coefficient η is introduced. η is defined as the number of attaching collisions caused by one electron drifting pro cm in the direction of electric field. The ionization coefficient α should be modified to effective ionization coefficient $\bar{\alpha}$, which is expressed as follow:

$$\bar{\alpha} = \alpha - \eta \qquad \textit{Eq. 7}$$

According to the experimental experience the equation can be given:

$$\frac{\bar{\alpha}}{p} = K\left[\frac{E}{p} - \left(\frac{E_b}{p}\right)_i\right] \qquad \textit{Eq. 8}$$

The break-down criteria for the plasma steamer mechanism are based on the critical number of electrons, which are achieved from the avalanche, when the length of the avalanche reaches a critical length $x_c$. Beginning with a single inception electron ($n_0$=1), the critical number of electrons $n_{cr}$ in the primary avalanche considering electron attachment when the length of the avalanche approaches critical length $x_c$ is given by:

$$\int_0^{x_c} \bar{\alpha} dx = \ln n_{cr} \approx 18.4 \qquad \textit{Eq. 9}$$

In our case, the conductor bar and ground electrode can be considered as a coaxial cylindrical electrode system (in a quasi-inhomogeneous field). The electric field distribution in a coaxial

cylinder with the radius $r_i$ of conductor bar and radius $r_o$ of ground electrode can be expressed by the following equation:

$$E_r = \frac{1}{r} \cdot \frac{U}{\ln\left(\frac{r_0}{r_i}\right)} \qquad \textit{Eq. 10}$$

$$E_{\max} = \frac{1}{r_i} \cdot \frac{U}{\ln\left(\frac{r_0}{r_i}\right)} \qquad \textit{Eq. 11}$$

From the Eq. 10 and Eq. 11 $E_r$ can be derived

$$E_r = \frac{r_i}{r} E_{\max} \qquad \textit{Eq. 12}$$

When a break-down occurs between the conductor bar and ground electrode, the maximum electric field strength $E_{max}$ should be acquired from the maximum break-down field strength $E_{b,max.}$ From the Eq. 7, Eq. 8, Eq. 9 and Eq. 12 the expression can be given by:

$$\overline{\alpha} = K \cdot \left( \frac{E_{b,\max} \cdot r_i}{r} - E_{bi} \right) \qquad \textit{Eq. 13}$$

To satisfy the streamer criterion, the Eq. 13 is substituted into Eq. 9, and putting $r_c=r_i+x_c$

$$\int_0^{x_c} K \cdot \left( \frac{E_{b,\max} \cdot r_i}{r} - E_{bi} \right) dx = \ln n_{cr} \approx 18.4 \qquad \textit{Eq. 14}$$

The initial break-down field intensity $E_{bi}$ can be expressed by $E_{rc}$ as follow:

$$E_{bi} = E(r_c) = \frac{r_i}{r_c} E_{b,\max} \qquad \textit{Eq. 15}$$

Here, a new factor $f_{max}$ ‘relative maximum break-down electric field strength’ is introduced:

$$f_{\max} = \frac{r_c}{r_i} = \frac{E_{b,\max}}{E_{bi}} \qquad \textit{Eq. 16}$$

Then the Eq. 14 can be calculated to,

$$f_{\max}\left(\ln f_{\max} - 1\right) = \frac{\ln n_{cr}}{K \cdot r_i \cdot E_{bi}} - 1 \qquad \textit{Eq. 17}$$

And the critical length of electron avalanche $x_c$ can be given by

$$x_c = r_i\left(f_{\max} - 1\right) \qquad \textit{Eq. 18}$$

In order to avoid break-down, we hope the critical length of electron avalanche is as long as possible. It means the electrons avalanche needs to move along a longer path so that electrons will reach its critical number. Afterwards the electron avalanche will turn into the steamer. Otherwise the gap between the conductor bar and ground electrode will not break down. With increasing conductor bar radius $r_i$ the critical length of electron avalanche $x_c$ increases. And it is easy to understand this circumstance as well: The maximum electric field strength occurs at the surface of conductor bar. According to Eq. 11 the $E_{max}$ at a smaller conductor bar radius is greater than $E_{max}$ at a larger conductor bar, whereas the initial break-down field strength $E_{bi}$ will not be changed. In the condition of lower $E_{max}$ electrons avalanche needs to move more to reach the critical number of electrons. Nevertheless, the increasing of conductor bar radius should be in the appropriate extent. Two aspects should be taken into account as well. On the one hand, as seen in Figure 20 $E_{max}$ is not a monotone decreasing function. When the radius of conductor bar is getting larger and larger, $E_{max}$ will not be decreased but increased. On the other hand, with the increasing of the conductor bar the distance between conductor bar and ground electrode will get smaller, the product of pd will get lower. The streamer mechanism will be invalid any more, if pd is smaller than 0.266mm·MPa. Furthermore, in the following chapter 3.1.3 considering the minimal electric field strength on the surface of conductor bar the optimal distance between $r_i$ and $r_o$ will be calculated. Therefore, in the further development of the bushing structure the radiuses of conductor bar and ground electrode should be set at appropriate value.

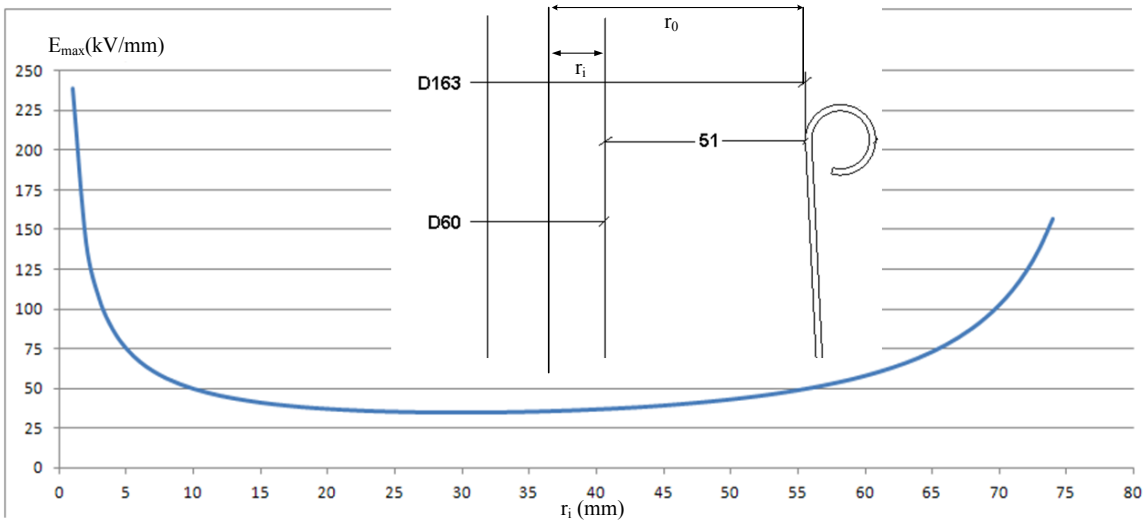


*Figure 20: The curve shape of $E_{max}$ under the considering original structure as the coaxial cylindrical system*

### 3.1.2 Polarity effect

Although the polarity effect normally occurs in the inhomogeneous field, and the electric field between conductor bar and ground electrode belongs to the quasi-inhomogeneous fields, the polarity effect between the conductor bar and ground electrode should still be taken into account. In our case, it is assumed that compared to the electron the positive ion stays in its position, because the electron moves much faster than the positive ion. Considering again that more than 80% lightning is negative polarity, the explanation is based on the negative polarity and similar to the α process. When the conductor bar is energized by the negative polarity of lightning impulses, the space close to the conductor bar is ionized. The ionized electrons will be subjected to the electric field force and move to the ground electrode. In the moving procedure the electrons will collide with the $SF_6$ molecules, and this leads to emit more electrons into the space. The electrons will move to the ground electrode. Compared with the electron the positive ion stays at its position, which causes the electric field distortion between the conductor bar and ground electrode. In the meantime due to the distortion of electric field more $SF_6$ molecules will be ionized and more electrons and positive ions will be emitted, so that the procedure of break-down will be accelerated and the break-down voltage of negative polarity will get lower than positive polarity. The conclusion can be drawn that the polarity effect is mainly caused by the effect of

space charge, and compared to positive polarity the break-down voltage of $SF_6$ is a little lower in the quasi-inhomogeneous field under the negative polarity lightning impulse. That is the reason why all assumptions are under the condition of negative polarity lightning impulse. Figure 21 shows the polarity effect under negative lightning impulse voltage in quasi-inhomogeneous field.

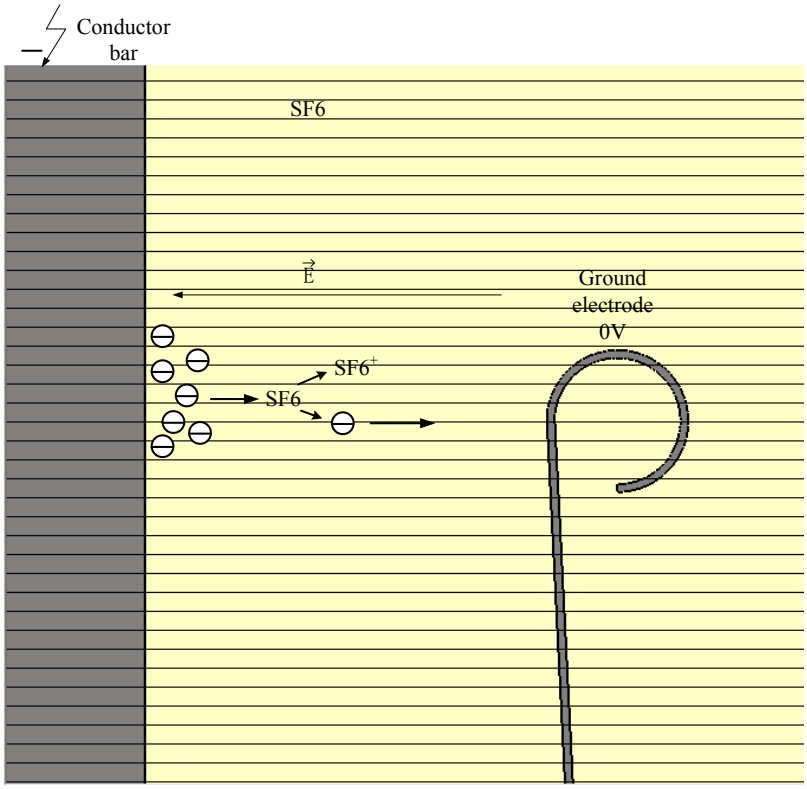


*Figure 21: Schematic illustration of the polarity effect under negative lightning impulse voltage*

### 3.1.3 Consideration of E on the surface of conductor bar

Considering the theory of the α process and the streamer theory with the appropriate increase of the radius of the conductor bar, the electric field strength in the gap is reduced, so that the ionization process will need more time to reach the critical number of electrons. It is shown in Figure 20 that the increasing of the conductor bar radius is not unlimited. In this section, in order to minimize the electric field strength on the surface of conductor bar, the optimal ratio of conductor bar radius $r_i$ and ground electrode radius $r_o$ will be determined.

The conductor bar and ground electrode can be approximately considered as two coaxial cylinders with inner and outer radius $r_i$ and $r_0$ respectively. For a coaxial cylindrical electrode system at a distance r from the conductor bar the field strength is given by

$$E_r = \frac{U}{r \cdot \ln \frac{r_0}{r_i}} \qquad \textit{Eq. 19}$$

In order to optimize the electric field strength $E_r$ on the surface of the conductor bar, we assume that U and outer radius $r_0$ have been given as constant value. The inner radius $r_i$ can be determined from the Eq. 19 by differentiating this equation with substituting $r=r_i$ and equating to 0.

$$\frac{dE_{ri}}{dr_i} = \frac{d}{dr_i}\left[\frac{U}{r_i \cdot \ln \frac{r_0}{r_i}}\right] = 0 \qquad \textit{Eq. 20}$$

Hence, the optimum ratio of $r_0$ to $r_i$ for the lowest electric field strength on the surface of conductor bar is given by,

$$\frac{r_0}{r_i} = e \approx 2.718 \qquad \textit{Eq. 21}$$

The radius of conductor bar is kept constant, the radius of ground electrode cannot be varied randomly. The optimal radius $r_0$ of ground electrode must approximate to $2.7 \cdot r_i$.

## 3.2 Partial discharge at top flange (Path.2 in Figure 17)

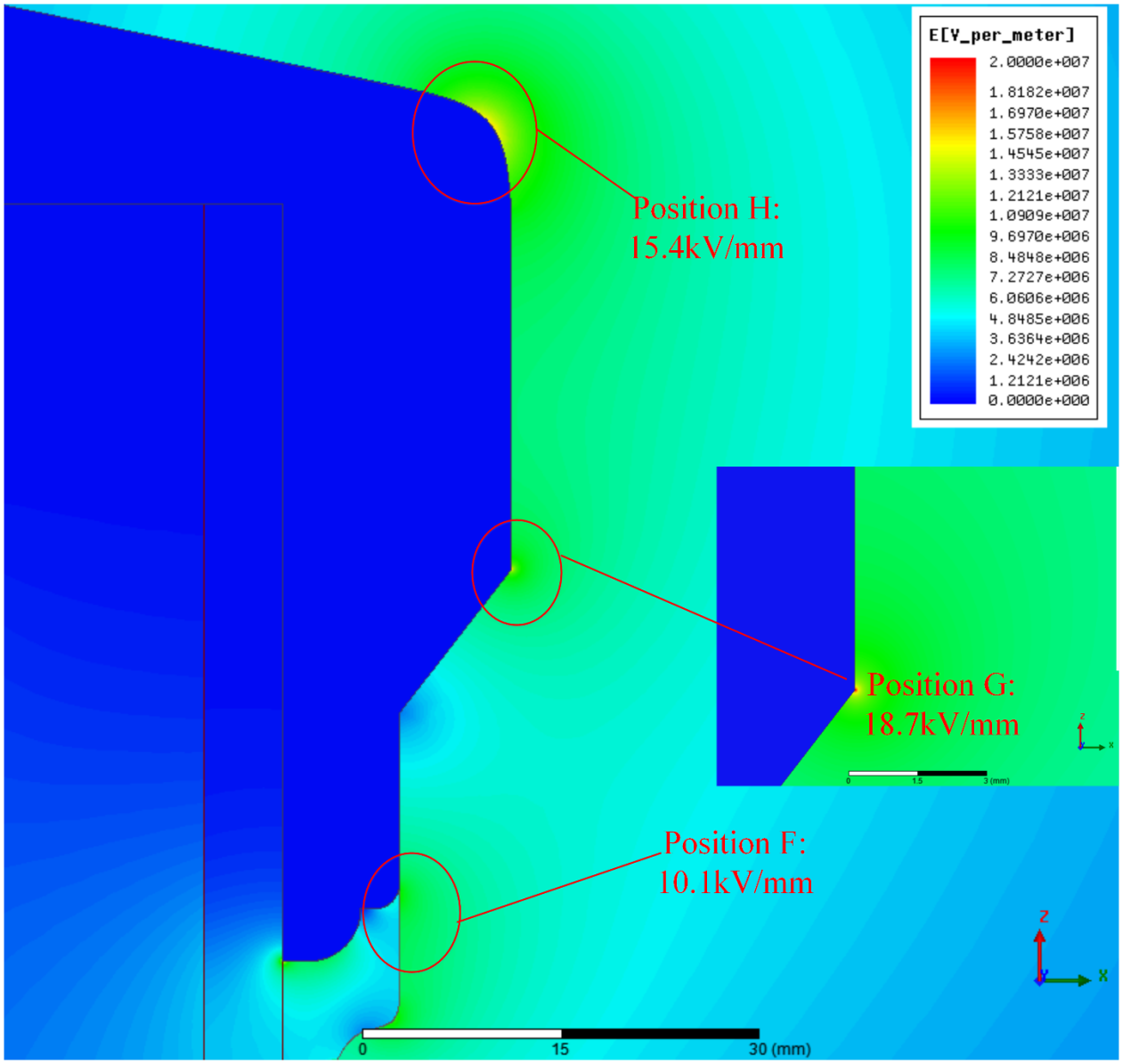


*Figure 22: Three critical locations at the top of flange under LIV 1050kV*

Taking into account that the peak values of the electric field strength is located at the periphery of top flange and at the triple point of top flange, silicon rubber insulator and air, which might lead to partial discharge. The mechanism of partial discharge can be explained by the following reasons.

1. Electric field strength at the triple point (See Figure 22, position F)

2. Contour periphery of top flange (See Figure 22, positions H and G)

$E_{peak}$ at positions H and G is attributed to flawed design of top flange. Therefore, the discussion concentrates on $E_{peak}$ at the triple points.

### 3.2.1 Electric field strength in the vicinity of triple point

The insulation system of triple point comprises of different dielectric materials (air, silicon rubber materials and aluminum alloy). Since the theory of electrical field strength enhancement at the triple point is hardly conclusive the discussion concentrates on the vicinity of the triple point. The interfaces between the air and aluminum alloy and between the air and silicon rubber are analyzed respectively. The behavior of different dielectric materials with respect to the electrostatic field is totally distinguished by their permittivities ε. The variation in parametric values of permittivity of dielectric materials leads to different potentials as well as different electric field distributions in individual dielectrics.

First of all, the permittivity of metal i.e. aluminum alloy under electrostatic and AC voltage is investigated. The permittivity of the metal material depends on the material polarization under the effect of the external field. [34][35] The polarization can be divided into three types i.e. the electron displacement polarization, ionic displacement polarization and the orientation polarization of intrinsic dipole moment. Since most of the metals belong to the atomic crystals, and there is a large number of free electrons inside of metal, so that typically an intrinsic dipole moment does not exist. Even if some of metals have the intrinsic dipole moment the crystal structure is so compact that the intrinsic dipole moment is difficult to orientate. Taking into account the mass of nucleus is much larger than the electron mass, and the velocity of ion is small, the contribution of ion displacement polarization can be neglected. Therefore, the polarization in metal mainly depends on the electron displacement polarization.

According to the classical electron theory, in the absence of an external electric field the electron rotates around the nucleus. The centers of positive and negative charge are overlapped, the intrinsic dipole moment is zero. When the external electric field is applied the electron orbit has displacement with the result that the centers of positive and negative charge are separated and

generate a dipole moment. This is also known as the induced electrical dipole moment. In order to estimate the induced electric dipole moment, electrons rotating around the nucleus can be considered as a simple resonant bounding electron model.[36] Each electron is bounded by a restoring force and by phenomenological damping force, so the motion equation of electrons in the dielectric under the external field is:

$$mr''+m\gamma r'+m\omega_0^2 r = eE_0 e^{-i\omega t}$$

*Eq. 22*

Where $\omega_0$ is the natural bounding frequency of electrons, ω is the frequency of the external field, γ is the damping coefficient. The solution of the above formula is

$$r = r_0 e^{-i\omega t} \qquad \textit{Eq. 23}$$

Eq. 23, then gives

$$r' = -i\omega r_0 e^{-i\omega t} = -i\omega r$$
$$r'' = (-i\omega)^2 r_0 e^{-i\omega t} = -\omega^2 r \qquad \textit{Eq. 24}$$

Substituting $r, r'$ and $r''$ into the Eq. 22, $r_0$ can be given:

$$r_0 = \frac{eE_0}{m(\omega_0^2 - \omega^2 - i\gamma\omega)} \qquad \textit{Eq. 25}$$

Substituting $r, r'$ and $r''$ into the Eq. 23, r can be given:

$$r = \frac{eE_0}{m(\omega_0^2 - \omega^2 - i\gamma\omega)} e^{-i\omega t} \qquad \textit{Eq. 26}$$

Therefore, the dipole moment contributed by an electron $P_e$ can be expressed:

$$P_e = er = \frac{e^2 E_0 e^{-i\omega t}}{m(\omega_0^2 - \omega^2 - i\gamma\omega)} = \frac{e^2}{m(\omega_0^2 - \omega^2 - i\gamma\omega)} E \qquad \textit{Eq. 27}$$

The number of atoms in the metal per unit volume is assumed as N, each atom owns the number of Z electrons, the natural frequency of each electron is $\omega_0$, the polarization of metal P can be deduced:

$$P = NZP_e = \frac{NZe^2}{m(\omega_0^2 - \omega^2 - i\gamma\omega)} E \qquad \textit{Eq. 28}$$

Taking into account $P = \varepsilon_0 \chi_e E$, $\varepsilon = \varepsilon_r \varepsilon_0 = (1 + \chi_e)\varepsilon_0$ , then gives

$$P = (\varepsilon - \varepsilon_0) E \qquad \textit{Eq. 29}$$

Comparing with Eq. 28 and Eq. 29, the permittivity ε can be given

$$\varepsilon = \varepsilon_0 + \frac{NZe^2}{m(\omega_0^2 - \omega^2 - i\gamma\omega)} \qquad \textit{Eq. 30}$$

$$\varepsilon_r = \frac{\varepsilon}{\varepsilon_0} = 1 + \frac{NZe^2}{m\varepsilon_0(\omega_0^2 - \omega^2 - i\gamma\omega)} \qquad \textit{Eq. 31}$$

In the above calculation, $\omega_0$ is the natural bounding frequency of electrons, γ is the damping coefficient. However, in fact the electrons may have different natural bounding frequencies of electrons and damping coefficients. It is assumed that the electrons have K different natural bounding frequencies and damping coefficients. Therefore, they own the number of $f_j$ $(\mathrm{j} = 1, 2, 3, .... \mathrm{K})$ electrons with different natural bounding frequencies of electrons $\omega_j$ and damping coefficients $\gamma_j$ , so the Eq. 31 can be rewritten into:

$$\varepsilon_r = 1 + \frac{Ne^2}{m\varepsilon_0} \sum_{j=1}^{K} \left[ \frac{f_j}{(\omega_j^2 - \omega^2 - i\gamma_j\omega)} \right] \qquad \textit{Eq. 32}$$

Where $\sum_{j=1}^{K} f_j = Z$ . Besides that, considering the existence of free electrons in the metal and so far as this part of electrons be concerned, $\omega_j = 0$ . It is assumed that each atom has the number of $f_0$ free electrons. If the contribution of this part of free electrons to the permittivity is separated from Eq. 32, the Eq. 32 can be expressed by the following variation:

$$\varepsilon_r = 1 + \frac{Ne^2}{m\varepsilon_0}\sum_{j=1}^{K}\left[\frac{f_j}{(\omega_j^2 - \omega^2 - i\gamma_j\omega)}\right] + i\frac{Nf_0e^2}{m\varepsilon_0\omega(\gamma_0 - i\omega)} \qquad \textit{Eq. 33}$$

Where $\sum_{j=1}^{K} f_j = Z - f_0$, $\gamma_0$ is the damping coefficient of a free electron under external electric field. The obtained Eq. 33 is a mathematic expression of metallic relative permittivity. It can be seen that from the Eq. 13 the permittivity of metal is complex value. The natural bounding frequencies of electrons $\omega_j$ has the order of magnitude $10^{15}$. The frequency of the external electric field $\omega$ is far less than the $\omega_j$ under the circumstance of electrostatic i.e. $\omega = 0$ and AC voltage i.e. $\omega = 100\pi$ . The Eq. 33 can be simplified into

$$\varepsilon_r = 1 + \frac{Ne^2}{m\varepsilon_0}\sum_{j=1}^{K}\frac{f_j}{\omega_j^2} + i\frac{Nf_0e^2}{m\varepsilon_0\omega\gamma_0} \qquad \textit{Eq. 34}$$

with the real component

$$\varepsilon_r' = 1 + \frac{Ne^2}{m\varepsilon_0}\sum_{j=1}^{K}\frac{f_j}{\omega_j^2} \qquad \textit{Eq. 35}$$

and with the imaginary component

$$\varepsilon_r'' = \frac{Nf_0e^2}{m\varepsilon_0\omega\gamma_0} \qquad \textit{Eq. 36}$$

So Eq. 34 can be rewritten into

$$\varepsilon_r = \varepsilon_r' + i\varepsilon_r'' \qquad \textit{Eq. 37}$$

The real component $\varepsilon_r'$ presents the relative permittivity under electrostatic and AC voltage. The imaginary component $\varepsilon_r''$ presents the influence of the electromagnetic wave on metal. Hence, only the real component $\varepsilon_r'$ is within the scope of the further discussion. The real component $\varepsilon_r'$ is a limited constant depending on the different natural bounding frequencies of electrons $\omega_j$ and irrelevant with external frequency $\omega$. If it is assumed that all the natural bounding frequencies $\omega_j$

equal to $\omega_0$, the bounding frequency of electron $\omega_0$ is equivalent to optical frequency i.e. $\omega_0 \approx 6\times10^{15} Hz$. In the metal $\sum_{j=1}^{K} f_j \approx 10^{29}$, and $\varepsilon_r'$ can be derived from Eq. 35

$$\varepsilon_r' = 1 + \frac{Ne^2}{m\varepsilon_0}\sum_{j=1}^{K}\frac{f_j}{\omega_j^2} = 1 + \frac{10^{29}\cdot(1.6\cdot10^{-19})^2}{9.1\cdot10^{-31}\cdot8.85\cdot10^{-12}\cdot(6\cdot10^{15})^2} \approx 10 \qquad \textit{Eq. 38}$$

Obviously, the relative permittivity of aluminum depends on the different natural bounding frequencies of aluminum electrons $\omega_j$. $\omega_j$ has the order of magnitude $10^{15}$. Therefore, the relative permittivity of aluminum is a constant larger than 1.

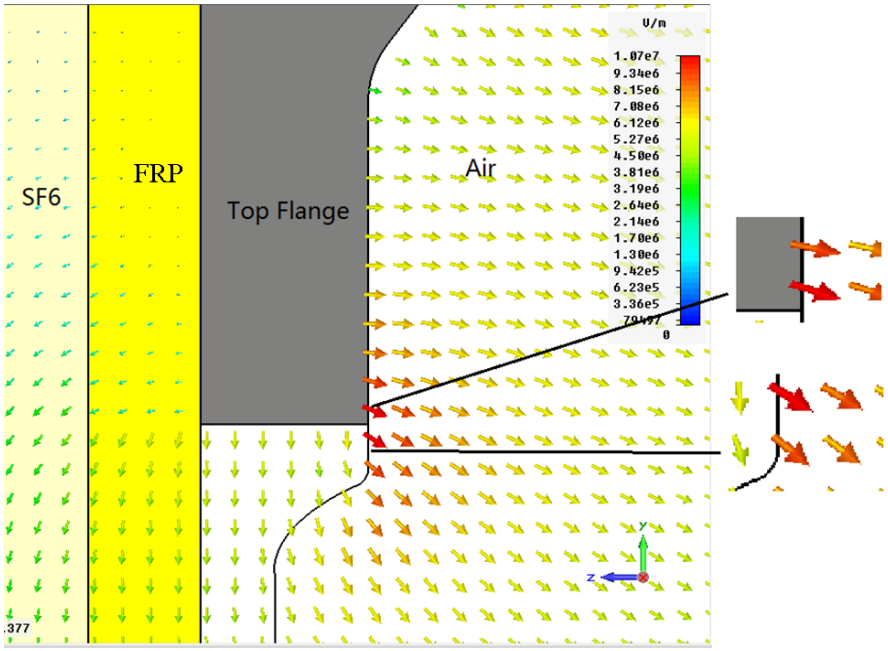


*Figure 23: Electric field line at the bottom of top flange*

The electric field strength at the interface between the air and silicon rubber and between air and aluminum can be calculated respectively. According the interface conditions for electric field strength:

Tangential: $\mathrm{E_{1t}} = \mathrm{E_{2t}}$ *Eq. 39*

Normal: $\varepsilon_1 \frac{\partial\varphi_1}{\partial n} - \varepsilon_2 \frac{\partial\varphi_2}{\partial n} = \sigma$ *Eq. 40*

If there is no free charge σ at the interface, the equation of normal component can be simplified to

$$\varepsilon_1 \frac{\partial \varphi_1}{\partial n} = \varepsilon_2 \frac{\partial \varphi_2}{\partial n}$$

$$\varepsilon_0 \varepsilon_{r1} E_{1n} = \varepsilon_0 \varepsilon_{r2} E_{2n}$$

$$\frac{E_{1n}}{E_{2n}} = \frac{\varepsilon_{r2}}{\varepsilon_{r1}} \qquad \textit{Eq. 41}$$

It shows that the normal component of electric field strength in two different dielectrics depends on their relative permittivity. The greater the permittivity of the material, the less the material withstands the electric field strength in normal component. In this case, at the periphery of silicon rubber side the normal component is apparently more dominant than the tangential component. The permittivity of composite material ($\varepsilon_r$=2.9) is about 3 times higher than air ($\varepsilon_r$=1). When the electric field is entering into the air, based on Eq. 39 the tangential component remains unchanged, whereas according to the Eq. 41 the normal component in air gets much greater. By the same argument and considering that the permittivity of aluminum ($\varepsilon_r$>1) is also larger than the permittivity of air ($\varepsilon_r$=1), the normal component in air gets greater as well. It leads to the mutation of electric field strength enhancement at the interface to the air side. In the vicinity of a triple point the electric field strength appears to be high in this area, and partial discharges might supervene.

## 3.3 Flash-over along the surface of silicon rubber insulator (Path.3 in Figure 17)

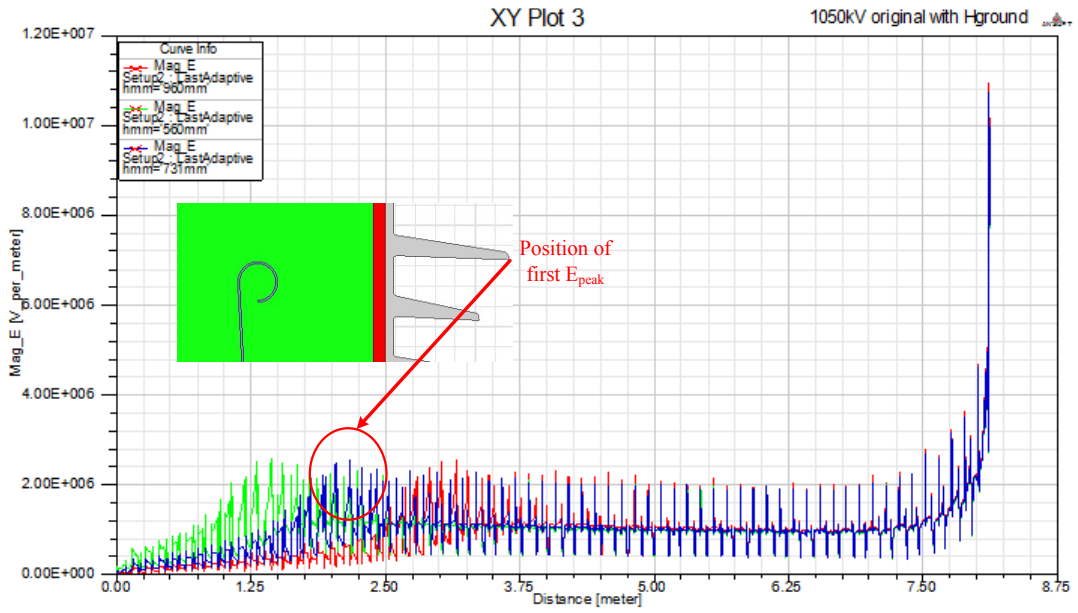


*Figure 24: E along the surface of silicon rubber insulator with different heights of ground electrode under the LIV 1050kV (measure line see Figure 14)*

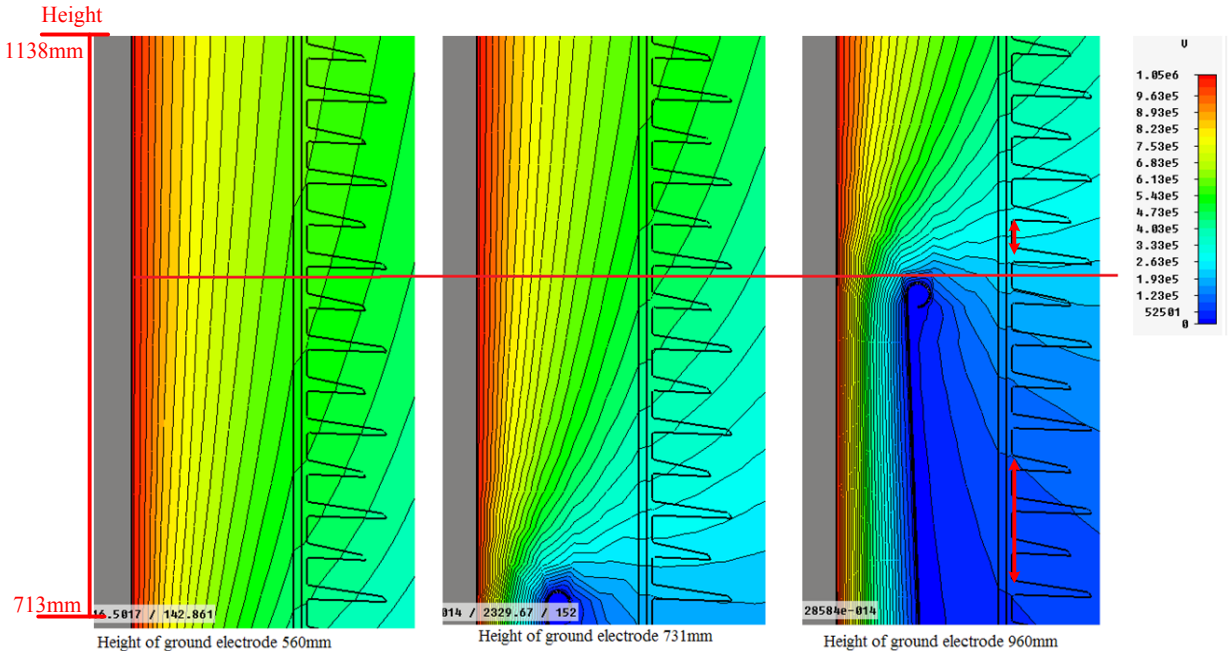


*Figure 25: Equipotential lines and potential distributions of 3 different heights of ground electrode (560mm, 731mm and 960mm) in the same position of bushing (713mm-1138mm)*

The flash-over supervenes between the top flange and the position of the first $E_{peak}$. Therefore, the first $E_{peak}$, the $E_{peak}$ at triple point and the E along the surface of silicon rubber insulator have a great influence on the flash-over occurrence. The Figure 24 shows E along the surface of the silicon rubber insulator with different heights of the ground electrode. With the increase of the ground electrode the first $E_{peak}$ (2.5kV/mm) moves with the height of the ground electrode. It is located always at the outside corresponding location near the ground electrode top. The explanation can be given by the Figure 25. As seen in the Figure 25 the ground electrode causes the equipotential lines to be more crowded internally, and at the same height the interval between the two equipotential lines becomes wider. It makes the increase of the potential at the lower part of insulator smooth. When the equipotential lines just disperse into the air side, the interval between two equipotential lines along the upper part of the ground electrode become narrower compared to the original position under the ground electrode (red arrow). At the ground electrode top the potential increases dramatically, which simultaneous leads to the $E_{peak}$ at the surface of the insulator. Besides that, the height of ground electrode varies the potential distribution on the surface of the insulator as well. A horizontal red line is drawn across the Figure 25. At the same position the potential with the higher ground electrode is lower than with the lower ground electrode, which means that more potential stress is distributed in the upper part of insulator. On the opposite side, at the same height the lower part of the insulator with a higher ground electrode is subjected to less potential.

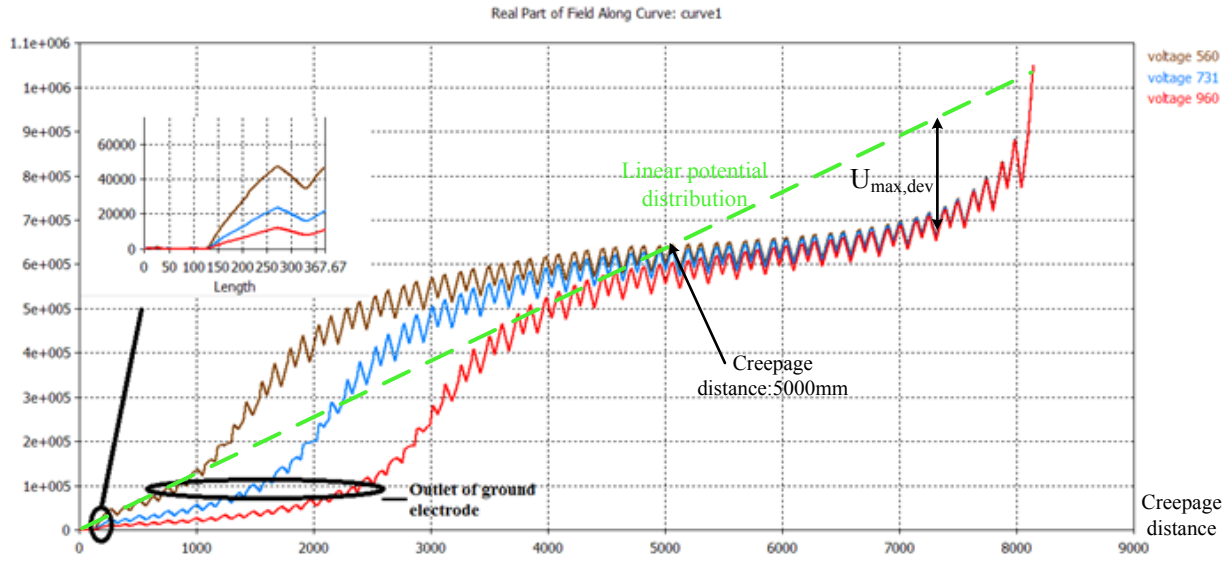


*Figure 26: The potential distribution along the surface of insulator with different height of ground electrodes (measure line see Figure 14)*

Figure 26 shows the potential distribution along the surface of the insulator. It can be seen that not only red curve (the bushing with the higher ground electrode) but also brown curve (the bushing with the lower ground electrode) appear a greater potential deviation between the positions of ground electrode top and of creepage distance 5000mm. The height of ground electrode affects potential distribution in the range of creepage distance 0mm to 5000mm. The more non-uniform potential distribution increases the possibility of flash-over along the surface of silicon rubber. The appropriate height of ground electrode may reduce the potential deviation and make potential distribution more uniform. However, above creepage distance 5000mm potential distribution is independent of the height of ground electrode, and three curves are overlapped together. The maximum potential deviation (detailed definition see 5.5) approaches at 27% and occurs at creepage distance 7300mm. This maximum value also affects flash-over along the surface of silicon rubber greatly.

## 3.4 Summary

In this chapter three hypothesizes of break-down mechanisms have been proposed. First of all, the break-down mechanisms between the conductor bar and ground electrode can be explained by the α process and streamer theory. According to the analysis in 3.1.3 the electric field strength is also relevant with the dimensions of ground electrode. Also, partial discharge inception at the top flange was investigated. The $E_{peak}$ at top flange mainly depends on the design of top flange periphery and triple points between the air, top flange and silicon rubber insulator. Flash-over along the surface of the silicon rubber insulator was discussed in 3.3. It attributes to the non-uniform potential distribution along the surface of silicon rubber insulator. From the three hypothesizes of break-down mechanisms, the following optimizations should concentrate on the four parts:

- Optimal design of the ground electrode to reduce the maximum electric field strength on the surface of the ground electrode and the conductor bar, so that the possibility of break-down between the ground electrode and the conductor bar will be decreased.
- Optimal design of top flange contour to reduce the maximum electric field strength on the top flange, so that the possibility of partial discharge on the top flange will be decreased.

- Optimal design of the triple point to avoid the electric field strength enhancement on the multi-dielectric medium.
- Make the potential distribution along the insulator more uniform to reduce the possibility of flash-over between the top flange and the ground flange.

# 4 Genetic algorithm

## 4.1 Introduction

Genetic algorithm (GA) is the search procedures on the basis of evolutionary algorithms, which is particular effective in searching the minimum or maximum value. The theory of genetic algorithm is largely based on the Wen-Shiush Chen's work *et al*. [22]. It has been widely and successfully applied to the optimization problems in many fields [28][29][30]. In this dissertation the GA optimizes the $SF_6$ bushing geometry to reduce the electric field strength (E) on the critical positions, so that the possibilities of break down will decrease correspondingly. Although the GA can easily converge to domain of optimum results, it is rather time-consuming to analyze the electric field strength by Ansoft Maxwell for searching a wide range of variable values. To improve the efficiency of the GA processes, the preliminary investigation is proposed, which eliminates the irrational variable values and assist to estimate proper initial values and ranges of variables for GA.

This chapter describes the principle of GA, the important parameters of GA and how the GA optimizes geometry of $SF_6$ bushing and reduces E on the critical positions.

## 4.2 Genetic algorithm

Concerning with optimization algorithms the common method uppermost in my mind is exhaust algorithm. In our case it is certain that the optimal structure could be obtained by the simulation of all the combinations of all parameters. However, it has a great disadvantage. The time-consuming for optimization cannot be afforded. The structure variant.2 is taken as a straightforward instance (see Figure 31 and Figure 32). In the variant.2 five correlated parameters (a, b, c, phi and r) of structure have to be modified to optimize the electric field strength between the ground electrode and conductor bar. The boundaries of parameters a, b, c, phi and r are assumed to be controlled between (4mm-5mm), (6mm-14mm), (110mm-124mm), (26°-36°) and (6-15mm). With step lengths of a b, c, phi and r of 0.1mm, 1mm, 1mm, 1° and 1mm respectively and based on the principal of permutation and combination there are 163350 possible combinations for optimization of the ground electrode structure of variant.2. This requires at least 15 minutes for one simulation model with low mesh cells. To complete the entire optimization it

costs more than 1700 days. For this reason the method of optimization should be considered and the further optimization should be realized by a search algorithm. In our case the genetic algorithm, which approaches the goal function related with structure parameters and electric field strength, will be introduced.

### 4.2.1 Parameters of genetic algorithm

The GA is a robust algorithm and has an ability to achieve optimal solution without the need of detailed information from object. It depends on several parameters, i.e. chromosomes, population size, maximal number of generation, goal function/fitness function, weighting factor, mutation rate, crossover rate, the ranges and initial values of all the parameters of ground electrode.

In the GA, the design variables are transferred into fixed length binary strings called individuals or chromosomes. A population contains a finite number of chromosomes, which determines the population size. The population size has a great effect on the optimization of the consuming-time. If a small population size is chosen, it increases the risk that the genes will be exhausted before the optimum value is found. However, if a large population size is chosen there will be more solver evaluations for the calculation of chromosomes. The genetic algorithm will stop after the maximal numbers of generation have been done.

The evaluation of the chromosomes performance is carried out by a goal function as following, which is called fitness function as well. The chromosome fitness measures its ability to survive and reproduce the offspring. In the contour optimization of $SF_6$ bushing, the fitness function can be represented as follow,

$$Fitness = w_1(E_{1,\max} - E_{1,G}) + w_2(E_{2,\max} - E_{2,G}) + \ldots + w_n(E_{n,\max} - E_{n,G}) \qquad \textit{Eq. 42}$$

Where $w_i$ denotes the weighting factor, which allows to give different importance to different critical points. It means that $w_i$ can put the emphasis on the maximum electric field strength of a certain position. Therefore, by configuration of weighting factor $w_i$ the fitness function can be changed, which has a great effect on the final optimal results. $E_{n,max}$, denotes maximum electric field strength of critical points in the simulation procedures. $E_{n,G}$ are the goal values of electric field strength in critical points. In case that $E_{n,\max} < E_{n,G}$, we set $E_{n,\max} - E_{n,G} = 0$. The lower the

total value of fitness in Eq. 42, the higher fitness of "fitness" is, which means the result is closer to the goal value.

The reproduction procedures including the strategy of elitism preservation, roulette selection, crossover operator and mutation operator choose chromosomes to become parents of the next generation and reproduce the next generation according to their fitness. The strategy of elitism preservation will preserve the best chromosomes in this generation as parents to the next generation. The rest of chromosomes are selected to participate in the next generation based on the roulette selection. The roulette selection is a criterion to determine the performance of chromosomes by its fitness value. The principle of roulette selection can be described as follow. The basic part of this selection process is to stochastically select from one generation to create the basis of the next generation. It is assumed that the fitness value associated with the $i^{th}$ chromosome can be denoted by $f_i$. The sum of function values in this generation can be presented by $f_{\text{sum}}$. The ratio $\frac{f_i}{f_{sum}}$ denotes the ranking of that chromosome in this generation. This ratio constructs a weighted roulette wheel, where each chromosome occupies an area on the wheel proportional to this ratio. Then the roulette wheel will determine the chromosomes that participate in next generation.

The crossover operator is a genetic operator used to exchange a portion of the binary string, which consists of chromosome, between two random chosen parents in order to generate new child chromosomes. The execution of the crossover operation is decided by crossover probability $P_c$, which is limited between the 0 and 1.

Mutation is another genetic operator used to maintain genetic diversity from one generation of a population of chromosomes to the next. Mutation alters one or more gene values (bits) in a binary encoded chromosome from its initial state. Therefore, the solution may change entirely from the previous solution. This process is carried out during evolution according to a definable mutation probability $P_m$.

The operation of crossover and mutation occur in order to replace the existing chromosomes and reproduce new ones in the next generation. The GA stops when the optimum is found or the maximum number of generations is reached.

### 4.2.2 Flowchart of optimizations for contour design of $SF_6$ bushing

The GA is structurally simple and can be considered as the tool for the optimizations of $SF_6$ contour designs. However, it is time-consuming to analyze the electric field strength for a large number of chromosomes. The costing time can be estimated as follow. We assume that "$N_p$" is the chromosomes in a generation and "$G_{max}$" is the maximal number of generation. "$t_s$" is the time for accomplishment of a simulation. The elitism strategy is adopted in the GA process to preserve the best chromosome in this generation. The roulette selection will choose a certain percentage of chromosomes as parents to the next generation. The elitism strategy preserve 50% chromosomes are assumed. The mutation and crossover operation will be adopted to reproduce the other 50% of chromosomes for the new generation. Accordingly, the overall optimization time works out

$$t = t_s \cdot (G_{\max} + 1) \cdot \frac{N_p}{2} \qquad \text{Eq. 43}$$

To improve this optimization more efficiently, calculate less inappropriate chromosomes and converge towards optimal results more quickly, the preliminary investigation is introduced before the GA optimization. The ranges of chromosomes are the candidates for the solution of optimization. In the theory, the first generation could be initiated randomly. However, a proper first generation, which is specified manually, would accelerate the convergence of the genetic algorithm. It can be determined by the results of preliminary investigation. The schematic diagram is shown in Figure 27 and the paragraph below describes detailed procedure of optimization for a $SF_6$ contour design.

The optimization procedure is divided into two steps, i.e. preliminary investigation and optimization by genetic algorithms. By the preliminary investigation a parameter is considered as a variable, in the meanwhile others are considered as constant. All the parameters are swept coarsely and the interconnection between every parameter and electric field strength on the critical points will be analyzed.

Afterwards based on the results of the preliminary investigation the initial values, ranges and goal values of every parameter will be determined in order to execute genetic algorithms. Obviously, by preliminary investigation the search ranges of every parameter are narrowed. Then the following GA process will be more targeted and efficient. The parameters are encoded into fixed length strings, i.e. chromosome. In the optimization the genetic algorithms consist of two loops. The purpose of an internal loop is the calculation of the electric field strength for the

chromosome. By the external loop the calculation will jump into the next generation. The computation of electric field strength will be carried out by Ansoft Maxwell. The computation will be stopped until the electric field strength reaches its own constrain condition. Otherwise the iteration will continue until accomplishment of all the generations by crossover and mutation operators of genetic algorithms. . In the procedure of genetic algorithms to ensure the better characteristics of the population can be left to the next generation, the strategy of elitism preservation will be carried out, which are parallel performed with Roulette-wheel selection, crossover and mutation operators. After the evolution procedure, the new population is generated and the iteration continues until the judgment is satisfied. In the chapter 5 the optimization of the ground electrode is taken as an example. The detailed analysis about preliminary investigation and whole optimizations are discussed in the section 5.1.7.

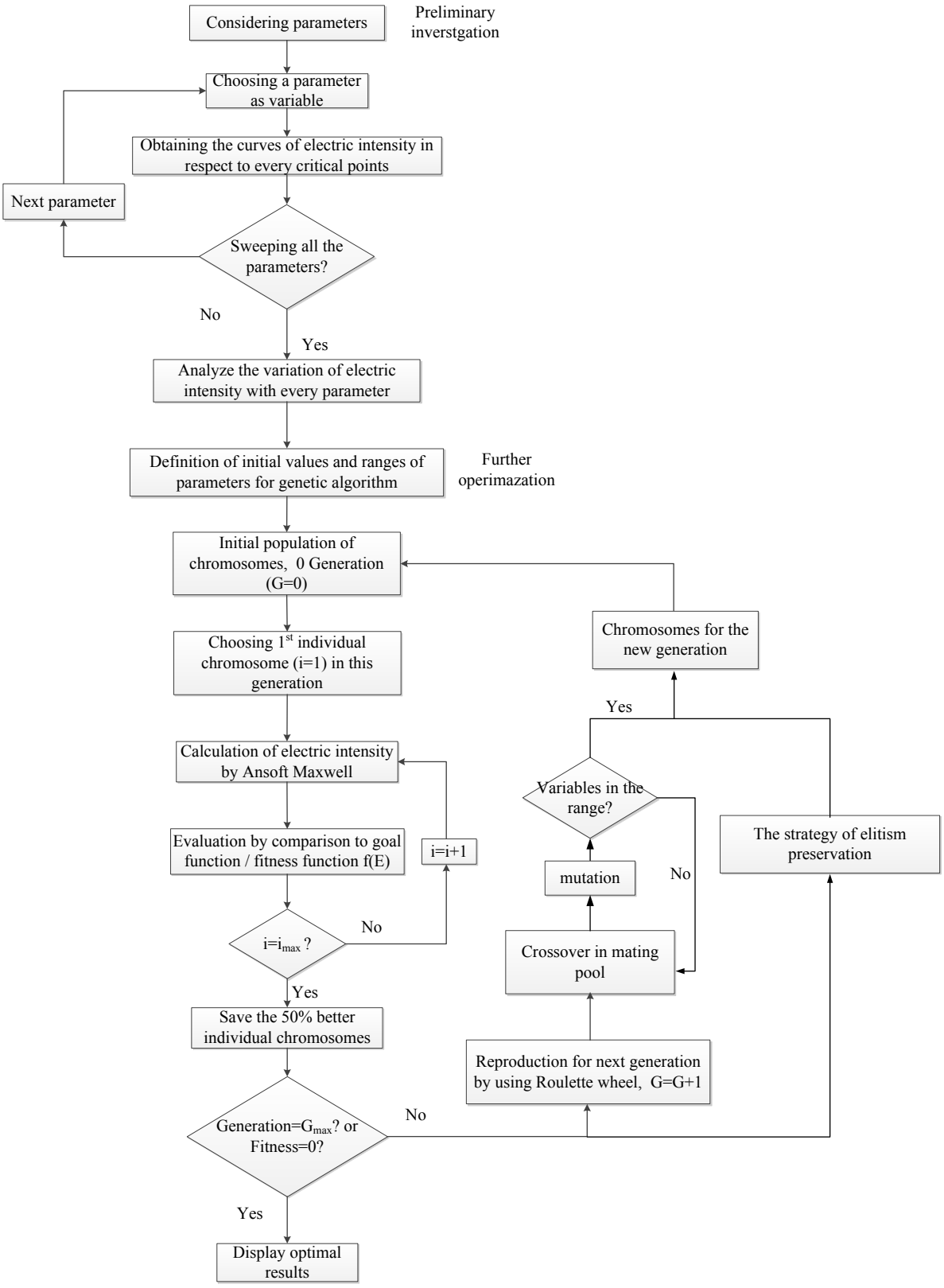


*Figure 27: Flowchart of the entire optimization procedures*

### 4.2.3 A simple example of genetic algorithm

For a better understanding of genetic algorithm procedures, a simple example will be presented as follows. Each step of genetic algorithm will be presented and calculated step by step. The task of this case is to search for a maximum value for the following function, where $x_1$ and $x_2$ can take values between 0 and 7.

$$\begin{aligned} Max: \quad & f(x_1, x_2) = x_1^2 + x_2^2 \\ & x_1 \in \{0,1,2,3,4,5,6,7\} \\ & x_2 \in \{0,1,2,3,4,5,6,7\} \end{aligned}$$

It is clear right away the solution is $f_{\max}(x_1, x_2) = 98$, when both $x_1$ and $x_2$ equal to 7, but this example shows the genetic algorithm operation basics intuitionally.

**Step 1: Encoding for the chromosome**

Genetic algorithm starts with a randomly chosen chromosome which is made up of binary strings. The reason is that in the genetic algorithm the target for operation is binary strings. The variables $x_1$ and $x_2$ have to be encoded into binary strings. In this case, the variables can be presented by the unsigned binary integer. Considering that the variables $x_1$ and $x_2$ are the integer varying from 0 to 7, a three-digit binary integer can express one variable. Two variables can be expressed by a six-digit unsigned binary integer, which consists of a chromosome. For instance, chromosome X=(101110) is equivalent to the variables $x_1$=5 and $x_2$=6. The transformation between the chromosome and variables can be carried out by encoding and decoding procedures.

**Step 2: Reproduction of initial population**

The initial population presents the starting searching values, which are given or reproduced randomly. In this case, the population size is assumed as 4, which means four initial chromosomes make up the population. The initial population is assumed and given in the following table:

| String No | Initial chromosome X | $x_1$ | $x_2$ |
|---|---|---|---|
| 1 | 011101 | 3 | 5 |
| 2 | 101011 | 5 | 3 |
| 3 | 011100 | 3 | 4 |
| 4 | 111001 | 7 | 1 |

*Table. 5 The initial chromosomes and corresponding variables $x_1$ and $x_2$*

**Step 3: Calculation for the fitness value**

A fitness function is a criterion function, which helps us to assess their performance and quality. Based on this information, it determines what are the possibilities of each chromosome to inherit to the next generation. In this case, the optimization target is solving the maximum value of this function. Therefore, the mathematical expression can be considered as fitness function directly.

**Step 4: Selection procedure**

The essence of genetic algorithms i.e. an evolutionary algorithms is that the fittest individuals have a greater chance of survival than weaker ones. The selection procedure simulates this process, which according to a certain rule or principle copies the chromosome to the next generation. It requires that the higher fitness value has a higher possibility to copy to the next generation. In this case, the odds, which are in directly proportional to the fitness value, is adopted to determine the number of copies which each chromosome will have at the construction of the next generation. The detailed procedures are presented as follow:

1. The fitness value of each chromosome is calculated. $f_i(\mathrm{x}_1, \mathrm{x}_2) \quad (\mathrm{i} = 1, 2, ..., \mathrm{M})$
2. The fitness value of each chromosome is summed up. $\sum_{1}^{i} f_i(\mathrm{x}_1, \mathrm{x}_2) \quad (\mathrm{i} = 1, 2, ..., \mathrm{M})$

3. The inheritance possibility of $i^{th}$ chromosome $P(X_i)$ to the next generation is calculated by the function $P(X_i) = \frac{f_i(x_1, x_2)}{\sum_{1}^{i} f_i(x_1, x_2)}$ $(i = 1, 2, ..., M)$. The sum of the inheritance possibility $\sum_{1}^{i} P(X_i)$ $(i = 1, 2, ..., M)$ should be equal to 1.

4. The selection procedure is operated by the roulette selection mentioned in subchapter 4.2.1. The requirement is that the fittest individuals have a greater chance of survival than weaker ones. This replicates nature in that fitter individuals will tend to have a better probability of survival. Figure 28 shows the diagram of selection procedures.

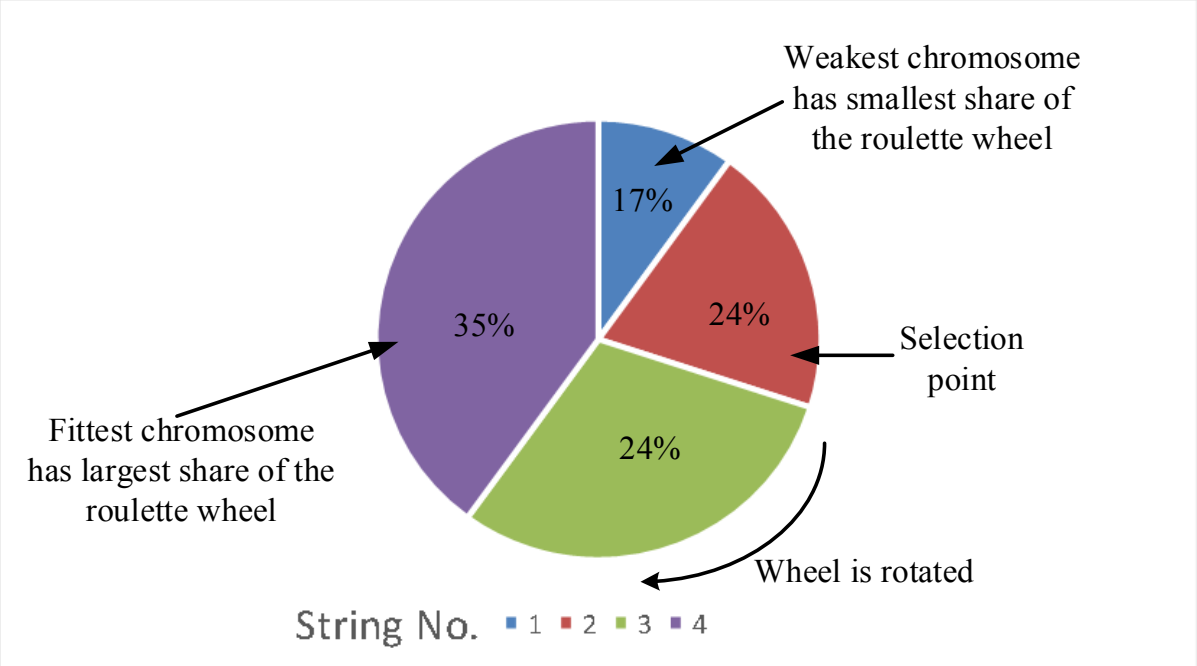


*Figure 28: The diagram of roulette selection*

The realization of roulette selection is based on the following three processes.

- In the interval [0, 1] a uniformly distributed random number $r$ is generated.
- If $r \le q_1$, the chromosome $X_1$ is selected
- If $q_{k-1} < r \le q_k$, the chromosome $X_k$ is selected. $(2 \le k \le M)$,

Where $q_i$ is called accumulated possibility of chromosome $X_i$ (i=1,2,…,M), the mathematical expression of $q_i$ is:

$$q_i = \sum_{1}^{i} P(X_i)$$

Therefore, in this case according to the possibility of each chromosome (see Table. 6), the roulette selection is carried out as follow:

- In the interval [0, 1] a uniformly distributed random number $r$ is generated.
- If $r \le 0.24$, the chromosome $X_1$ is selected
- If $0.24 < r \le 0.48,$ , the chromosome $X_2$ is selected
- If $0.48 < r \le 0.65,$ , the chromosome $X_3$ is selected
- If $0.65 < r \le 1,$ , the chromosome $X_4$ is selected

According to population size, the roulette selection is carried out four times to generate four offspring. Table. 6 shows the reproduced offspring by selection procedure.

| String No. | Initial chromosome | $x_1$ | $x_2$ | $f_i(x_1, x_2)$ | $\frac{f_i(x_1, x_2)}{\sum_{1}^{i} f_i(x_1, x_2)}$ | Selected times | Reproduced offspring |
|---|---|---|---|---|---|---|---|
| 1 | 011101 | 3 | 5 | 34 | 0.24 | 1 | 011101 |
| 2 | 101011 | 5 | 3 | 34 | 0.24 | 1 | 111001 |
| 3 | 011100 | 3 | 4 | 25 | 0.17 | 0 | 101011 |
| 4 | 111001 | 7 | 1 | 50 | 0.35 | 2 | 111001 |
| Sum | | | | 143 | 1 | | |

*Table. 6: Reproduced offspring by selection procedure*

**Step 5: Crossover operator**

As mentioned in subchapter 4.2.1, the crossover operator is a genetic operator used to exchange a portion of the binary string, which consists of chromosome, between two randomly chosen parents in order to generate new child chromosomes. The execution of the crossover operation is decided by a certain crossover probability $P_c$. In this case, the single-point crossover is adopted, the detailed processes are carried out as follow:

- The chromosomes are paired randomly.
- The position of crossover is set
- The portion of chromosome will be exchanged.

| String No. | Reproduced offspring | Pairing | Position of crossover | Offspring after crossover |
|---|---|---|---|---|
| 1 | 01 \| 1101 | 1-2 | 1-2:2 | 011001 |
| 2 | 11 \| 1001 | 1-2 | 1-2:2 | 111101 |
| 3 | 1010 \| 11 | 3-4 | 3-4:4 | 101011 |
| 4 | 1110 \| 01 | 3-4 | 3-4:4 | 111001 |

*Table. 7: Offspring after crossover*

**Step 6: Mutation operator**

Mutation alters one or more gene values (bits) in a binary encoded chromosome from its initial state. It is another genetic operator used to maintain genetic diversity from one generation of a population of chromosomes to the next. In this case, one bit is mutated, the detailed processes are carried out as follow:

- The position of mutation is determined randomly. The third row in Table. 8 shows the position for mutation.

- The mutation process reverses the gene value at the mutated position.

| String No. | Offspring after crossover | Position for mutation | Mutated offspring | $x_1$ | $x_2$ | $f_i(x_1, x_2)$ | $\frac{f_i(x_1, x_2)}{\sum_1^i f_i(x_1, x_2)}$ |
|---|---|---|---|---|---|---|---|
| 1 | 011001 | 4 | 011101 | 3 | 5 | 34 | 0.14 |
| 2 | 111101 | 5 | 111111 | 7 | 7 | 98 | 0.42 |
| 3 | 101011 | 2 | 111001 | 7 | 1 | 50 | 0.21 |
| 4 | 111001 | 6 | 111010 | 7 | 2 | 53 | 0.23 |
| Sum | | | | | | 235 | 1 |

*Table. 8: Mutated offspring*

After the operation of roulette selection, crossover and mutation, a new population P(t+1) is reproduced by population P(t). It can be seen from the above Table. 8 that after one generation evolves, the fitness values have been improved. In fact, the maximum value"111111" has been found. In order to illustrate the procedure of genetic algorithm, the good mutated offspring are selected and the iteration for new offspring takes only one time. It should be noticed that in the practical operation it takes several even hundreds times iterations to obtain the best result.

## 4.3 Summary

Genetic algorithm (GA) is one of the optimization procedures on the basis of evolutionary algorithms to search the optimal value. The principle and parameters of GA were introduced at the beginning of this chapter. However, GA has the drawback that it is time-consuming to reach the optimal results. Therefore, considering narrowing search ranges of variables quickly, the preliminary investigation has been proposed to improve the GA in order to converge the optimal results more efficiently. The whole procedure of GA was discussed and shown in the section 4.2.2. An example of solving the maximum value was taken in the chapter 4.2.3 to illustrate how the GA works.

# 5 Optimization of bushing designs

## 5.1 Optimizations of the ground electrode

In the optimizations of the ground electrode, several new structures of the ground electrode will be proposed and its characteristic will be briefly described. Each structure of the ground electrode will be parameterized and simulated by Ansoft Maxwell in order to predetermine the ranges of ground electrode parameters. Based on the results from the preliminary analysis and the approximate ranges of parameters the genetic algorithms will be carried out. From the genetic algorithms the results of the optimized ground electrode will be discussed.

### 5.1.1 Original ground electrode (Variant.1)

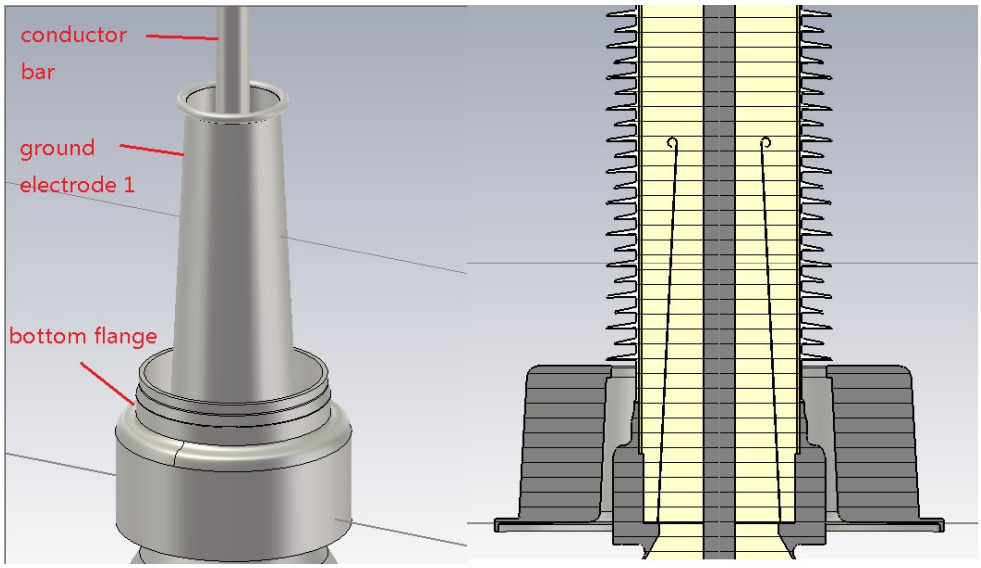


*Figure 29: Variant.1, conical ground electrode with grading ring (3D view and sectional view)*

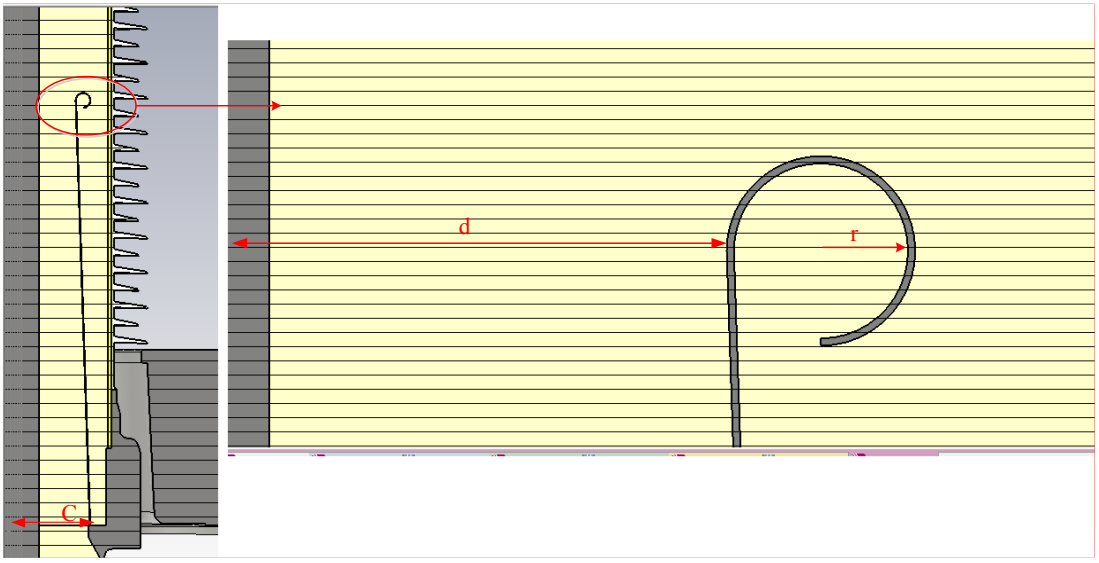


*Figure 30: Parameters of variant.1*

Figure 29 and Figure 30 show the cross section of the original conical ground electrode with axial symmetry in geometry. Parameters c and d represent the radius of ground electrode at the bottom side and the top side. At the top of the ground electrode a grading ring is arranged. The radius of the grading ring is represented by the parameter r. The initial parameters are assumed at c=117.5mm, d=81mm, r=9mm and the thickness of the ground electrode material a=1mm. The original structure is regarded as variant.1.

### 5.1.2 Ground electrode with ring profile (Variant.2,3)

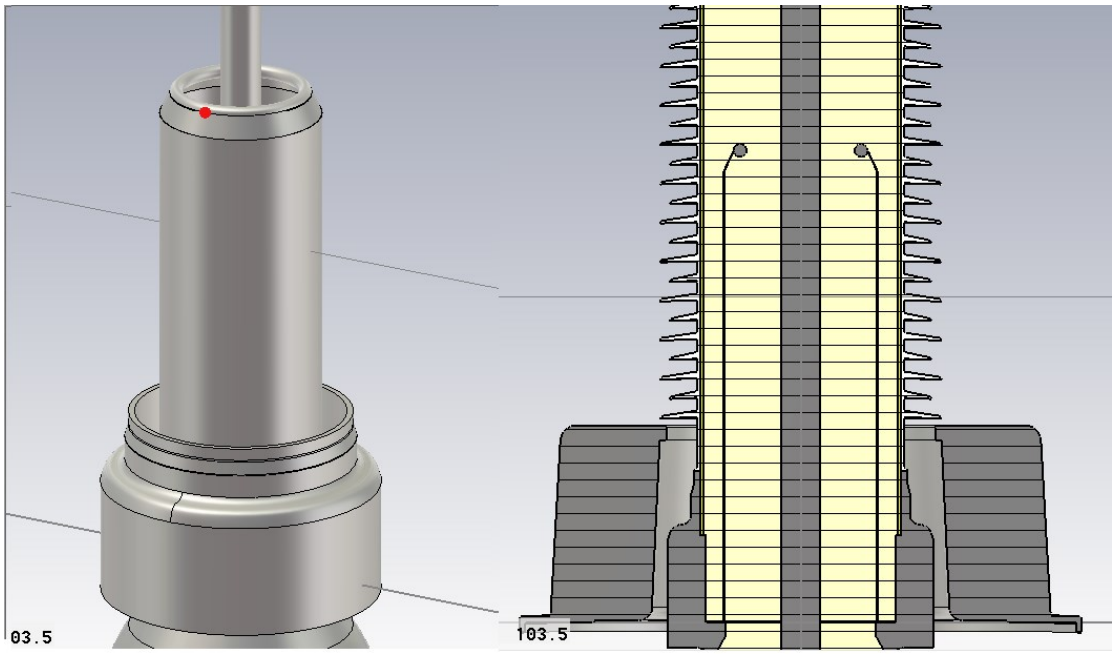


*Figure 31: Variant.2, cylindrical ground electrode with grading ring (3D view and sectional view)*

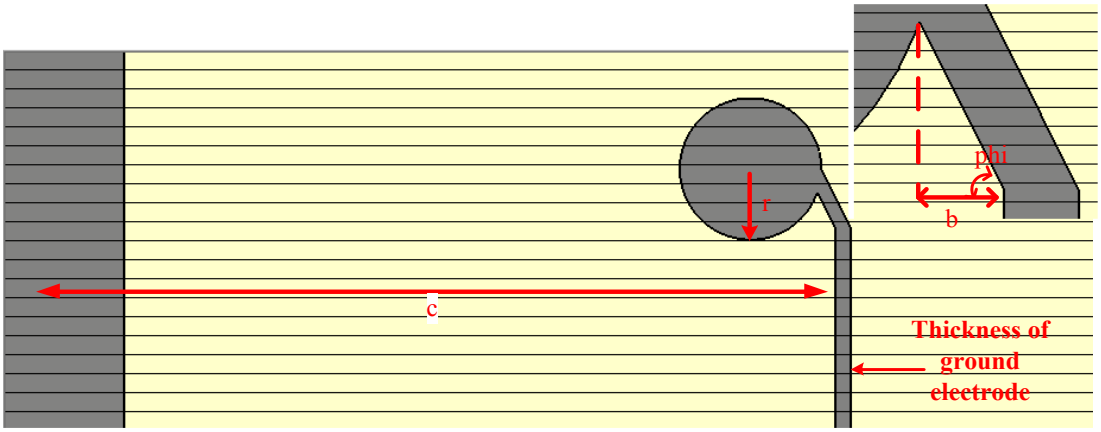


*Figure 32: Parameters of variant.2*

The cross section of the ground electrode (variant.2) with its axial symmetry in geometry is shown in Figure 31. The variant.2 is composed of a cylindrical ground electrode. At the top side the ground electrode slopes inside and connects with a grading ring. Parameter c represents the radius of the ground electrode. Parameter b represents the clearance, with which the ground electrode slopes towards the conductor bar at its top side. The height of the slope part is controlled by slope angle φ. At the top of ground electrode a grading ring is arranged. The radius

of the grading ring is represented by the parameter r. The initial parameters are assumed to be b=10mm, c=107.5mm, phi=25°, r=7.5mm and the thickness of the ground electrode material a=1mm.

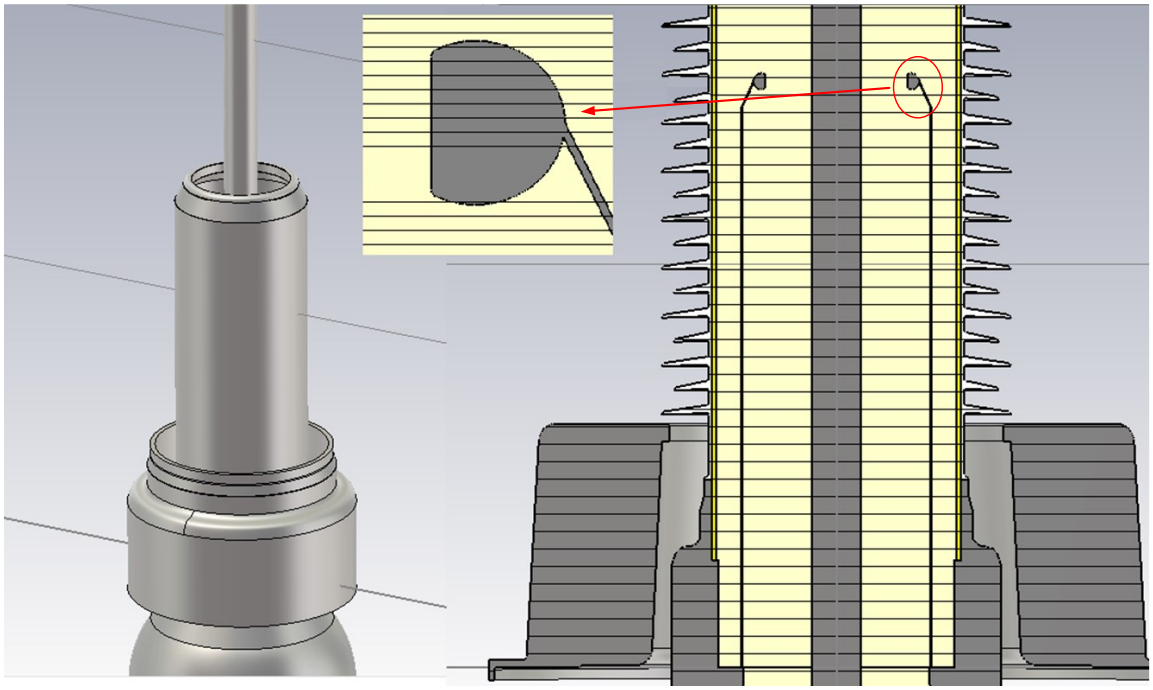

*Figure 33: Variant.3, cylindrical ground electrode with cut hemi-ring profile (3D view and sectional view)*

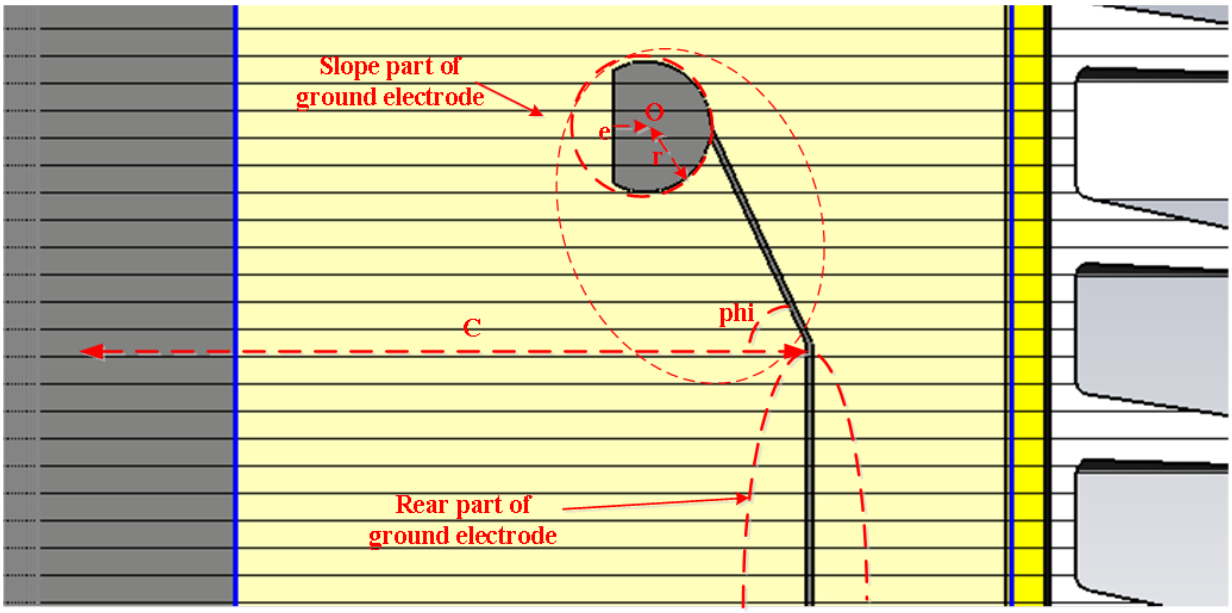


*Figure 34: Parameters of variant.3*

Figure 33 and Figure 34 indicate the cross section of the ground electrode (variant.3) with axial symmetry in geometry. In comparison with variant.2 this structure is little different. At the top side the ground electrode slopes inside and connects with a grading ring. The grading ring is partly cut in order to investigate, whether the plane of the grading ring has an effect on the electric field strength between the conductor bar and ground electrode. The radius of the grading ring is represented by the parameter r. Parameter c represents the radius of the ground electrode. The height of the slope part is fixed at 33mm. The clearance between the slope part and the rear part is controlled by slope angle φ. Parameter e represents the distance between the center of grading ring O and chord of grading ring. The initial parameters are assumed at c=118.5mm, e=5mm, φ=25°, r=10mm the thickness of ground electrode material a=2mm and the height of rear part and slope part of ground electrode $h_1$=690mm $h_2$=33mm.

### 5.1.3 Ground electrode with Rogowski profile (Variant.4,5)

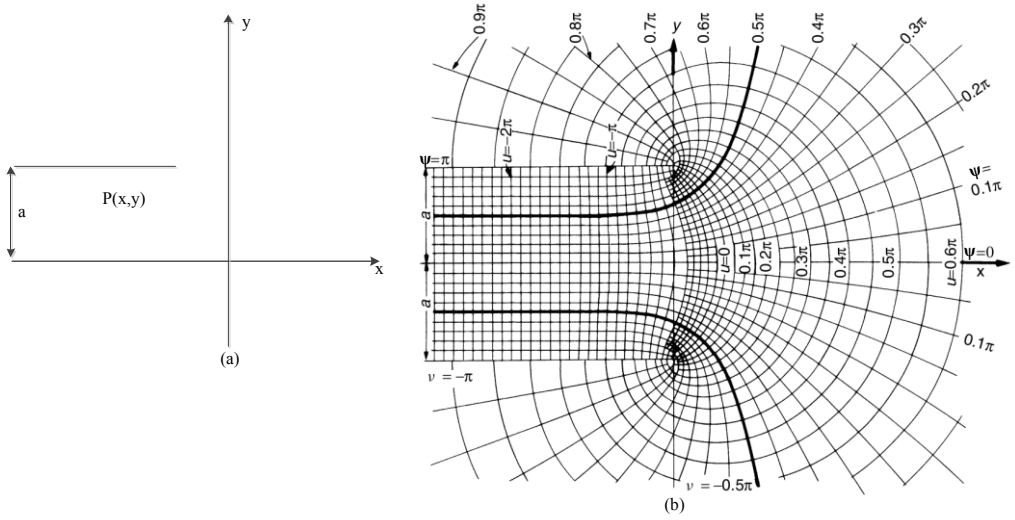


*Figure 35: Plate-plate electrode arrangement (a) and Rogowski's profile (b)*

The coordinate of a certain point P in the plate-plate electrode can be presented by the equations as follow,

$$\begin{cases} x = A \cdot (\phi + e^{\phi} \cos \psi) \\ y = A \cdot (\psi + e^{\phi} \sin \psi) \end{cases} \qquad \textit{Eq. 44}$$

where ψ represents equipotential lines and Φ are lines of electrostatic force. A is the separation factor between the two plates: $A = \frac{a}{\pi}$. The electric field is calculated and plotted by assuming a certain ψ and solving Eq. 44 for a series of values Φ. In the investigation of different ψ the uniform electric field can be obtained by substituting $\psi = \frac{\pi}{2}$. In my models, the Rogowski curve varies based on the y axis. The length of Rogowski's profile cannot be infinite, which means Rogowski's profile will be truncated at certain point. Therefore, the Eq. 44 has to be modified into the following,

$$\begin{cases} y(\varphi) = \frac{a\varphi}{\pi} - \frac{ag}{\pi} + h_1 \\ x(\varphi) = \frac{a}{\pi}(\frac{\pi}{2} + e^{\varphi}) - \frac{a}{\pi}(\frac{\pi}{2} + e^{g}) + d \\ g \le \varphi \le f \end{cases} \qquad \textit{Eq. 45}$$

The Eq. 45 describes the modified Rogowski curve applied in the variant.4 and 5. Parameter φ represents the step length of the Rogowski curve. Parameter $h_1$ is the height of the rear part of the ground electrode. g and f indicate the minimum and the maximum value of parameter φ, which limits the Rogowski curve in a certain range. A hemi-ring is designed to reduce the effect of the electric field strength on the surface of FRP tube inside. Parameter c determines radius of ground electrode. For the conical structure (variant.5) an extra parameter d represents the clearance between conductor bar and ground electrode at the top side.

The initial parameters of variant.4 and 5 are set at the same values. They are assumed at a=40, f=1, g=-2.5 c=118.5mm, r=5mm, the thickness of the ground electrode material $a_1$=2mm and the height of the rear part of the ground electrode $h_1$=690mm. For a conical structure (variant.5) extra parameter d is set at 81mm.

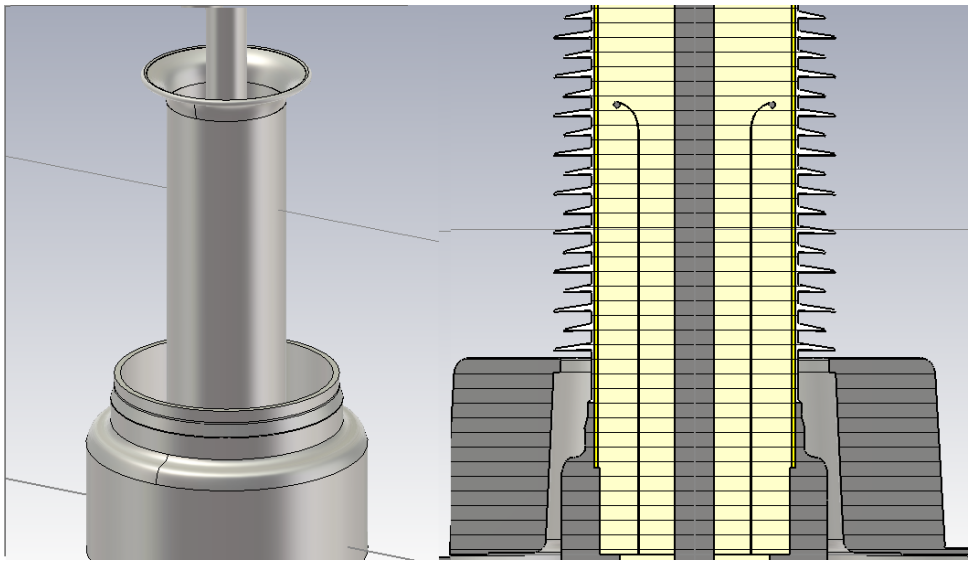

*Figure 36: Variant.4, cylindrical ground electrode with Rogowski profile (3D view and sectional view)*

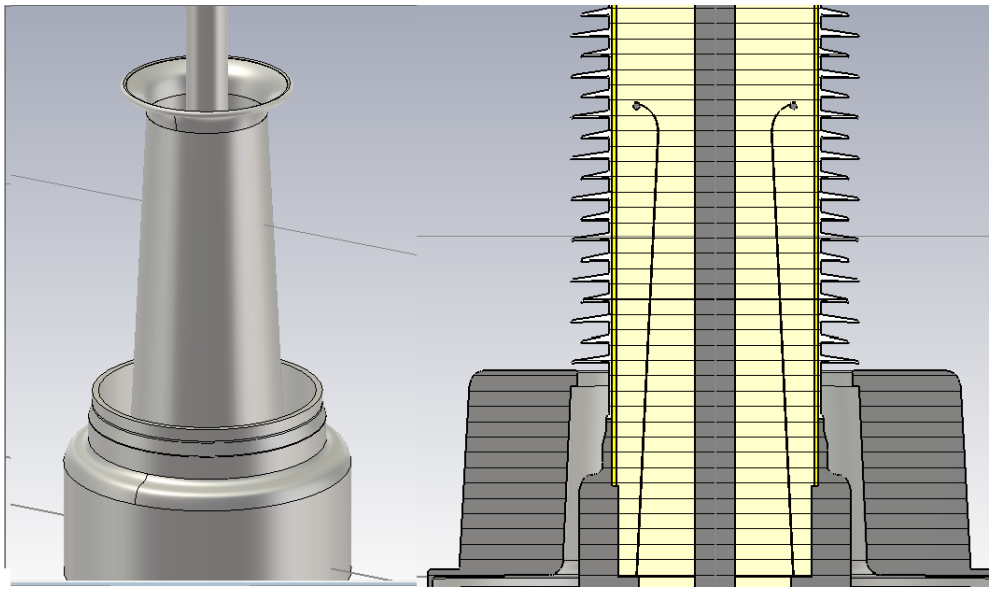

*Figure 37: Variant.5, conical ground electrode with Rogowski profile (3D view and sectional view)*

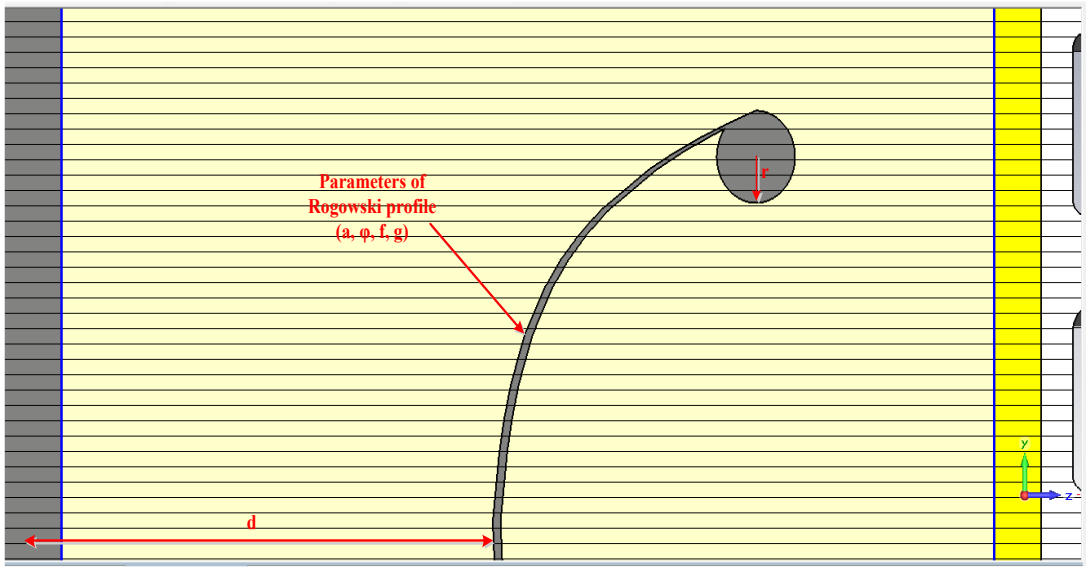


*Figure 38: Parameters of variant.4 and 5*

The main difference is that variant.4 has a cylindrical structure and variant.5 has a conical structure. For the smoothing of the electric field enhancement at the periphery of the ground electrode top the Rogowski profile is designed to increase the radius of curvature gradually so that the electric field strength at the edge does not exceed the mean value between the ground electrode and the conductor bar. Also it makes the electric field uniform.

### 5.1.4 Ground electrode with cubic Bézier profile (Variant.6,7,8)

Compared with variant.4 and variant.5 a new contour called Bézier curve is applied in the following three models. The Bézier curve is widely used to model smooth contours. The Bézier curve is defined by the convex hull of its control points, which are apices of a polygon. The control points manipulate the shape of the curve. By shifting the control points the Bézier curve will try to close the polygon and change its contour. The starting and ending points of Bézier curves are fixed, and the starting line and ending line are tangential to the Bézier curves. The rest of points are the control points.

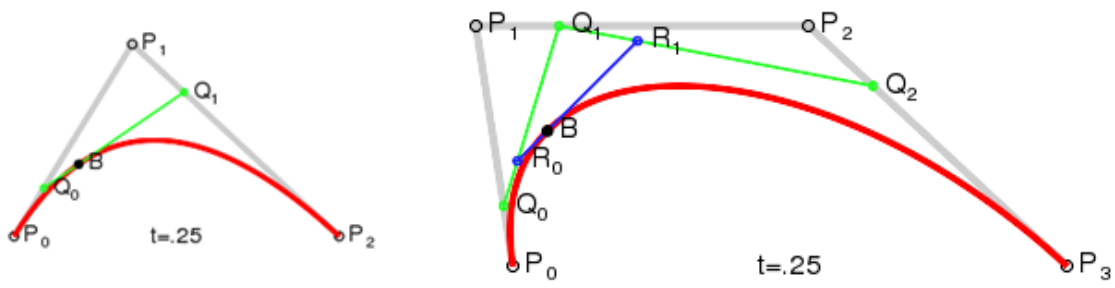


*Figure 39: A quadratic Bézier curve (left) and a cubic Bézier curve (right)[31]*

The Bézier curve has many advantages. Due to its attachment to the shape of a polygon the establishment of a Bézier curve is very intuitively and convenient. Moreover, the main characteristic of Bézier curves is geometrical invariability, which means the shape of curve is irrelevant to its own coordinates. It totally depends on the parameters of apices, i.e. the coordinates of the control points. Furthermore, the parametric expression of a Bézier curve is multinomial and the order of expression can be modified based on the application. However, it also has several disadvantages. The curve is greatly affected and limited by control points. The modification of each control point will change the entire shape. Such changes in shape of a curve are limited to certain extend. The curve has to be located in the interior of the polygon, and it attaches to the shape of the polygon.

Generally, the Bézier curve can be expressed as follow,

$$\mathrm{B}(\mathrm{t})=\sum_{i=0}^{n} P_i B_{i,n}(t),(0\le \mathrm{t}\le 1) \qquad \textit{Eq. 46}$$

Where $P_i(0,1,2\cdots$ $P_i(0,1,2\cdots n)$ are a set of control points, which composes of the polygon. *n* is called its order (*n*=1 for linear, 2 for quadratic, 3 for cubic etc.). $B_{i,n}(t)=C_n^i t^i(1-t)^{n-i}$ $B_{i,n}(t)=C_n^i t^i(1-t)^{n-i}$, $i=1,2\cdots$ $i=1,2\cdots n$, which is n order of Bernstein multinomial. The parameter t is a smooth coefficient of the Bézier curve. The shorter the interval of Δt is, the more accurate Bézier curve can be expressed.

In our case, the cubic Bézier curve is applied for the contour of ground electrode. The cubic Bézier curve has four points $P_0$, $P_1$, $P_2$ and $P_3$. $P_0$ and $P_3$ are starting and ending point. $P_1$ and $P_2$ are control points. In the Figure 39 the curve starts at $P_0$ going toward $P_1$ and arrives at $P_3$ coming

from the direction of $P_2$. It will not pass through $P_1$ or $P_2$; these points are only there to provide directional information. The distance between $P_0$ and $P_1$ determines "how long" the curve moves into direction $P_2$ before turning towards $P_3$. The cubic Bézier curve (n=3) can be given as follow,

$$\mathrm{B}(\mathrm{t}) = \sum_{i=0}^{3} P_i B_{i,n}(t), (0 \le \mathrm{t} \le 1) \qquad \textit{Eq. 47}$$

Inserting third order of Bernstein multinomial into the equation,

$$\mathrm{B}(\mathrm{t}) = P_0 B_{0,3}(t) + P_1 B_{1,3}(t) + P_2 B_{2,3}(t) + P_3 B_{3,3}(t) \qquad \textit{Eq. 48}$$

$B_{i,3}(t)$ $B_{i,3}(t)$ is third order of Bernstein multinomial and can be expounded as follow,

$$\begin{cases} B_{0,3}(t) = (1-t)^3 \\ B_{1,3}(t) = 3t(1-t)^2 \\ B_{2,3}(t) = 3t^2(1-t) \\ B_{3,3}(t) = t^3 \end{cases} \qquad \textit{Eq. 49}$$

Therefore,

$$\mathrm{B}(\mathrm{t}) = P_0 \cdot (1-t)^3 + P_1 \cdot 3t(1-t)^2 + P_2 \cdot 3t^2(1-t) + P_3 \cdot t^3 \qquad \textit{Eq. 50}$$

t is the step length of the function, which determines the precision of the Bézier curve. Or the expression can be modified into a matrix form

$$B(t) = \begin{bmatrix} t^3 & t^2 & t & 1 \end{bmatrix} \begin{bmatrix} -1 & 3 & -3 & 1 \\ 3 & -6 & 3 & 0 \\ -3 & 3 & 0 & 0 \\ 1 & 0 & 0 & 0 \end{bmatrix} \begin{bmatrix} P_0 \\ P_1 \\ P_2 \\ P_3 \end{bmatrix} \qquad \textit{Eq. 51}$$

Introducing x and y coordinates of four points $\mathbf{P}_0$, $\mathbf{P}_1$, $\mathbf{P}_2$ and $\mathbf{P}_3$, the expression can be given by

$$x(t) = \begin{bmatrix} t^3 & t^2 & t & 1 \end{bmatrix} \begin{bmatrix} -1 & 3 & -3 & 1 \\ 3 & -6 & 3 & 0 \\ -3 & 3 & 0 & 0 \\ 1 & 0 & 0 & 0 \end{bmatrix} \begin{bmatrix} x_0 \\ x_1 \\ x_2 \\ x_3 \end{bmatrix}$$ *Eq. 52*

$$y(t) = \begin{bmatrix} t^3 & t^2 & t & 1 \end{bmatrix} \begin{bmatrix} -1 & 3 & -3 & 1 \\ 3 & -6 & 3 & 0 \\ -3 & 3 & 0 & 0 \\ 1 & 0 & 0 & 0 \end{bmatrix} \begin{bmatrix} y_0 \\ y_1 \\ y_2 \\ y_3 \end{bmatrix}$$ *Eq. 53*

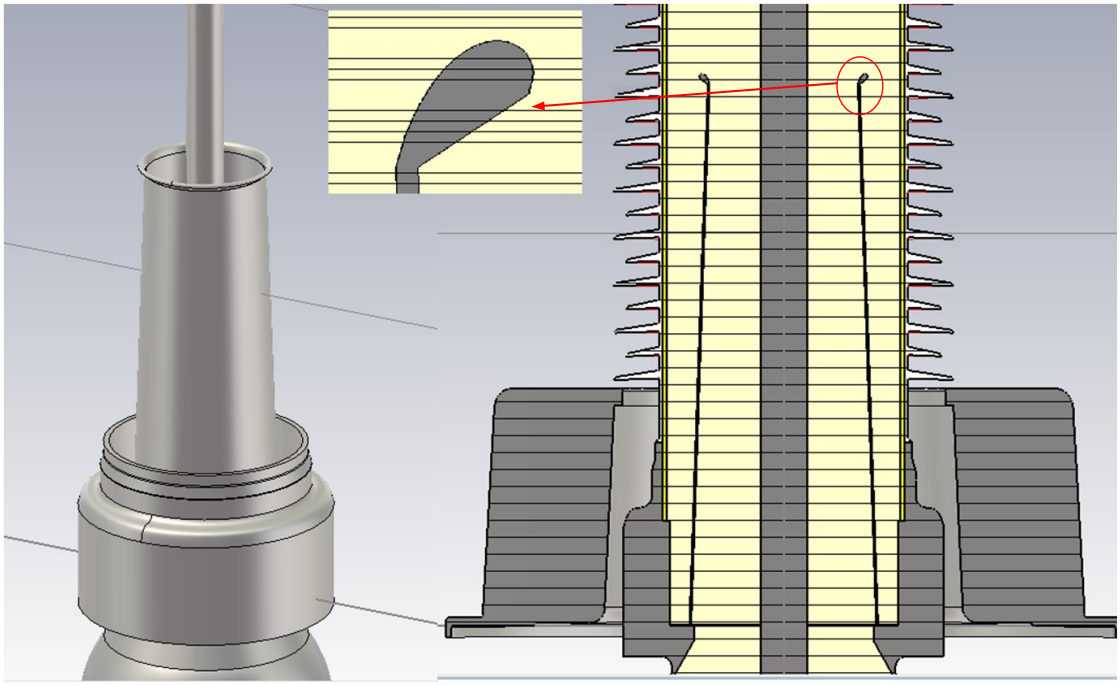

*Figure 40: Variant.6, conical ground electrode with cubic Bézier profile (3D view and sectional view)*

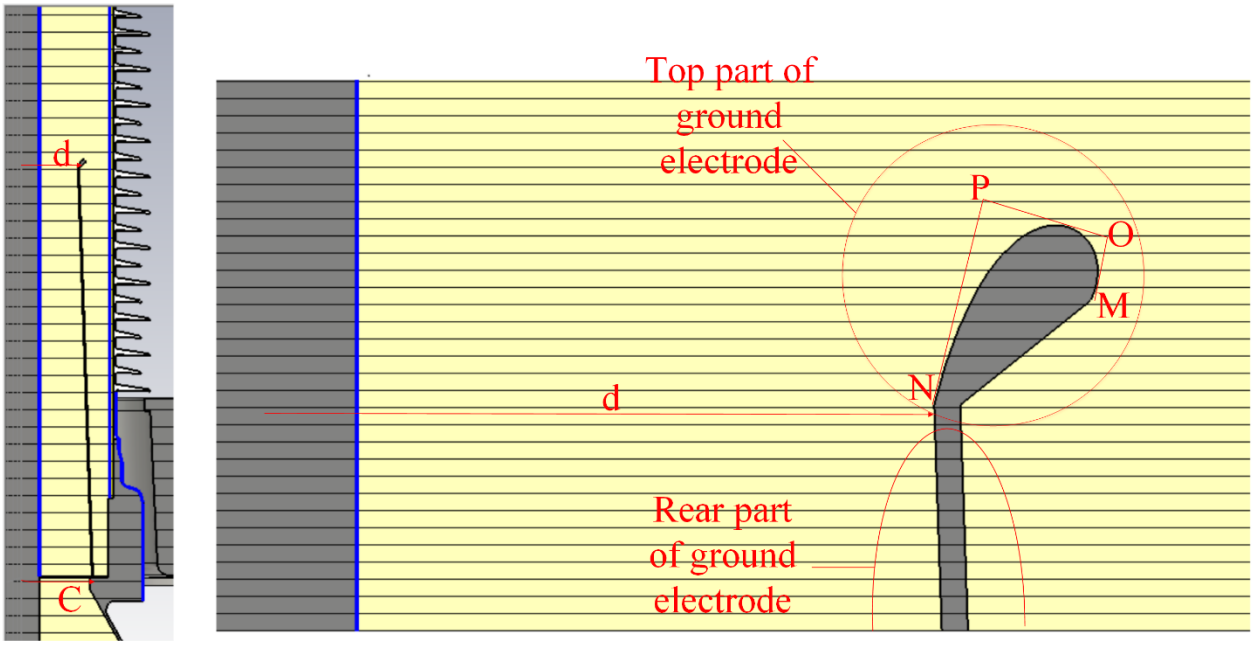


*Figure 41: Parameters of variant.6*

Figure 40 and Figure 41 show the cross section of the ground electrode (variant.6) with axial symmetry in geometry. The variant.6 is a conical ground electrode. At the top part of the ground electrode the contour is based on the cubic Bézier profile. Due to the conical structure parameters c and d represent the radius of the ground electrode at the bottom side and top side. The Bézier curve is controlled by the four points, i.e. starting point N, ending point M, control points P and O.

The initial parameters are assumed at d=95mm, c=118.5mm, the thickness of the ground electrode material a=2mm and the height of the rear part of the ground electrode $h_1$=690mm. The four points N, M, P, O are located at (95,690) (100,710) (110,704) (107,698) respectively.

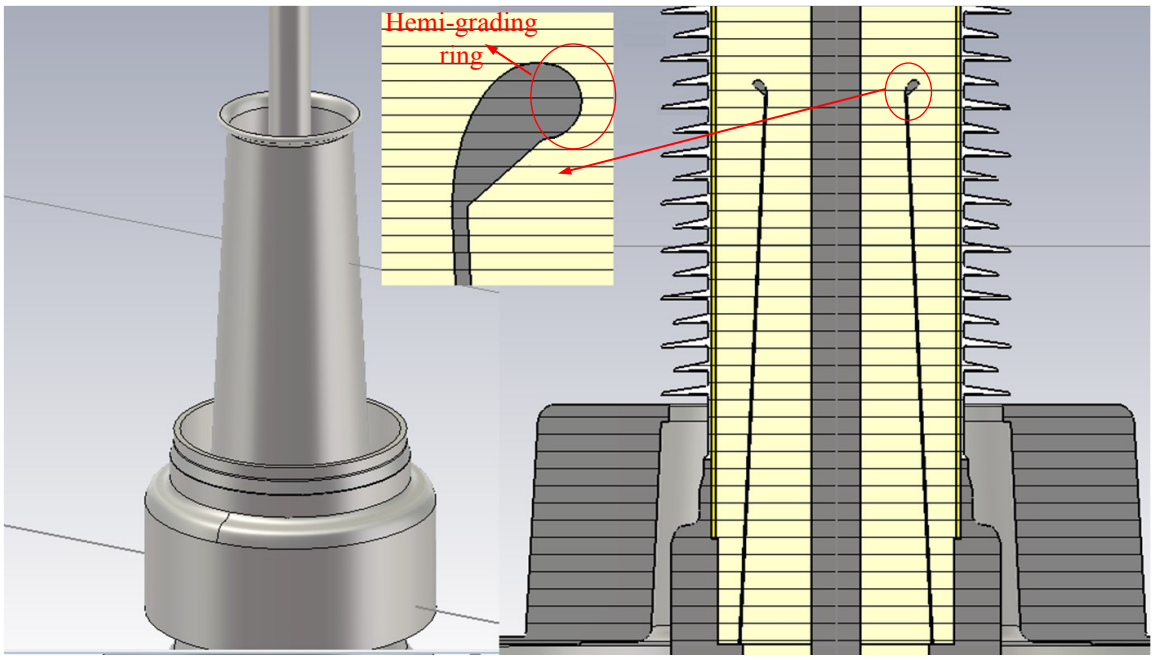


*Figure 42: Variant.7, conical ground electrode with cubic Bézier profile and hemi-grading ring (3D view and sectional view)*

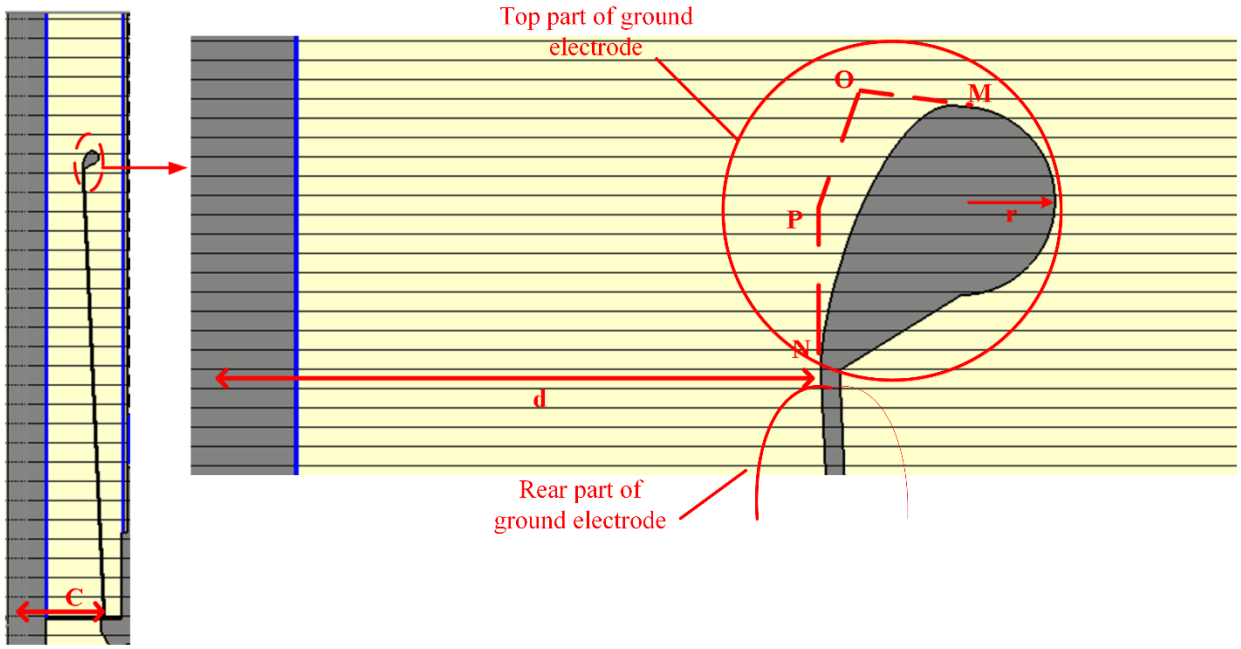


*Figure 43: Parameters of variant.7*

Figure 42 and Figure 43 show the cross section of the ground electrode (variant.7) with axial symmetry in geometry. The variant.7 is a conical ground electrode. At the top side of the ground electrode the contour is based on cubic Bézier curve. Comparing with variant.6 at the outside a

hemi-ring is taken into account to reduce the effect of the electric field strength on the inside surface of the glass fiber tube. Due to the conical structure parameters c and d represent the radius of the ground electrode at the bottom and top side. The Bézier curve is controlled by the four points, i.e. starting point N, ending point M, control points P and O. The radius of the hemi-grading ring is represented by the parameter r.

The dimensions of the ground electrode are assumed at d=86mm, c=118.5mm, r=10mm, the thickness of the ground electrode material 2mm and the height of rear part of ground electrode $h_1$=690mm. The four points N, M, P, O are located at (86,690) (98,709) (86,700) (91,710) respectively.

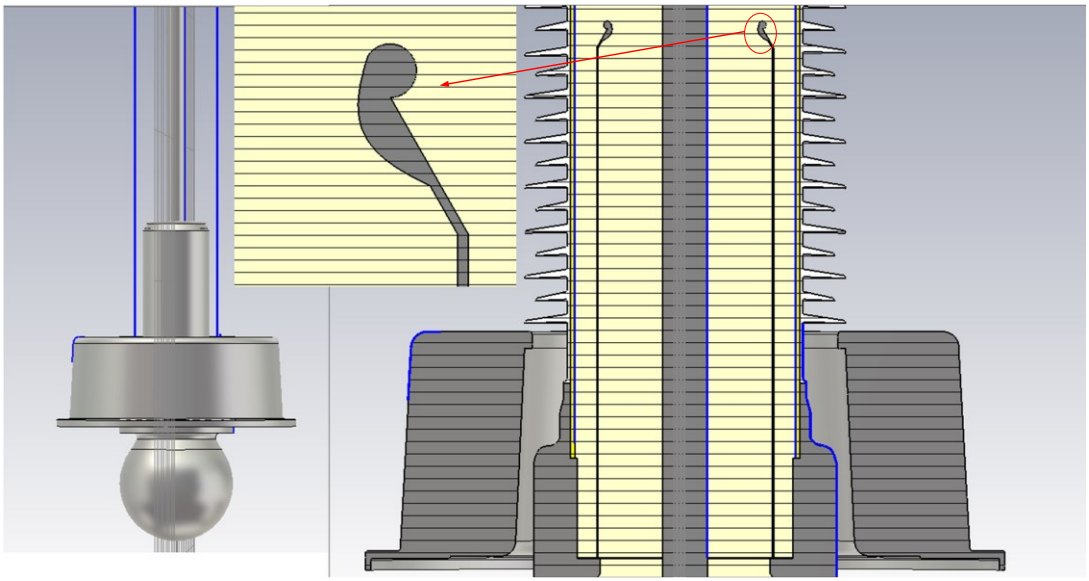

*Figure 44: Variant.8, cylindrical ground electrode with cubic Bézier profile and grading ring (3D view and sectional view)*

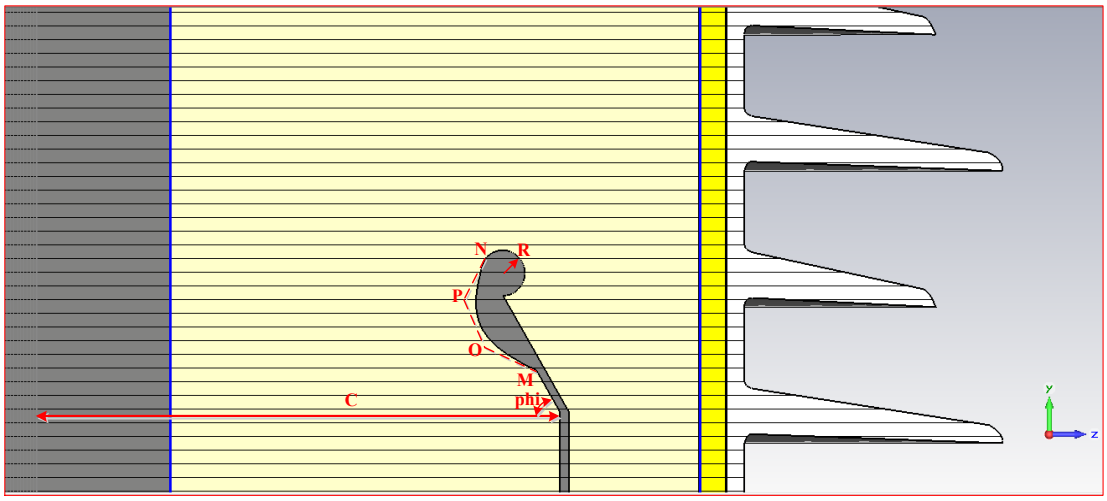


*Figure 45: Parameters of variant.8*

Figure 44 and Figure 45 show the cross section of the ground electrode (variant.8) with axial symmetry in geometry. The variant.8 is a cylindrical structure. At the top of the ground electrode the side towards the conductor bar is designed by a cubic Bézier profile. At the other side a grading ring is arranged to increase the curvature on top of the ground electrode, which reduces the effect of electric field strength on the surface of the FRP inside and the surface of the ground electrode. Parameter c indicates the radius of the ground electrode. At the top the ground electrode slopes towards the inside with the angle φ. The Bézier profile is controlled by the four points, i.e. starting point N, ending point M, control points P and O. The starting point N and ending point M are fixed. By changing the positions of P and O the contour of the Bézier profile can be modified. The radius of the hemi-grading ring is represented by the parameter r.

It is assumed that the initial parameters are set at c=117.5mm, r=5mm, φ=30°, and the thickness of the ground electrode material a=2mm. The four points N, M, P, O are located at (100.45, 713) (110.45, 685) (95.45, 698) (100.45, 693) respectively.

### 5.1.5 Ground electrode with two grading rings (Variant.9)

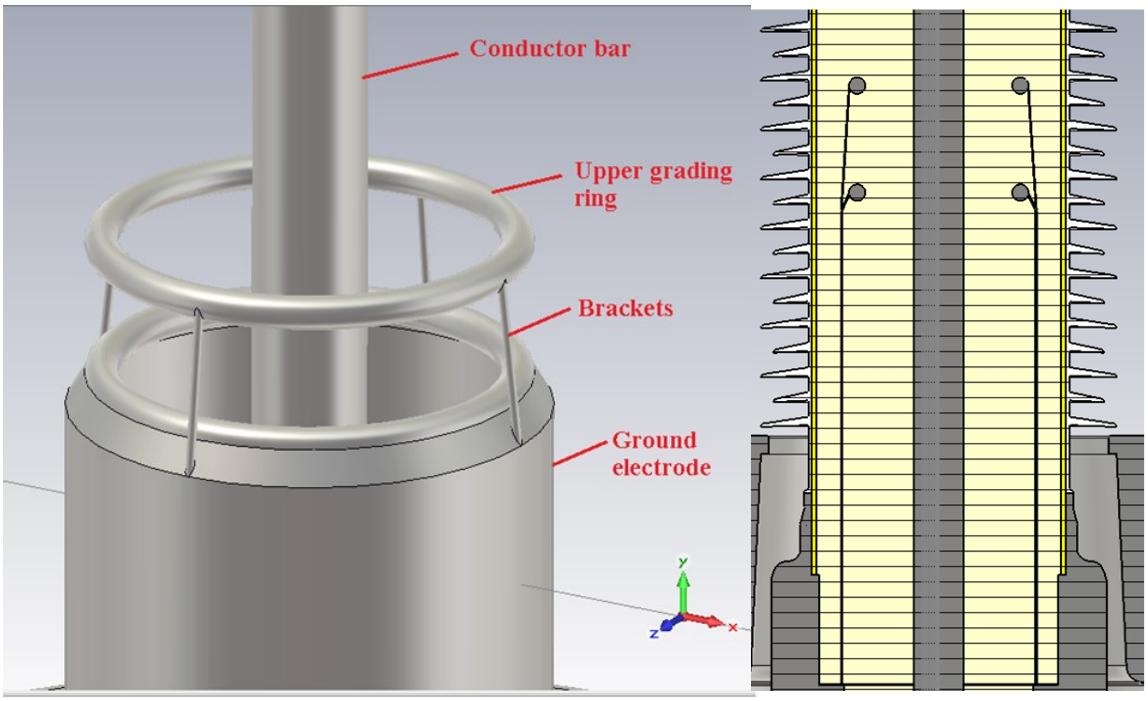


*Figure 46: Variant.9, cylindrical ground electrode with extra grading ring (3D view and sectional view)*

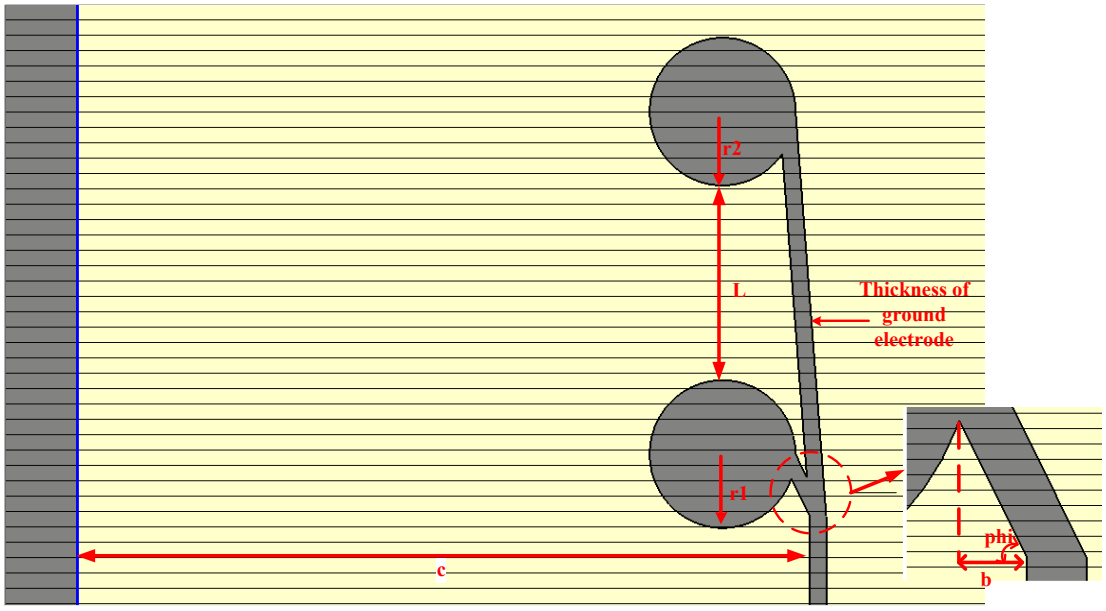


*Figure 47: Parameters of variant.9*

Figure 46 and Figure 47 show the cross section of a ground electrode (variant.9) with axial symmetry in geometry. This structure is modified based on variant.2. It is composed of a lower cylindrical ground electrode with a grading ring, which is totally the same as the variant.2. At the top of the ground electrode it connects with another grading ring by four brackets. Parameter c represents the radius of the ground electrode. The b represents the clearance, with which the ground electrode slopes towards conductor bar at the top side. The height of slope part is controlled by slope angle φ. A grading ring is arranged at the lower part. At the top of the ground electrode another grading ring is fixed. The radius of the two grading rings is represented by the parameters $r_1$ and $r_2$ respectively. The clearance between the two grading rings is expressed by parameter L. The parameters are assumed at b=10mm, c=107.5mm, phi=25°, $r_1$= $r_2$=7.5mm L=100mm and the thickness of the ground electrode material a=1mm.

Apparently the design of variant.9 with two grading rings differs from the above eight single profiles. In my point of view, by optimization of the single profile, the electric field strength between the conductor bar and ground electrode could be reduced greatly, whereas, simultaneously it might not satisfy the requirement of electric field strength in the inside of the FRP tube. The optimization might have negative effects on the electric field strength of FRP inside surface. The purpose of variant.9 is to eliminate such negative influences as much as possible. It even decreases the electric field strength of the FRP inside surface, when the electric field strength between the conductor bar and ground electrode is optimized. In the variant.2 the equipotential lines bend near the periphery of the ground electrode. The distances between two equipotential lines become narrower resulting in a high tangential component of the electric field strength on the inside surface of the FRP tube. Compared to the variant.2 another grading ring is arranged in the structure of variant.9, which means that there is a gap between the two grading rings. The equipotential lines will tend to turn around the grading rings. Consequently, the distances between two equipotential lines are getting wider, which makes the tangential component of the electric field strength on the inside surface of FRP tube in the vicinity of the ground electrode smoother. Besides that, by the interaction between the upper and lower grading rings the electric field strength on the surfaces of ground electrode and conductor bar decreases further compared with variant.2.

### 5.1.6 Summaries of ground electrode designs

The initial parameters and electric field strength for different ground electrodes before optimization are tabulated as follow:

| Structure | Variant | Parameters(unit: mm, φ: ° ) | | | | | | | | |
|---|---|---|---|---|---|---|---|---|---|---|
| Original structure | 1 | a | c | d | r | | | | | |
| | | 1 | 117.5 | 81 | 9 | | | | | |
| Structure with ring profile | 2 | a | b | c | r | φ | $h_1$ | | | |
| | | 1 | 10 | 107.5 | 7.5 | 25° | 6 | | | |
| | 3 | a | c | e | φ | r | $h_1$ | $h_2$ | | |
| | | 2 | 118.5 | 5 | 25° | 10 | 690 | 33 | | |
| Structure with Rogowski profile | 4 | $a_1$ | c | r | $h_1$ | | Parameters of Rogowski profile | | | |
| | | | | | | | a | f | g | |
| | | 2 | 118.5 | 5 | 690 | | 40 | 1 | -2.5 | |
| | 5 | $a_1$ | c | r | $h_1$ | d | Parameters of Rogowski profile | | | |
| | | | | | | | a | f | g | |
| | | 2 | 118.5 | 5 | 690 | 81 | 40 | 1 | -2.5 | |
| Structure with Bézier profile | 6 | a | c | d | $h_1$ | | Parameters of Bézier profile | | | |
| | | | | | | | N | M | P | O |
| | | 2 | 118.5 | 95 | 690 | | (95, 690) | (100, 710) | (110, 704) | (107, 698) |
| | 7 | a | c | d | $h_1$ | r | parameters of Bézier profile | | | |
| | | | | | | | N | M | P | O |

| | | | | | | | | | | |
|---|---|---|---|---|---|---|---|---|---|---|
| | | 2 | 118.5 | 86 | 690 | 10 | (86, 690) | (98, 709) | (86, 700) | (91, 710) |
| | 8 | a | c | r | φ | | parameters of Bézier profile | | | |
| | | | | | | | N | M | P | O |
| | | 2 | 117.5 | 5 | 30° | | (100.5, 713) | (110.5, 685 | (95.5, 698) | (100.5 693) |
| Structure with double grading rings | 9 | a | b | c | φ | $r_1$ | $r_2$ | L | | |
| | | 1 | 10 | 107.5 | 25° | 7.5 | 7.5 | 100 | | |

*Table. 9: Summaries of initial parameters for different ground electrodes*

| Variant / kV/mm / Positions | 1 | 2 | 3 | 4 | 5 | 6 | 7 | 8 | 9 |
|---|---|---|---|---|---|---|---|---|---|
| $E_{max}$ of conductor bar | 32.7 | 27.9 | 26.9 | 32.1 | 32.7 | 27.9 | 30.9 | 26.1 | 27.3 |
| $E_{max}$ on surface of ground electrode | 28.3 | 30.4 | 53.4 | 20.8 | 22.3 | 34.1 | 27.1 | 32.4 | 29.2/ 24.5 |
| $E_{max}$ of inside of FRP | 4 | 3.9 | 3.9 | 3.9 | 3.8 | 3.85 | 3.76 | 3.85 | 3.96 |
| $E_{max}$ of inside of FRP (close to ground electrode) | 2.3 | 2.2 | 2.45 | 2.97 | 2.61 | 2.24 | 2.02 | 2.29 | 1.93 |
| $E_{max}$ of bottom flange | 0.14 | 0.13 | 0.10 | 0.17 | 0.17 | 0.15 | 0.14 | 0.08 | 0.11 |
| $E_{max}$ of rim of transformer cover | 0.98 | 0.96 | 0.98 | 1.09 | 1.09 | 1.08 | 1.08 | 1 | 1.05 |

*Table. 10: Summary of electric field strength for different ground electrodes before optimization (V.1 original structure, V.2,3 inside sloped structure, V.4,5 Rogowski profile, V.6,7,8 cubic Bézier profile, V.9 double grading rings)*

### 5.1.7 Optimal design of the ground electrode

As we discussed in the chapter 4, the complete optimal design of the ground electrode is classified into two steps: the predetermination of parameter ranges by preliminary investigation and optimization by genetic algorithms. The structure variant.2 is taken as an example for the optimal design. For variant.2 five parameters (a,b,c,φ and r) are swept coarsely. In the preliminary investigation a parameter will be considered as variable, in the meanwhile others are fixed in the investigation. To optimize the ground electrode the discussions are mainly focused on the electric field strength on the surface of ground electrode, conductor bar and FRP inside in the vicinity of ground electrode. From Figure 48 to Figure 62 it shows the interconnections between the electric field strength and every parameter. In the most of figures the curves of electric field strength go up or down monotonically with the increasing of a parameter. However, the variation of E-curves doesn't tend to decrease or increase monotonically in several charts. E-curve in Figure 52 is growing intermittently with the increase of parameter b. The E-curves fluctuate between the 26.5kV/mm to 30.5kV/mm in Figure 58 and 26.5kV/mm to 33kV/mm in Figure 61 with the variation of a parameter.

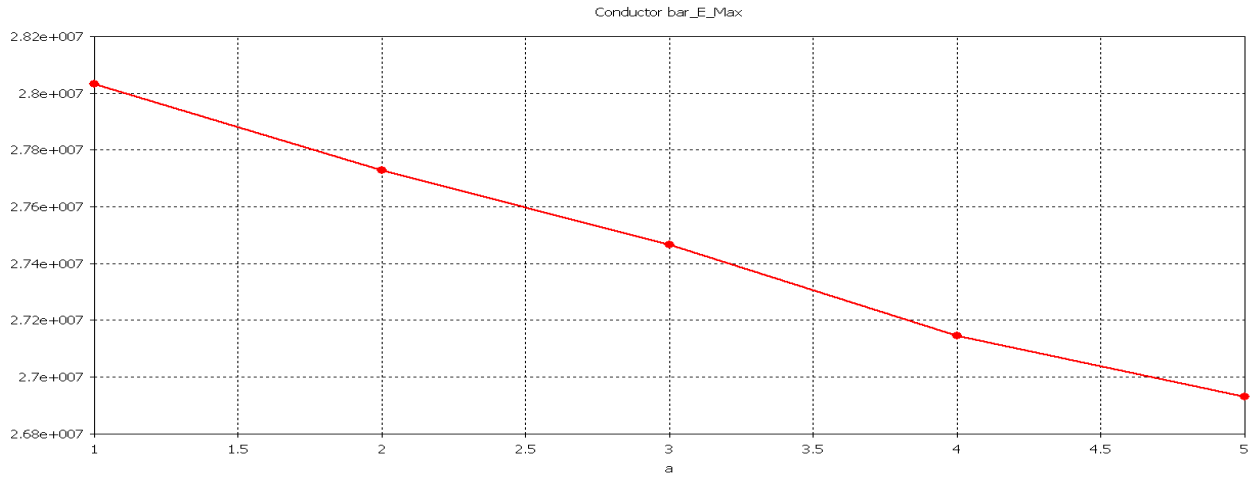


*Figure 48: Maximum E of conductor bar with the variation of parameter a*

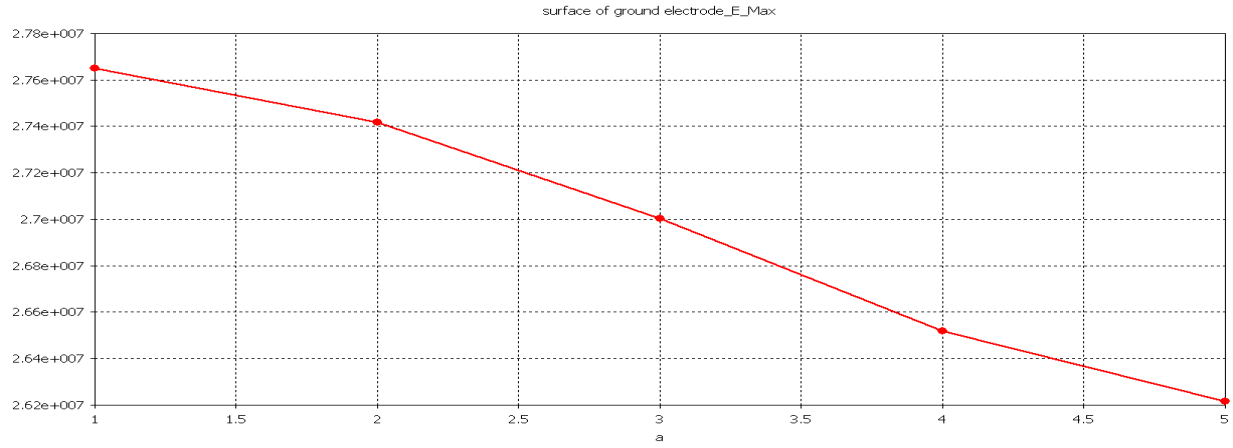


*Figure 49: Maximum E on the surface of ground electrode with the variation of parameter a*

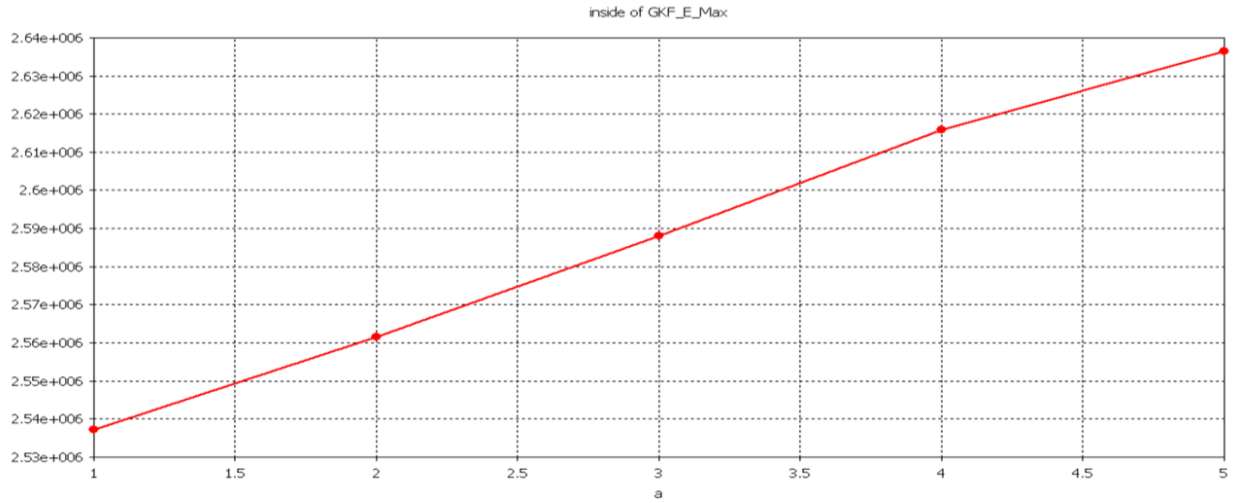


*Figure 50: Maximum E of FRP inside closing to ground electrode with the variation of parameter a*

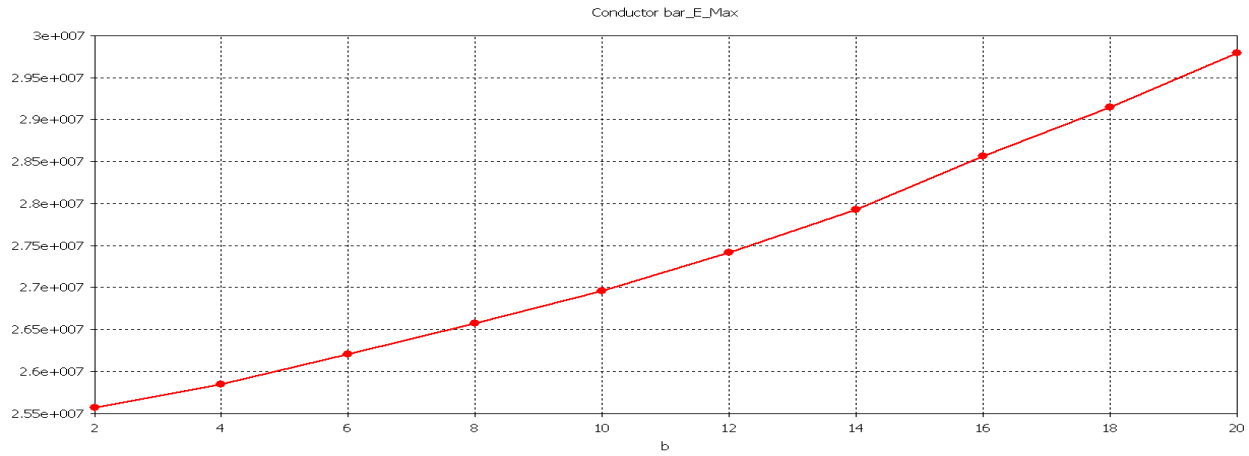


*Figure 51: Maximum E of conductor bar with the variation of parameter b*

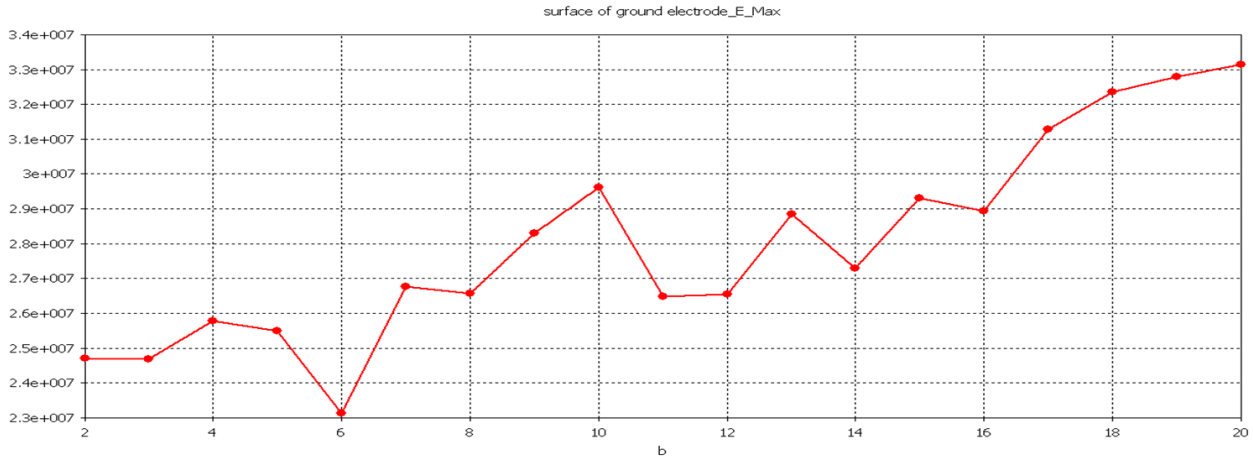


*Figure 52: Maximum E on the surface of ground electrode with the variation of parameter b*

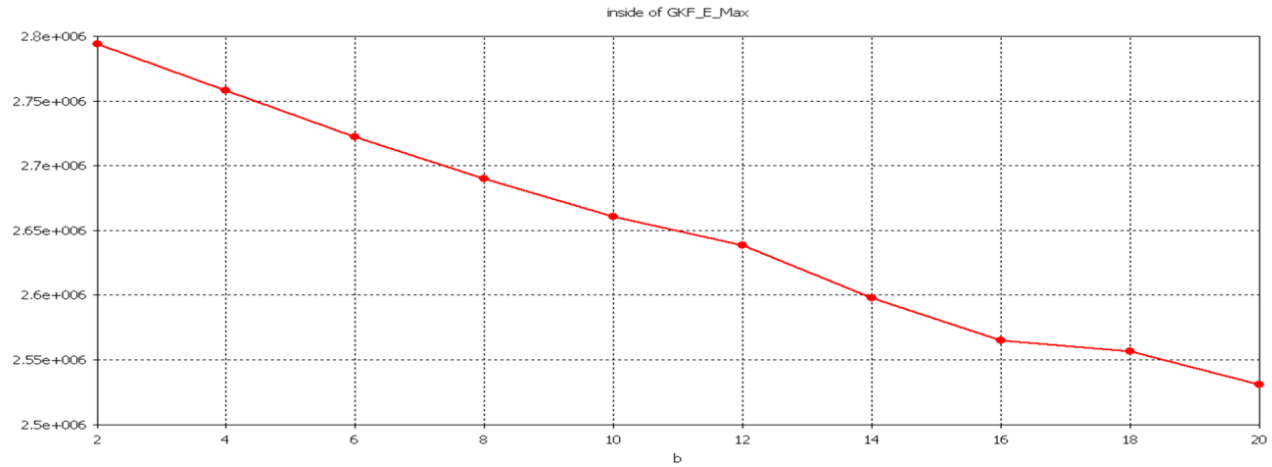


*Figure 53: Maximum E of FRP inside closing to ground electrode with the variation of parameter b*

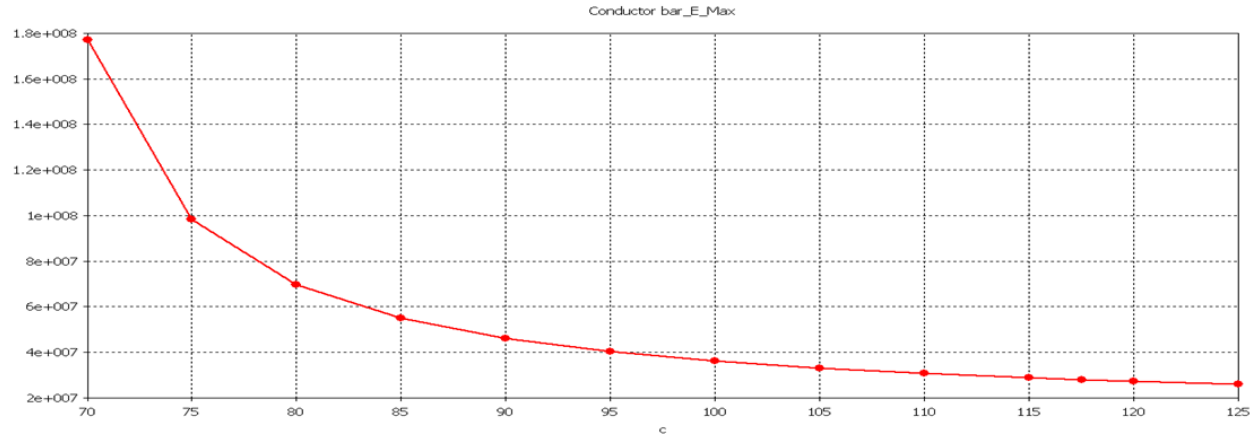


*Figure 54: Maximum E of conductor bar with the variation of parameter c*

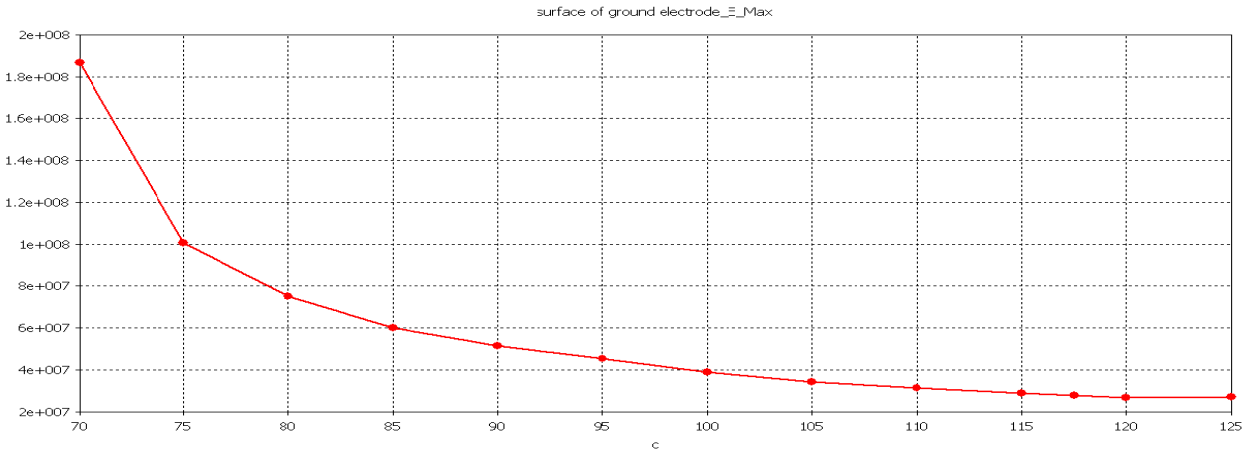


*Figure 55: Maximum E on the surface of ground electrode with the variation of parameter c*

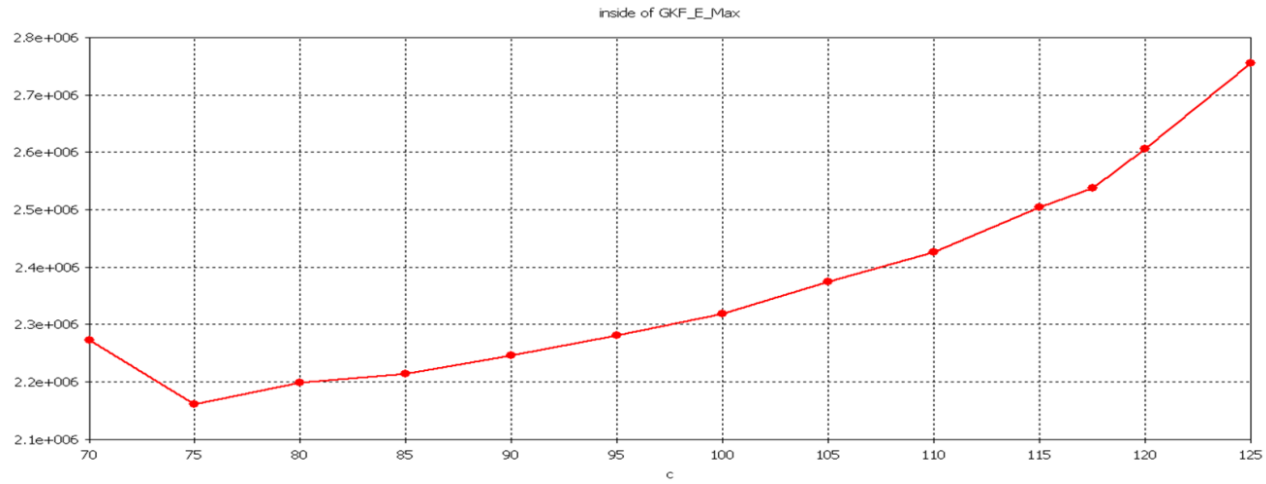


*Figure 56: Maximum E of FRP inside closing to ground electrode with the variation of parameter c*

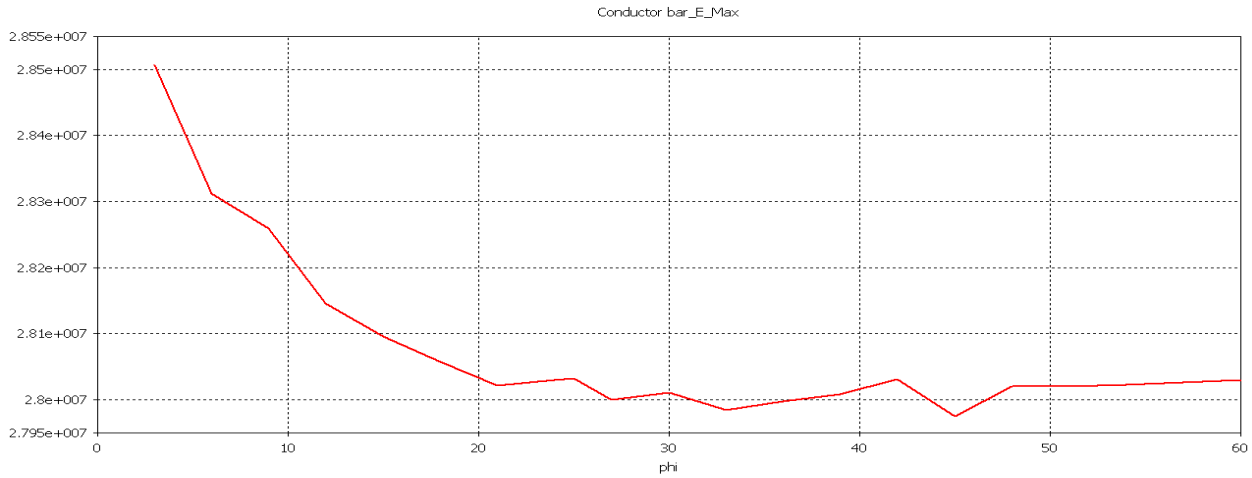


*Figure 57: Maximum E of conductor bar with the variation of parameter φ*

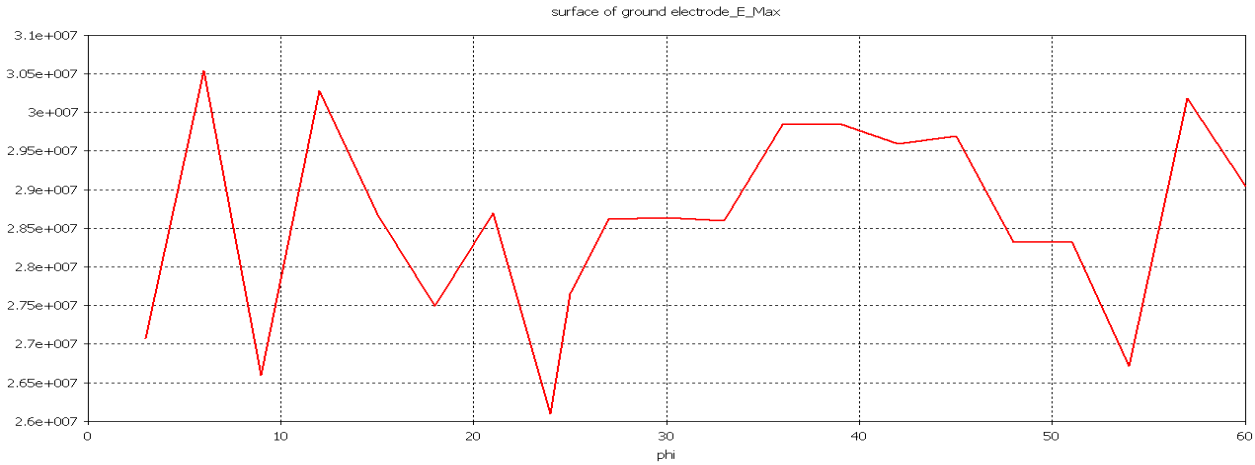


*Figure 58: Maximum E on the surface of ground electrode with the variation of parameter φ*

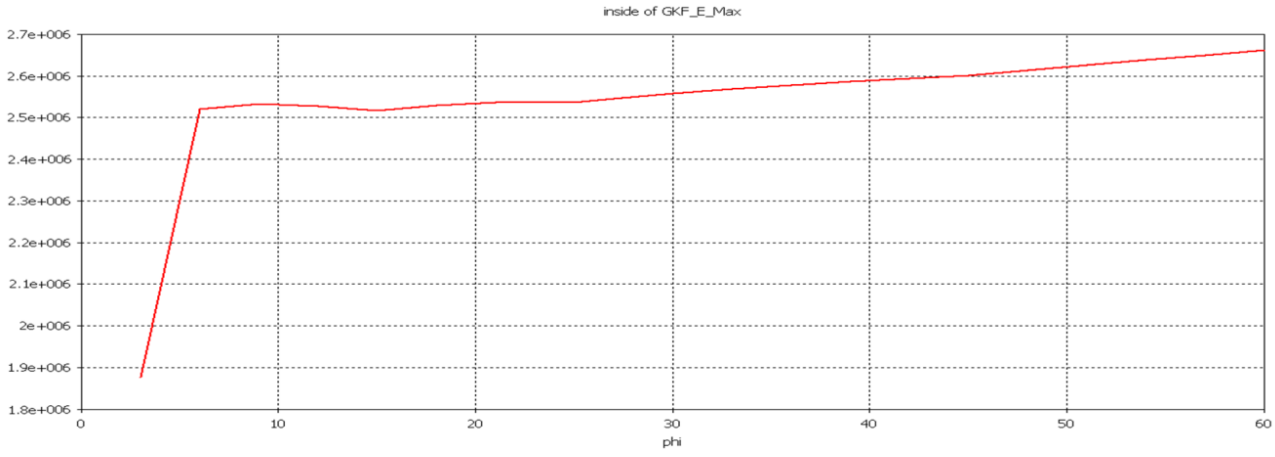


*Figure 59: Maximum E of FRP inside closing to ground electrode with the variation of parameter φ*

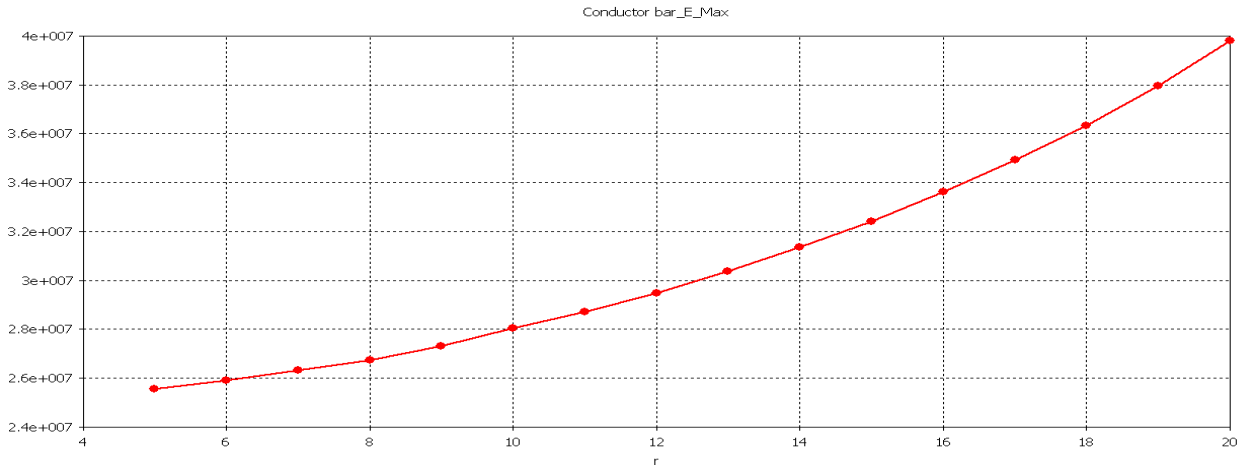


*Figure 60: Maximum E of conductor bar with the variation of parameter r*

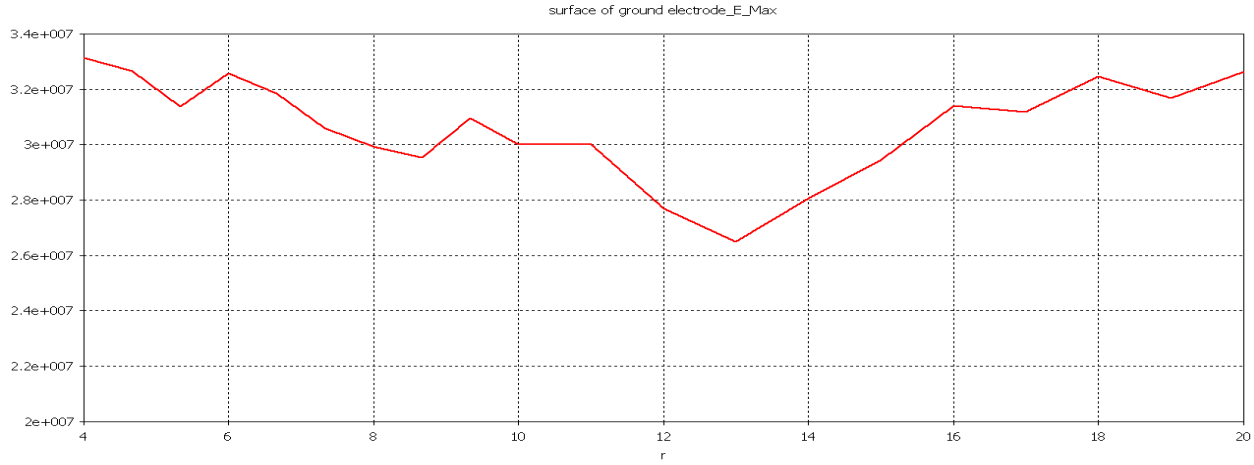


*Figure 61: Maximum E of surface of ground electrode with the variation of parameter r*

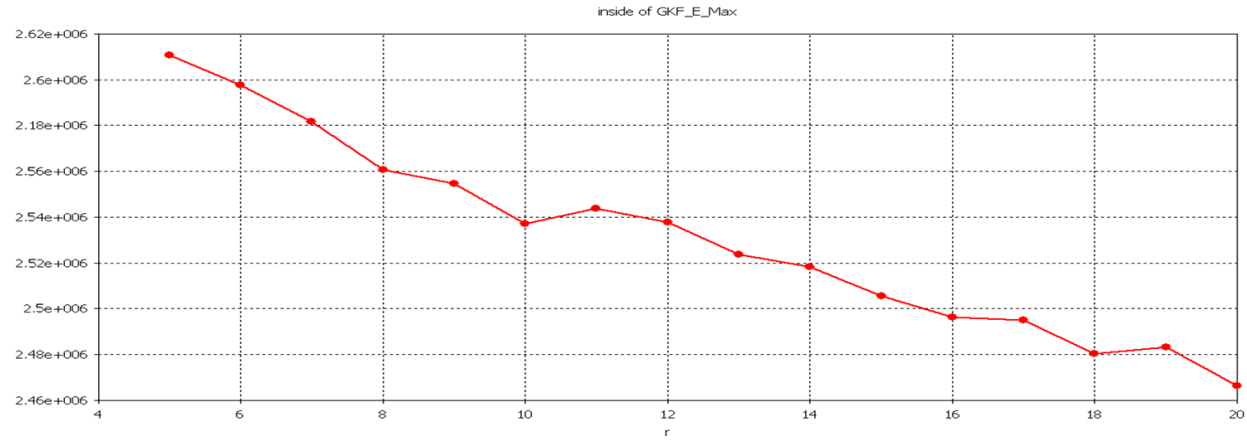


*Figure 62: Maximum E of FRP inside closing to ground electrode with the variation of parameter r*

After coarse sweeping the boundaries of parameters, the further optimization of parameters regarding with ground electrode will be performed by genetic algorithms. Maximum electric field strength is defined as goal function, which will be computed by simulation. The electric field strength of critical points will be defined to be constrain condition, which is regard as fitness function in the genetic algorithms. For variant.2 there are five different parameters, which should be optimized. The individual chromosome can be expressed as follows

$$x = [a, b, c, \varphi, r]$$

Where "a" represents the thickness of ground electrode. "b" represents the clearance, which at the top side the ground electrode slopes to conductor bar. "c" represents the radius between the conductor bar and ground electrode. The height of slope part is controlled by slope angle φ. "r" is the radius of grading ring. By the preliminary investigation the values of parameters, which conform not to the structure of ground electrode obviously, are eliminated out of the range. Depending on the results from the preliminary investigation the parameters could be set to a:(4mm-5mm), b:(6mm-14mm), c:(110mm-124mm), φ:(26°-36°) and r:(6-15mm). The initial values of parameters could be properly set to a=4mm, b=6mm, c=110mm, φ=26° and r=10mm.

There is neither linear relationship nor straightforward expression between the maximum electric field strength of critical points and parameters of ground electrode. Therefore, the fitness function of variant.2 works out to be

$$Fitness = w_1[E_{S,\max}(x) - E_{S,G}(x)] + w_2[E_{C,\max}(x) - E_{C,G}(x)] + w_3[E_{FRP,\max}(x) - E_{FRP,G}(x)] \quad \textit{Eq. 54}$$

Where $E_{S,max}$, $E_{C,max}$ and $E_{FRP,max}$ indicate the simulation values of maximum electric field strength regarding surface of ground electrode, conductor bar and FRP tube in the vicinity of ground electrode. $w_1$, $w_2$ and $w_3$ represent the corresponding weighting factor respectively. $E_{S,G}$, $E_{C,G}$ and $E_{FRP,G}$ are the corresponding goal values The goal values of electric field strength are set as follow

$$E_{S,G} = 28kV/mm,\ E_{C,G} = 27kV/mm,\ E_{FRP,G} = 2.8kV/mm$$

Substituting weighting factors $w_1$=0.222, $w_2$=0.444 and $w_3$=0.333, the expression of fitness function for the variant.2 can be given by follow,

$$Fitness = 0.222 \cdot [E_{S,\max}(x) - 28 \cdot 10^6] + 0.444 \cdot [E_{C,\max}(x) - 27 \cdot 10^6] + 0.333 \cdot [E_{FRP,\max}(x) - 2.8 \cdot 10^6]$$

*Eq. 55*

It is assumed that $E_{S,\max} < 28kV/mm$, $E_{S,\max} - E_{S,G} = 0$; $E_{C,\max} < 27kV/mm$, $E_{C,\max} - E_{C,G} = 0$; $E_{S,\max} < 2.8kV/mm$, $E_{FRP,\max} - E_{FRP,G} = 0$, Under this condition, the lower fitness value is considered as a better result. The population size ($N_p$) and the maximal number of iterations/generations ($G_{max}$) must be chosen. The population size, i.e. the number of individual chromosome in a generation, might be set to $N_p$=32. The number of generations could be set to 30. The fitness function is evaluated for each chromosome in the population, and the population will be sorted in the order of better fitness. The mutation with rate of 30% will be applied to reproduce the 50% of chromosomes in the new generation. After 30 generations the genetic algorithms converge to an acceptable result. The following table summarizes of optimized parameters and maximum electric field strengths on critical points of different ground electrodes after optimization.

| Structure | Variant | Parameters(unit: mm, φ: ° ) | | | | | | | | |
|---|---|---|---|---|---|---|---|---|---|---|
| Original structure | 1 | a | c | d | r | | | | | |
| | | 2.5 | 117.5 | 101.3 | 6.1 | | | | | |
| Structure with ring profile | 2 | a | b | c | r | φ | $h_1$ | | | |
| | | 4.7 | 10.4 | 117.3 | 8.9 | 30.5 | 693 | | | |
| | 3 | a | c | e | φ | r | $h_1$ | $h_2$ | | |
| | | 3.2 | 115.8 | 2.1 | 10.3° | 3 | 33 | 690 | | |
| Structure with Rogowski profile | 4 | $a_1$ | c | r | $h_1$ | | Parameters of Rogowski profile | | | |
| | | | | | | | a | f | g | |
| | | 2.2 | 96 | 6.4 | 652 | | 31 | 0.73 | -1.42 | |
| | 5 | $a_1$ | c | r | $h_1$ | d | Parameters of Rogowski profile | | | |
| | | | | | | | a | f | g | |

| | | | | | | | | | | |
|---|---|---|---|---|---|---|---|---|---|---|
| | | 2.6 | 117.5 | 6.4 | 652 | 89.5 | 31 | 0.73 | -1.42 | |
| Structure with Bézier profile | 6 | a | c | d | $h_1$ | | Parameters of Bézier profile | | | |
| | | | | | | | N | M | P | O |
| | | 1.7 | 113 | 90 | 690 | | (90, 690) | (90.9, 706.8) | (105.5, 711.5) | (103.7, 696.9) |
| | 7 | a | c | d | $h_1$ | r | Parameters of Bézier profile | | | |
| | | | | | | | N | M | P | O |
| | | 3.8 | 117.3 | 99.8 | 693 | 5.1 | (99.8, 693) | (99.8, 707) | (105.3 ,717.9 ) | (115.4, 717.9) |
| | 8 | a | c | r | φ | | Parameters of Bézier profile | | | |
| | | | | | | | N | M | P | O |
| | | 1.1 | 117.5 | 9.3 | 22° | | (105.3 ,713) | (101.2 ,690.6 ) | (106.7 ,685) | (127.3, 685) |
| Structure with double grading rings | 9 | a | b | c | φ | $r_1$ | $r_2$ | L | | |
| | | 4.7 | 10 | 122.3 | 30.5° | 8.9 | 8.9 | 54 | | |

*Table. 11: Summary of optimized parameters for different ground electrodes*

| Variant / kV/mm / Positions | 1 | 2 | 3 | 4 | 5 | 6 | 7 | 8 | 9 |
|---|---|---|---|---|---|---|---|---|---|
| $E_{max}$ of conductor bar | 27.5 | 26.5 | 25.3 | 30.2 | 30.6 | 30.2 | 28.2 | 26.1 | 25.3 |
| $E_{max}$ of surface of ground electrode/second grading ring | 22.4 | 26.2 | 38.3 | 22.5 | 22.7 | 28.3 | 19.7 | 22.1 | 24.9/ 18.9 |
| $E_{max}$ of ground electrode outside | | | | | | | | | 13.1 |
| $E_{max}$ of inside of FRP | 4.12 | 3.98 | 4.35 | 3.9 | 3.96 | 3.91 | 4.05 | 3.93 | 3.9 |
| $E_{max}$ of inside of FRP (close to ground electrode) | 3.1 | 3 | 3.05 | 2.85 | 2.85 | 2.7 | 3.05 | 3.6 | 2.67 |
| $E_{max}$ of bottom flange | 0.1 | 0.1 | 0.15 | 0.15 | 0.12 | 0.16 | 0.12 | 0.11 | 0.15 |
| $E_{max}$ of rim of transformer cover | 0.9 | 0.84 | 0.94 | 1.06 | 0.89 | 1.12 | 0.97 | 0.92 | 1.04 |

*Table. 12: Summary of maximum electric field strength of different ground electrodes after optimization under LIV 1050kV*

From the Table. 12 we can observe that by the genetic algorithms the satisfactory results are obtained from several optimized ground electrodes (variant.1, 2, 7 and 9). Due to asymmetric structure the variant.9 is not suitable for 2D cylindrical simulation. In the 3D construction there are still several problems regarding with boundary conditions and mesh generations to solve. Therefore, the discussion about variant.9 is suspended in the dissertation. In the structures of variant.1, 2, and 7 $E_{max}$ of conductor bar and surface of ground electrode decrease greatly, $E_{max}$ of

conductor bar concentrates on about 26-27kV/mm and $E_{max}$ of surface of ground electrode fluctuates from 19kV/mm to 26kV/mm, whereas, the optimal structure yields to a little negative influence on the electric field strength of glass fiber tube (FRP) inside. $E_{max}$ of FRP inside closing to ground electrode increases a lot. On the one hand, the expanding of radius of ground electrode makes the periphery of ground electrode close to FRP, which causes the negative influence on the FRP. On another hand, it depends on the strategy of optimization, i.e. weighting factor of genetic algorithms. In this optimization, the electric field strength of conductor bar is dominant in the weighting factors, which means the optimal parameters tend to converge to a structure with lower electric field strength on the surface of conductor bar. In the optimization, the opposite weighting factor, i.e. the higher weighting factor of FRP has been attempted to set in the optimization procedure as well. However, the result giving rise to enhancement of $E_{max}$ of conductor bar and surface of ground electrode cannot be accepted. It could be acceptable that the electric field strength increases a little or keeps its original value. The optimizations of FRP in next chapter 5.2 are based on the optimized results (variant.1, 2 and 7) of this chapter.

## 5.2 Optimization of fiber-reinforced plastic tube (FRP)

In this subchapter the diameter of FRP in three optimized structures (variant.1,2 and 7) will be reduced so that the new design could fulfill less usage of $SF_6$ and more compact structure. In the first section 5.2.1 the criteria for the reduction of FRP will be illustrated briefly. A detailed description of methodology for a reduction will be discussed in section 5.2.2. The results of three optimized structures will be summarized and compared with each other in the final section.

### 5.2.1 Criteria for the optimization of FRP

Under LIV referring to criteria of $SF_6$ withstand electric field strength at 0.7MPa in Table. 3 and results from Ansoft Maxwell the maximum electric field ($E_{max}$) at the ground electrode and $E_{max}$ of the conductor bar should be no more than the maximum value in the original conical structure and criteria values of $SF_6$, i.e. $E_{max}$ at the ground electrode <28kV/mm and $E_{max}$ at the conductor bar <32.3kV/mm. In this section we are focusing on the influence on the optimization of the FRP, which concentrates mainly on electric field strength near the ground electrode. The $E_{max}$ at the FRP close to the ground electrode ($E_{max,\ FRPG}$) and its absolute tangential component ($E_{tangential,\ FRPG}$) should be less than the maximum value in the original cylindrical structure respectively i.e. $E_{max,\ FRPG}$ <3.3kV/mm and $E_{tangential,\ FRPG}$ <2.5kV/mm.

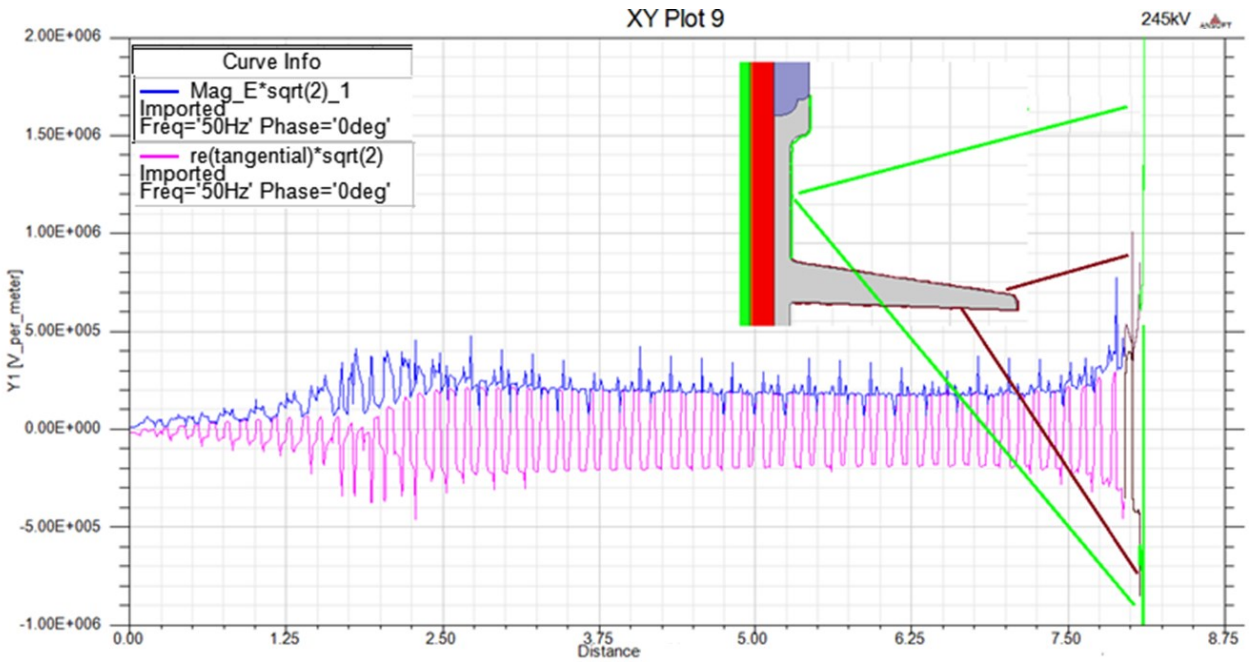


*Figure 63: E curve and its tangential component along silicon rubber sheds in original structure under AC voltage* $\frac{245kV}{\sqrt{3}}$ *(measure line see Figure 14)*

Under AC voltage more attention should be paid on the outside interface between silicon and air, which might lead to surface discharge on the silicon rubber sheds and corona discharge on the top flange. The maximum effective value of the tangential electric field strength along silicon rubber sheds should be no more than $0.5 \cdot \sqrt{2}$ approx. 0.7kV/mm (peak value). Figure 63 shows the E curve and its tangential component along the silicon rubber sheds in the original structure. At the tail of the curve, i.e. at the first sheath and first weather shed, the tangential components of E are greater than the critical values. Maximum $E_{peak,tangential}$ of the first sheath reaches approx. 1kV/mm (green), and of the first weather shed reaches approx. 0.85kV/mm (wine-red). The corresponding maximum $E_{peak}$ at the first sheath reaches approx. 2kV/mm (green), and at the first weather shed reaches approx. 1kV/mm (wine-red). Apparently the tangential component of E in this region is not influenced by the structure of the ground electrode or the diameter of FRP; however it is mainly influenced by the contour of the top flange. Therefore, the maximum $E_{peak,tangential}$ at the first weather shed and the above part are outside the scope of the following considerations in this section. They will be optimized in the following subchapters 5.3 and 5.4. Tab. 5 lists the summary of criteria for optimization of the FRP under LIV and AC voltage to summarize all the mentioned criteria.

| | Under LIV | Under AC Voltage |
|---|---|---|
| $E_{max}$ of ground electrode | <27kV/mm | |
| $E_{max}$ of conductor bar | <33kV/mm | |
| $E_{max,FRPG}$ | <3.3kV/mm | |
| $E_{tangential,FRPG}$ (absolute value) | <2.5kV/mm | |
| $E_{tangential}$ of silicon / air (absolute peak value) | | <0.7kV/mm |

*Table. 13: Summary of criteria for optimization of FRP*

## 5.2.2 Three methods for the optimization of FRP

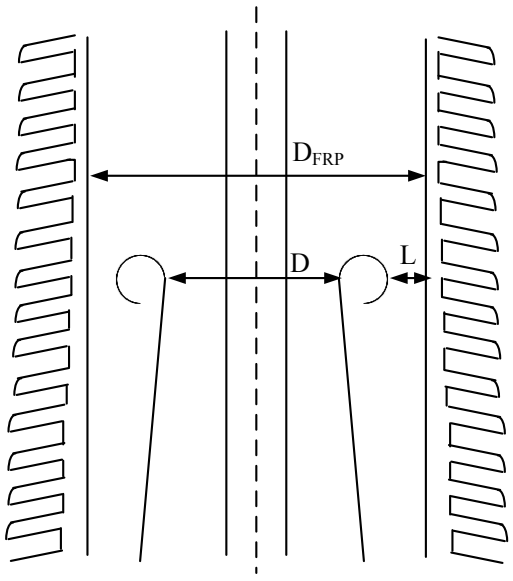


*Figure 64: Rough sketch of HV bushing*

Figure 64 shows a rough configuration of the HV bushing. For the optimization of FRP three parameters are involved, i.e. diameter of the FRP ($D_{FRP}$), diameter of the ground electrode (D) and the distance between ground electrode and FRP (L). These three parameters could be modified by the following three methods to observe the changing trends of electric field strength and determine the optimized diameter of the FRP.

**Method A:** Keeping the ratio of $\frac{D}{D_{FRP}}$

When $D_{FRP}$ is reduced, D will be reduced proportionally based on the below equation:

$$\frac{D}{D_{FRP}} = \frac{D - \Delta D}{D_{FRP} - \Delta D_{FRP}}$$

Where $\Delta D$ and $\Delta D_{FRP}$ are the change of D and change of $D_{FRP}$

**Method B:** Reduction of L

The reduction of the FRP is totally dependent on the distance between the ground electrode and FRP. The diameter of ground electrode (D) is fixed.

$$\begin{cases} \Delta D_{FRP} = \Delta L \\ \Delta D = 0 \end{cases}$$

**Method C:** Reduction of D

The reduction of FRP is totally dependent on the diameter of the ground electrode. The distance between ground electrode and FRP (L) is fixed.

$$\begin{cases} \Delta D_{FRP} = \Delta D \\ \Delta L = 0 \end{cases}$$

Where $\Delta L$ is the change of L

These three methods are applied on the ground electrode variant.1 (V.1), variant.2 (V.2) and variant.7( V.7).

### 5.2.3 Analysis of results

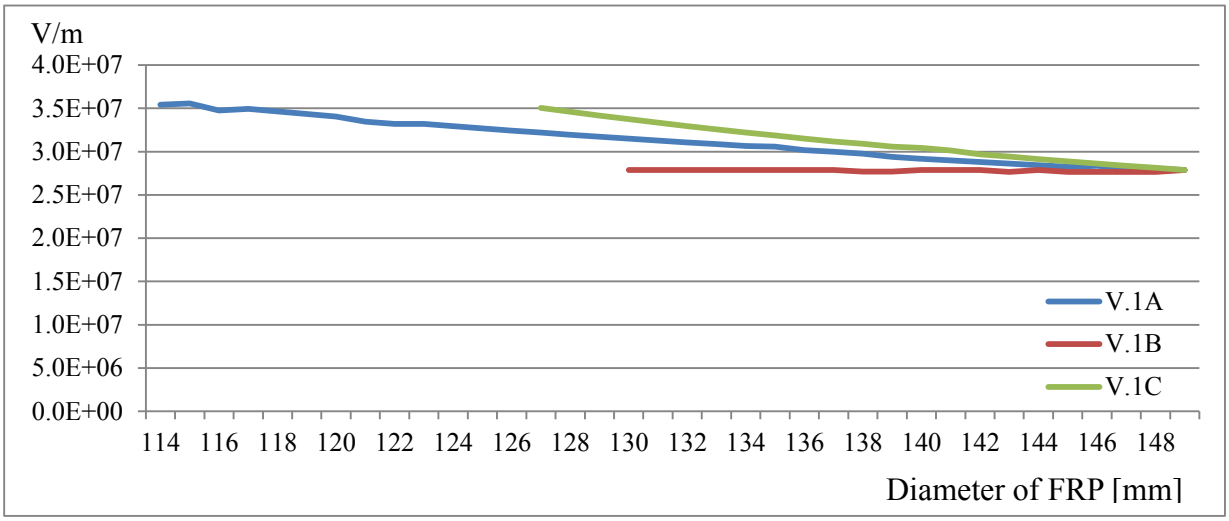


*Figure 65 $E_{max}$ of conductor bar with different diameter of FRP by three methods*

Figure 65 presents relationship between $E_{max}$ of the conductor bar and the diameter of FRP by three different methods. The curve of V.1B remains at approx. 27.8kV/mm, which indicates that the reduction of L (method B) has no effect on E of the conductor bar. If the structure of the ground electrode is fixed, $E_{max}$ on the conductor bar depends on the diameter of the ground electrode D. By keeping the ratio of $\frac{D}{D_{FRP}}$ (method A) and by reduction of D (method C) E of the conductor bar rises in varying degrees. Compared to the method C due to proportional reduction of D by method A $E_{max}$ of the conductor bar rises gradually.

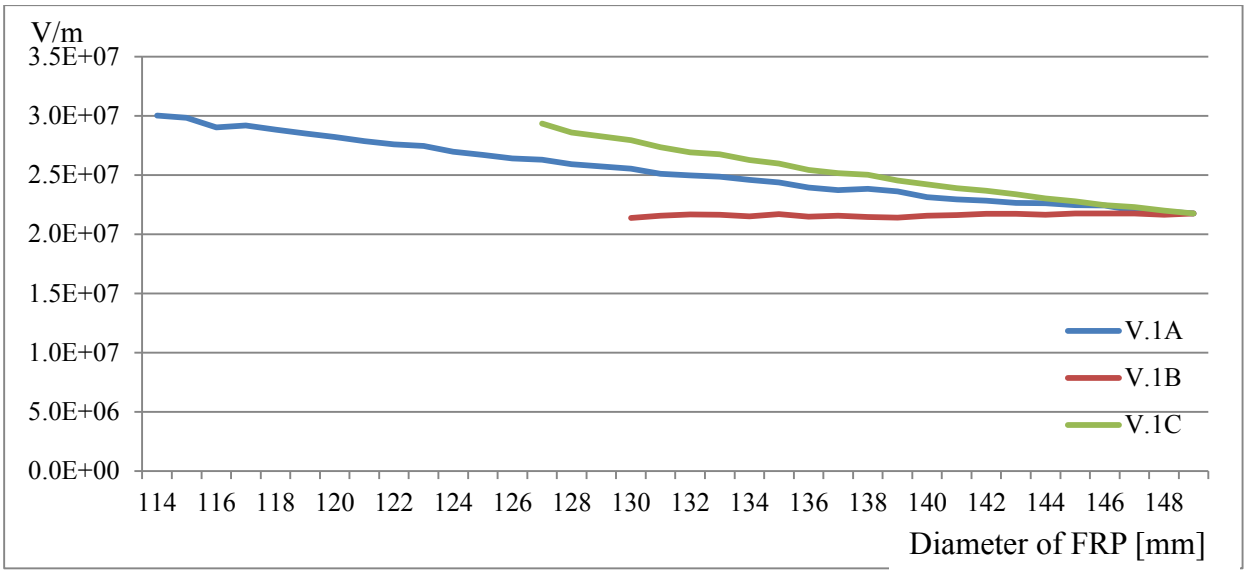


*Figure 66: $E_{max}$ of ground electrode with different diameter of FRP by three methods*

Figure 66 demonstrates the relationship between $E_{max}$ of the ground electrode and the diameter of FRP by three different methods. Likewise, because of non-effect on $E_{max}$ of the ground electrode it remains at approx. 21kV/mm by method B. $E_{max}$ of the ground electrode increases with the reduction of diameter of FRP by method A and C. Method A has a greater influence on the increase in $E_{max}$ of the ground electrode.

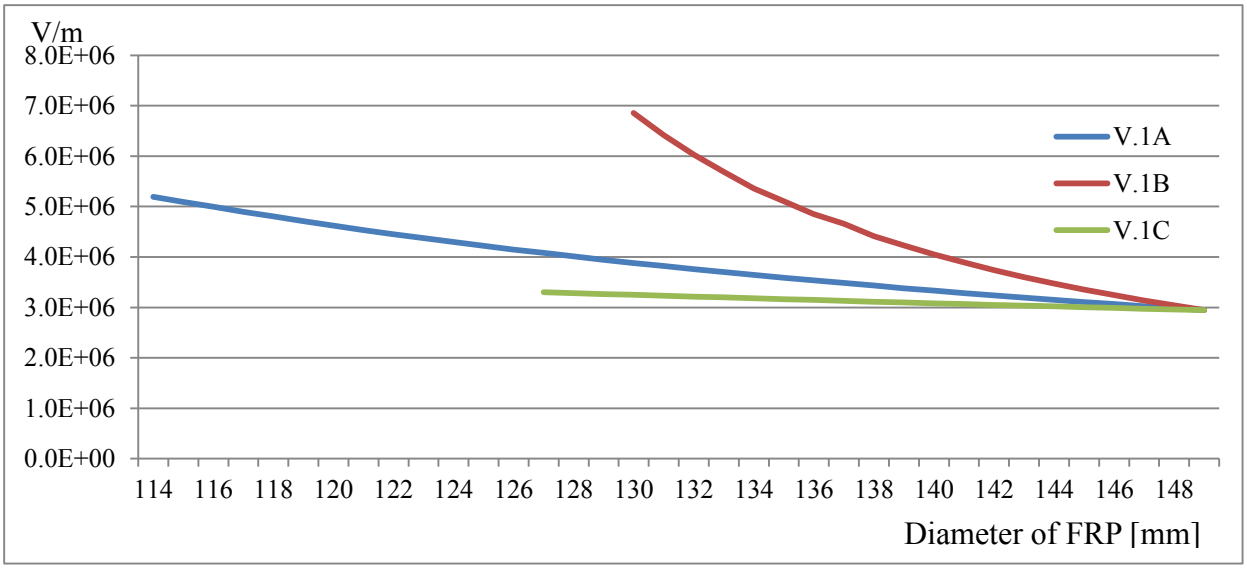


*Figure 67: $E_{max,\ FRPG}$ with different diameter of FRP by three methods*

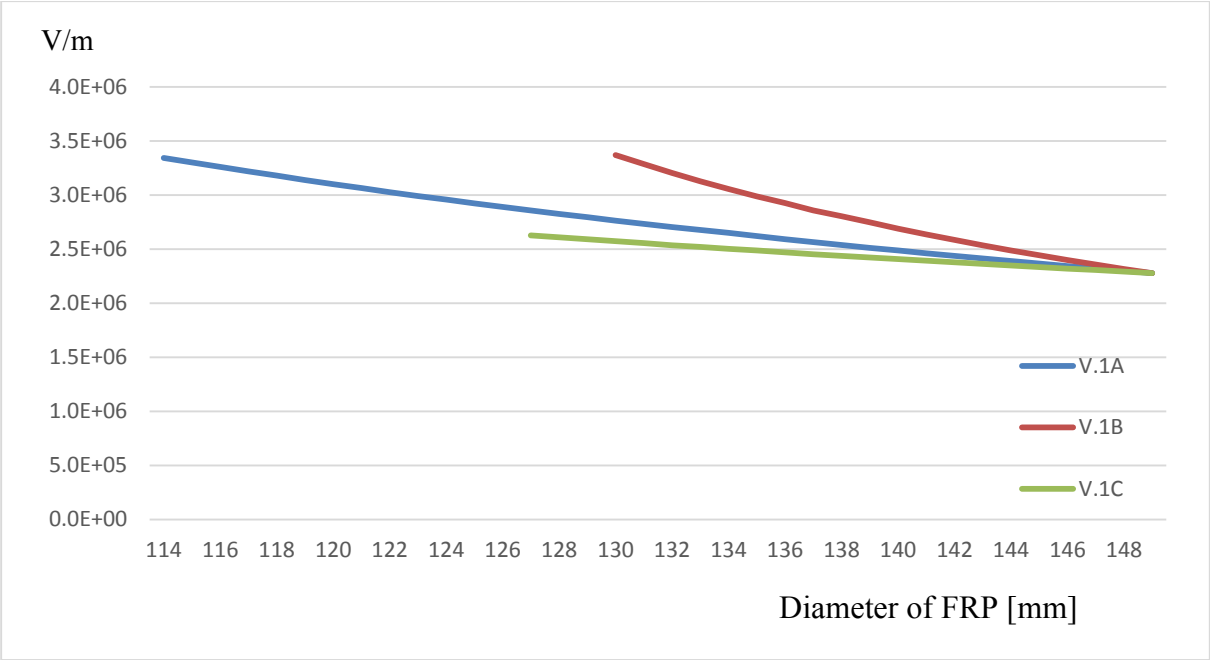


*Figure 68: $E_{tangential,\ FRPG}$ with different diameter of FRP by three methods*

Figure 67 and Figure 68 show $E_{max,\ FRPG}$ and $E_{tangential,\ FRPG}$ with different diameters of the FRP tube by three methods. The changing tendency of $E_{tangential,\ FRPG}$ is equivalent to the $E_{max,\ FRPG}$. The analysis is only concentrated on $E_{max,\ FRPG}$. The three curves by three methods go up in different degrees. Although the distance between the ground electrode and FRP is kept, it is indispensable that $E_{max,\ FRPG}$ continues to climb up in unobvious range. It means not only the reduction of L influences the $E_{max}$ of FRP negatively, but also the reduction of diameter of FRP, i.e. being close to the conductor bar has a more or less negative effect on $E_{max,\ FRPG}$ as well. The curve V.1B has attracted a lot of attention in Figure 67. With the reduction of the distance L between the ground electrode and FRP it brings great increase in $E_{max,\ FRPG}$. From the characteristic of varying of curve V.1B it is clear that $E_{max,\ FRPG}$ depends on a large extent on L.

From the above four figures, the results of the most proper methods for each variant (V.1, V.2 and V.7) are shown in the following Figure 69, Figure 70, and Figure 71 respectively. The equivalent changing trends on the electric field strength are also presented for the three variants.

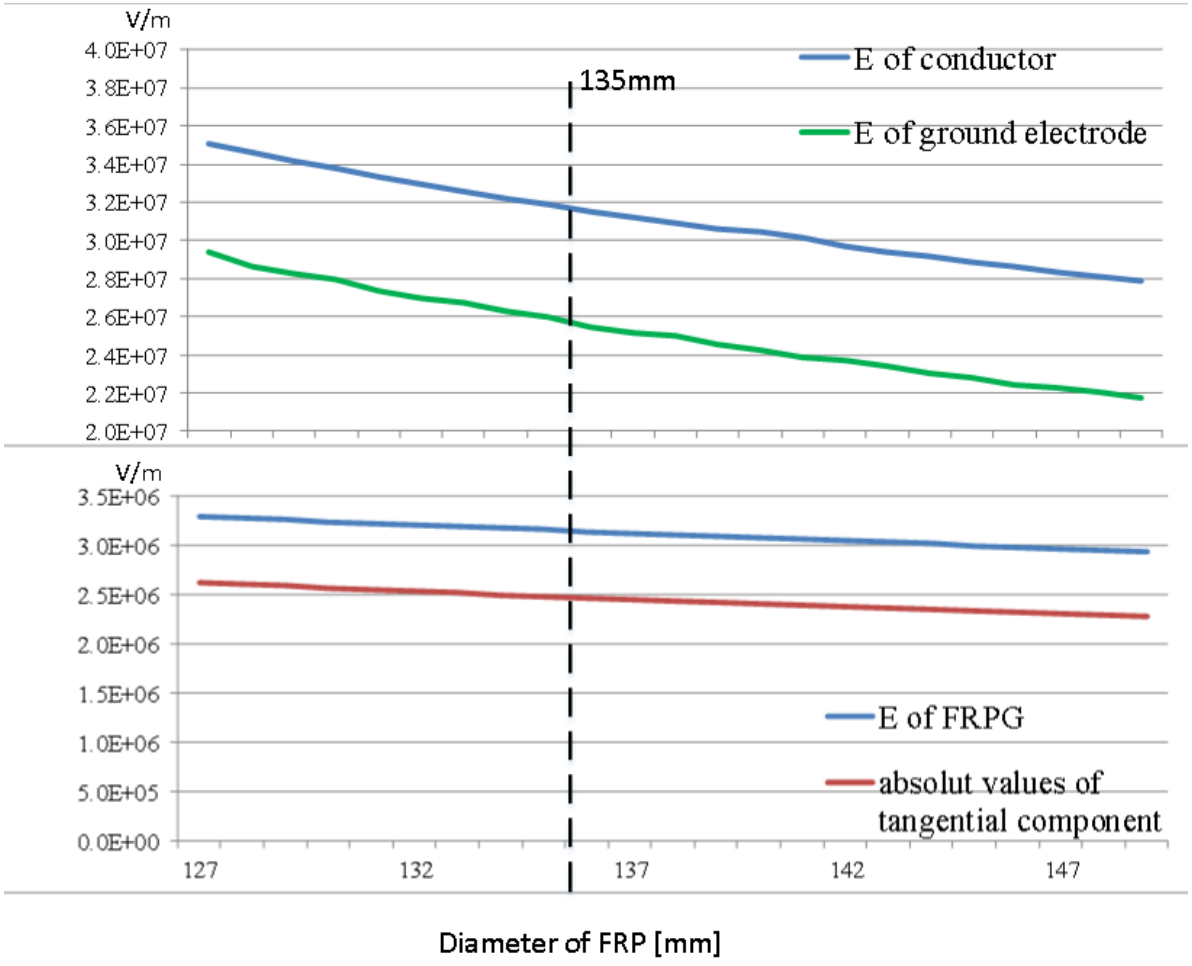


*Figure 69: Effect of Reduction of D (method C) in optimized V.1 on maximum electric field strength*

According to the criteria mentioned in the above section no more reduction of diameter of FRP will be considered, when maximum electric field strength on a critical point exceeds the criterion value. By carrying out three different methods the most proper method reaching minimal diameter of FRP is method C, i.e. reduction of D, which could reduce the diameter of FRP to 135mm. The absolute value of the tangential component reaches 2.48kV/mm at 135mm, which nearly equals the criterion value of the tangential component (2.5kV/mm). The electric field strength on other critical points keeps still a small amount of margin.

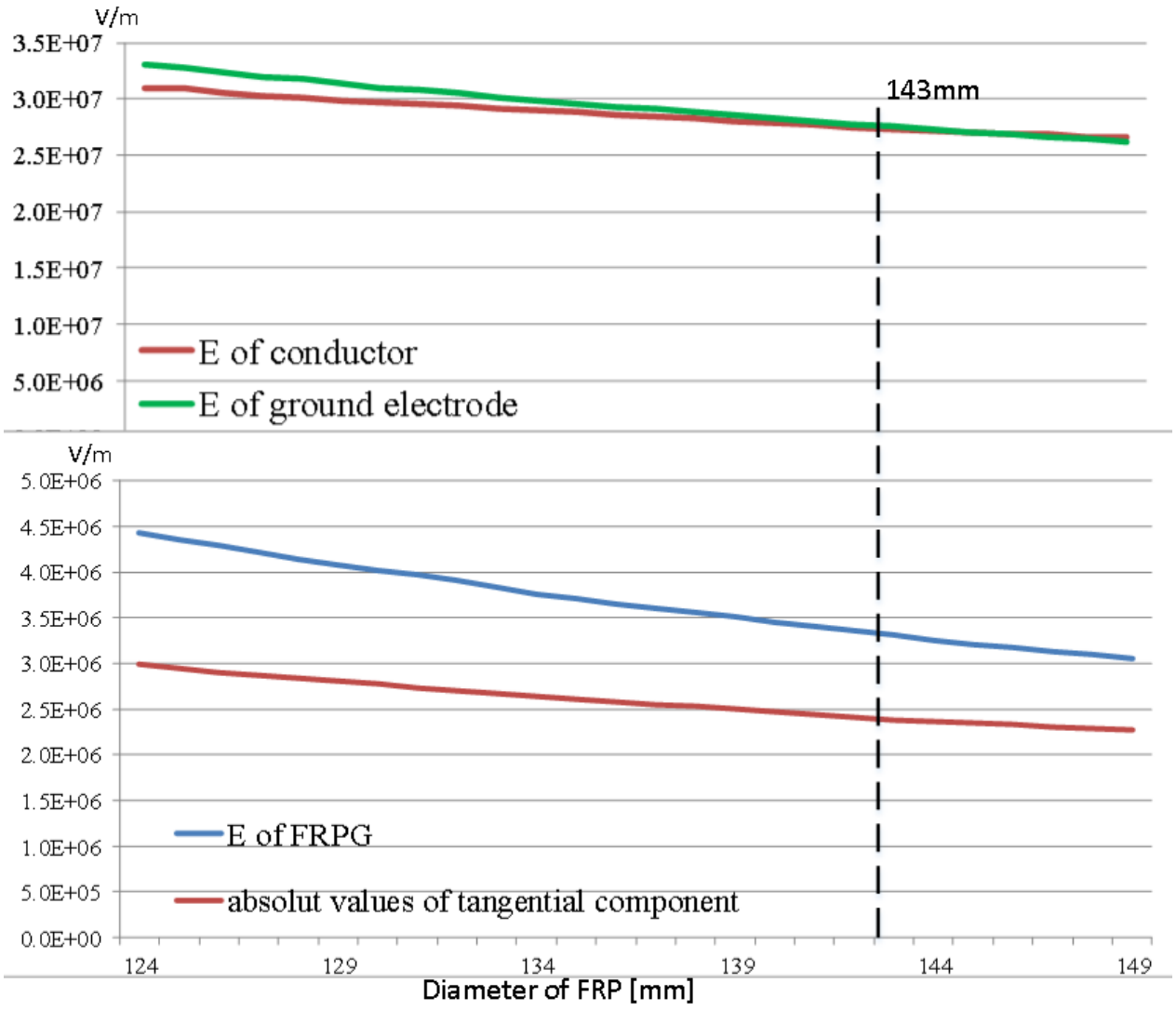


*Figure 70: Effect of keeping the ratio of* $\frac{D}{D_{FRP}}$ *(method A) in V.2 on maximum electric field strength*

From three methods the most suitable method for variant.2 is method A, which can reduce the diameter of FRP to 143mm. The original V.2 structure has its own disadvantage. The natural defect is that $E_{max}$ of the ground electrode is near to the criterion value, and for $E_{max}$ of FRP it has not enough margins either. With the reduction of the diameter of FRP these values exceed the criterion value very quickly. The electric field strength on the conductor bar has still a huge amount of margin. $E_{max}$ of the conductor bar reaches only 27.3kV/mm under LIV.

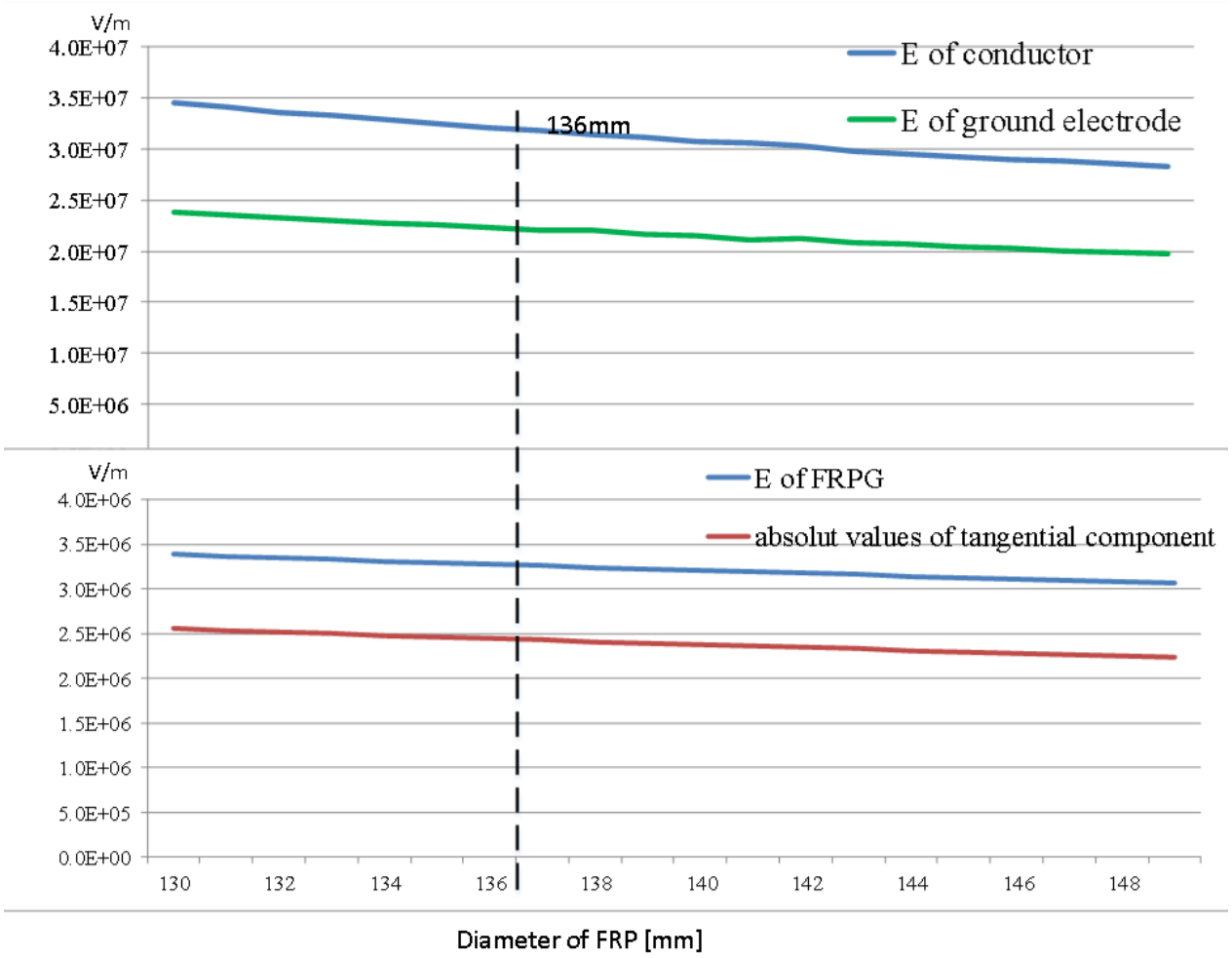


*Figure 71: Effect of reduction of D (method C) in V.7 on maximum electric field strength*

The most proper method for variant.7 is method C, which can reduce the diameter of FRP to 136mm. The $E_{max}$ of conductor bar reaches its criterion value at 136mm. The E of FRP and the corresponding absolute value of the tangential component are going up to 3.27kV/mm resp. 2.44kV/mm. At the position of 136mm the $E_{max}$ of ground electrode still retains a great amount of margin (22.4kV/mm).

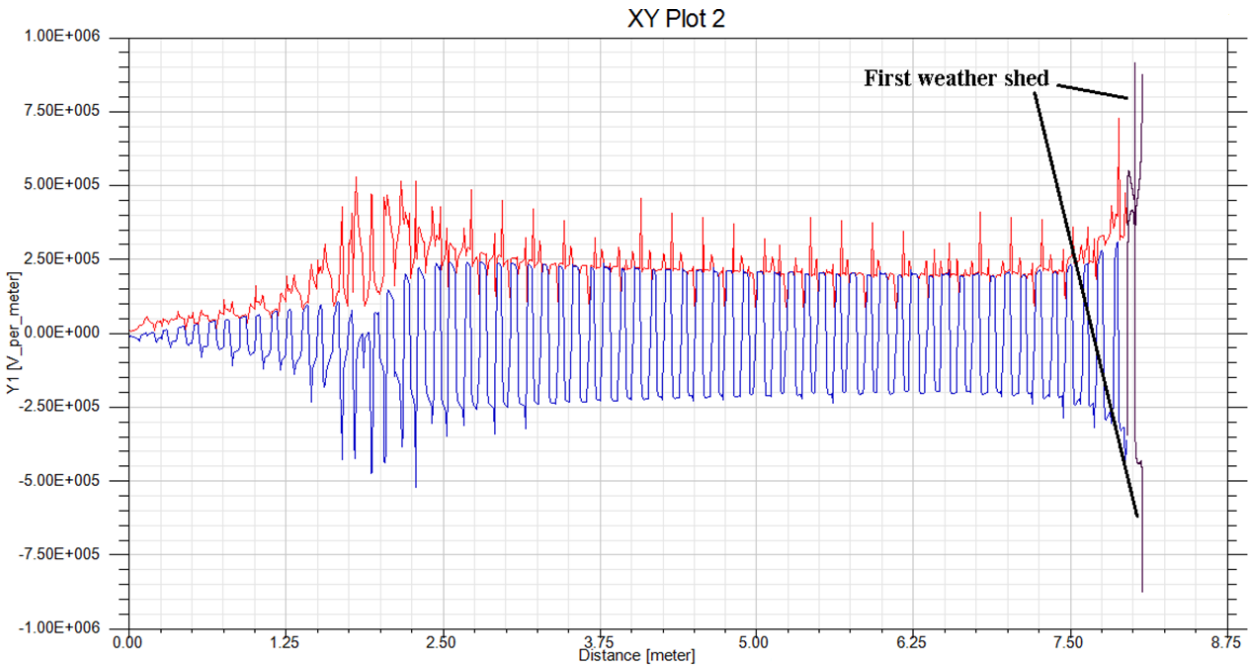


*Figure 72: $E_{peak}$ curve and its tangential component along silicon rubber sheds in V.1C structure (135mm) under AC voltage* $\frac{245kV}{\sqrt{3}}$ *(measure line see Figure 14 )*

In the investigation, the negative impact has been noticed by the reduction of diameter of FRP. Figure 72 shows the E curve and its tangential component along the silicon rubber sheds in V.1 under AC voltage. $E_{peak}$ and its tangential component close to the ground electrode increased from 0.42kV/mm to 0.52kV/mm resp. from 0.37kV/mm to 0.47kV/mm. Both values are within the criteria. E and its tangential component on the first weather shed remain at the original value 0.85kV/mm. The conclusion could be drawn that diameter of FRP has an effect on the E and its tangential component along silicon rubber sheds close to the ground electrode. The reduction of diameter of FRP causes the increase in these values. However, the E and its tangential component along the surface of the first silicon rubber weather shed and the above part, i.e. closing to top flange is independent of reduction of the diameter of FRP. It is only related to the structure of the top flange.

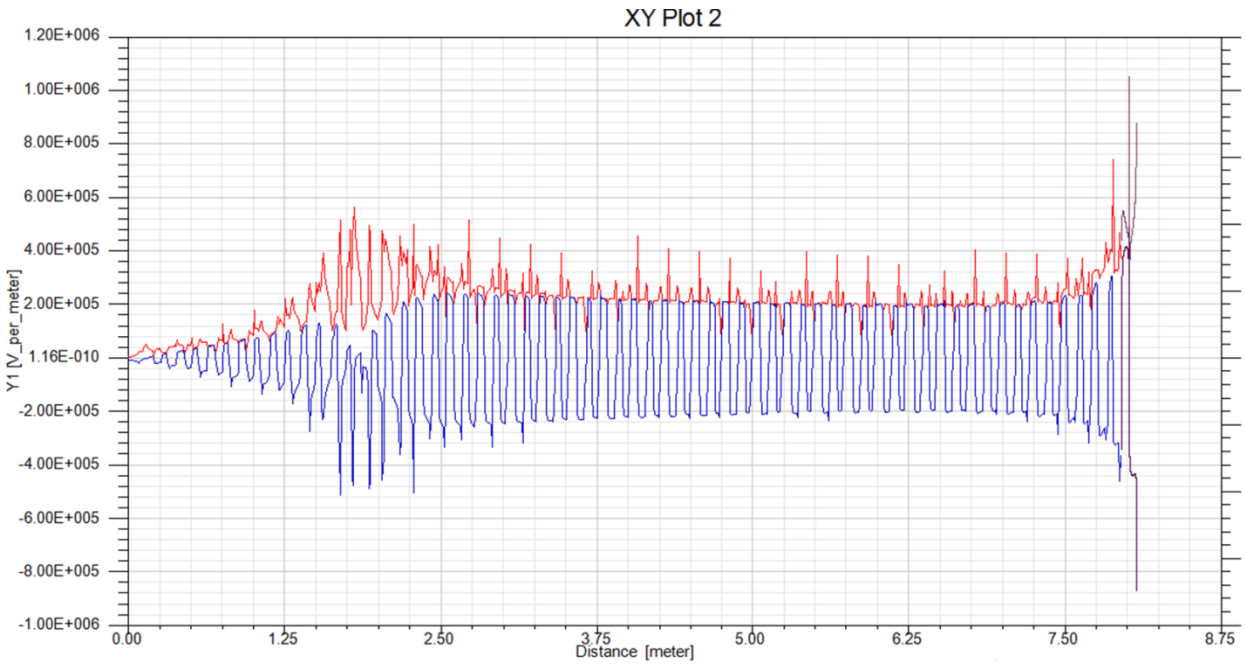


*Figure 73: $E_{peak}$ curve and its tangential component along silicon rubber sheds in V.2A structure (143mm) under AC voltage $\frac{245kV}{\sqrt{3}}$ (measure line see Figure 14)*

Figure 73 illustrates $E_{peak}$ curve and its tangential component along the silicon rubber sheds in V.2 under AC voltage. $E_{peak}$ and its tangential component close to the ground electrode increased to 0.56kV/mm resp. to 0.48kV/mm. Both values are within the scope of criteria. The first sheath and the above part are left out of consideration.

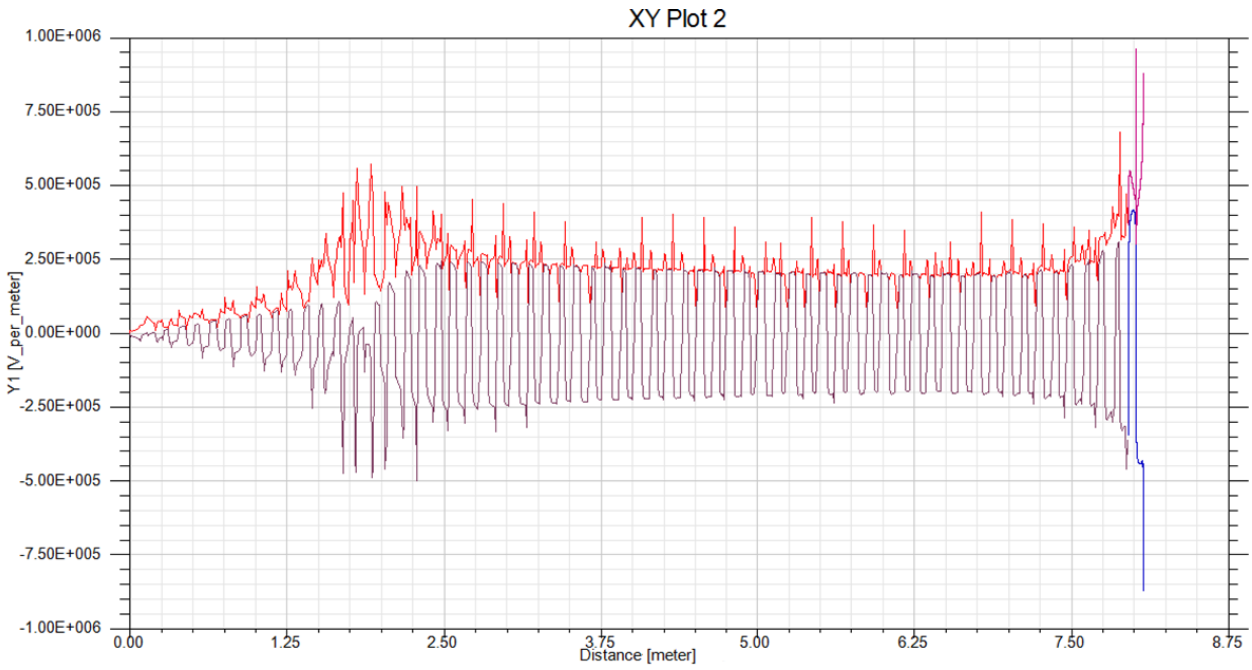


*Figure 74: $E_{peak}$ curve and its tangential component along silicon rubber sheds in V.7C structure (136mm) under AC voltage* $\frac{245kV}{\sqrt{3}}$ *(measure line see Figure 14)*

Figure 74 delineates the $E_{peak}$ curve and its tangential component along the silicon rubber sheds in V.7 under AC voltage. $E_{peak}$ and its tangential component close to the ground electrode increased to 0.57kV/mm and to 0.48kV/mm respectively. Both values are satisfied with criteria of AC voltage. The $E_{peak}$ curve and its tangential component of first weather shed are depicted by pink and blue color.

| Variant. / kV/mm | | Original conical structure | Original cylindrical structure | 1C | 2A | 7C |
|---|---|---|---|---|---|---|
| Diameter of the FRP $D_{FRP}$ (mm) | | 149 | 149 | 135 | 143 | 136 |
| Diameter of the ground electrode D (mm) | | 81 | 97.5 | 87.3 | 90.1 | 86.8 |
| Distance between the ground electrode and FRP tube L (mm) | | 49.5 | 30.5 | 30.5 | 24.7 | 28.5 |
| Under LIV 1050kV | $E_{max}$ of ground electrode | 27 | 23.2 | 25.9 | 27.5 | 22.4 |
| | $E_{max}$ of conductor bar | 33.4 | 25.8 | 31.8 | 27.3 | 32.1 |
| | $E_{max,FRPG}$ | 2.5 | 3.3 | 3.16 | 3.31 | 3.27 |
| | $E_{tangential,\ FRPG}$ (absolute value) | 2 | 2.5 | 2.48 | 2.37 | 2.44 |
| Under AC $\frac{245kV}{\sqrt{3}}$ | $E_{peak}$ of silicon / air (absolute value, exclusive first sheath and above part) | 0.43 | 0.55 | 0.52 | 0.56 | 0.57 |
| | $E_{tangential,peak}$ of silicon / air (absolute value, exclusive first sheath and above part) | 0.4 | 0.51 | 0.47 | 0.48 | 0.48 |

*Table. 14: Summary of $E_{max}$ on critical points for different ground electrodes after reduction of FRP*

From Figure 69, Figure 70 and Figure 71 the $E_{max}$ of ground electrode, of conductor bar, $E_{max,FRPG}$ and its tangential component at reduced diameter of the FRP tube can be read. The corresponding $E_{max}$ under AC voltage can be obtained from Figure 72, Figure 73 and Figure 74. The parameters of D and L can be derived from the mathematical expression of method A, B and C. The optimal results of $E_{max}$ on critical points for different ground electrodes after the reduction of the FRP

diameter have been tabulated in Table. 14. From the assessment the satisfactory results should be these two ground electrodes (variant.1C and 7C. Method C refers to 5.2.2). In the variant.1C and 7C the FRP diameter has been reduced greatly from 149mm to approx. 135mm. Simultaneously, based on criteria in 5.2.1 the electric field strengths on the critical points are still in the permissible range. $E_{max}$ of the ground electrode and $E_{max}$ of the conductor bar in variant.1C and 7C are lower than the values in the original conical structure. Compared to E in the original conical structure the $E_{max,FRPG}$ in variant.1C and 7C increases. However, it is still lower than the criteria values and values in original cylindrical structure. Therefore, these two structures (1C: conical ground electrode with grading ring. 7C: conical ground electrode with Bézier curve.) can be accepted for further application. But from the aspect of manufacture the structure of variant.1C simplifies the process of fabrication and is easy to realize.

## 5.3 New design of top flange

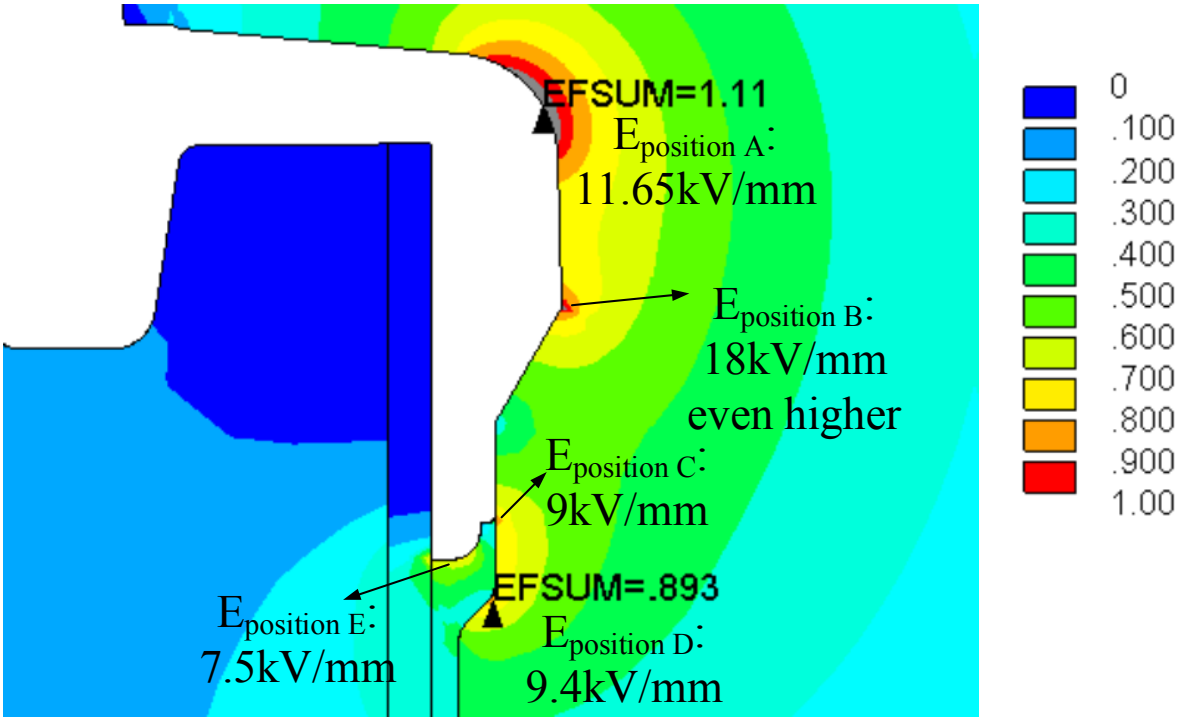


*Figure 75: Tthe critical positions of original top flange*

Figure 75 illustrates the critical positions of the original top flange. The E of every critical position is converted into kV/mm on basis of % kV/mm and color intensity. The most attention shall be paid on the following five critical points, i.e. the upper periphery of the top flange ($E_{position\ A}$ = 11.65kV/mm), the protrusion of the top flange ($E_{position\ B}$ ≈18kV), the triple point of the air, top flange and silicone rubber sheds ($E_{position\ C}$ ≈9kV/mm), the $E_{position\ D}$ =9.4kV/mm, and the interface between silicone rubber sheds and top flange ($E_{position\ E}$ ≈7.5kV). By the optimization of the top flange E of the critical points will decrease and be more uniform.

### 5.3.1 Optimal design of top flange

Considering the good performance of Bézier curves in the optimization of the ground electrode, it will continue to be adopted for the optimization of the top flange. However, compared to the single Bézier curve on the ground electrode multi-Bézier curves are used for the optimization of the top flange. In the first section, the properties of continuity of multi-Bézier curves will be discussed. The conditions of continuity will be proposed. Afterwards, as in the optimization of the ground electrode, the optimization of the top flange is carried out by genetic algorithms, which divided into two steps, i.e. rough sweeping for parameters of three Bézier curves and optimization by genetic algorithms (GA). By rough investigation parameters of three Bézier curves will be swept in a huge scope to investigate the interconnection between every parameter and E on the critical points. Then, on the principal of rough investigation the initial values and boundaries of every parameter will be determined in order to support GA. The process of GA for the top flange is similar to GA for the ground electrode.

#### 5.3.1.1. Introduction of multi-Bézier curve

When the curve is located at starting point, the following relationship according to the equation of Bézier curve could be deduced:

For t=0, $\mathrm{B}\acute{e}(0)=\sum_{i=0}^{n}P_iB_{i,n}(0)=P_0B_{0,n}(0)+P_1B_{1,n}(0)+\ldots+P_nB_{n,n}(0)$ *Eq. 56*

Apparently, $0^i=\begin{cases}1 & i=0\\ 0 & i\neq 0\end{cases}$ *Eq. 57*

Introducing Bernstein multinomial into the first equation,

$$\begin{aligned}&B_{0,n}(0)=C_n^0\cdot 0^0(1-0)^{n-0}=1\\&B_{1,n}(0)=C_n^1\cdot 0^1(1-0)^{n-1}=0\\&\vdots\\&B_{n,n}(0)=C_n^n\cdot 0^n(1-0)^{n-n}=0\end{aligned}$$ *Eq. 58*

Therefore, $\mathrm{B}\acute{e}(0)=P_0$

Similar results can also be derived as follow,

For t=1, $\mathrm{B}\acute{e}(1)=\sum_{i=0}^{n}P_iB_{i,n}(1)=P_0B_{0,n}(1)+P_1B_{1,n}(1)+\ldots+P_nB_{n,n}(1)=P_n$ *Eq. 59*

The conclusion could be drawn that the starting point and end point of Bézier curve overlap the starting point and end point of its characteristic polygon.

The tangential vector of Bézier curves can be expressed by the 1st-derivative of Bézier curve's equation as follow:

$$\left[\mathrm{B}\acute{e}(t)\right]'=\left[\sum_{i=0}^{n}P_iB_{i,n}(t)\right]'=\sum_{i=0}^{n}P_iB'_{i,n}(t)$$ *Eq. 60*

Where the 1st-derivative of Bernstein multinomial $B'_{i,n}(t)$ can be deduced as follow:

$$B'_{i,n}(t) = [C_n^i t^i (1-t)^{n-i}]' = [\frac{n!}{i!(n-i)!} t^i (1-t)^{n-i}]'$$

$$= \frac{n!}{i!(n-i)!}[it^{i-1}(1-t)^{n-i} - t^i(n-i)(1-t)^{n-i-1}]$$

$$= \frac{n!}{(i-1)!(n-i)!} t^{i-1}(1-t)^{n-i} - \frac{n!}{i!(n-i-1)!} t^i (1-t)^{n-i-1} \qquad \textit{Eq. 61}$$

$$= nC_{n-1}^{i-1}(1-t)^{n-i} \cdot t^{i-1} - nC_{n-1}^{i}(1-t)^{n-i-1} \cdot t^i$$

$$= n[B_{i-1,n-1}(t) - B_{i,n-1}(t)], \quad i = 0,1,\cdots$$

Introducing the solution of $B'_{i,n}(t)$ into the 1st-derivative of Bézier curve's equation:

$$\left[\text{B}\acute{e}(t)\right]' = \left[\sum_{i=0}^{n} P_i B_{i,n}(t)\right]' = \sum_{i=0}^{n} P_i B'_{i,n}(t) = n\sum_{i=0}^{n} P_i \cdot [B_{i-1,n-1}(t) - B_{i,n-1}(t)] \qquad \textit{Eq. 62}$$

For t=0, $\left[\text{B}\acute{e}(0)\right]' = n\sum_{i=0}^{n} P_i \cdot [B_{i-1,n-1}(0) - B_{i,n-1}(0)]$

The above equation can be divided into two parts, i.e. $\sum_{i=0}^{n} P_i \cdot [B_{i-1,n-1}(0)]$ and $\sum_{i=0}^{n} P_i \cdot [B_{i,n-1}(0)]$, which can be expanded as follow:

$$\sum_{i=0}^{n} P_i \cdot [B_{i-1,n-1}(0)] = P_0 \cdot B_{-1,n-1}(0) + P_1 \cdot B_{0,n-1}(0) + \ldots + P_1 \cdot B_{n-1,n-1}(0) \qquad \textit{Eq. 63}$$

Where
$$\begin{aligned} &B_{-1,n-1}(0) = C_n^{-1} 0^{-1} (1-0)^{n+1} = 0 \\ &B_{0,n-1}(0) = C_n^0 0^0 (1-0)^{n-0} = 1 \\ &\vdots \\ &B_{n-1,n-1}(0) = C_n^{n-1} 0^{n-1} (1-0)^1 = 0 \end{aligned} \qquad \textit{Eq. 64}$$

Hence, $n\sum_{i=0}^{n} P_i \cdot [B_{i-1,n-1}(0)] = nP_1$

and a similar solution could be derived

$$n\sum_{i=0}^{n} P_i \cdot [B_{i,n-1}(0)] = nP_0 \qquad \textit{Eq. 65}$$

The expression of $\left[\mathrm{B}\acute{e}(t)\right]'$ for t=0 can be simplified into

$$\left[\mathrm{B}\acute{e}(0)\right]' = n(P_1 - P_0) \qquad \textit{Eq. 66}$$

By similar derivation $\left[\mathrm{B}\acute{e}(t)\right]'$ for t=1 is given by

$$\left[\mathrm{B}\acute{e}(1)\right]' = n(P_n - P_{n-1}) \qquad \textit{Eq. 67}$$

Therefore, one may conclude that the tangential direction of starting and end point of a Bézier curve is identical to the direction of first and last edge of its characteristic polygon.

It is assumed that the control points of two Bézier curves are $P_i$ (i=0,1,…n) and $Q_j$ (j=0,1,…n). If P(t) and Q(t) keep the continuity, the following sufficient and essential conditions should be totally satisfied:

- The continuity of curves segments ($G^0$)

- The continuity of tangent ($G^1$)

The condition of $G^0$ ensures the segments of two Bézier curves are connected, which means the connection of end point of P curve ($P_n$) and starting point of Q curve ($Q_0$). However, this condition cannot guarantee the smooth connection between two curves. Figure 76 illustrates the connection of two cubic Bézier curves under the condition of $G^0$.

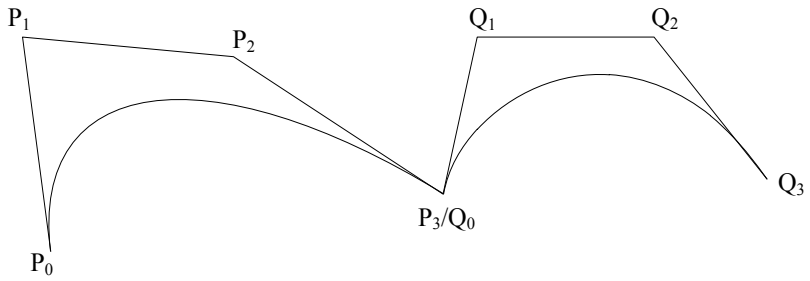


*Figure 76: Connection of two cubic Bézier curves under the condition of $G^0$*

Obviously, it is not enough that the connection of two Bézier curves only satisfies the condition of $G^0$. The continuity of tangent ($G^1$) means that 1st order derivative agrees at joints of two Bézier curves (P and Q curve). In another word, the tangential direction of a Bézier curve (P curve) at end point is equal to the tangential direction of another Bézier curve (Q curve) at the starting point. The expression can be described as follow:

$$\left[P(1)\right]' = \left[Q(0)\right]' \qquad \textit{Eq. 68}$$

From the equation of the tangential vector of the Bézier curve above discussed, $\left[P(1)\right]'$ and $\left[Q(0)\right]'$ can be expressed by follow:

$$\left[P(1)\right]' = n(P_n - P_{n-1}) \qquad \textit{Eq. 69}$$

$$\left[Q(0)\right]' = m(Q_1 - Q_0) \qquad \textit{Eq. 70}$$

From the above equations and considering the condition of $G^0$, the following expression can be derived:

$$\begin{cases} n(P_n - P_{n-1}) = m(Q_1 - Q_0) \\ P_n = Q_0 \end{cases} \qquad \textit{Eq. 71}$$

Hence, according to the conditions of $G^0$ and $G^1$, the conclusion could be drawn that $P_{n-1}$, $P_n$=$Q_0$ and $Q_1$ should be arrayed in order and lay through the same straight line (collinear). Figure 77 delineates smooth connection of two Bézier curves under the condition of $G^0$ and $G^1$

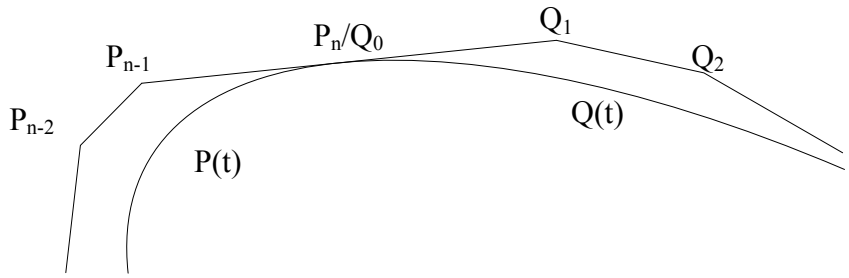


*Figure 77: Smooth connection of two Bézier curves under the condition of $G^0$ and $G^1$*

### 5.3.1.2. Optimizations by genetic algorithms

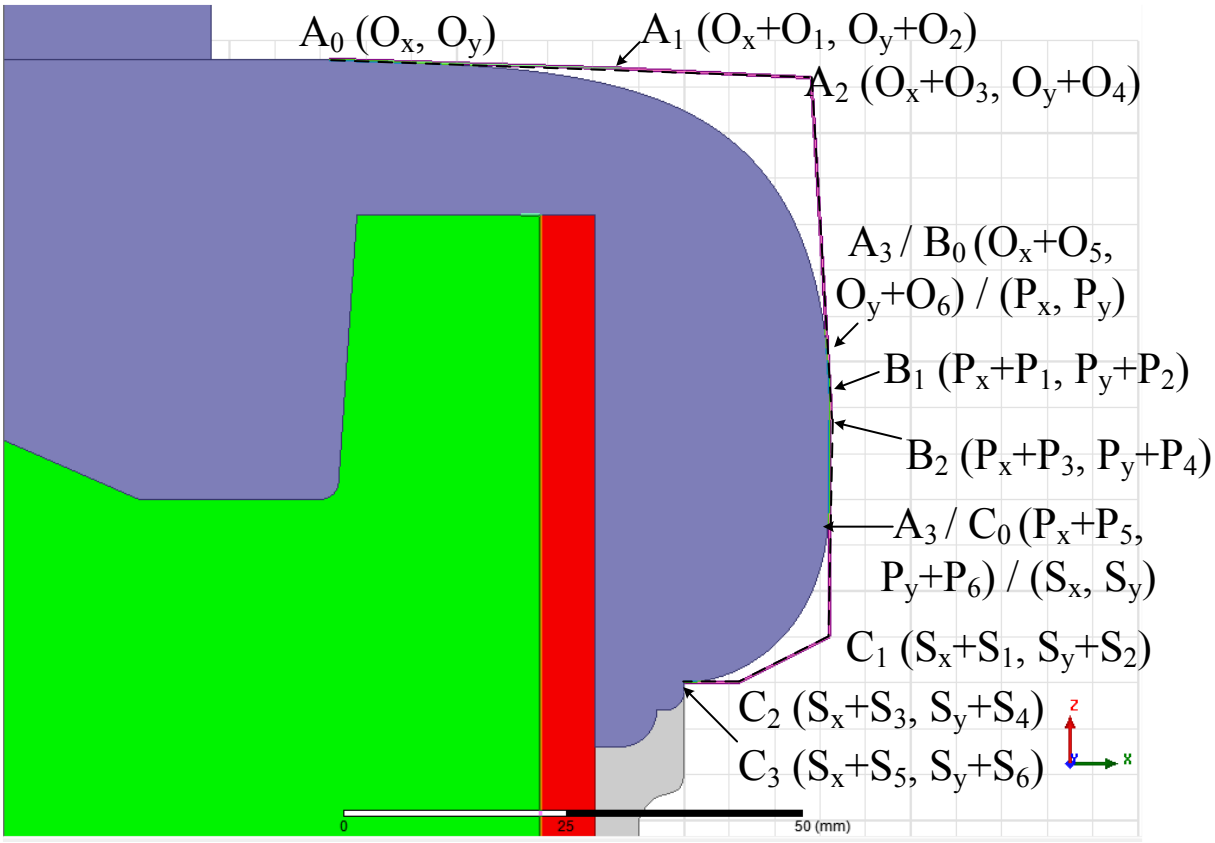


*Figure 78: New contour of top flange by smooth connection of three Bézier curves*

Figure 78 shows a new contour of the top flange, which consists of three Bézier curves A(t), B(t) and C(t). The position of $A_0$ is fixed. By controlling of the parameters $O_1$, $O_2$, $O_3$, $O_4$, $O_5$ and $O_6$ the Bézier curve A(t) can be modified. $A_3/B_0$ is not only the end point of Bézier curve A(t), but also the starting point of Bézier curve B(t). In order to fulfill the continuity of multi-Bézier curve, $A_2$, $A_3/B_0$ and $B_1$ should be collinear. Parameters $P_1$, $P_2$, $P_3$, $P_4$, $P_5$ and $P_6$ manipulate Bézier curve B(t). Likewise the point $A_3/B_0$, $B_3/C_0$ is not only the end point of Bézier curve B(t), but also the starting point of Bézier curve C(t). Similarly, B2, B3/C0 and $C_1$ should be collinear. The Bézier curve C(t) is manipulated by parameters $S_1$, $S_2$, $S_3$, $S_4$, $S_5$ and $S_6$. The end point $C_3$ is fixed. Considering collinear connection of multi-Bézier curves and fixed points $A_0$ and $C_3$, parameters $O_1$, $O_2$, $O_3$, $O_4$, $O_5$, $O_6$, $P_2$, $P_4$, $P_5$, $P_6$, $S_2$, $S_4$ and $S_5$will be modified in the following optimization.

Before starting the genetic algorithms the preliminary investigation will be performed. The irrational values will be eliminated and proper initial values and boundaries of parameters will be determined by the rough sweeping. For optimization of top flange 13 parameters ($O_1$, $O_2$, $O_3$, $O_4$, $O_5$, $O_6$, $P_2$, $P_4$, $P_5$, $P_6$, $S_2$, $S_4$ and $S_5$ ) will be swept one by one, which means a parameter will be considered as variable in the investigation, in the meanwhile others are fixed. To optimize the top flange the investigation will be mainly focus on the $E_{max}$ on Bézier curve A, Bézier curve B and Bézier curve C. Likewise to the pre-investigation in the optimization of ground electrode, the similar charts are not shown again in this section. Depending on the results from the preliminary investigation the parameters could be set to $O_1$:(27mm─32mm), $O_2$:(-5mm─0mm), $O_3$:(37mm─43mm), $O_4$:(-6mm─0mm) and $O_5$:(48mm─53mm) $O_6$:(-25mm─-15mm) $P_2$:(-15mm─-8mm) $P_4$:(-25mm─-15mm) $P_5$:(5mm─10mm) $P_6$:(-35mm─-25mm) $S_2$:(-20mm─-10mm) $S_3$:(-20mm─-10mm) and $S_4$:(-35mm─-25mm). The initial values of parameters could be properly set to $O_1$=27mm, $O_2$=-3mm, $O_3$=40mm, $O_4$=-6mm and $O_5$=50mm $O_6$=-25mm, $P_2$=-10mm, $P_4$=-23mm, $P_5$=5mm, $P_6$=-32mm, $S_2$=-18mm, $S_3$=-17mm and $S_4$:=-33mm.

The further optimization of parameters regarding the top flange will be performed by genetic algorithms. Considering three Bézier curves with smooth connection there are thirteen different parameters which could be optimized. The individual chromosome can be expressed as follows

$$x = [O_1, O_2, O_3, O_4, O_5, O_6, P_2, P_4, P_5, P_6, S_2, S_3, S_4,]$$

Where $O_1$, $O_2$, $O_3$, $O_4$, $O_5$ and $O_6$ represent parameters of the first Bézier curve. $P_2$, $P_4$, $P_5$ and $P_6$ represent parameters of the second Bézier curve. $S_2$, $S_3$, and $S_4$ represent parameters of the third Bézier curve.

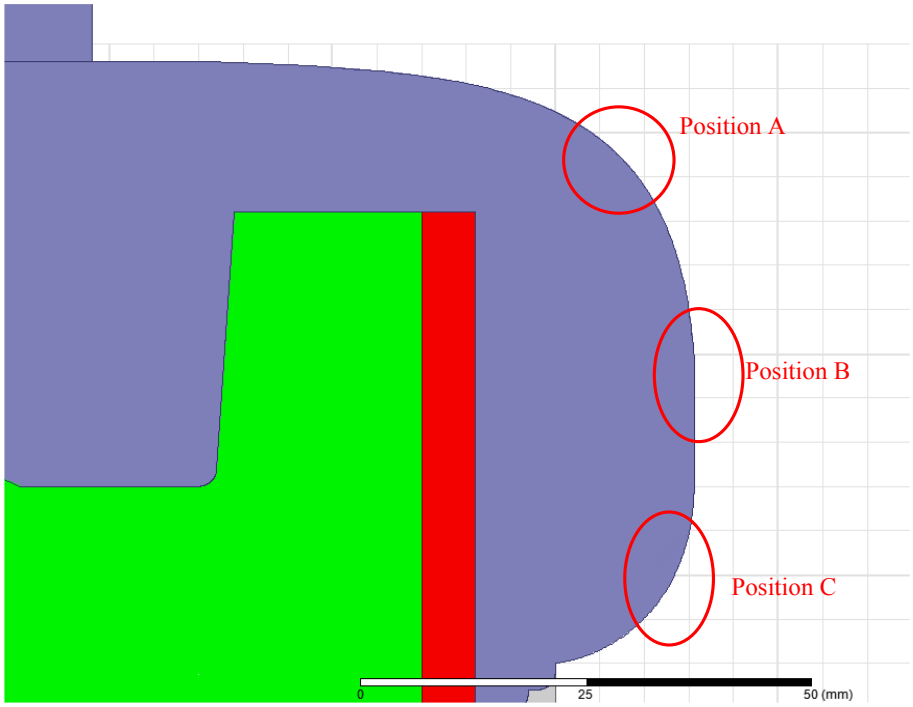


*Figure 79: Potential positions of $E_{max}$*

The fitness function is constructed and given by as follow:

$$Fitness = w_1[E_{A,\max}(x) - E_{A,G}(x)] + w_2[E_{B,\max}(x) - E_{B,G}(x)] + w_3[E_{C,\max}(x) - E_{C,G}(x)] \quad \textit{Eq. 72}$$

Where $E_{A,max}$, $E_{B,max}$ and $E_{C,max}$ indicate the simulation values of $E_{max}$ in potential positions of top flange (see Figure 79) . $w_1$, $w_2$ and $w_3$ represent the corresponding weighting factor respectively. $E_{A,G}$, $E_{B,G}$ and $E_{C,G}$ are the goal values of E in the potential positions of top flange. According to a preliminary investigation, which is not included in this thesis, the goal values are set as follows

$$E_{A,G} = 8kV/mm,\ E_{B,G} = 8kV/mm,\ E_{C,G} = 9.5kV/mm$$

Substituting weighting factors $w_1$=0.4, $w_2$=0.2 and $w_3$=0.4, the expression of fitness function can be given by follow,

$$Fitness = 0.4 \cdot [E_{A,\max}(x) - 8 \cdot 10^6] + 0.2 \cdot [E_{B,\max}(x) - 8 \cdot 10^6] + 0.4 \cdot [E_{C,\max}(x) - 9.5 \cdot 10^6] \quad \textit{Eq. 73}$$

It is assumed that $E_{A,\max} < 8kV/mm$ , $E_{A,\max} - E_{A,G} = 0$ ; $E_{B,\max} < 8kV/mm$ , $E_{B,\max} - E_{B,G} = 0$ ; $E_{C,\max} < 9.5kV/mm$, $E_{C,\max} - E_{C,G} = 0$ , Under this condition, the lower fitness value is considered to be a better result. The population size ($N_p$) and the maximal number of iterations/generations ($G_{max}$) must be chosen. The population size i.e. the number of individual chromosomes in a generation, might be set to $N_p$=32. The number of generations could be set to 30. The fitness function is evaluated for each chromosome in the population, and the population will be sorted in the order of better fitness. The elitism strategy preserve two best chromosomes in a generation. The mutation with rate of 30% will be applied to reproduce 18 chromosomes in the new generation. After approx. 40 generations the genetic algorithms converge to an acceptable result. The following table lists the summary of the optimized parameters and $E_{max}$ on potential positions of top flange after optimization.

| | | | | | | |
|---|---|---|---|---|---|---|
| Parameters of Bézier curve A | $O_1$ | $O_2$ | $O_3$ | $O_4$ | $O_5$ | $O_6$ |
| | 29.6 | -0.9 | 41.5 | -4.5 | 51.6 | -20.6 |
| Parameters of Bézier curve B | $P_1$ | $P_2$ | $P_3$ | $P_4$ | $P_5$ | $P_6$ |
| | 5.7 | -9.1 | 7.4 | -20.1 | 7.4 | -29.6 |
| Parameters of Bézier curve C | $S_1$ | $S_2$ | $S_3$ | $S_4$ | | |
| | 0 | -14.1 | -15.3 | -30 | | |

*Table. 15: Summary of optimized parameters for top flange*

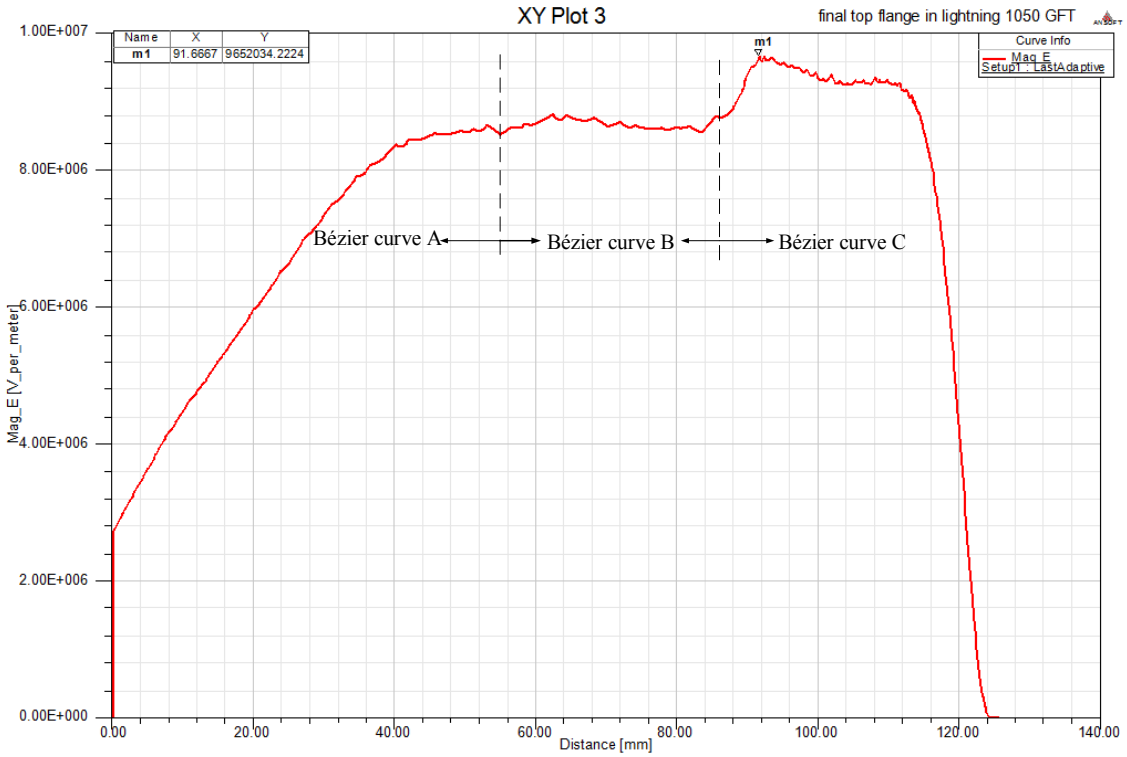


*Figure 80: E along the surface of optimized top flange under LIV 1050kV (measure line see Figure 15)*

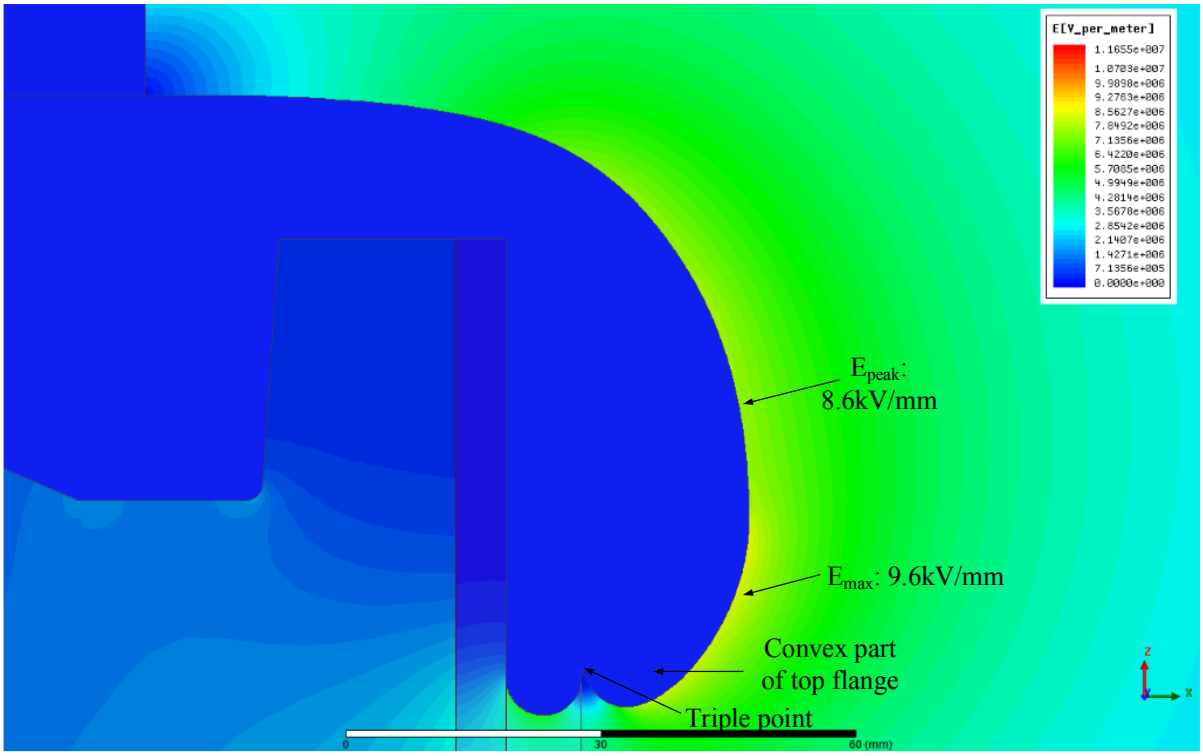


*Figure 81: 2D plot E of optimized top flange*

Figure 80 and Figure 81 show E along the surface and a 2D plot E of the optimized top flange. The protrusion on the top flange is avoided. In order to make a clear comparison, the color intensity in Figure 81 is adopted as same as in Figure 75. From Figure 80 the $E_{max}$ appears at the range of 3rd Bézier curve and drops into 9.6kV/mm compared with $E_{max}$ (18kV/mm) in Figure 75. The position where the peak value occurs in the original structure in Figure 75 is optimized very well. The peak E in same position decreases from 11.65kV/mm to 8.6kV/mm. By optimization the position of the protrusion in Figure 75 ($E_{position\ B}$) is totally avoided. By utilization of the convex part of the top flange the triple point of air, metal and silicone rubber is shielded. The E of triple point drops to a very low value.

### 5.3.2 Optimal design of interface between the top flange and insulator

Several interfaces between the top flange and silicone rubber sheds are proposed. Every structure will be described briefly. The E on critical points of different structures will be summarized and compared. Considering that the mechanical strength must be kept between the silicone rubber sheds and FRP tube, the position of triple point T should be no lower than in the original structure, i.e. 2283mm. The coordinate of position T is marked in every proposed structure.

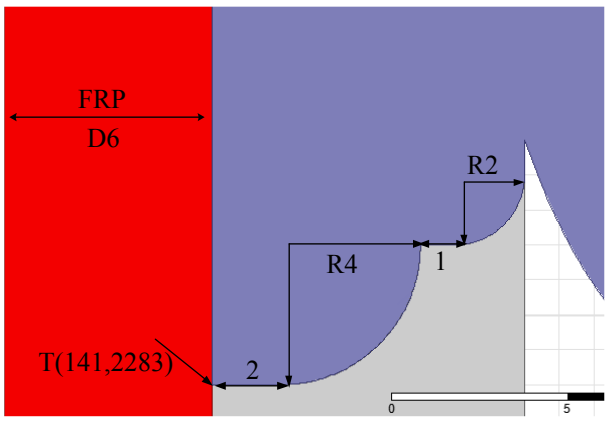


*Figure 82: Original interface between the top flange and silicone rubber sheds*

Figure 82 delineates original interface between the top flange and silicone rubber sheds. The interface consists of two ¼ arcs with radius 4mm and 2mm. The straight line connects between two arcs and becomes a perpendicular interface at the triple point of top flange, FRP and silicone

rubber sheds. The height of the triple point T is located at 2283mm. All the dimensions have been marked in the Figure 82.

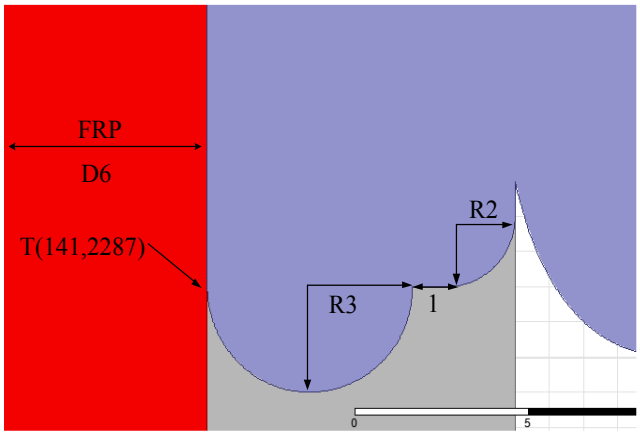


*Figure 83: Interface.1 between the top flange and silicone rubber sheds*

Figure 83 delineates the interface.1 between the top flange and silicone rubber sheds. The interface consists of a half circle with radius 3mm and a ¼ arc with radius 2mm. The straight line connects between a half circle and a ¼ arc. At the triple point of top flange, FRP and silicone rubber sheds it becomes a convex interface. The height of position T is located at 2287mm. All the dimensions have been marked in the Figure 83.

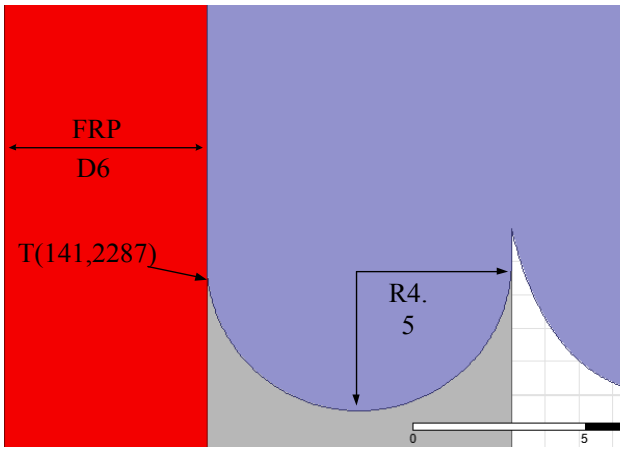


*Figure 84: Interface.2 between the top flange and silicone rubber sheds*

Figure 84 delineates interface.2 between the top flange and silicone rubber sheds. The interface consists of a half circle with radius 4.5mm. At the triple point of the top flange, FRP and silicone

rubber sheds it becomes a convex interface. The height of position T is located at 2287mm. All the dimensions have been marked in the Figure 84.

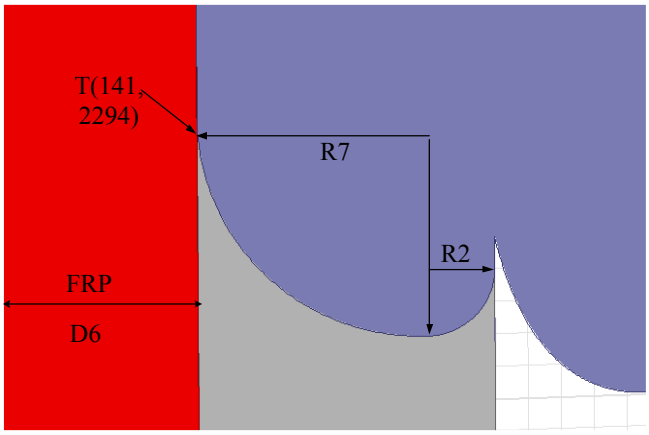


*Figure 85: Interface.3 between the top flange and silicone rubber sheds*

Figure 85 delineates interface.3 between the top flange and silicone rubber sheds. The interface consists of two ¼ arcs with radius 7mm and 2mm. Two arcs connect directly without straight line. At the triple point of top flange, FRP and silicone rubber sheds it becomes a convex interface. Due to relative large radius the height of position T is located at 2294mm. All the dimensions have been marked in the Figure 85.

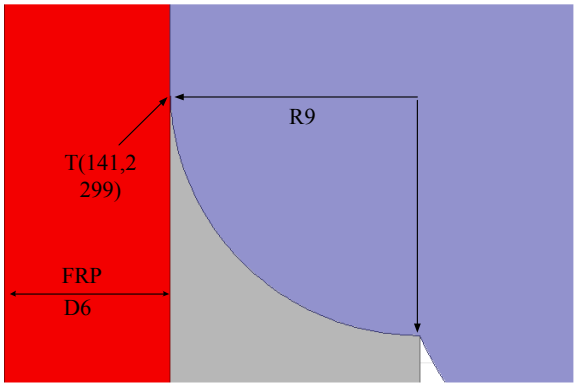


*Figure 86: Interface.4 between the top flange and silicone rubber sheds*

Figure 86 delineates interface.4 between the top flange and silicone rubber sheds. The interface consists of only a ¼ arc with radius 9mm. The arc connect the triple point of top flange, FRP and silicone rubber sheds and triple point of air, top flange and silicone rubber sheds. The interface is still kept as convex contour. Due to even larger radius the height of position T is located at 2299mm. All the dimensions have been marked in the Figure 86.

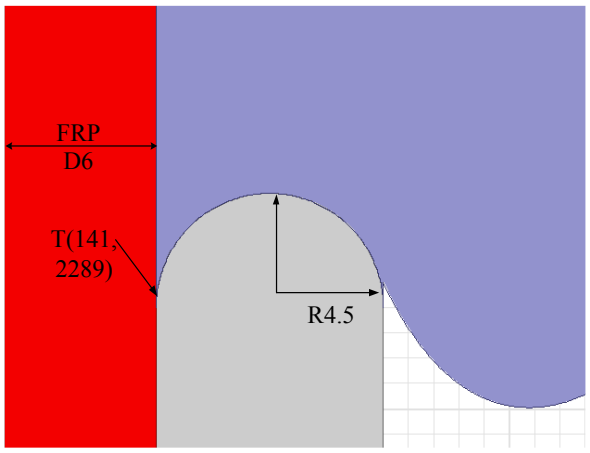


*Figure 87: Interface.5 between the top flange and silicone rubber sheds*

Figure 87 delineates interface.5 between the top flange and silicone rubber sheds. Compared to the above structures the interface is designed by concave contour. The interface consists of a half concave circle with radius 4.5mm. The half circle connects two triple points. The height of position T is located at 2294mm. All the dimensions have been marked in the Figure 87.

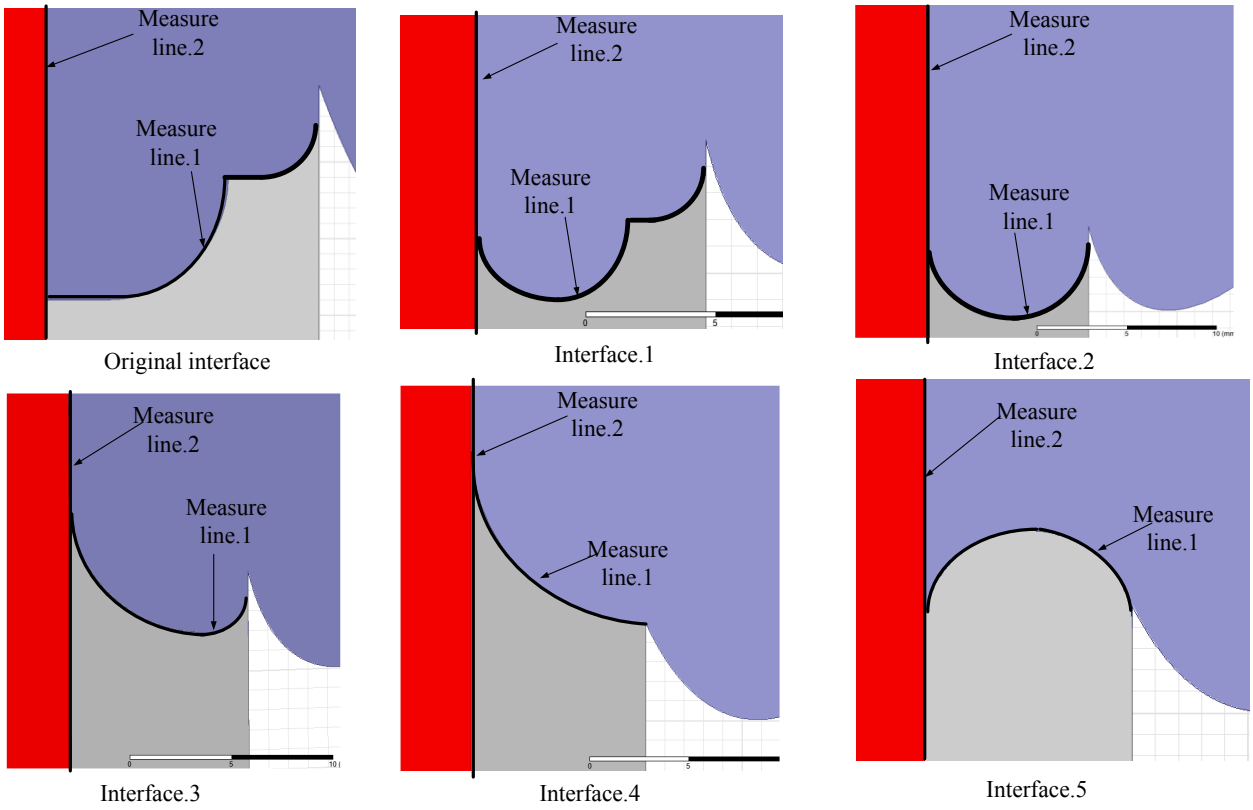


*Figure 88: Measure lines for the two interfaces*

Figure 88 describes the measure lines for the two interfaces. The measure line.1 estimates E of the interface between the top flange and silicone rubber sheds. Measure line.2 estimates not only E of the interface between FRP and silicone rubber sheds, but also E of the interface between FRP and top flange. The effect of the surface on $E_{max}$ of the top flange should be paid attention. All the $E_{max}$ of measure line.1 are located at the vicinity of the triple point.

| kV/mm | Original | 1 | 2 | 3 | 4 | 5 |
|---|---|---|---|---|---|---|
| $E_{max}$ of top flange | 18 | 9.7 | 9.7 | 10.3 | 11.4 | 11.2 |
| $E_{max}$ of measure line.1 | ≈7.5 | 7.6 | 6.5 | 5.5 | 4.3 | 13.4 |
| $E_{max}$ of measure line.2 | ≈7.5 | 4.3 | 3.7 | 3.2 | 3.0 | 22 |

*Table. 16: Summary of $E_{max}$ at two interfaces and effect on $E_{max}$ of top flange*

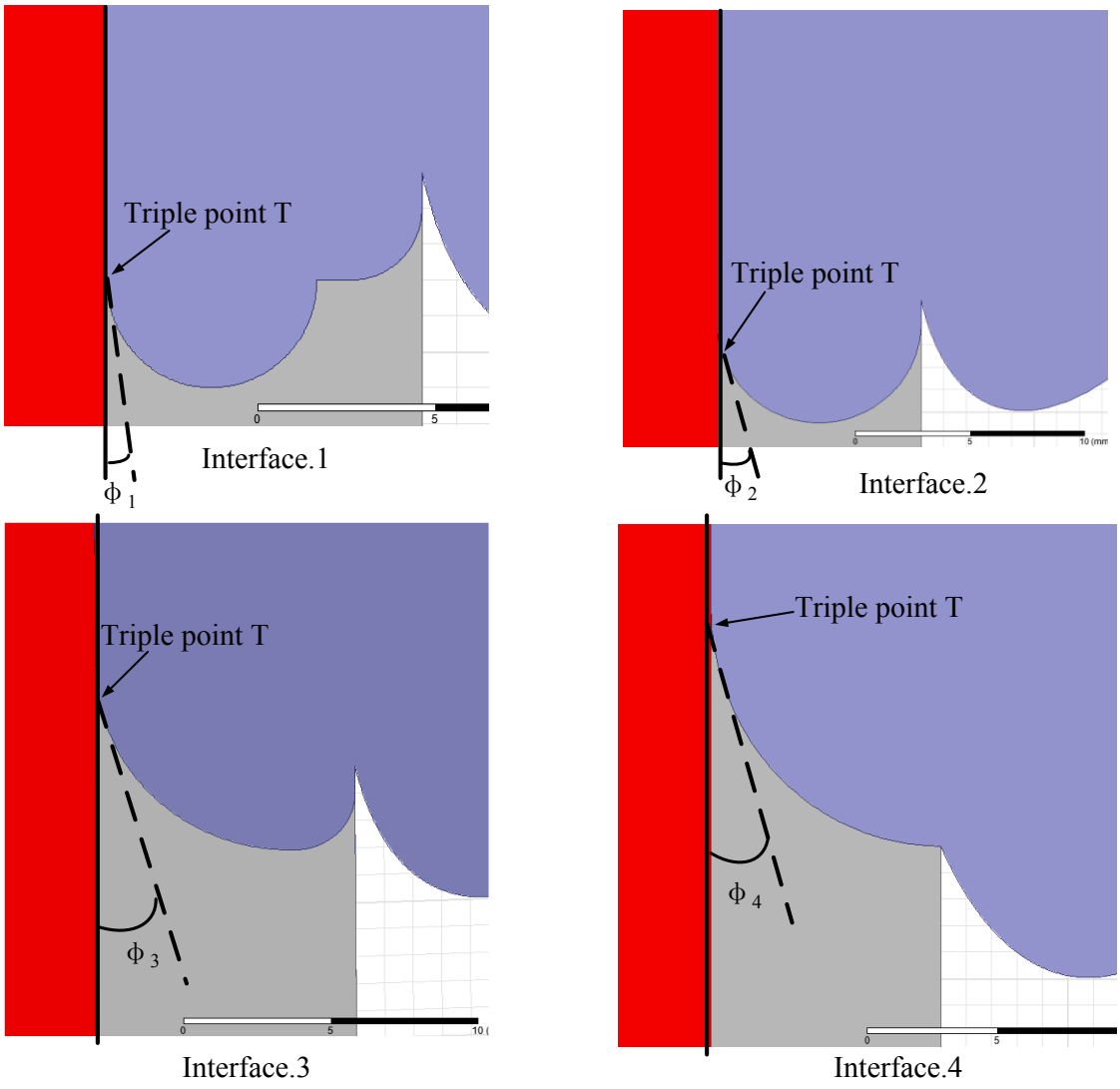


*Figure 89: the effect of tangential angle at the triple point on $E_{max}$*

Compared to $E_{max}$ of the original structure, $E_{max}$ of the convex structures (interface.1, 2, 3 and 4) drops in different degrees. The concave structure interface.5 cannot be acceptable. Whereas, in the structures of interface.3 and 4 a convex structure has a negative influence on $E_{max}$ of the top flange. $E_{max}$ of the top flange increases into more than 10kV/mm. Figure 89 illustrates the effect of the tangential angle at the triple point on $E_{max}$. Apparently, $\phi_1 < \phi_2 < \phi_3 < \phi_4$ and with increase of curvature of arc the tangential angle φ at the triple point is getting larger, which decreases $E_{max}$ at the triple point and $E_{max}$ of the interface between top flange and silicone rubber sheds. However, with the increase of curvature of arc the position of triple point shifts higher and higher, which might lead to the increase of $E_{max}$ on the top flange. Therefore, the structure of interface.2 is proposed to be the optimized structure for the top flange.

## 5.4 Optimal design of region above first weather shed

This section discusses optimization of region above first weather shed. For optimization a new curve i.e. cubic natural spline is introduced. The new contour above the first weather shed is modeled by cubic natural spline. Genetic algorithms is continued to apply. Finally, the optimal results are represented and compared to original ones.

### 5.4.1 Introduction of cubic natural spline

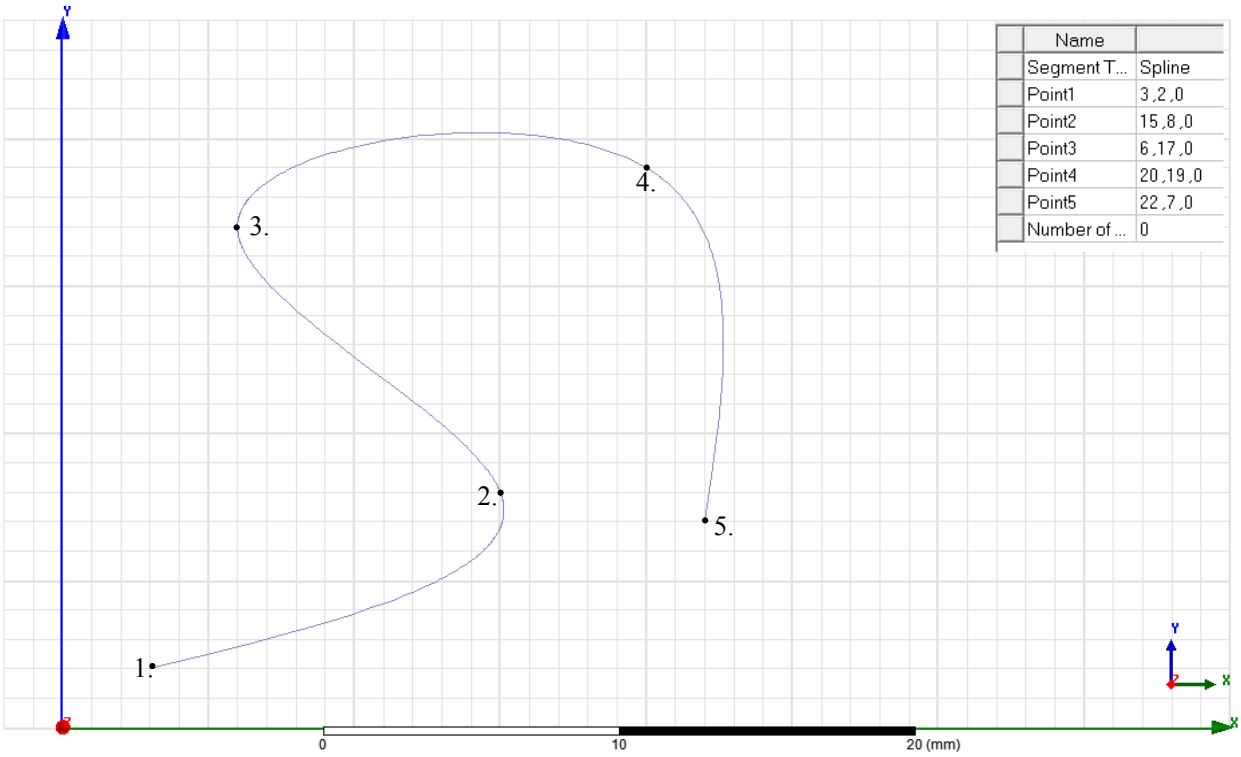


*Figure 90: A cubic spline with five control points (15mm,10mm), (65mm,10mm), (35mm,55mm), (15mm,30mm) and (75mm,10mm)*

A cubic spline $S(x)$ is a spline constructed of piecewise third-order polynomials passing through a set of m control points and satisfying following conditions:

- In a given interval $[a,b]$ and $a = x_0 < x_1 < ... < x_n = b$ $S(x) = S_i(x)$ is cubic polynomial on each subinterval $[x_i, x_{i+1}]$ for $i = 0,1,...,n-1$
- S interpolates all the points, which indicates $S_i(x) = y_i$ for $i = 0,1,...,n$
- In the interval $[a,b]$ S has a continuous second derivative.

Therefore a piecewise cubic spline $S_i(x)$ in the subinterval $[x_i, x_{i+1}]$ can be written as

$S_i(x) = a_i x^3 + b_i x^2 + c_i x + d_i$, for $i = 0,1,...,n-1$, where $a_i$, $b_i$, $c_i$ and $d_i$ represent 4n unknown coefficients.

Considering the definition of cubic spline, equations relating the coefficients are determined as follow:

$S_i(x_i) = y_i$ for $i = 0,1,...,n-1$

$S_i(x_{i+1}) = y_{i+1}$ for $i = 0,1,...,n-1$

Taking the derivative continuity in each subinterval, then gives

$S'_{i-1}(x_i) = S'_i(x_i)$ for $i = 1,2,...,n-1$

$S''_{i-1}(x_i) = S''_i(x_i)$ for $i = 1,2,...,n-1$

By above four mathematical expressions, $4n-2$ equations can be determined and established. Assumed that the second derivative of cubic spline at node points is function $M$ and can be expressed as follow:

$M_i = f''(x_i)$ for $i = 0,1,...,n$

Therefore, $S''(x)$ in the subinterval $[x_i, x_{i+1}]$ can be written as form of piecewise linear interpolation:

$$S''(x) = \frac{x - x_{i+1}}{x_i - x_{i+1}} M_i + \frac{x - x_i}{x_{i+1} - x_i} M_{i+1} \qquad \textit{Eq. 74}$$

Assuming $h_i = x_{i+1} - x_i$, then gives

$$S''(x) = \frac{x_{i+1} - x}{h_i} M_i + \frac{x - x_i}{h_i} M_{i+1} \qquad \textit{Eq. 75}$$

By two times integration of above $S''(x)$, $S(x)$ can be deduced:

$$S'(x) = \frac{-(x_{i+1} - x)^2}{2h_i} M_i + \frac{(x - x_i)^2}{2h_i} M_{i+1} + c$$

$$S(x) = \frac{(x_{i+1} - x)^3}{6h_i} M_i + \frac{(x - x_i)^3}{6h_i} M_{i+1} + cx + d$$

$$S(x) = \frac{(x_{i+1} - x)^3}{6h_i} M_i + \frac{(x - x_i)^3}{6h_i} M_{i+1} + C(x_{i+1} - x) + D(x - x_i) \qquad \textit{Eq. 76}$$

Substituting $S_i(x_i) = y_i$ and $S_i(x_{i+1}) = y_{i+1}$ into the above equation, then gives

$$C = \frac{y_i}{h_i} - \frac{h_i M_i}{6} \qquad \textit{Eq. 77}$$

$$D = \frac{y_{i+1}}{h_i} - \frac{h_i M_{i+1}}{6} \qquad \textit{Eq. 78}$$

Now $S(x)$ in the subinterval $[x_i, x_{i+1}]$ can be rewritten as

$$S(x) = \frac{(x_{i+1} - x)^3 M_i + (x - x_i)^3 M_{i+1}}{6h_i} + \frac{(x_{i+1} - x) y_i + (x - x_i) y_{i+1}}{h_i} - \frac{h_i}{6}\left[(x_{i+1} - x) M_i + (x - x_i) M_{i+1}\right]$$

$x \in [x_i, x_{i+1}]$, for $i = 1, ..., n$ *Eq. 79*

Taking the equation $S'_{i-1}(x_i) = S'_i(x_i)$ ,then gives

$$\mu M_{i-1} + 2M_i + \lambda_i M_{i+1} = d_i \text{ for } i = 1, 2, ..., n-1$$

$M_0$ and $M_i$ are called endpoints or boundary condition of cubic spline. When $M_0$ and $M_i$ are given, the above equation can be expressed by a tri-diagonal matrix as follow:

$$\begin{pmatrix} 2 & \lambda_1 & & & & \\ \mu_2 & 2 & \lambda_2 & & & \\ & \ddots & \ddots & \ddots & & \\ & & \mu_{n-2} & 2 & \lambda_{n-2} & \\ & & & \mu_{n-1} & 2 & \end{pmatrix} \begin{pmatrix} M_1 \\ M_2 \\ \vdots \\ M_{n-2} \\ M_{n-1} \end{pmatrix} \begin{pmatrix} d_1 - \mu_1 M_0 \\ d_2 \\ \vdots \\ d_{n-2} \\ d_{n-1} - \mu_{n-1} M_n \end{pmatrix} \qquad \textit{Eq. 80}$$

Where $h_i = x_{i+1} - x_i$ , $\lambda_i = \frac{h_i}{h_i + h_{i-1}}$ , $\mu_i = 1 - \lambda_i$ and $d_i = \frac{6}{h_i + h_{i-1}} (\frac{y_{i+1} - y_i}{h_i} - \frac{y_i - y_{i-1}}{h_{i-1}})$ for $i = 1,2,...,n-1$

For a cubic natural spline the second derivative of endpoints are zero, i.e. $M_0 = 0$ and $M_i = 0$, which provides boundary condition that completes the tri-diagonal matrix. The tri-diagonal matrix of cubic natural spline will be rearranged as follow:

$$\begin{pmatrix} 2 & \lambda_1 & & & & \\ \mu_2 & 2 & \lambda_2 & & & \\ & \ddots & \ddots & \ddots & & \\ & & \mu_{n-2} & 2 & \lambda_{n-2} & \\ & & & \mu_{n-1} & 2 & \end{pmatrix} \begin{pmatrix} M_1 \\ M_2 \\ \vdots \\ M_{n-2} \\ M_{n-1} \end{pmatrix} \begin{pmatrix} d_1 \\ d_2 \\ \vdots \\ d_{n-2} \\ d_{n-1} \end{pmatrix} \qquad \textit{Eq. 81}$$

### 5.4.2 Optimization of region above first weather shed

The process of optimization for the region above the first weather shed is similar to optimization for the ground electrode and the top flange. The optimization is divided into two parts, preliminary investigation and genetic algorithm. The detailed figures of preliminary investigation are not shown in this section. However, the initial values and ranges of parameters are set based on results of the preliminary investigation. Except for the different configurations of chromosomes, goal function and goal value, the procedure of genetic algorithm (GA) is the same as for GA for the ground electrode and the top flange.

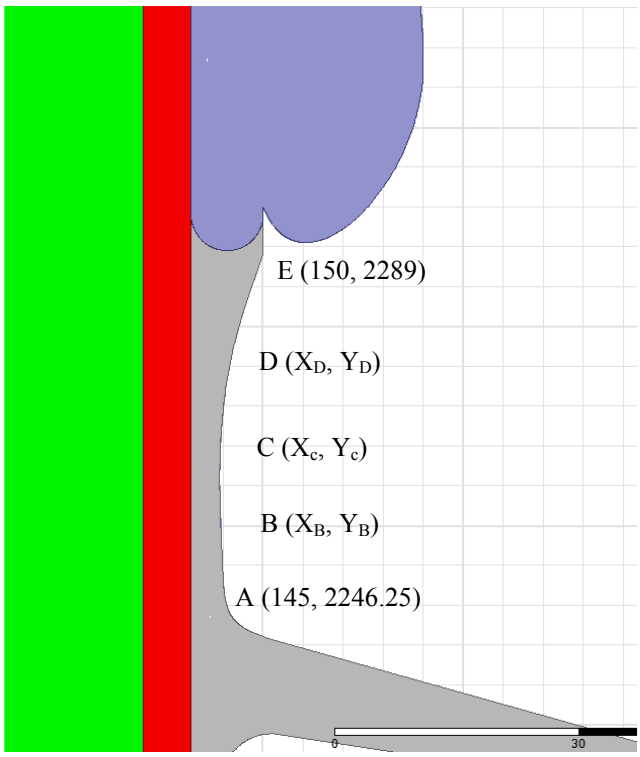


*Figure 91: New contour of region above first weather shed by cubic natural spline*

Figure 91 shows new contour of the region above the first weather shed. Points A and E are fixed. By controlling the points B, C and D the cubic natural spline can be varied. The contour can be expressed by cubic natural spline as follow:

$$S(x)=\begin{cases} a_1x^3+b_1x^2+c_1x+d_1 & x\in[145,x_B] \\ a_2x^3+b_2x^2+c_2x+d_2 & x\in[x_B,x_C] \\ a_3x^3+b_3x^2+c_3x+d_3 & x\in[x_C,x_D] \\ a_4x^3+b_4x^2+c_4x+d_4 & x\in[x_C,150] \end{cases} \qquad \textit{Eq. 82}$$

In the proposed algorithms, the optimization concentrates on the minimization of the maximum electric field strength of the region above the first weather shed. Simultaneously, the negative effect on top flange and end of first weather shed should be minimized as far as possible. Considering four piecewise cubic natural splines with two fixed points, six parameters are varied in the optimization. The individual chromosome can be expressed as follows:

$$chromosome=[x_B,x_C,x_D,y_B,y_C,y_D]$$

Where $x_B, x_C, x_D, y_B, y_C$ and $y_D$ represent the coordinates of points B, C and D.

$x_B, x_C$ and $x_D$ vary between 145mm and 150mm. $y_B, y_C$ and $y_D$ vary between two fixed points, i.e. 2246.25mm and 2289mm. Moreover, to avoid an impractical or even unreasonable contour in application, the optimization has to subjected to the following constrains.

- The x coordinates of the upper contour must be increased progressively with the increasing y coordinates to prevent improper structure.
- The y coordinates of the lower point must be smaller than those of the upper point, i.e. $2246.25mm \le y_B \le y_C \le y_D \le 2289mm$

Due to the above described constrains, the contour optimization of the region above the first weather shed is formulated by the following fitness function

$$Fitness = \sum_{1}^{N} \left| w_i \cdot \varepsilon_i \right| \text{ for } i = 1,2...N$$

$$Fitness = w_1 \cdot \left| E_{A,\max}(x) - E_{A,G}(x) \right| + w_2 \cdot \left| E_{B,\max}(x) - E_{B,G}(x) \right| + w_3 \cdot \left| E_{C,\max}(x) - E_{C,G}(x) \right| + w_4 \cdot \left| U_{dev,\max}(x) - U_{dev,G}(x) \right| \quad \textit{Eq. 83}$$

where $E_{A,\max}$, $E_{B,\max}$, $E_{C,\max}$ and $U_{dev,\max}$ indicate $E_{max}$ and maximum potential deviation (see 5.5) in the vicinity of the region above the first weather shed (see Figure 92). $w_1$, $w_2$, $w_3$ and $w_4$ represent the corresponding weighting factor respectively. $E_{A,G}$, $E_{B,G}$ $E_{C,G}$ and $U_{dev,G}$ are the goal values of E and potential deviation. The goal values are based on the preliminary investigation set as follow:

$E_{A,G} = 5kV/mm$, $E_{B,G} = 3.7kV/mm$, $E_{C,G} = 9.6kV/mm$ and $U_{dev,G} = 26.5$

Substituting weighting factors $w_1$=2, $w_2$=1.5, $w_3$=1.2 and $w_4$=0.15 and normalizing, the fitness function can be given,

$$Fitness = 2 \cdot \left| E_{A,\max}(x) - 5 \right| + 1.5 \cdot \left| E_{B,\max}(x) - 3.7 \right| + 1.2 \cdot \left| E_{C,\max}(x) - 9.6 \right| + 0.15 \cdot \left| U_{dev,\max}(x) - 26.5 \right|$$

*Eq. 84*

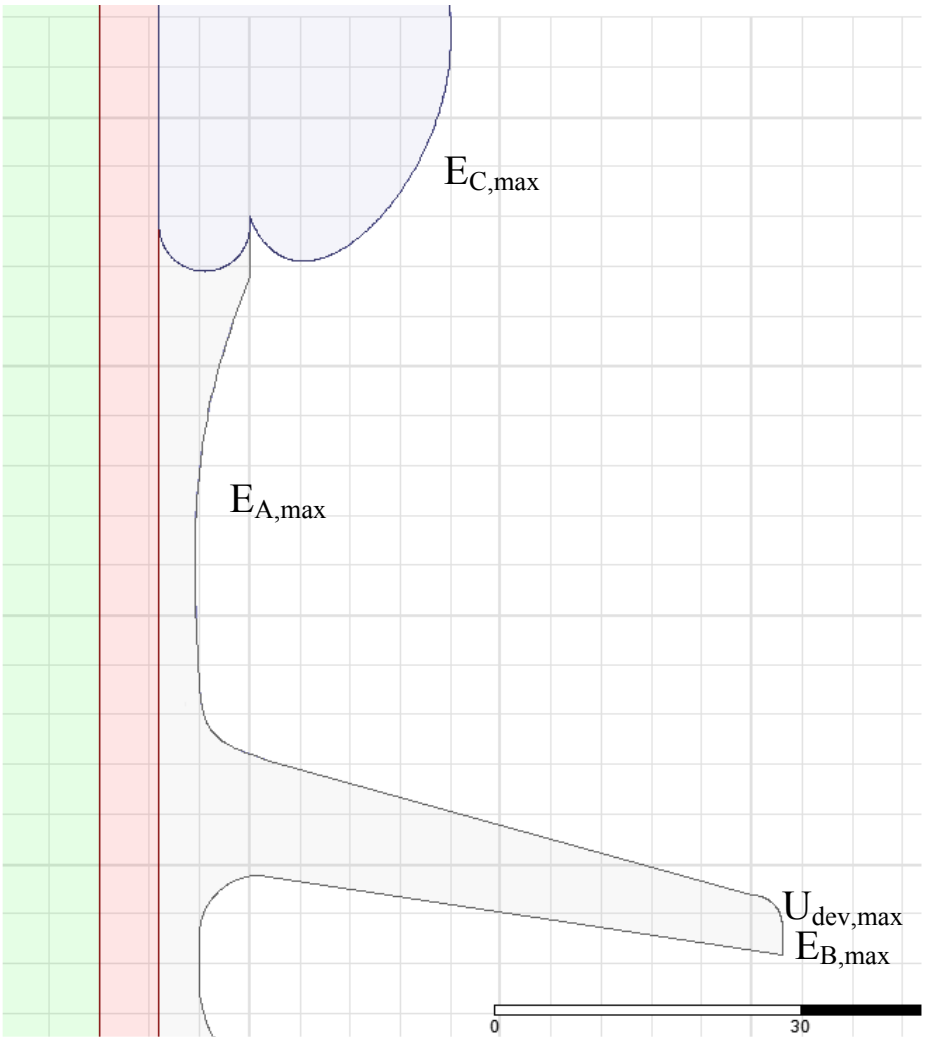


*Figure 92: Positions of potential $E_{max}$ and maximum of potential deviation*

Under this condition, the lower fitness value is considered a better result. The population size ($N_p$) and the maximal number of iterations/generations ($G_{max}$) must be chosen. The population size ($N_p$), i.e. the number of individual chromosomes in a generation, is set to $N_p$=20. The number of generations ($G_{max}$) is set to 50. The fitness function evaluates each individual chromosome, and the population will be sorted in the order of better fitness. The elitism strategy preserve two best chromosomes. The mutation with rate of 30% is applied to reproduce the 18 chromosomes in the next generation. After approximate 35 generations the genetic algorithms converge to an acceptable result. The following table and figures list the summary of fitness results, comparison between original and optimized structure and 2D plot E distribution.

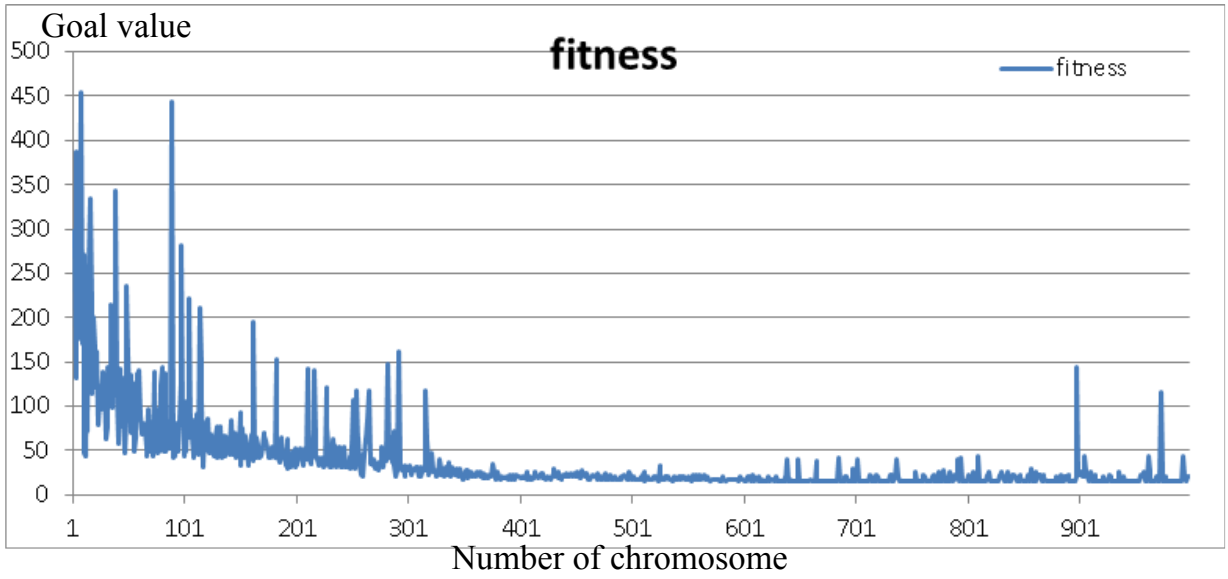


*Figure 93: Results of fitness function*

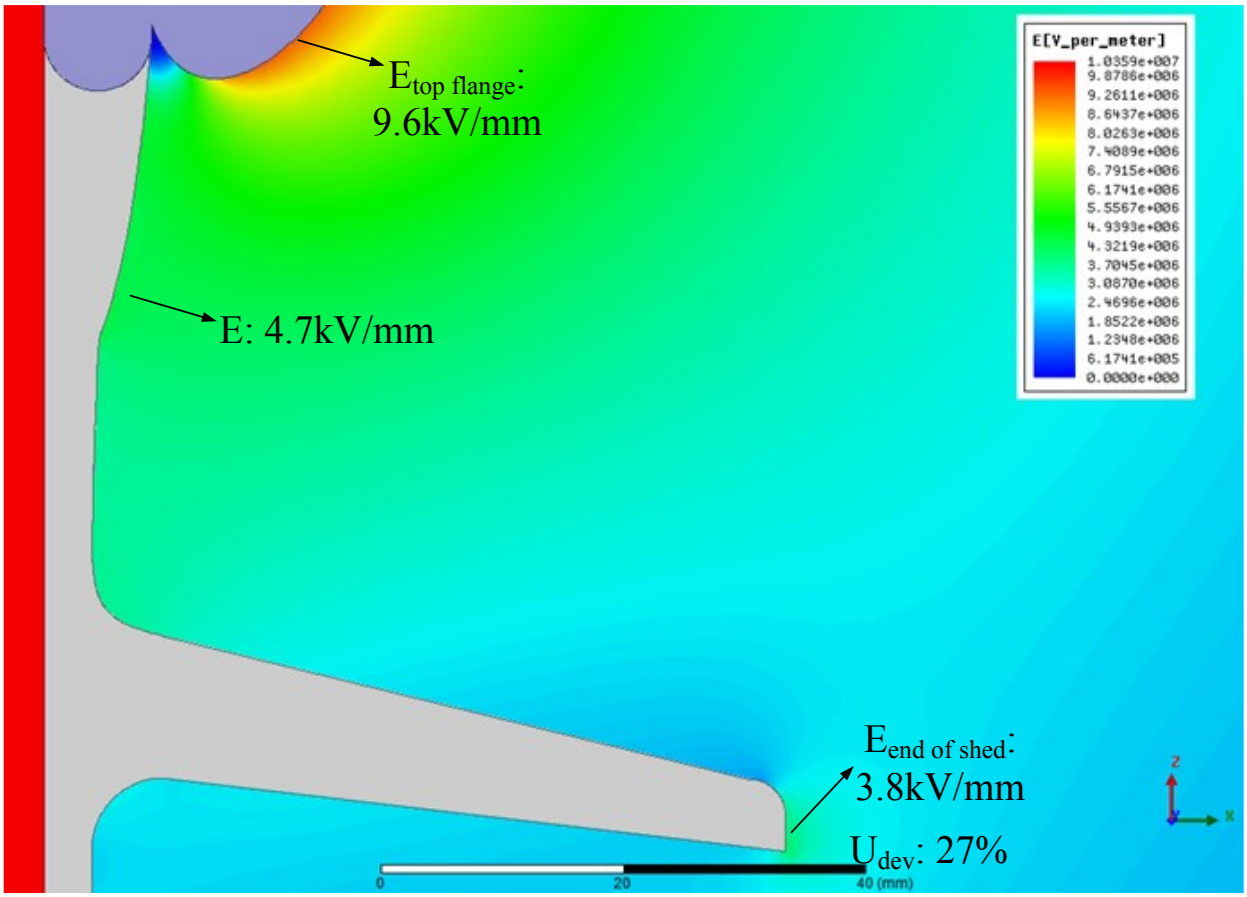


*Figure 94: 2D plot E of region above first weather shed after optimization*

| | $E_{max}$(kV/mm) | | | Maximum potential deviation (%) |
|---|---|---|---|---|
| | Top flange | Above first weather sheds | End of first weather shed | |
| Original structure | 18 | 9.4 | approx. 4.2 | 27 |
| Before optimization of the region above first weather sheds | 9.6 | 6.6 | 3.8 | 27.1 |
| After optimization | 9.6 | 4.7 | 3.8 | 27 |

*Table. 17: Comparison between the original and optimized structure under lightning impulse voltage 1050kV*

Table. 17 lists the comparison between the original and optimized structure. By the constrain condition of fitness expression in the algorithm the negative effect on end of first weather shed and top flange has minimized. At the same time, $E_{max}$ of region above first weather shed drops from 9.4kV/mm into 4.7kV/mm. The concept of maximum potential deviation will be discussed in following chapter 5.5.

## 5.5 Optimization of potential deviation ($U_{dev}$) along the surface of insulator

The first section discusses effects of several parameters on potential distribution on the silicone rubber weather shed profile. The different structures of shed profiles are proposed and simulated by Ansoft Maxwell 2D. Then, the structural parameters of shed are investigated, whether the structural parameters of shed has the effect on potential distribution on the surface of silicon rubber shed. Afterwards a new design shield with high potential (HP) is introduced to reduce the potential deviation along the silicone rubber weather shed. By the optimization the same algorithms, i.e. genetic algorithms, is continued to apply. Finally, the optimal results are represented and compared to original ones.

### 5.5.1 Effects of several parameters on $U_{dev}$ along silicone rubber weather shed

Five different shed profiles are presented in this section, which are shown in Figure 95. The design of each shed profile needs to yield contentment in standard IEC 60815-3. [32]

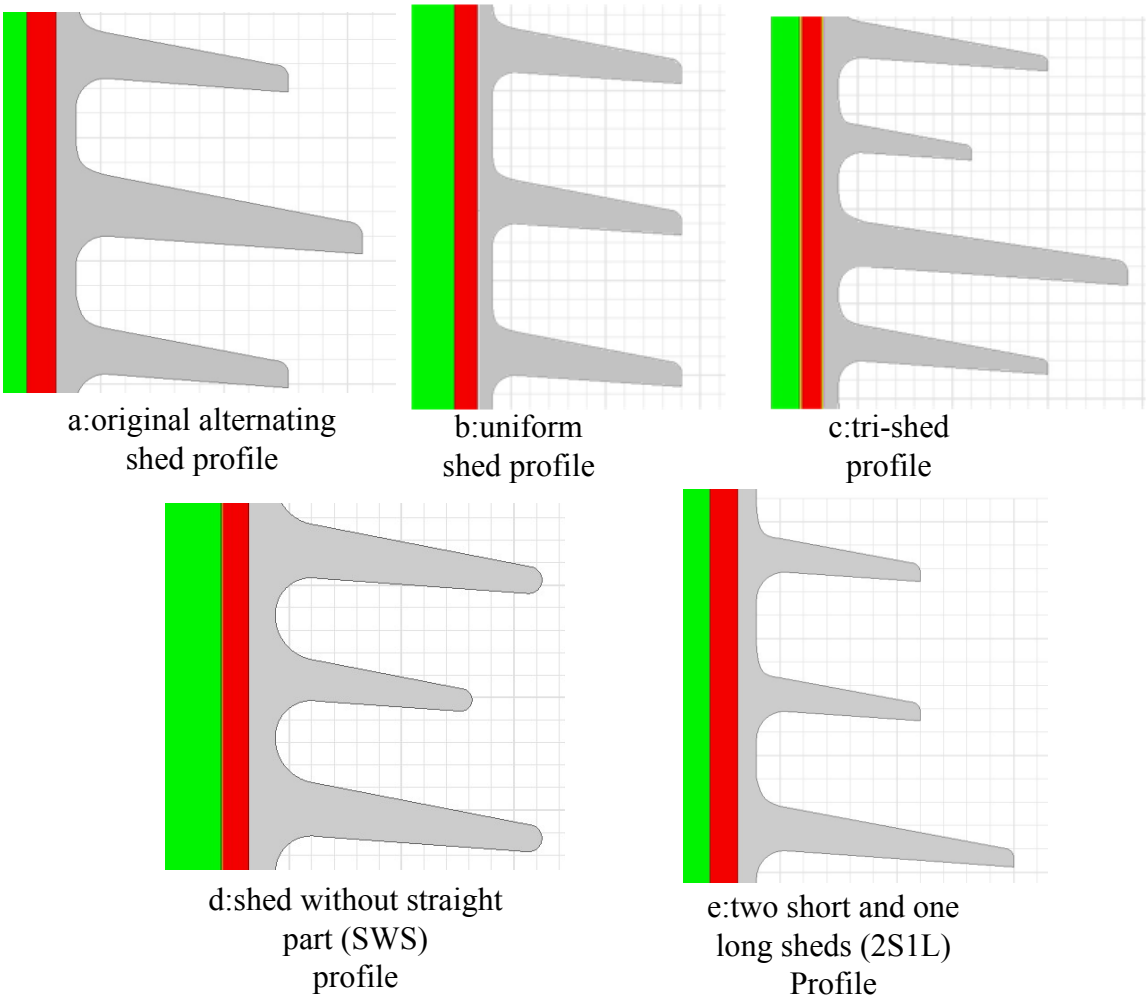


*Figure 95: Five different profiles of silicon rubber sheds*

The original alternating profile (Figure 95.a) refers to the technical dimension of the original structure. Compared with an uniform profile the original alternating profile has a relative longer creepage distance while ensuring satisfactory wet performance and self-cleaning properties. The uniform profile (see Figure 95.b) is the more simple structure than the other three structures. It is generally acceptable in all types of environmental conditions. The tri-sheds profile (see Figure 95.c) has the longest creepage distance to reduce the possibility of rain bridging and local short-

circuiting between the sheds. The profile d (see Figure 95.d) has no straight part between the transition radiuses of the weather shed and the rounded shed, which makes a larger transition radius in the same spacing between two weather sheds. The profile e (see Figure 95.e) is a variation of profile c. It has two identical short weather sheds and a long weather shed as a group of shed.

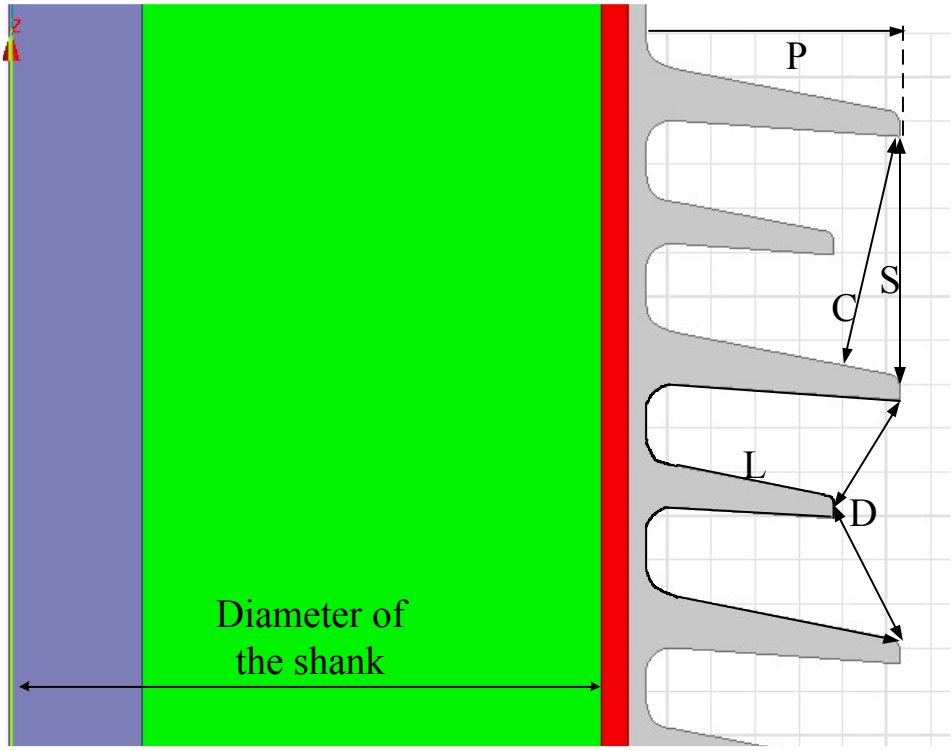


*Figure 96: Critical parameters of shed profile*

Figure 96 presents critical parameters of the shed profile. The definition of critical parameters follows the standard IEC 60815-3. Spacing “S” is defined as vertical distance between two identical sheds. Weather shed “P” is defined as horizontal distance between the shank and maximum shed. The ration of Spacing “S” versus Weather shed “P” is the critical parameter for the assessment of the performance of a shed profile. “C” is the minimum distance between adjacent two identical sheds by drawing a perpendicular from the lowest point of rim of the upper shed to the next identical shed below one. “D” is the straight air distance between two points on the insulating part. “L” is the part of the creepage distance measured between the above two points. The ratio of “L” versus “D” is a more localized check of the risk of bridging by arcs when dry bands or uneven hydrophobicity occur. The details of profile critical parameters are listed in the following table.

| Sheds profile (See Figure 95) | Original alternating | Uniform | Tri-sheds | SWS | 2S1L |
|---|---|---|---|---|---|
| Diameter of shank (mm) | 145 | 145 | 145 | 147 | 145 |
| Spacing S (mm) | 56.5 | 36.5 | 76 | 57.4 | 55 |
| Weather shed P (mm) | 58 | 50 | 76 | 59.1 | 82.6 |
| S/P | 0.97 | 0.73 | 1 | 0.97 | 1.5 |
| Minimum distance between sheds C (mm) | 53 | 43.1 | 73 | 50.4 | 79.5 |
| Part of creepage distance L (mm) | 237.5 | 135.8 | 378.5 | 225.6 | 305.37 |
| Straight air clearance D (mm) | 59 | 36.5 | 110.8 | 62.2 | 96.13 |
| L/D | 4.02 | 3.72 | 2.92 | 3.63 | 3.17 |
| Creepage distance $L_c$ (mm) | 7964.2 | 6358.3 | 9455 | 8045 | 7194.6 |

*Table. 18: Critical profile parameters of five different shed structures*

To investigate the deviation between the real potential distribution along the sheds and ideal potential distribution, the function of potential deviation $f(L)$ is defined as following [33]

$$f(L) = |\varphi - \varphi_{lin}| \qquad \text{Eq. 85}$$

$\varphi = \varphi(L)$ presents potential along the surface of sheds in the air. $\varphi_{lin}$ presents the linear potential distribution in the ideal situation. For the comparison between the different creepage distances in different shed profiles a method is applied to establish a unitary distance on which to base subsequent calculations. The creepage distance of sheds is normalized into the percentage of length.

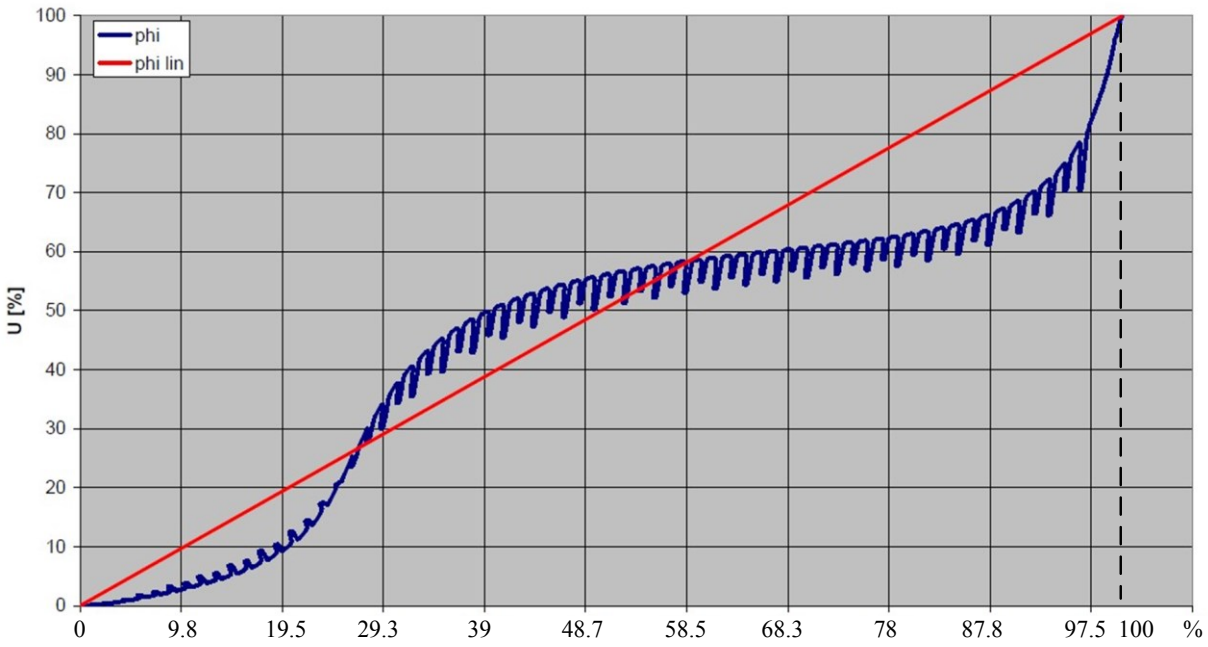


*Figure 97: Linear potential distribution and potential distribution along sheds (original bushing, measure line see Figure 14)*

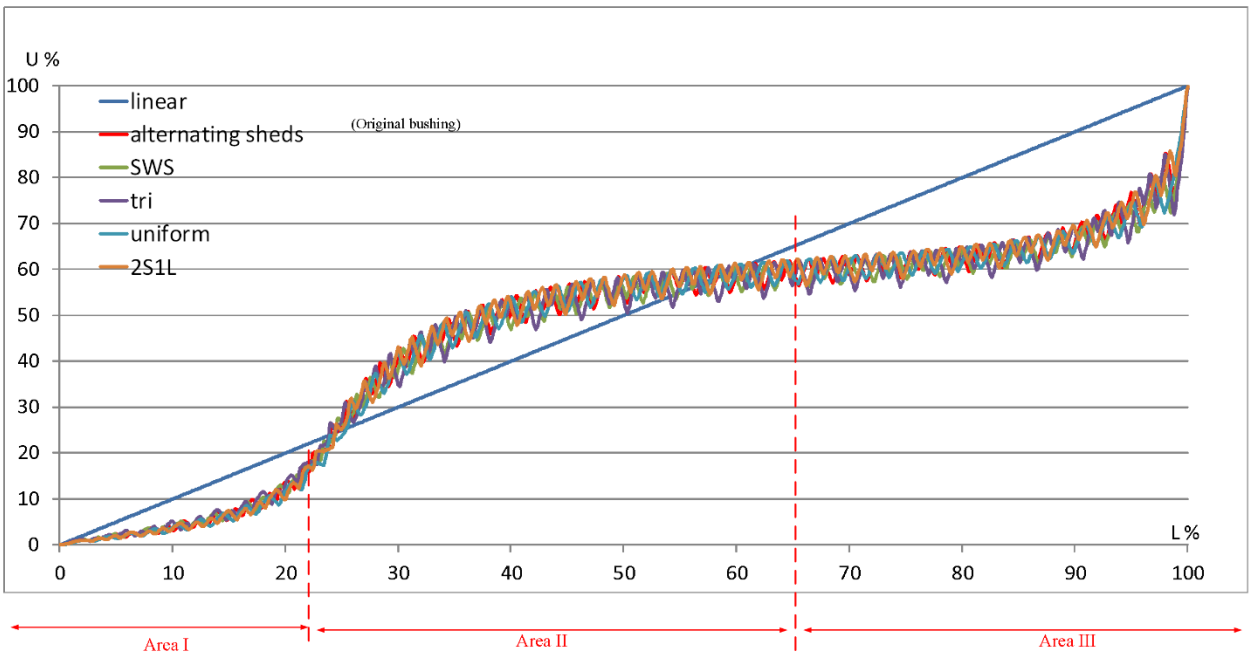


*Figure 98: Linear potential distribution and potential distributions along different sheds (measure line see Figure 14)*

Figure 97 and Figure 98 describe the potential distribution along original sheds and different sheds. The potential distribution in Figure 98 is analogous to the original potential distribution.

The curves are laid to overlap each other. For the further analysis the potential distribution is divided into three parts (see Figure 98). In the range of area I the curves are under the linear curve. While the curves go into the area II, the potential distribution becomes much higher than linear distribution until the curves reach into area III. Within area III the curves are rising relatively flatly. The 95% length of shed profile distributes only approx. 80% potential. Along last 5% length of shed profile 20% potential is allocated, which might lead to electric field strength enhancement.

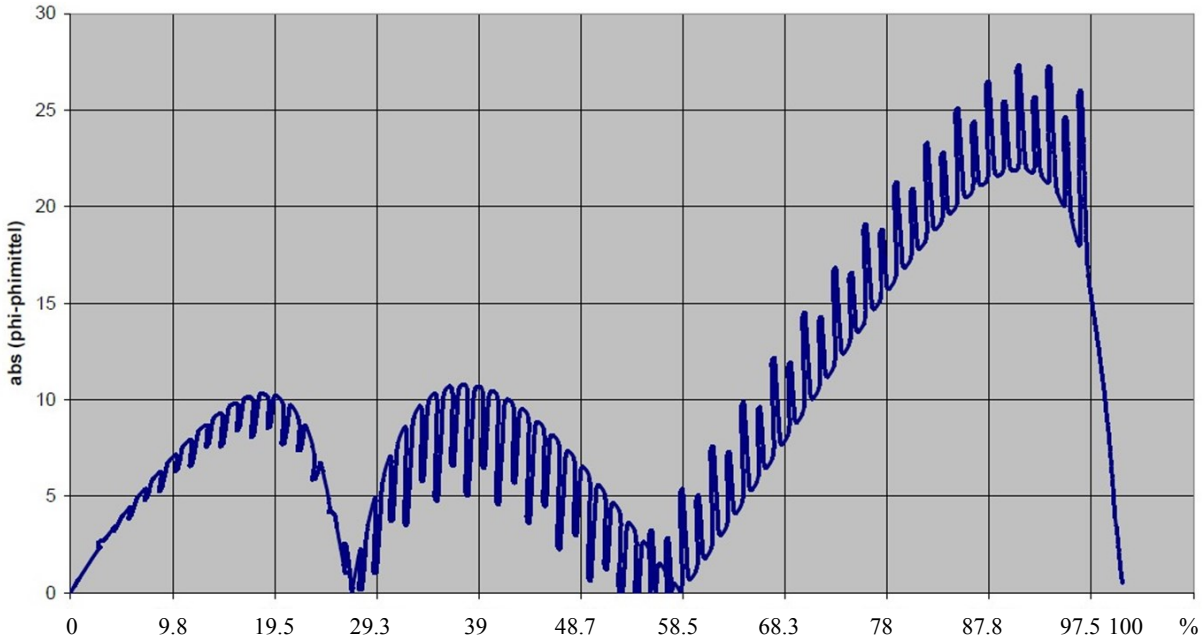


*Figure 99: Potential deviation f (L) along sheds (original bushing)*

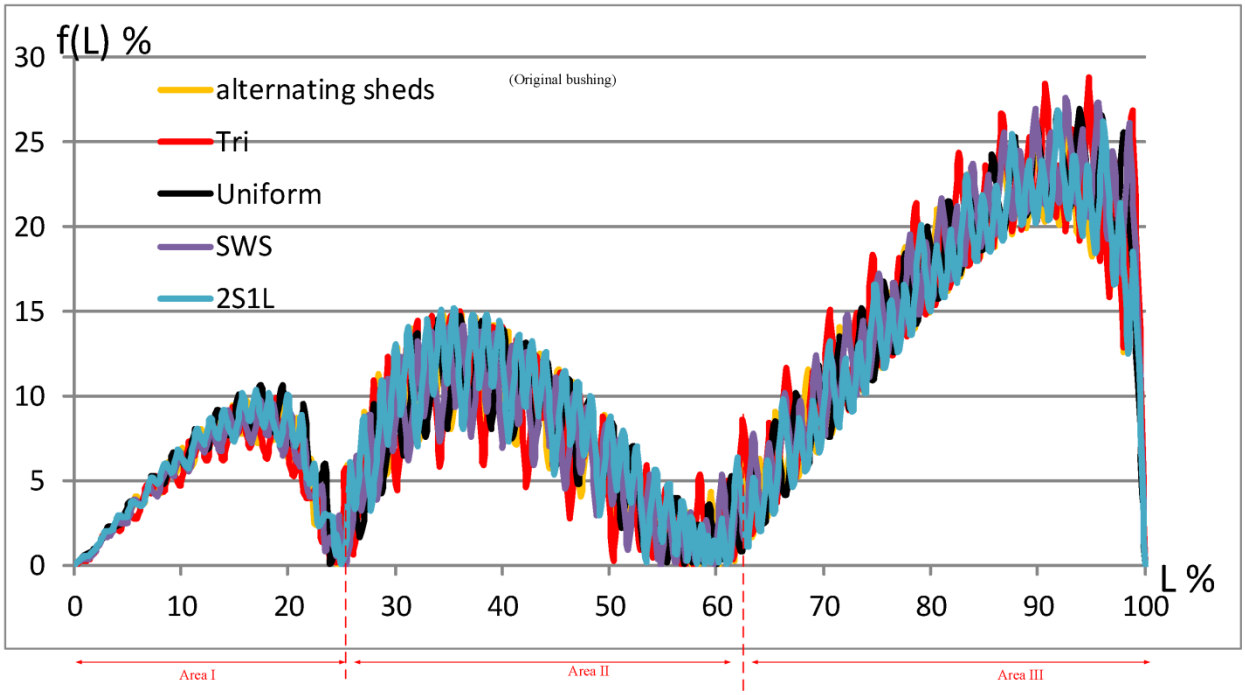


*Figure 100: Potential deviations f(L) along five different sheds*

For a clear comparison Figure 99 and Figure 100 show the potential deviations $f(L)$ along the original shed and five different sheds. In Figure 99 the maximum potential deviations for three areas are 10%, 10% and 27% separately. The most critical area of a shed profile locates at area III, which has the maximum deviation from a linear potential distribution (see Figure 99). The worse the non-linearity of the potential distribution is the greater the value of electric field strength occurs, which increases the possibility of partial discharges. In Figure 100 the potential deviations of the different five profiles in area I and III are similar to the original results. However, in the area II the potential deviations are increasing and approx. 5% higher than the original result, which indicates that the reduction of FRP diameter brings sheds even closer to the ground electrode. This has negative effect on the potential distribution along the sheds. From a comparison between the five different shed profiles the first conclusion can be drawn that different profiles have different creepage distances. Different profiles may appear to have different characteristics and an outstanding performance under anti-contamination test. However, they cannot make the potential distribution more linear and have no great effect on the potential distribution.

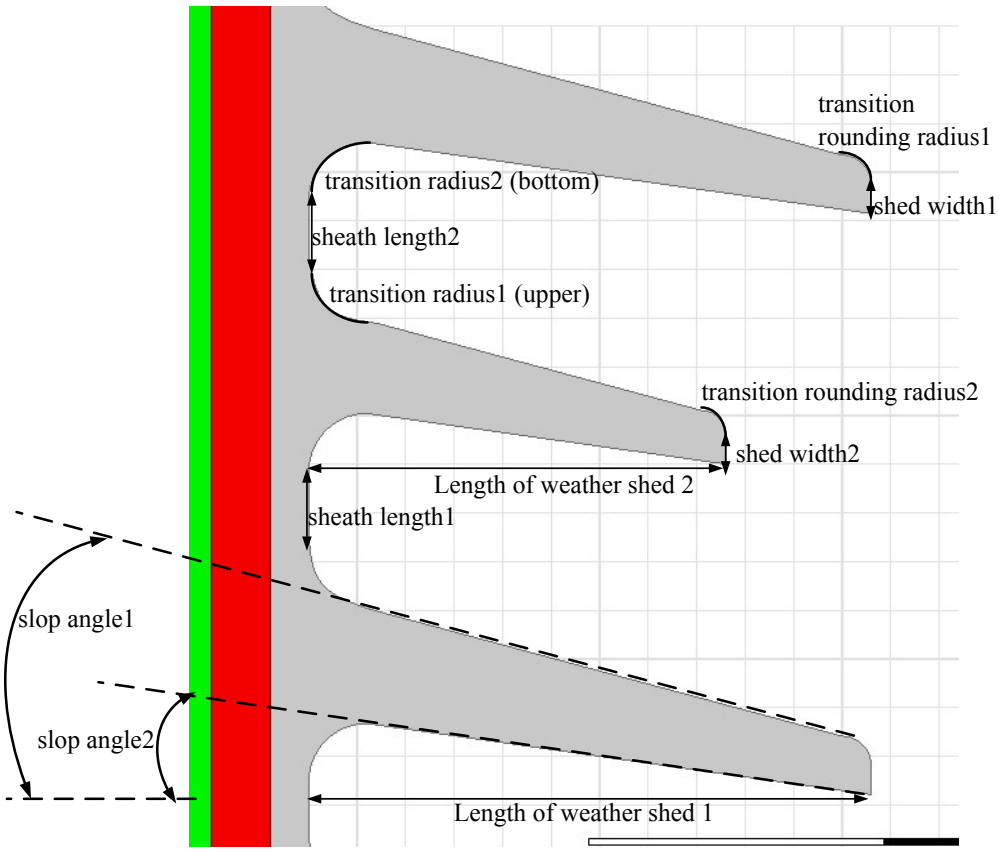


*Figure 101: Critical parameters of shed profile*

There are still many design parameters of a shed profile, such as sheath transition rounding radius, shed spacing, shed overhand etc. that can be varied. In the following several design parameters are selected and studied by using an alternating shed profile model to illustrate the influence on the potential distribution along the shed. All critical parameters of the shed profile under study are shown in Figure 101. The detailed analysis of critical parameters went substantially beyond the scope of the dissertation. Therefore, only the results are discussed in the following.

The parameters of weather shed length and transition radius at sheath has the effect on potential deviation in the range of area III. With the variation of height of the ground electrode potential deviations in area I and II are interacted. The slope angle of the weather shed with different $\Delta\varphi$ has the greatest influence on the whole curve of potential deviation. The influence of transition rounding radiuses, widths of weather shed, slope angle of the weather shed with fixed $\Delta\varphi$ and sheath length on the potential distribution can be ignored. In generally, most of shed parameters have a limited or even no influence on the potential distribution along the silicon weather sheds.

Only with the variation of the slope angle Δφ of weather shed the potential deviation at the area III drops to 26%.

### 5.5.2 New design for optimization of $U_{dev}$ along the silicon weather sheds

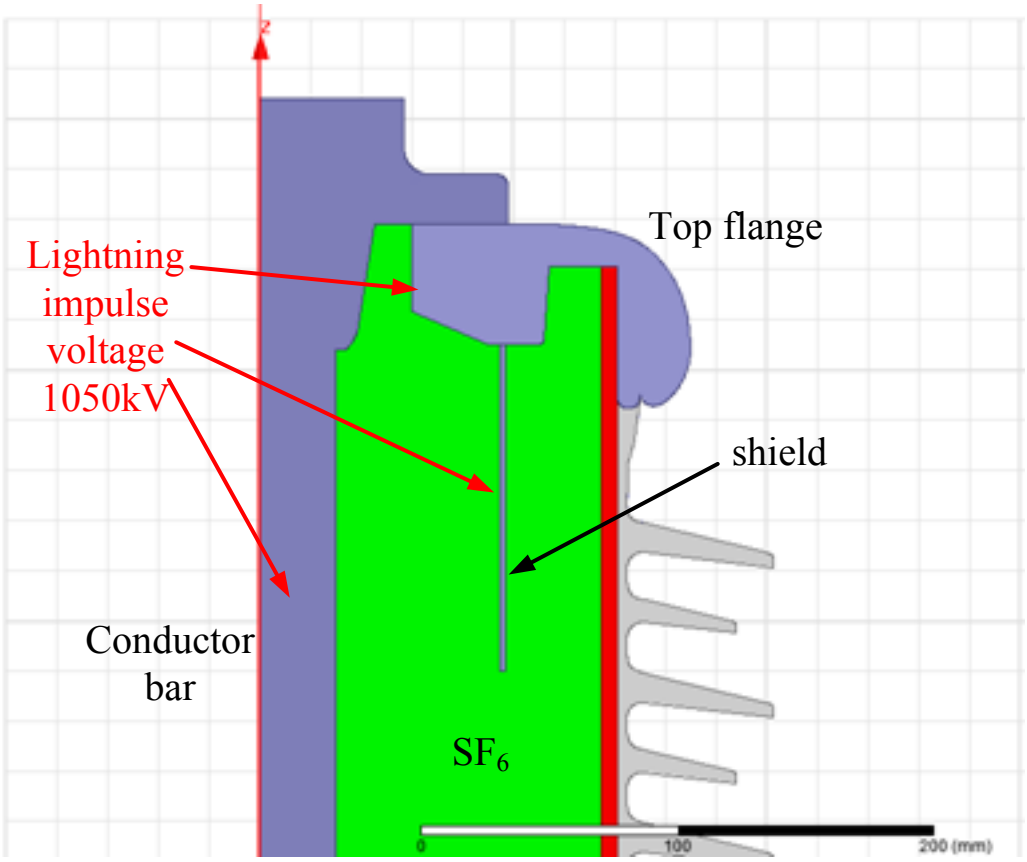


*Figure 102: Sketch diagram of Shied with HP for reducing potential deviation along the weather sheds*

For optimization of the potential deviation ($U_{dev}$) along weather sheds a new structure shield with high potential (HP) is designed as seen in Figure 102. In the simulation the shield is energized to LIV 1050kV. This shield has great influence on the potential deviation along the weather sheds. By using a rough shield with HP the potential deviation drops from 27% to 24.2%. In the following three different structures of shield with HP are proposed.

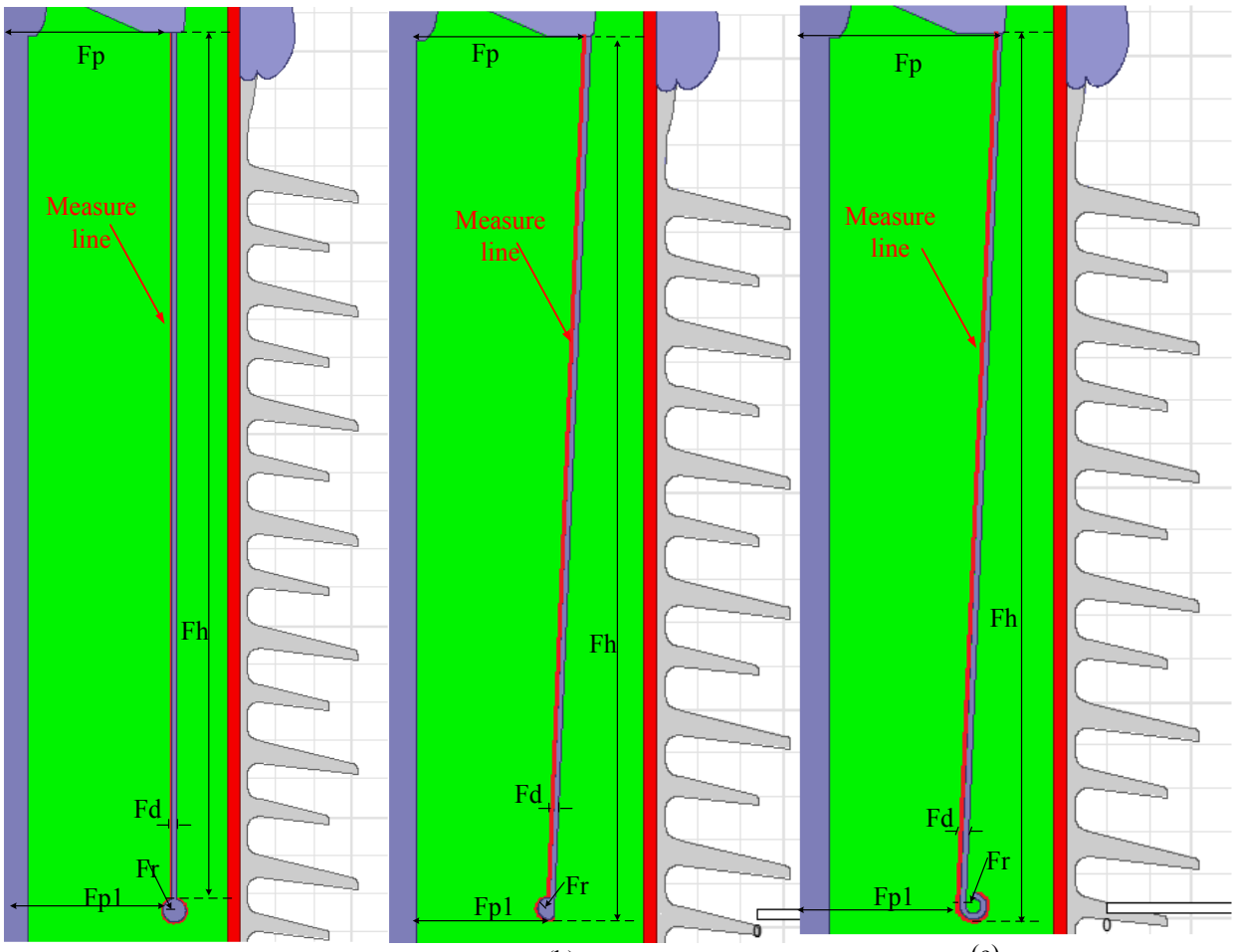


*Figure 103: Three parameterized structures of shield with HP*

Figure 103 shows three parameterized shields with HP. At the end of structure (a) a grading ring is constructed. By varying the diameter at the end of shield, the structure (a) could be conical and cylindrical. This structure is also referred to as basic structure to investigate whether the dimension of the grading ring has a negative effect on the silicone rubber sheds and FRP tube. At the end of structure (b) a semi-grading ring is attached. At the end of structure (c) a hollow ring similar to the ground electrode is attached. By the investigation E along the surface of the shield with HP fluctuates between 15kV/mm and 17kV/mm. Structure (a) performs better than others. However, E of all three structures are not larger than permitted withstand E in $SF_6$ under 0.7 MPa.

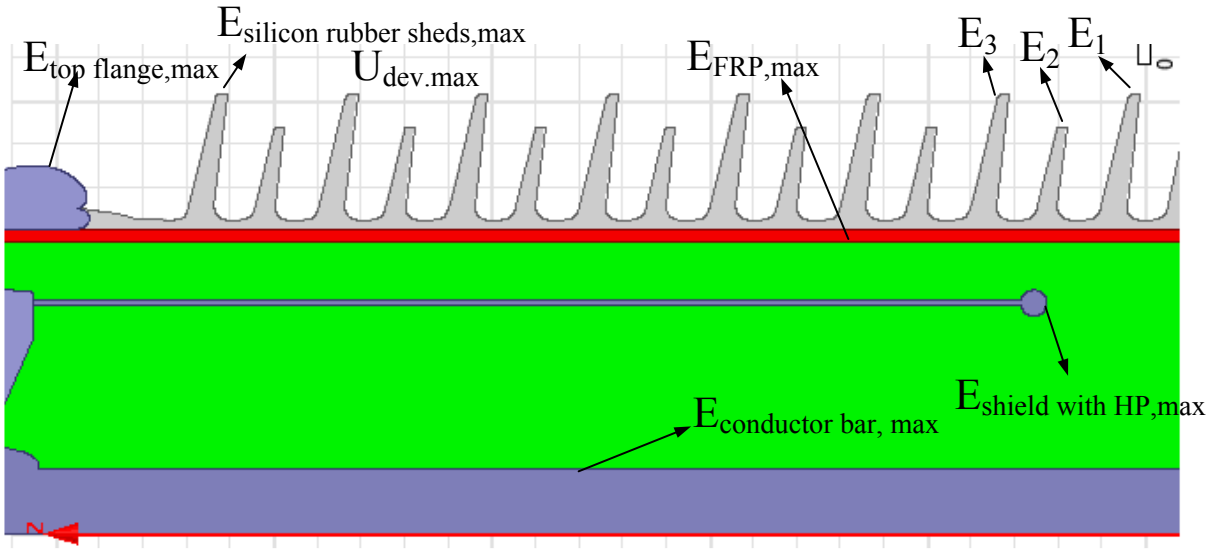


*Figure 104: Measuring positions for structure (a)*

Likewise to the previous optimization at the first step the irrational values will be eliminated and proper initial values and boundaries of parameters for GA will be determined by a rough sweeping. Five parameters (Fp, Fp1, Fr, Fh and Fd) are swept one by one, which indicates in the investigation a parameter will be considered as variable, in the meanwhile others are fixed in the investigation. The observed critical positions are marked in Figure 104. The critical positions include conventional critical positions (e.g. FRP inside, top flange conductor bar etc.) and several special positions i.e. $E_1$, $E_2$ and $E_3$. $E_1$, $E_2$ and $E_3$, which locate at the end of the silicon rubber sheds near the structure (a). The similar charts of preliminary investigation are not shown again in this section. Taking into account the influence of all critical positions the structure (a) performs worst and is excluded from further consideration. Based on the results from the preliminary investigation the chromosomes could be expressed as follow:

$$x = [Fp, Fp1, Fd, Fh, Fr]$$

The ranges of parameters for structure (b) and (c) are shown in the following.

$(b)$: $Fp : [90mm, 108mm]$, $Fp1 : [80mm, 100mm]$, $Fr : [5mm, 10mm]$, $Fh : [300mm, 500mm]$, $Fd : [2mm, 3mm]$

$(c)$: $Fp:[95mm,108mm]$, $Fp1:[90mm,100mm]$, $Fr:[4mm,10mm]$, $Fh:[200mm,500mm]$, $Fd:[1mm,3mm]$

The contour optimization of shield with HP is formulated as the following fitness function

$$Fitness=\sum_{1}^{N}\left|w_i\cdot\varepsilon_i\right| \text{ for } i=1,2...N$$

For both structures

$$Fitness=w_1\cdot\left|\frac{E_{A,\max}(x)-E_{A,G}(x)}{1\cdot10^6}\right|+w_2\cdot\left|\frac{E_{B,\max}(x)-E_{B,G}(x)}{1\cdot10^7}\right|+w_3\cdot\left|\frac{E_{C,\max}(x)-E_{C,G}(x)}{1\cdot10^7}\right|$$
$$+w_4\cdot\left|\frac{E_{D,\max}(x)-E_{D,G}(x)}{1\cdot10^6}\right|+w_5\cdot\left|\frac{E_{E,\max}(x)-E_{E,G}(x)}{1\cdot10^6}\right|+w_6\cdot\left|U_{dev,\max}(x)-U_{dev,G}(x)\right|$$

*Eq. 86*

where $E_{A,\max}$, $E_{B,\max}$, $E_{C,\max}$ $E_{D,\max}$, $E_{E,\max}$, and $U_{dev,\max}$ indicate $E_{max}$ of inside of FRP tube, shield with HP, conductor bar, top flange, silicon rubber weather sheds and maximum potential deviation of silicon rubber weather sheds. $w_1$, $w_2$, $w_3$ $w_4$ $w_5$ and $w_6$ represent the corresponding weighting factor respectively. $E_{A,G}$, $E_{B,G}$ $E_{C,G}$ $E_{D,G}$ $E_{E,G}$ and $U_{dev,G}$ are the goal values of E and potential deviation. The goal values are evaluated by preliminary investigation and are set as follow:

For structure (b)

$E_{A,G}=4.0kV/mm$, $E_{B,G}=26.1kV/mm$, $E_{C,G}=31.2kV/mm$ $E_{D,G}=8.5kV/mm$ $E_{E,G}=3.9kV/mm$ and $U_{dev,G}=17$

For structure (c)

$E_{A,G}=4.5kV/mm$, $E_{B,G}=26.1kV/mm$, $E_{C,G}=31.2kV/mm$ $E_{D,G}=8.5kV/mm$ $E_{E,G}=4kV/mm$ and $U_{dev,G}=18$

Substituting weighting factors $w_1$=2, $w_2$=1, $w_3$=1 $w_4$=4 $w_5$=5 and $w_6$=20 and normalizing, the fitness function for structure (b) can be given,

$$Fitness_b = 2\cdot\left|\frac{E_{A,\max}(x)}{1\cdot10^6}-4.0\right|+1\cdot\left|\frac{E_{B,\max}(x)}{1\cdot10^7}-26.1\right|+1\cdot\left|\frac{E_{C,\max}(x)}{1\cdot10^7}-31.2\right|$$
$$+4\cdot\left|\frac{E_{D,\max}(x)}{1\cdot10^6}-8.5\right|+5\cdot\left|\frac{E_{E,\max}(x)}{1\cdot10^6}-3.9\right|+20\cdot\left|U_{dev,\max}(x)-17\right|$$

*Eq. 87*

Substituting weighting factors $w_1$=1, $w_2$=1, $w_3$=1 $w_4$=2 $w_5$=5 and $w_6$=5 and normalizing, the fitness function for structure (c) can be given,

$$Fitness_c = 1\cdot\left|\frac{E_{A,\max}(x)}{1\cdot10^6}-4.5\right|+1\cdot\left|\frac{E_{B,\max}(x)}{1\cdot10^7}-26.1\right|+1\cdot\left|\frac{E_{C,\max}(x)}{1\cdot10^7}-31.2\right|$$
$$+2\cdot\left|\frac{E_{D,\max}(x)}{1\cdot10^6}-8.5\right|+5\cdot\left|\frac{E_{E,\max}(x)}{1\cdot10^6}-4\right|+5\cdot\left|U_{dev,\max}(x)-18\right|$$

*Eq. 88*

Under this condition, the lower fitness value is considered a better result. The population size ($N_p$) and the maximal number of iterations/generations ($G_{max}$) must be chosen. The population size ($N_p$), i.e. the number of individual chromosomes in a generation, is set to $N_p$=30. The number of generations ($G_{max}$) is set to 50. The fitness function evaluates each individual chromosome, and the population will be sorted in the order of better fitness. The elitism strategy preserve two best chromosomes. The mutation with rate of 30% is applied to reproduce the 18 chromosomes in the next generation. The following figures depict the optimal results, comparison between original and optimized structure and 2D plot E distribution.

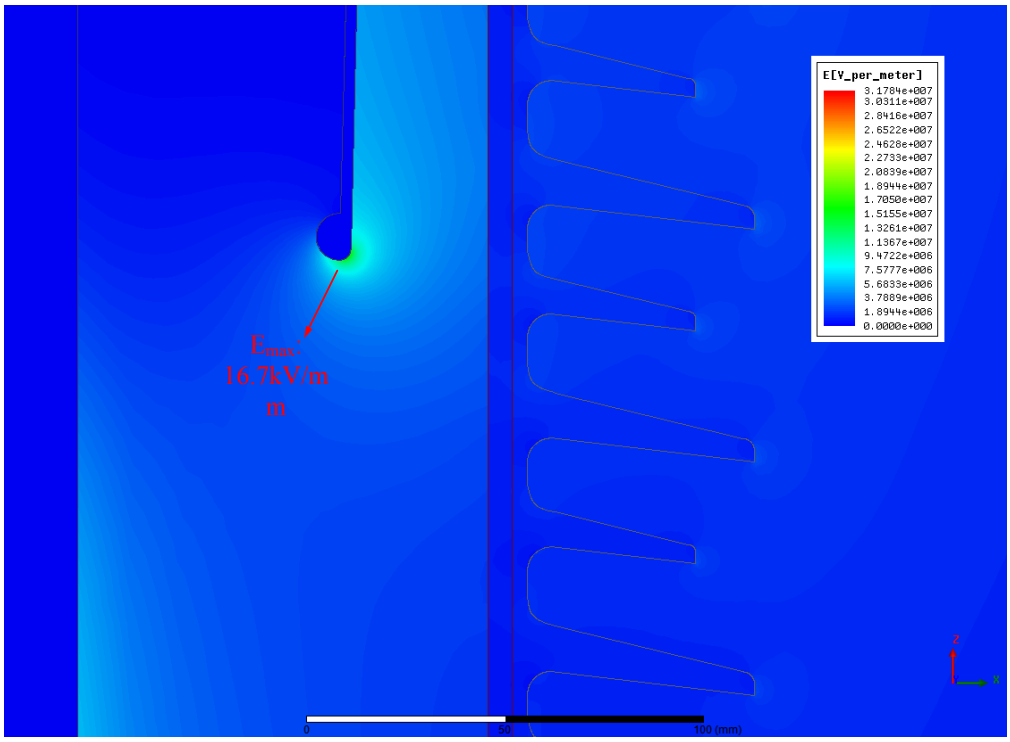


*Figure 105: 2D plot E of optimized shield (structure b)*

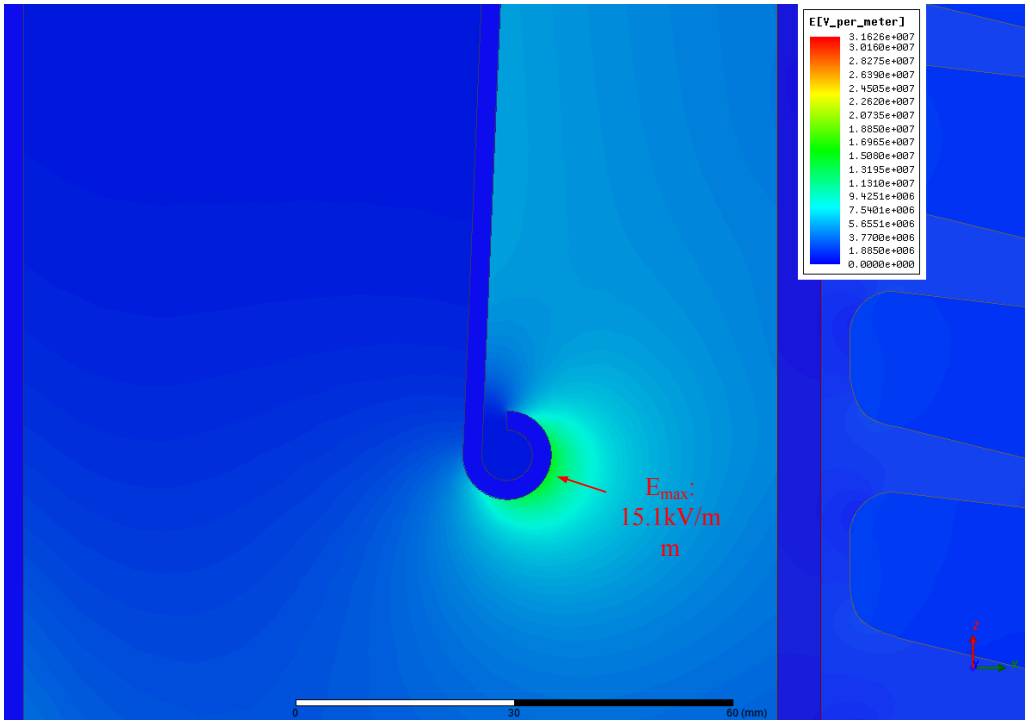


*Figure 106: 2D plot E of optimized shield (structure c)*

$E_{max}$ along the surface of the shield with HP still keeps at relative fixed value of approx. 17kV/mm in structure (b) and approx. 15kV/mm in structure (c). The value of $E_{max}$ fluctuates in a small range by the variation of parameters. Besides that, the peak value locates near to the FRP tube rather than to the conductor bar. The reason is that the shield and conductor bar are energized by the same high potential.

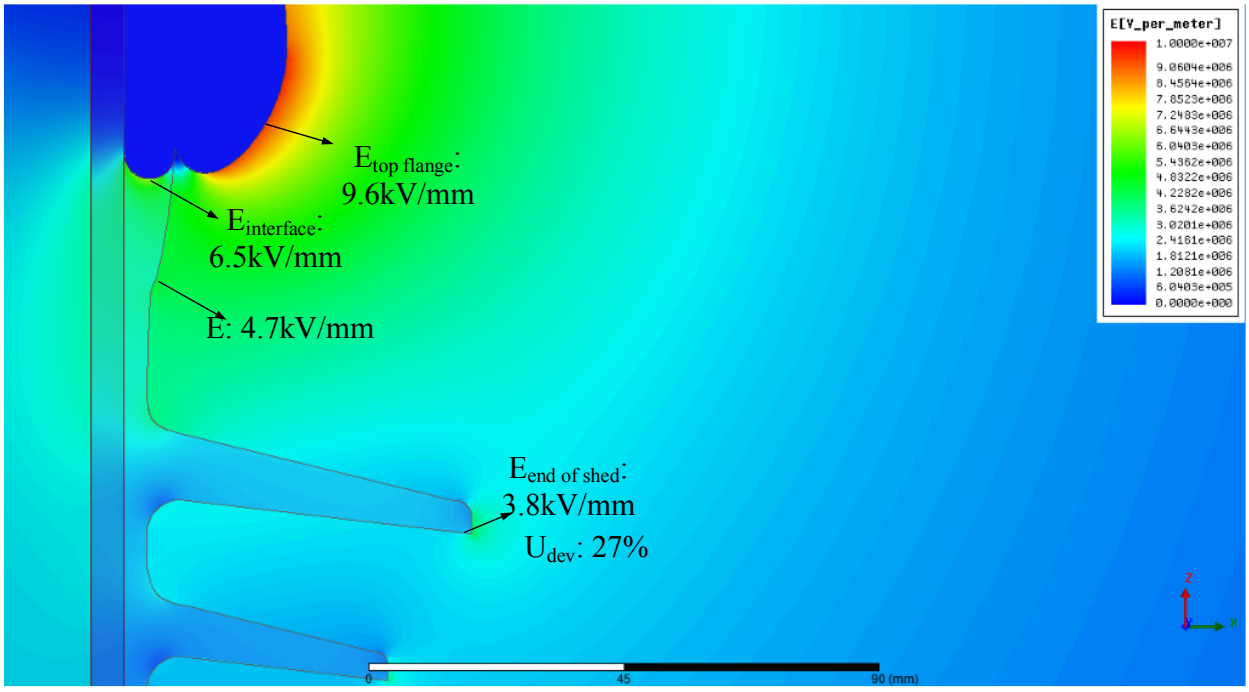


*Figure 107: 2D plot E of region above first weather shed without shield with HP (before optimization)*

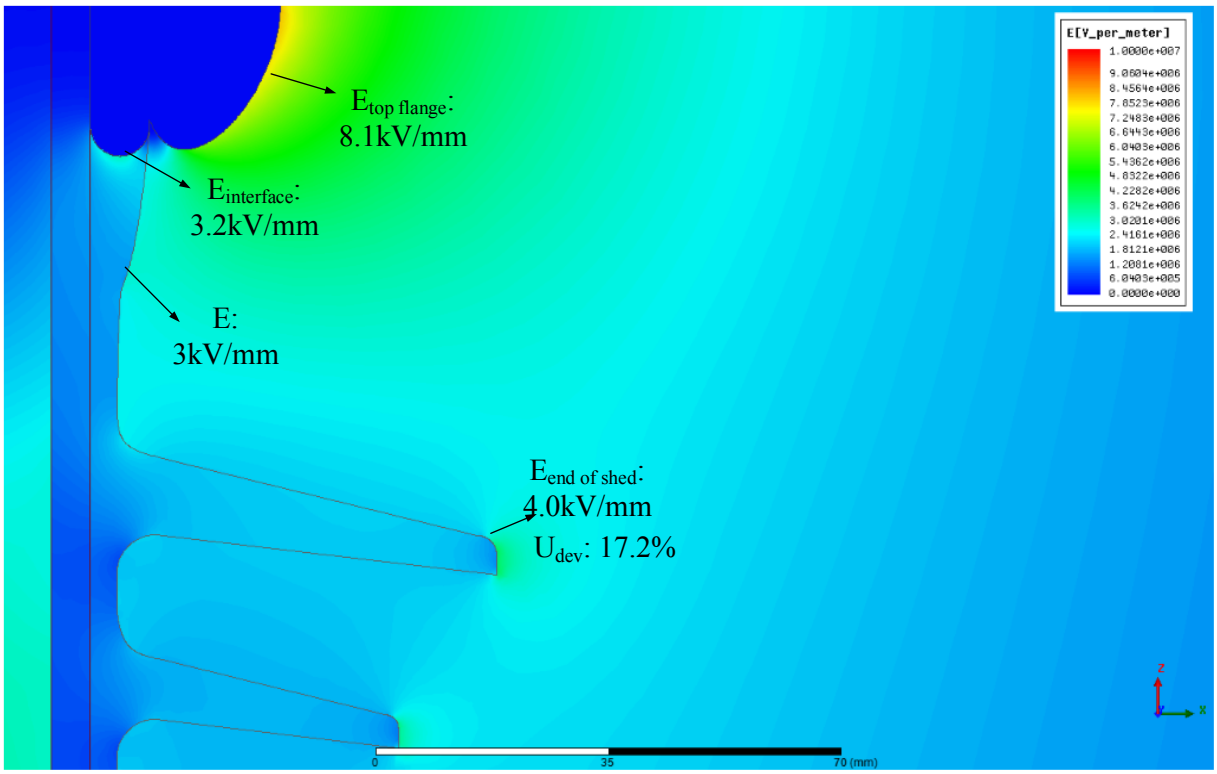


*Figure 108: 2D plot E of the region above the first weather shed with optimized shield with HP (structure b)*

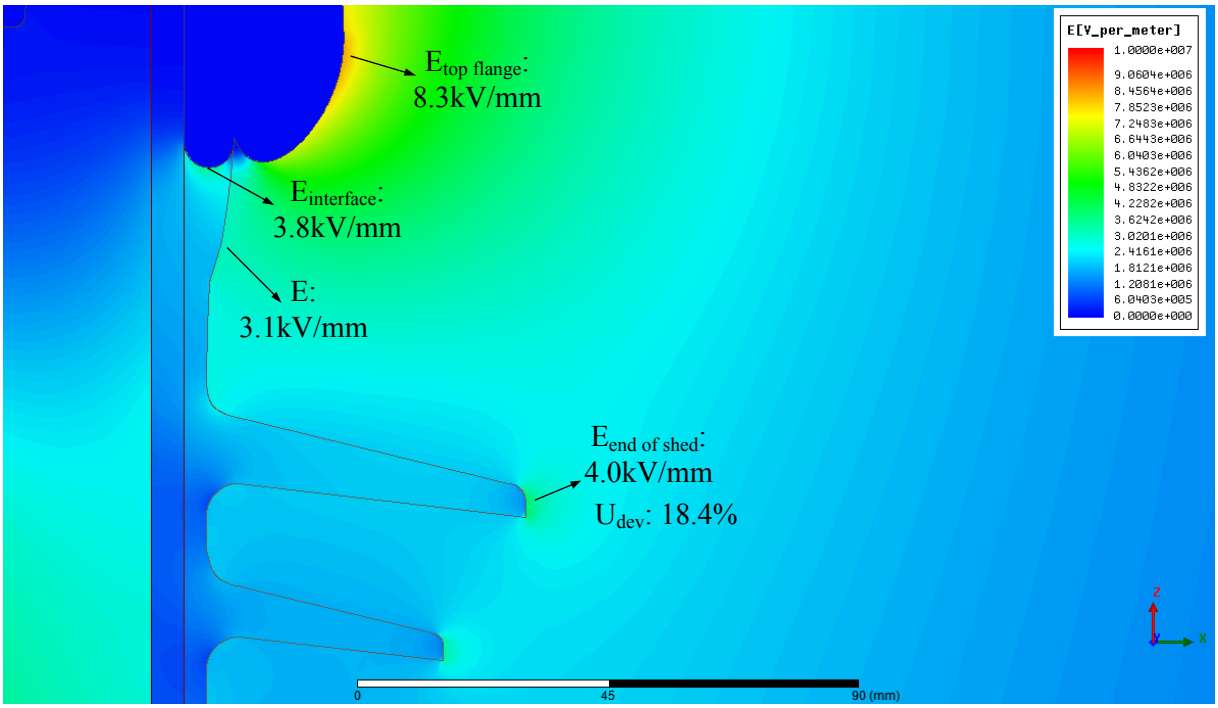


*Figure 109: 2D plot E of the region above the first weather shed with optimized shield with HP (structure c)*

In order to make a clear comparison, Figure 107 Figure 108 and Figure 109 are adopted the same color intensity. After optimization $E_{max}$ of the top flange and above the first weather shed drops from 9.6kV/mm to approx. 8.0kV/mm and from 4.7kV/mm to approx. 3kV/mm. However, due to the shield with HP E at the end of the first weather shed increases a little from 3.8kV/mm to 4.0kV/mm.

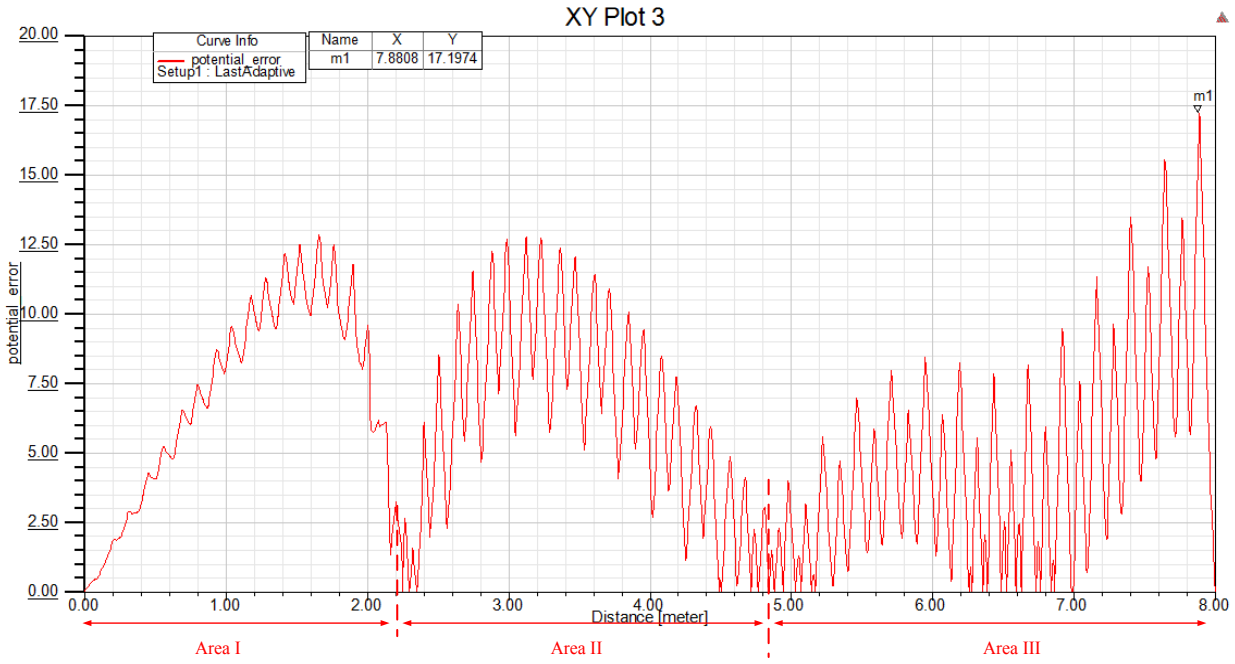


*Figure 110: Potential deviation along the surface of silicon rubber weather sheds with optimized shield structure (b)*

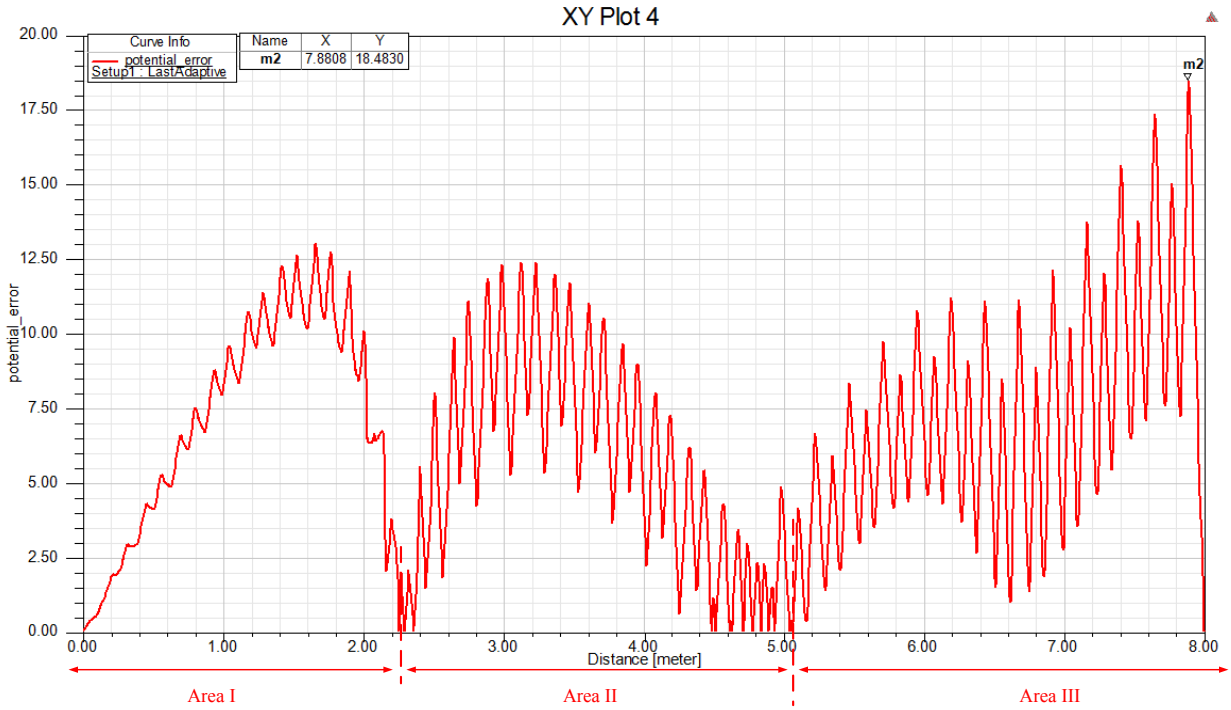


*Figure 111: Potential deviation along the surface of silicon rubber weather sheds with optimized shield structure (c)*

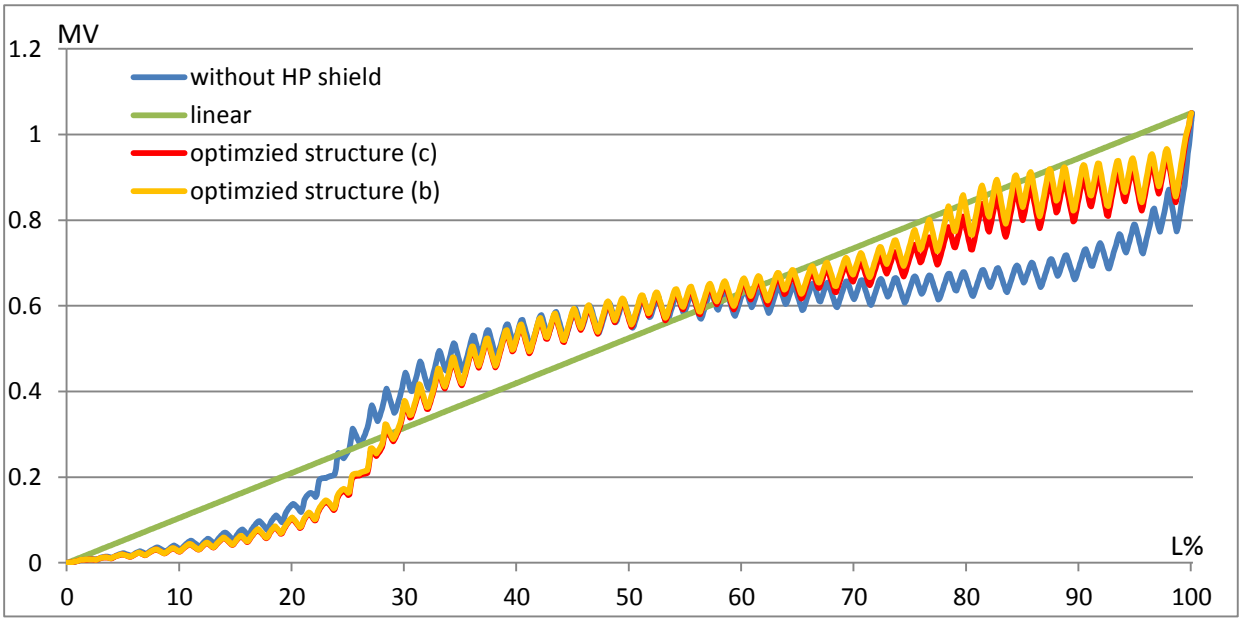


*Figure 112: Comparison of potential distribution along the silicon rubber weather sheds between linear, with and without shield*

From Figure 110, Figure 111, and Figure 112 we can derive that the maximum potential deviation is reduced greatly in the range of area III. The new design of shield with high potential achieves

the purpose of more linear potential distribution. The structure (b) performs better than structure (c). Therefore, structure (b) is proposed as shield for bushing. Simultaneously, the potential deviation at area I and II increase from 10.2% into 12.5%, which indicates the shield with HP has a tiny negative influence on potential deviation in area I and II.

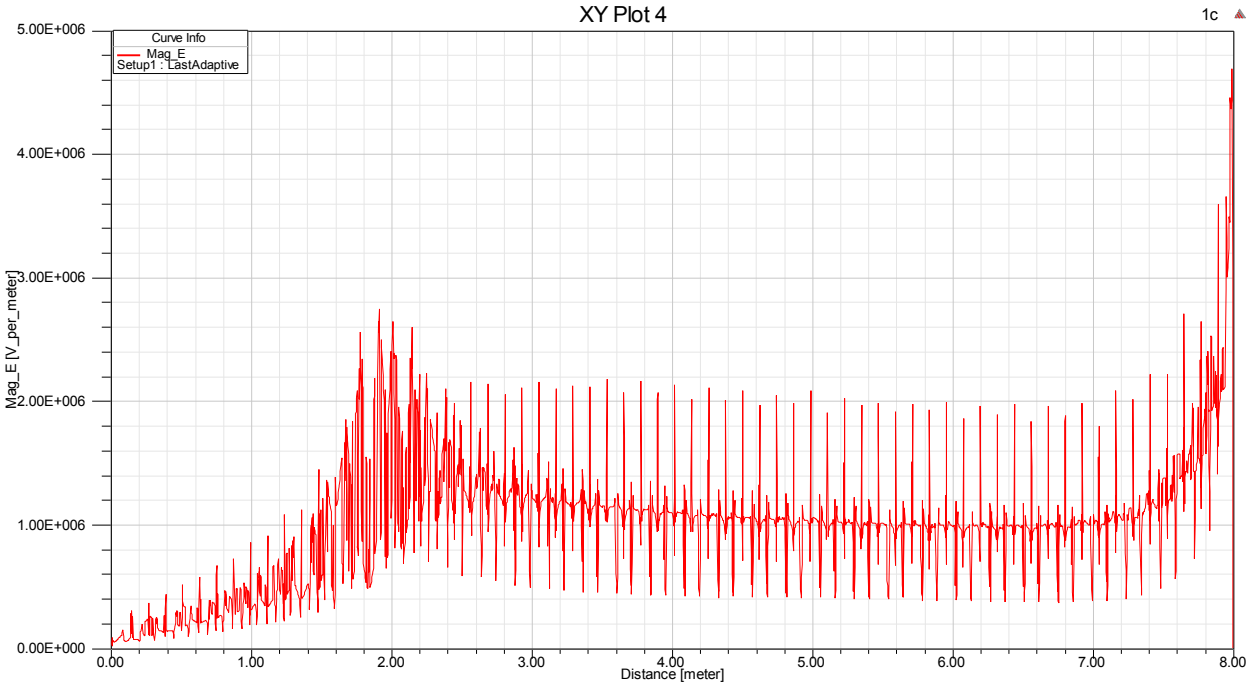


*Figure 113: E along the silicon rubber weather sheds under LIV voltage (without shield, measure line see Figure 14)*

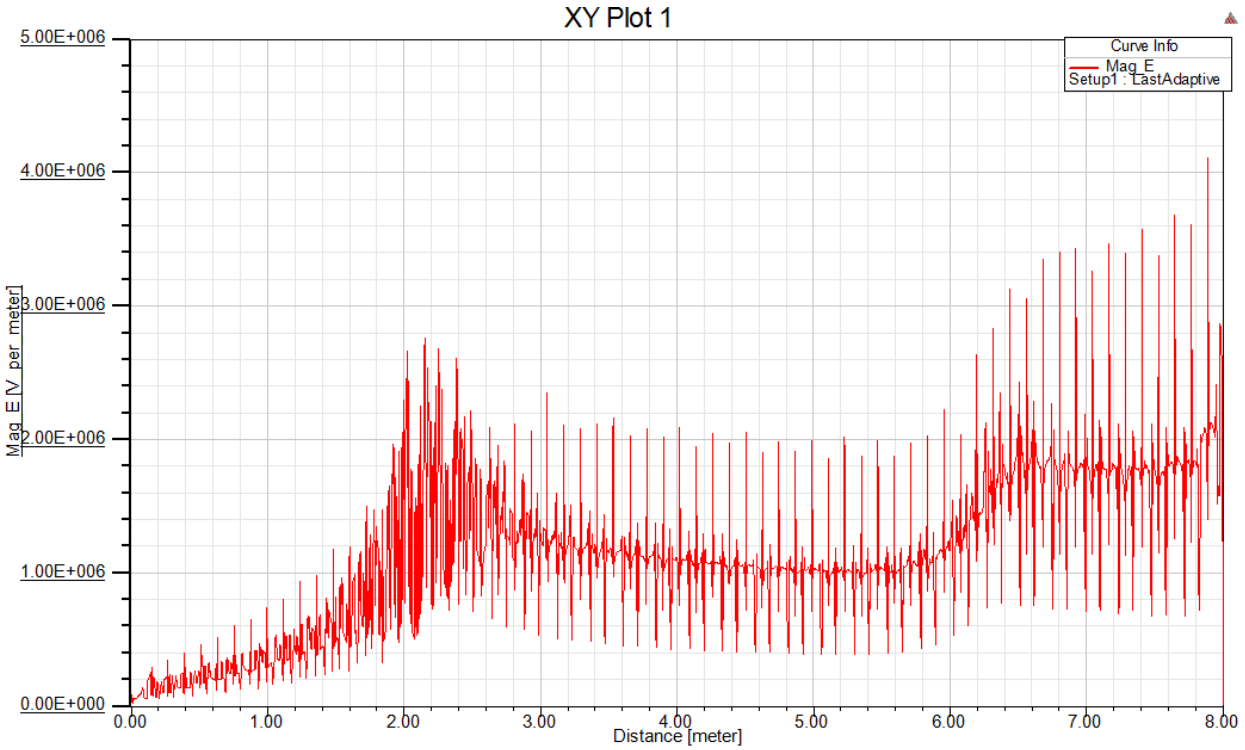


*Figure 114: E along the silicon rubber weather sheds under LIV voltage (shield structure b, measure line see Figure 14)*

Figure 113 and Figure 114 show E along the silicon rubber weather sheds under AC voltage. Even if the shield with HP reduces the $E_{max}$ of the silicon rubber weather sheds it has still negative influence on E along the silicon rubber weather sheds. From the height above the beginning of shield the values of E increase. The $E_{peak}$ of the first weather shed increases from 3.8kV/mm into 4kV/mm. The following table lists the summaries and comparisons between the original, the optimized structure without and with shield structure b.

| $E_{max}$ (kV/mm) | Original | Optimized without shield | Optimized with shield (structure b) |
|---|---|---|---|
| Conductor bar | 33.7 | 31.2 | 31.8 |
| Ground electrode | 28 | 25.8 | 26.2 |
| FRP inside | 4 | 3.2 | 4.1 |
| Top flange | 18 | 9.6 | 8 |
| Region above first weather shed | 9.4 | 4.7 | 3 |
| First weather shed end | 4.2 | 3.8 | 4 |
| Interface between the top flange and composited sheds | 7.3 | 6.7 | 3.2 |
| Shield with HP | | | 16.7 |
| Maximum potential deviation (%) | 27 | 27 | 17.2 |

*Table. 19: Summaries and comparisons between the original, optimized structure without and with shield (b)*

The shield with HP reduces the maximum potential deviation on the silicon rubber. In Table. 19 it is still worthwhile to note that the shield with HP also reduces the electric field stress on the top flange and region above first weather shed.

## 5.6 Optimal design of weather shed end

In this chapter the position of the weather shed with $E_{peak}$ will be investigated. The GA approach will be applied for the contour optimal design of a weather shed end. The assessments of optimal results will be shown and discussed.

### 5.6.1 The problematic positions of weather sheds

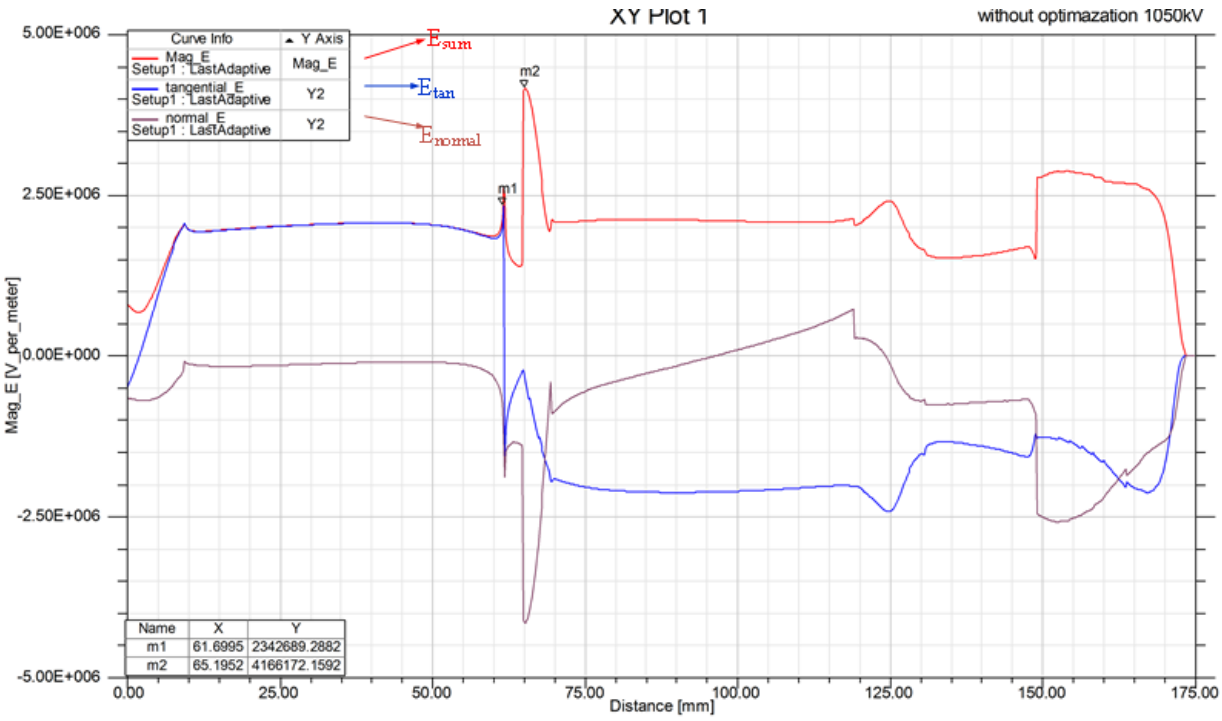


*Figure 115 :E(red), $E_{tan}$(blue) and $E_{normal}$(brown) along the first weather shed and above region*

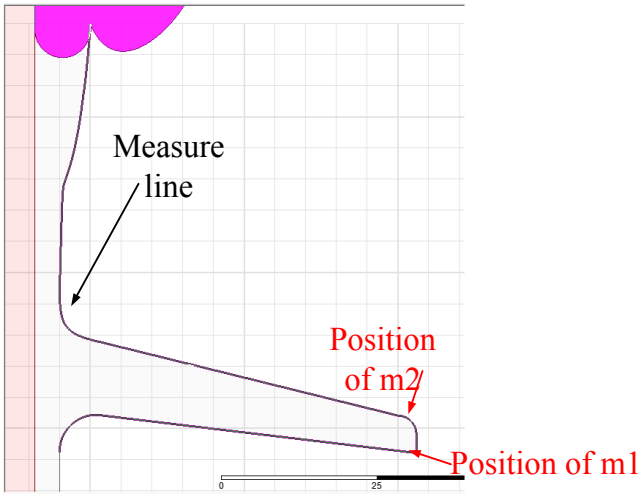


*Figure 116: The corresponding critical positions of the weather shed*

Figure 115 and Figure 116 illustrate the peak values and critical positions of the weather shed. The peak values of E concentrate on weather shed end. The uppermost attention shall be paid is the first weather shed end. The shield with HP impacts negatively on E on the weather shed end.

Compared to the previous structure, E of first weather shed end increases from 3.8kV/mm before the optimization in chapter 5.5 to 4.0kV/mm after the optimization in in chapter 5.5. Moreover, $E_{max,tangential}$ and $E_{max,normal}$ are not situated at the same position. Maximum E of weather shed end is mainly affected by the $E_{max,normal}$. For this reason, $E_{max,normal}$ has most priority in the optimization. However, $E_{max,tangential}$ should be no greater than the permissible $E_{max}$ of surface discharge on the silicon weather shed.

### 5.6.2 Optimization of weather shed end

Considering good performance of Bézier curves in the optimization of the top flange, it will continue to be adopted for the optimization of the weather shed end.

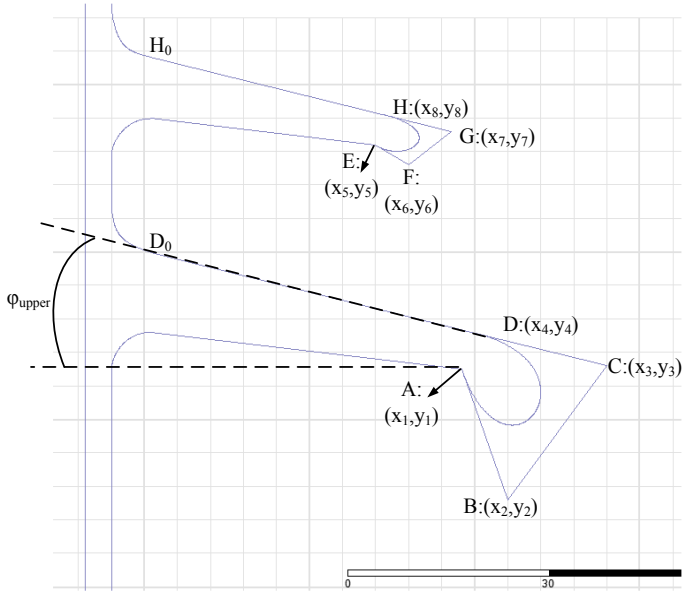


*Figure 117: New contour of the weather shed end by smooth connection of Bézier curve*

Figure 117 shows the new structure of weather shed end. It is designed by using a Bézier curve. For the long weather shed, the positions of A and D are fixed. By controlling of points B and C the contour of the weather shed end can be modified. In order to satisfy the continuity of line CD and the surface of weather shed, i.e. line $DD_0$, the coordinate of $x_3$ is defined by the following equation.

$$x_3 = \frac{y_4 - y_3}{\tan \varphi_{upper}} + x_4 \qquad \textit{Eq. 89}$$

Like the long weather shed the short weather shed is manipulated by the controlling points F and G. Points E and H are fixed. And lines $H_0H$ and HG are collinear. Due to the same procedure of optimizations for long and short weather sheds only the optimization of a long weather shed will be presented in the following.

The main task of GA is the reduction of $E_{max}$ on the surface of weather sheds. At the same time, great concerns on $E_{max,tangential}$ and $U_{max,deviation}$ should also be taken. Considering three parameters for a long weather shed the individual chromosome can be expressed as follows:

$$\text{Chromosome} = \left[ x_2, y_2, y_3 \right]$$

Based on the results from the preliminary investigation the ranges of parameters show in the following.

$$x_2 : [202mm, 210mm],\ y_2 : [290mm, 309mm],\ y_3 : [310mm, 315mm],$$

The fitness function can be formulated as follow

$$Fitness = w_1 \cdot \left| \frac{E_{\max}(x)}{1 \cdot 10^6} - E_G(x) \right| + w_2 \cdot \left| \frac{E_{\max,\tan}(x)}{1 \cdot 10^6} - E_{G,\tan}(x) \right| + w_3 \cdot \left| U_{d,\max}(x) - U_{d,G}(x) \right| \qquad \textit{Eq. 90}$$

where $E_{\max}$, $E_{\max,\tan}$, and $U_{d,\max}$ indicate the simulation values of maximum E on the surface of weather sheds, maximum tangential component of E on the surface of weather sheds and maximum potential deviation. $E_G$, $E_{G,tan}$ and $U_{d,G}$ are their own goal values. $w_1$, $w_2$, and $w_3$ represent the corresponding weighting factor respectively. The goal values can be set as follow:

$$E_G = 3.6kV/mm \quad E_{G,\tan} = 2.4kV/mm \text{ and } U_{d,G} = 17$$

Substituting weighting factors $w_1$=5, $w_2$=2 and $w_3$=2 and normalizing, the fitness function for optimization of weather shed end can be given,

$$Fitness = 5 \cdot \left| \frac{E_{A,\max}(x)}{1 \cdot 10^6} - 3.6 \right| + 2 \cdot \left| \frac{E_{B,\max}(x)}{1 \cdot 10^6} - 2.4 \right| + 2 \cdot \left| U_{d,\max}(x) - 17 \right|$$

*Eq. 91*

Under this condition, the lower fitness value is considered a better result. The population size ($N_p$) and the maximal number of iterations/generations ($G_{max}$) must be chosen. The population size ($N_p$) i.e. the number of individual chromosome in a generation is set to $N_p$=30. The number of generations ($G_{max}$) is set to 50. The fitness function evaluates each individual chromosome, and the population will be sorted in the order of better fitness. The elitism strategy preserve two best chromosomes. The mutation with rate of 30% is applied to reproduce 18 chromosomes for the next generation. The following figures depict the comparison between original and optimized structure by 2D plot E distribution and E curve along surface of the weather sheds.

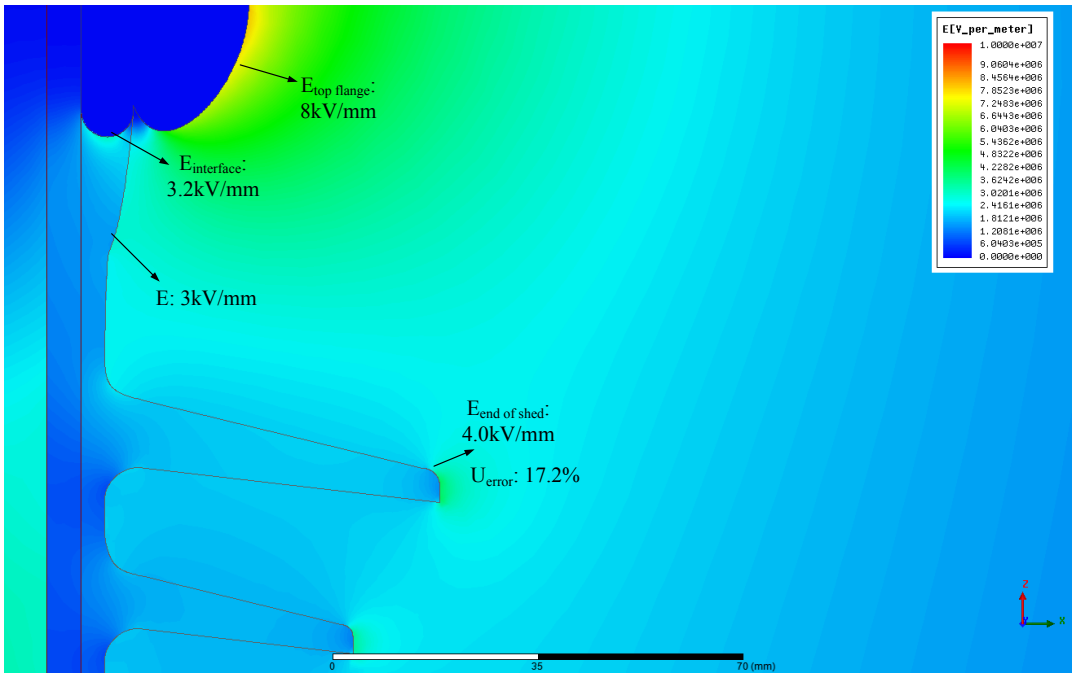


*Figure 118: 2D plot E distributions under 1050kV LIV before optimization*

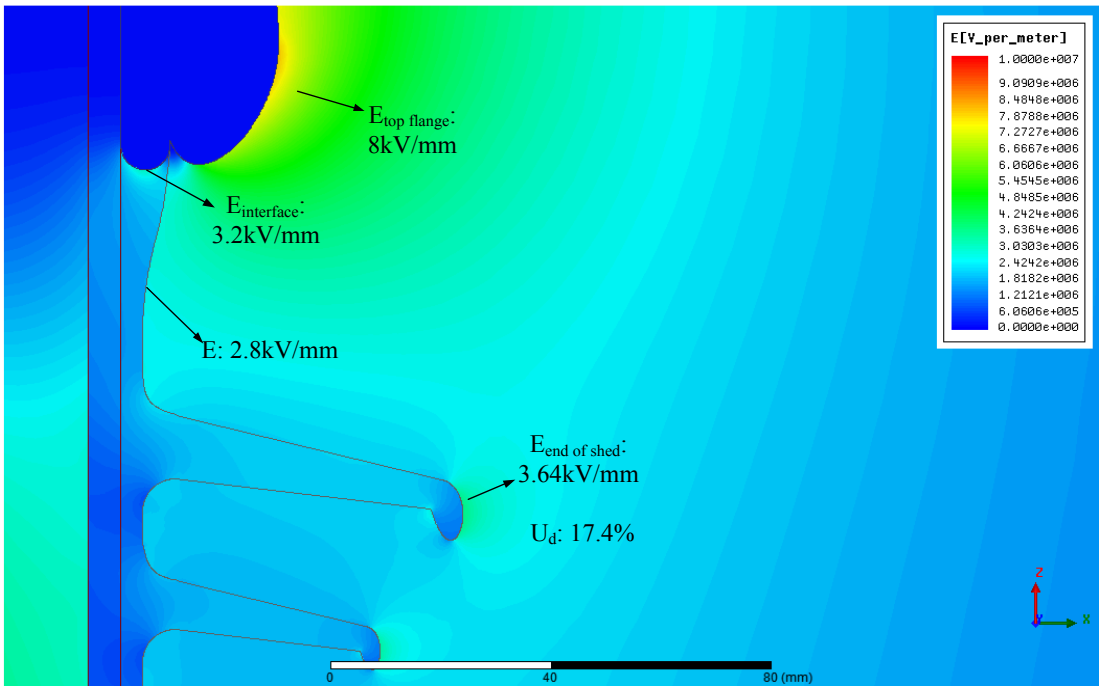


*Figure 119: 2D plot E distributions under 1050kV LIV after optimization*

In order to make a clear comparison, Figure 118 and Figure 119 are using the same color intensity. As it can be seen that after optimization $E_{max}$ of the weather shed end drops from 4.1kV/mm to 3.64kV/mm. The optimization still affects E of the region above the first weather shed positively. It decreases by 0.2kV/mm. In the meanwhile, the new structure has an negative effect on the tangential component, which increases a little comparing with previous structure. Anyway, it is less than the original result. During the optimization even better results turn up. However, the ratio of spacing versus shed overhang $\frac{s}{p}$ and minimum distance between sheds do not content with standard IEC 60815-3. [32]

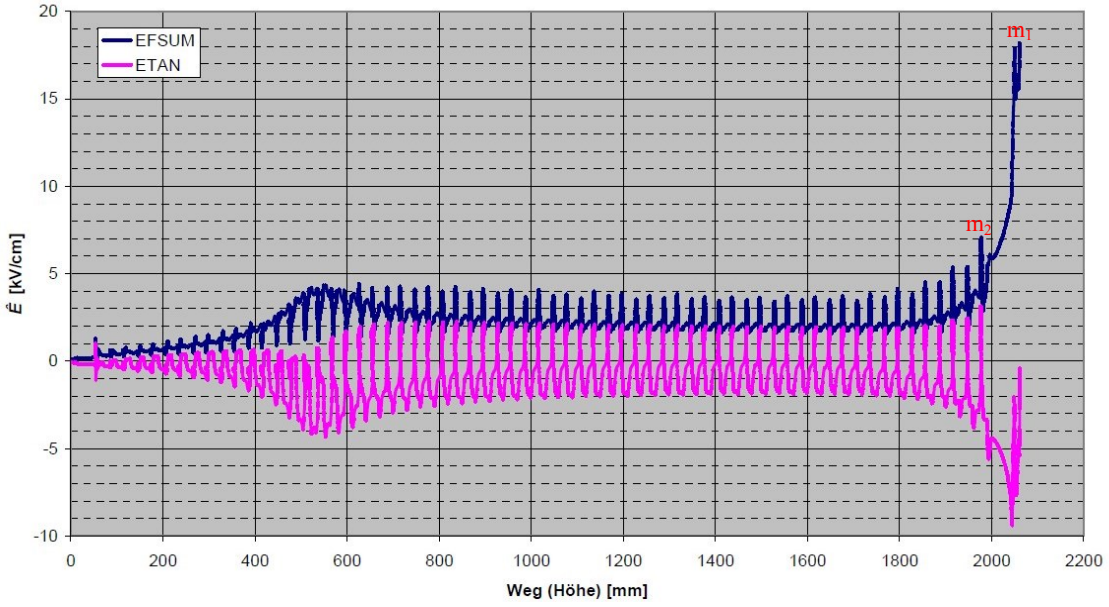


*Figure 120: E along the surface of weather sheds under* $\frac{245kV}{\sqrt{3}}$ *AC voltage (original structure, measure line see Figure 14)*

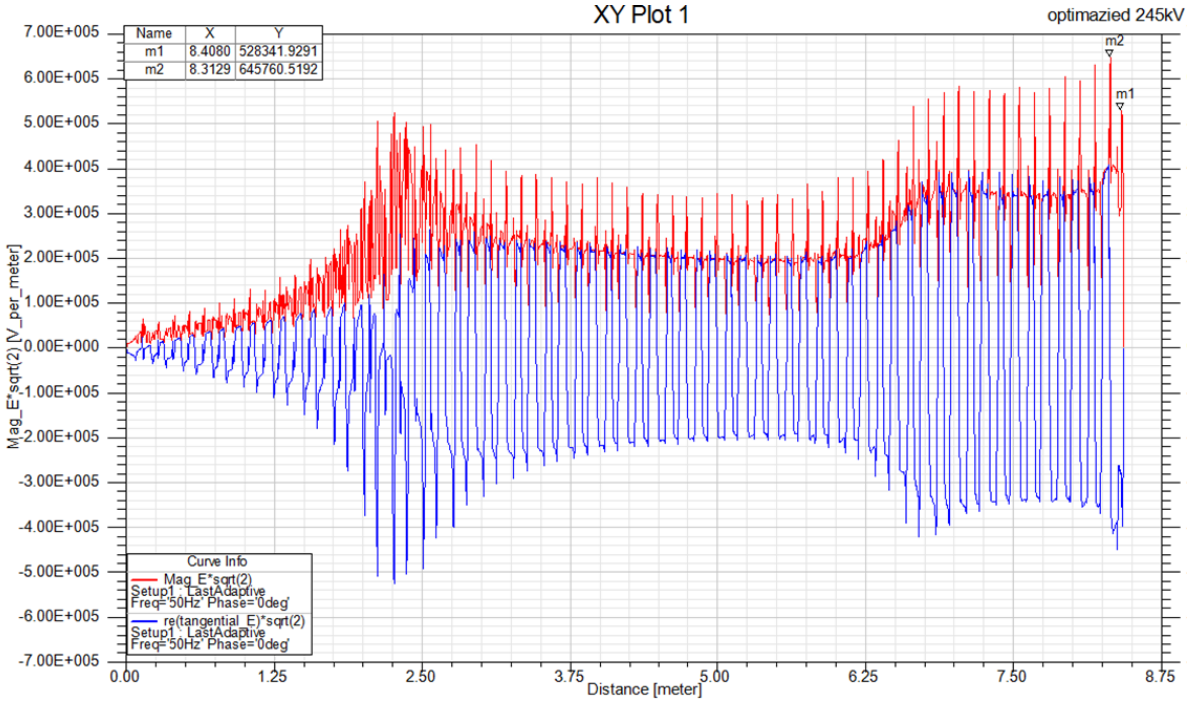


*Figure 121: E along the surface of weather sheds after optimization under* $\frac{245kV}{\sqrt{3}}$ *AC voltage (measure line see Figure 14 )*

The comparison is also made under AC voltage. Point $m_1$ locates at $E_{max}$ of the region above the first weather shed and point $m_2$ on first weather shed. Because of the optimization of top flange $E_{max}$ of the region above the first weather shed has decreased by 70% after the optimization. $E_{max}$ of first weather shed decreases from 0.71kV/mm into 0.65kV/mm. The following table lists the summaries and comparisons between the original and optimized structure under $\frac{245kV}{\sqrt{3}}$ and 1050kV.

| | Under $\frac{245kV}{\sqrt{3}}$ AC voltage | | | Under 1050kV LIV | | |
|---|---|---|---|---|---|---|
| $E_{max}$(kV/mm) | Original | Before the optimization | After the optimization | Original | Before the optimization | After the optimization |
| Region above first weather shed (RA FWS) | 1.8 | 0.54 | 0.53 | 9.4 | 3 | 2.8 |
| First weather shed (FWS) | 0.71 | 0.67 | 0.65 | 4.2 | 4.02 | 3.64 |
| Tangential component of RA FWS | 0.94 | 0.45 | 0.45 | | 2.4 | 2.4 |
| Tangential component of FWS | 0.57 | 0.39 | 0.41 | | 2.34 | 2.5 |
| Maximum potential deviation (%) | 27 | 17.3 | 17.5 | 27 | 17.2 | 17.4 |

*Table. 20: Summaries and comparisons under $\frac{245kV}{\sqrt{3}}$ AC voltage and LIV 1050kV (before and after the optimization of weather shed contour)*

## 5.7 Reduction of creepage distance

In the first part the criterion and requirements for the reduction of the creepage distance will be discussed. Afterwards the impacts on E of critical points and the maximum potential deviation by reduction of creepage distance will be investigated. Finally the creepage distance will be reduced.

### 5.7.1 Feasibility and requirements for reduction of creepage distance

Composite weather sheds present certain advantages when compared to porcelain weather sheds due to their form and materials. These advantages include a generally improved contamination withstand behavior, if we compare to equal creepage distance of porcelain weather sheds. This improvement is even more pronounced by use of high-temperature polymer electrolyte membrane (HTM). Therefore, from the contamination withstand or flashover point of view, the conclusion could be drawn that for composite weather sheds the reduction of creepage distance might be feasible. However, compared to glass or porcelain traditional insulating materials, composite weather sheds are more vulnerable to degradation by electric fields enhancement, arc activity and external environment. Standard IEC 60815-3 gives specific information on this effect, which can be concluded to following points:[32]

- Reduced creepage distance may, in certain site conditions, result in increased discharge activity and negate any advantage in contamination performance if hydrophobicity is totally lost, and may lead to flashover or degradation.
- Conversely, risk of material changes or degradation due to localized arc activity may be increased when creepage distance per unit length is excessively large.

Other points of importance are as follows:

- More pollution may accumulate on surfaces of composite sheds, and may reduce their contamination performance advantage.
- Some polymers could be subject to fungal growths which affect hydrophobicity.

Therefore, according to the considerations from standard IEC 60815 in many cases it could be proposed to accept improved pollution performance and avoid degradation or flashover problems by using the same creepage distance as recommended for porcelain weather sheds. Consequently, in our case, the creepage distance in new structure should be no less than in original structure.

### 5.7.2 Impact on E of critical points and maximum potential deviation by reduction of creepage distance

Bushings with different creepage distance will be modeled to investigate whether the reduction of creepage distance has an effect on electric field strength of critical points and maximum potential deviation.

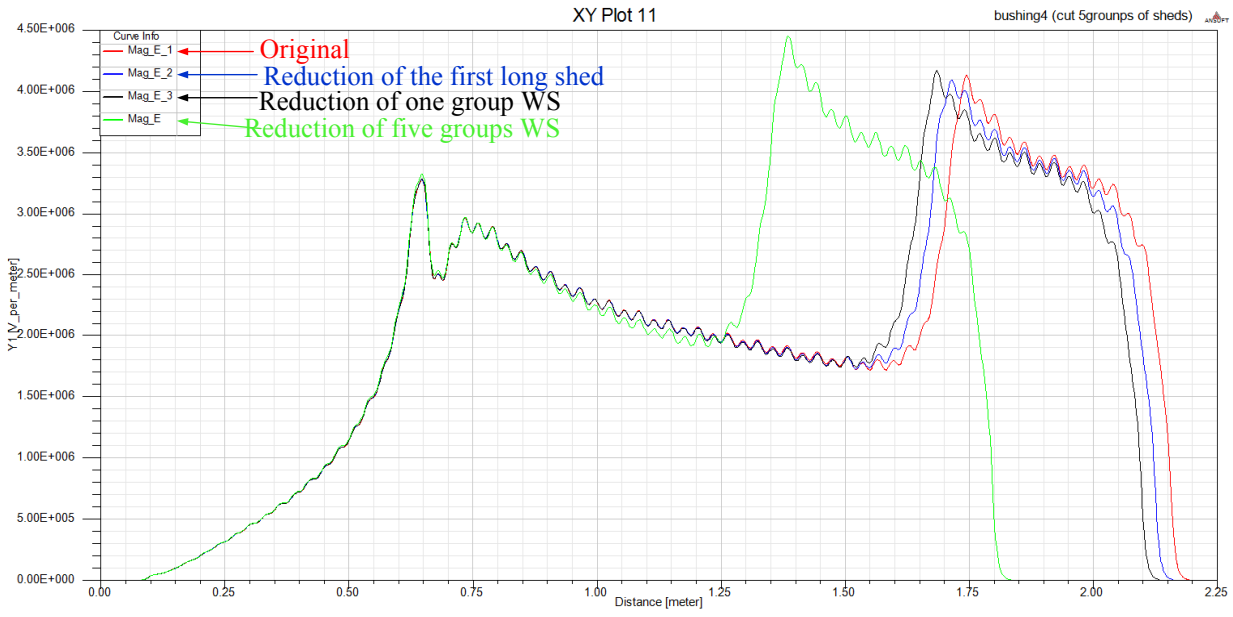


*Figure 122: E along the FRP inside in bushings with different creepage distances (measure line see Figure 11)*

In order to make a clear comparison, four bushings with different creepage distances, i.e. original, reduction of first long weather shed(WS), reduction of a group of WS and reduction of five groups of WS, are constructed. Figure 122 shows E along the inside of FRP tube with different creepage distances. From the figure the reduction of creepage distances has no perceptible

impacts on E along the inside of FRP tube. Even when five groups of WS were eliminated the maximum $E_{FRP}$ increases from 4.1kV/mm to 4.5kV/mm.

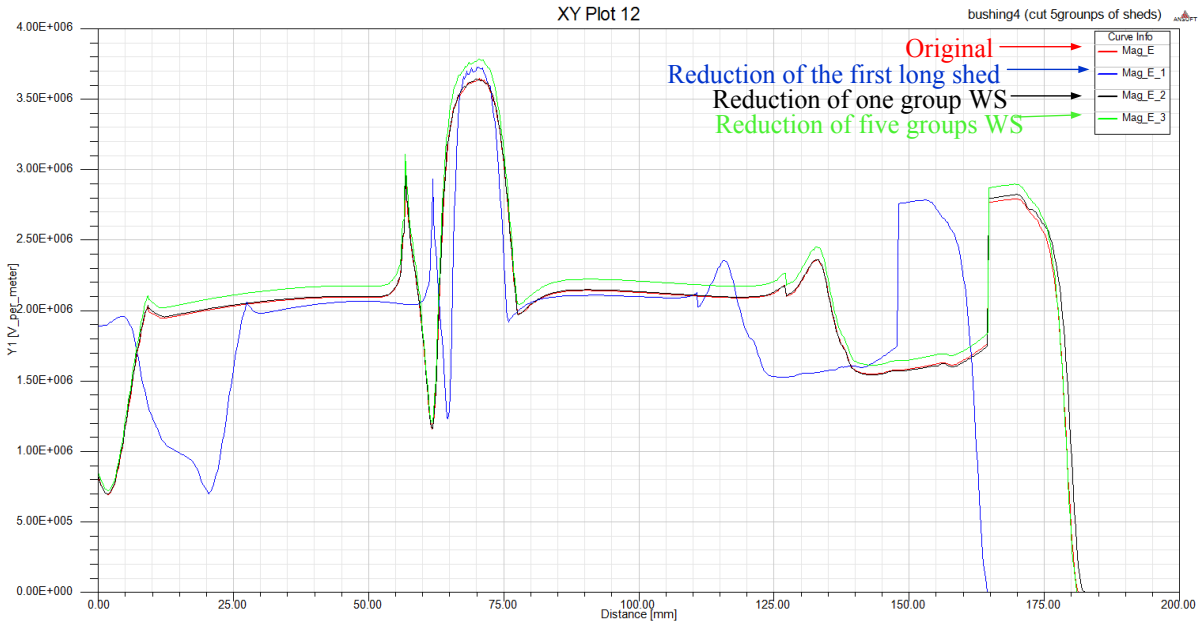


*Figure 123: E along first WS with different creepage distances (measure line see Figure 116)*

Figure 123 shows E along the first WS with different creepage distances. The situation of E along the first WS is similar to E along the inside of FRP in Figure 122. With the reduction of creepage distances $E_{max}$ along the WS increases slightly. The following table summarizes $E_{max}$ on the critical points and maximum $U_{dev}$ under different creepage distances. The conclusion can be drawn that the reduction of creepage distances has no significant influence on the electric field strength and the potential deviation.

| Creepage distance (mm) / $E_{max}$ (kV/mm) | Original | Reduction of the first long WS | Reduction of one group WS | Reduction of five groups WS |
|---|---|---|---|---|
| | 7993 | 8278 | 8168 | 6893 |
| FRP | 4.13 | 4.1 | 4.16 | 4.45 |
| WS | 3.64 | 3.72 | 3.65 | 3.78 |
| Top flange | 8.1 | 8.11 | 8.13 | 8.38 |
| Shield | 16.9 | 17 | 17.1 | 18.6 |
| Conductor bar | 31.5 | 31.8 | 31.3 | 31.7 |
| Ground electrode | 25.9 | 26 | 26.2 | 26.1 |
| Max potential deviation (%) | 17.5 | 17.2 | 17.5 | 17.8 |

*Table. 21: Summaries of $E_{max}$ on critical points and maximum $U_{dev}$ under different creepage distances*

### 5.7.3 Reduction of creepage distance

From sections 5.7.1 and 5.7.2 it is known that the reduction of creepage distances has no obvious influence on the electric field strength and potential deviation. However, taking into account IEC 60815-3 and the contamination performance and avoiding degradation or flashover problems the same creepage distance as recommended for porcelain WS is advisable. Due to the optimization

of weather shed profiles, the creepage distance in optimized bushing is larger than the original one. Therefore, the reduction of creepage distance is based on the optimized structure. However, the creepage distance cannot be reduced greatly. The new creepage distance should be no less than the original creepage distance. First of all, for reduction of creepage distance the unified specific creepage distance (USCD) of the original bushing can be determined as follow:

$$USCD_{original} = \frac{Total\ creepage\ distance}{U_{rms}} = \frac{7993.47mm}{141.45kV} = 56.51mm/kV$$

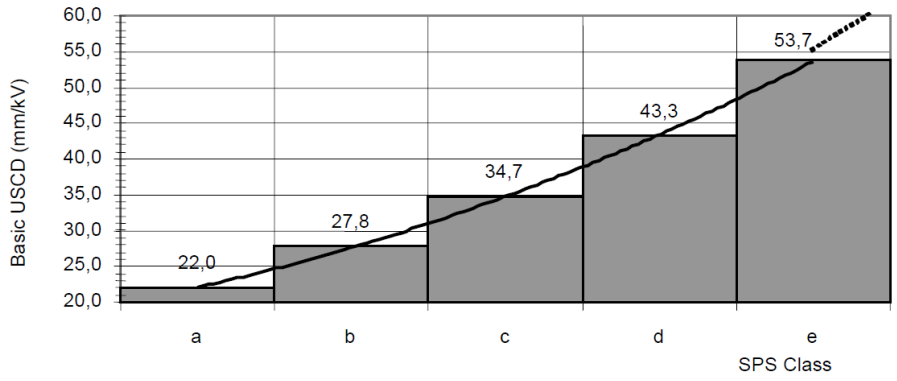


*Figure 124: Relationship between class of site pollution severity (SPS) and USCD[32]]*

Figure 124 shows the relation between USCD and SPS class for composite weather sheds. For the purposes of standardization, five classes of contamination characterizing the site severity are defined in Figure 124, from very light pollution class a to very heavy pollution class e. The bars are preferred values representative of a minimum requirement for each class. Obviously, the considered $USCD_{original}$ is located at the SPS class e very heavy pollution. In the following bushings with different creepage distance are calculated.

| | Creepage distance (mm) | USCD (mm/kV) |
|---|---|---|
| Original structure | 7993 | 56.5 |
| Optimized structure | 8423 | 59.5 |
| Reduction of the first long WS | 8278 | 58.5 |
| Reduction of one group WS | 8168 | 57.7 |
| Reduction of two groups WS | 7912 | 55.9 |
| Reduction of five groups WS | 6893 | 48.7 |

*Table. 22: Creepage distance and USCD in different bushings*

It is shown in the Table. 22 that only the bushing with reduction by one group WS fulfills the requirements. Even though USCD of bushing with reduction by two groups WS is larger than the standard value of SPS E (53.7mm/kV), but it is smaller than the value of $USCD_{original}$. The bushing with reduction by one group WS is chosen to be new structure.

## 5.8 Summary

In chapter 5 the structure of the $SF_6$ bushing was optimized by genetic algorithm (GA). In the section 5.1.7 by GA the structures of variant.1, 2, and 7 $E_{max}$ of conductor bar and surface of ground electrode decrease greatly, $E_{max}$ of conductor bar concentrates on about 26-27kV/mm and $E_{max}$ of surface of ground electrode fluctuates from 19kV/mm to 26kV/mm. The further optimizations in 5.2 were based on the optimized structures variant.1, 2, and 7. Three methods were applied in this section. The FRP diameters of variant.1C and 7C have been successfully

reduced from 149mm into approx. 135mm. The electrical field strength on the critical points before and after optimization are shown in the Figure 125 and Figure 126. Afterwards the multi-Bézier curve was applied for the design of top flange. By the application of Bézier curve the position of the protrusion in Figure 75 ($E_{position\ B}$) was totally avoided. In the meanwhile the $E_{max}$ on the top flange has decreased from 18kV/mm to 9.6kV/mm. The triple point between air, metal and silicone rubber was shielded. The E of triple point has dropped to a very low value. (See Figure 127 and Figure 128) Then, in the section 5.4 the region between the top flange and first weather shed was optimized. A new curve i.e. cubic natural spline was applied for the design. By the GA $E_{max}$ of region above first weather shed has dropped from 9.4kV/mm into 4.7kV/mm. In order to make the potential distribution on the surface of insulator, a new component shield with high potential was designed and optimized by GA. The shield with HP has reduced the maximum potential deviation on the silicon rubber from approx.27% into 17%. (See from Figure 108 to Figure 111, Figure 129 and Table. 19) And it was still worthwhile to note that the shield with HP also had positive effect on the electric field strength on the top flange and region above first weather shed. With the effect of shield with HP $E_{max}$ on the top flange has decreased from 9.6kV/mm to 8.1kV/mm and $E_{max}$ of region above first weather shed has dropped from 4.7kV/mm into 2.8kV/mm. Based on the multi-Bézier curve, the weather shed end has been optimized. $E_{max}$ of first weather shed end has decreased from 0.71kV/mm into 0.65kV/mm under operation voltage. In the last section 5.7 according to the standard IEC 60815-3 the creepage distance was reduced.

Generally, the optimized results show that the combinations of GA and Bézier curve and cubic natural spline can dramatically improve the structure of a SF6 bushing. The $E_{max}$ on the critical points and maximum potential deviation along the silicon rubber sheds obtained by the proposed GA are smaller than the original values. Thus, the effectiveness of the proposed GA for the optimization of SF6 bushings can be validated. However, the optimal structure yields to a little negative influence on the electric field strength of glass fiber tube (FRP) inside. $E_{max}$ of FRP inside closing to ground electrode increases a lot. On the one hand, the expanding of radius of ground electrode makes the periphery of ground electrode close to FRP, which causes the negative influence on the FRP. On another hand, it depends on the strategy of optimization, i.e. weighting factor of genetic algorithms. Based on the criteria in 2.2 it could be acceptable that the electric field strength increases a lot compared with its original value. The final summaries and comparison between the original structure and optimized structure are shown in the figures and tables. The detail dimensions of optimized structures are attached in appendix (Chapter 10). The

following figures summary the electrical field strength on the critical points before and after optimizations.

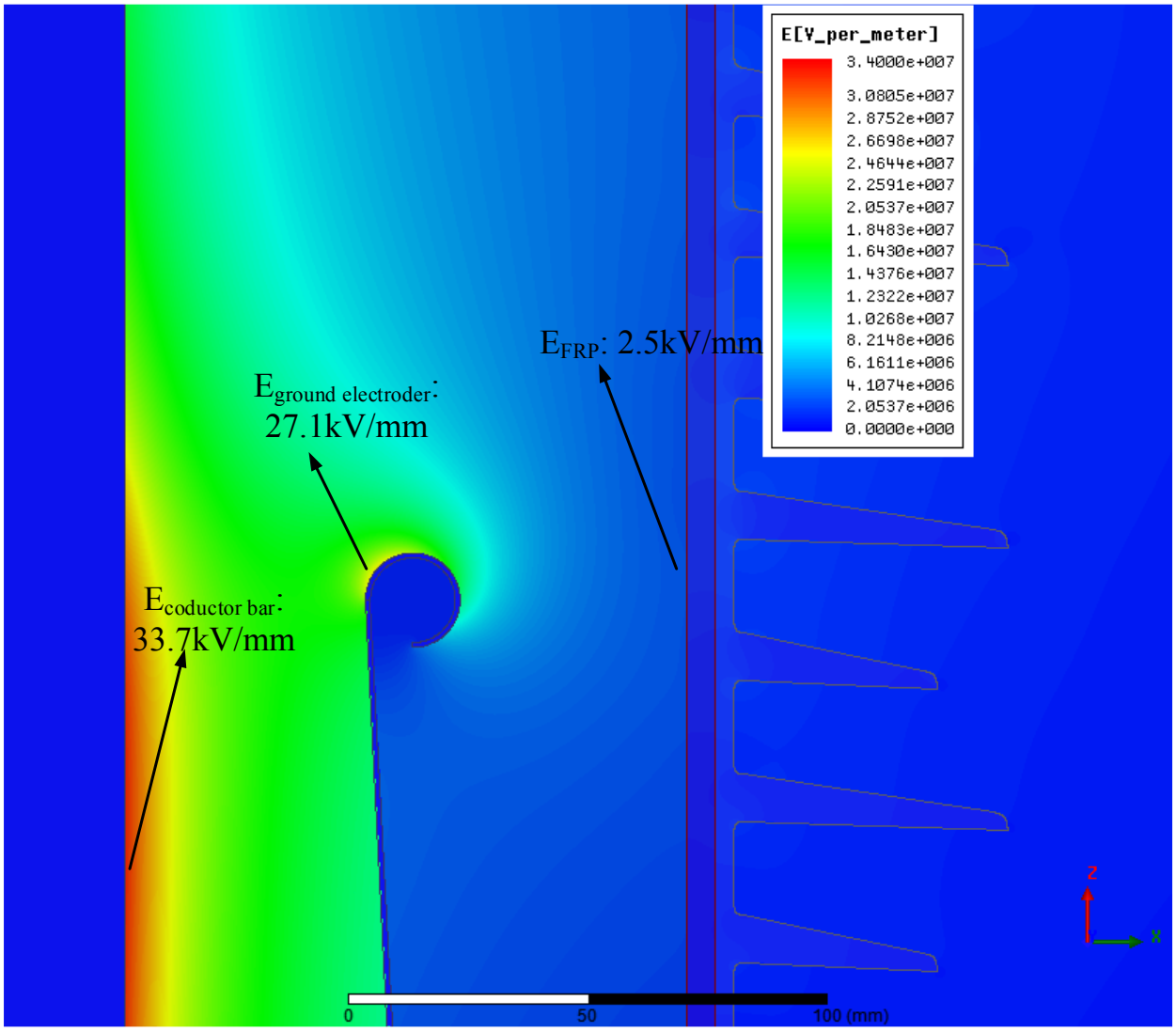


*Figure 125: Critical positions in the vicinity of ground electrode before the optimizations*

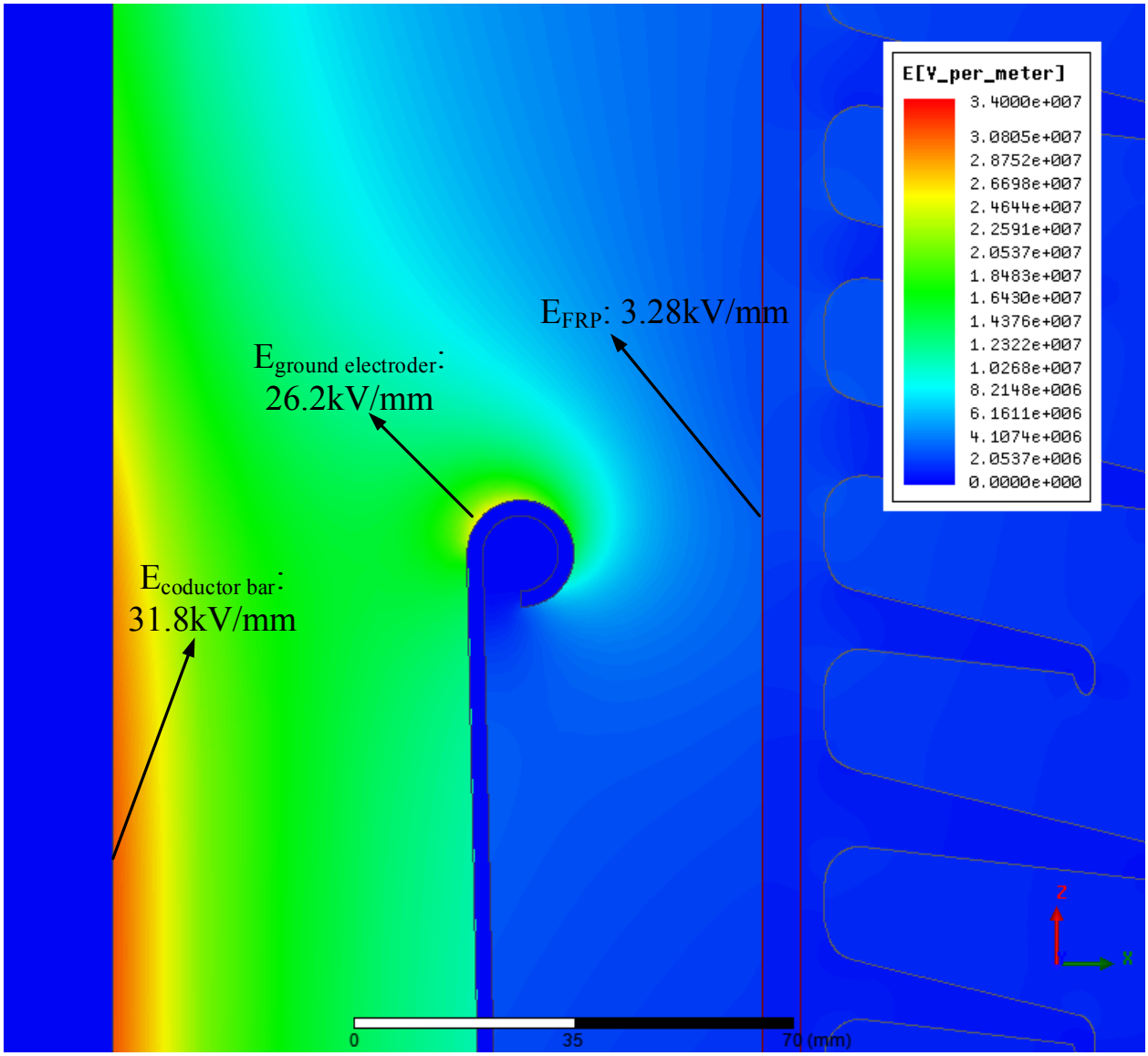


*Figure 126: Critical positions in the vicinity of ground electrode after the optimizations*

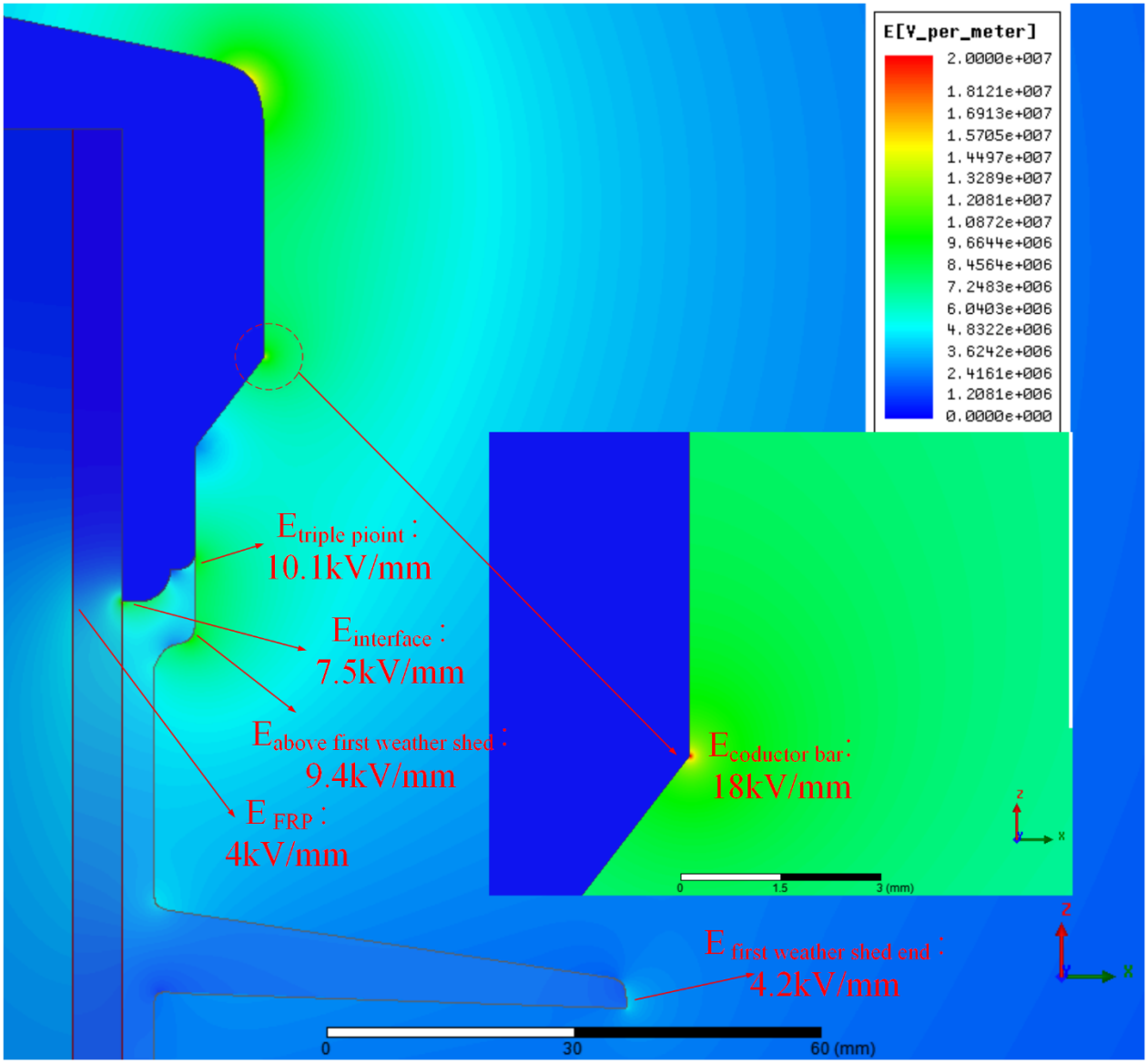


*Figure 127: Critical positions in the vicinity of top flange before the optimizations*

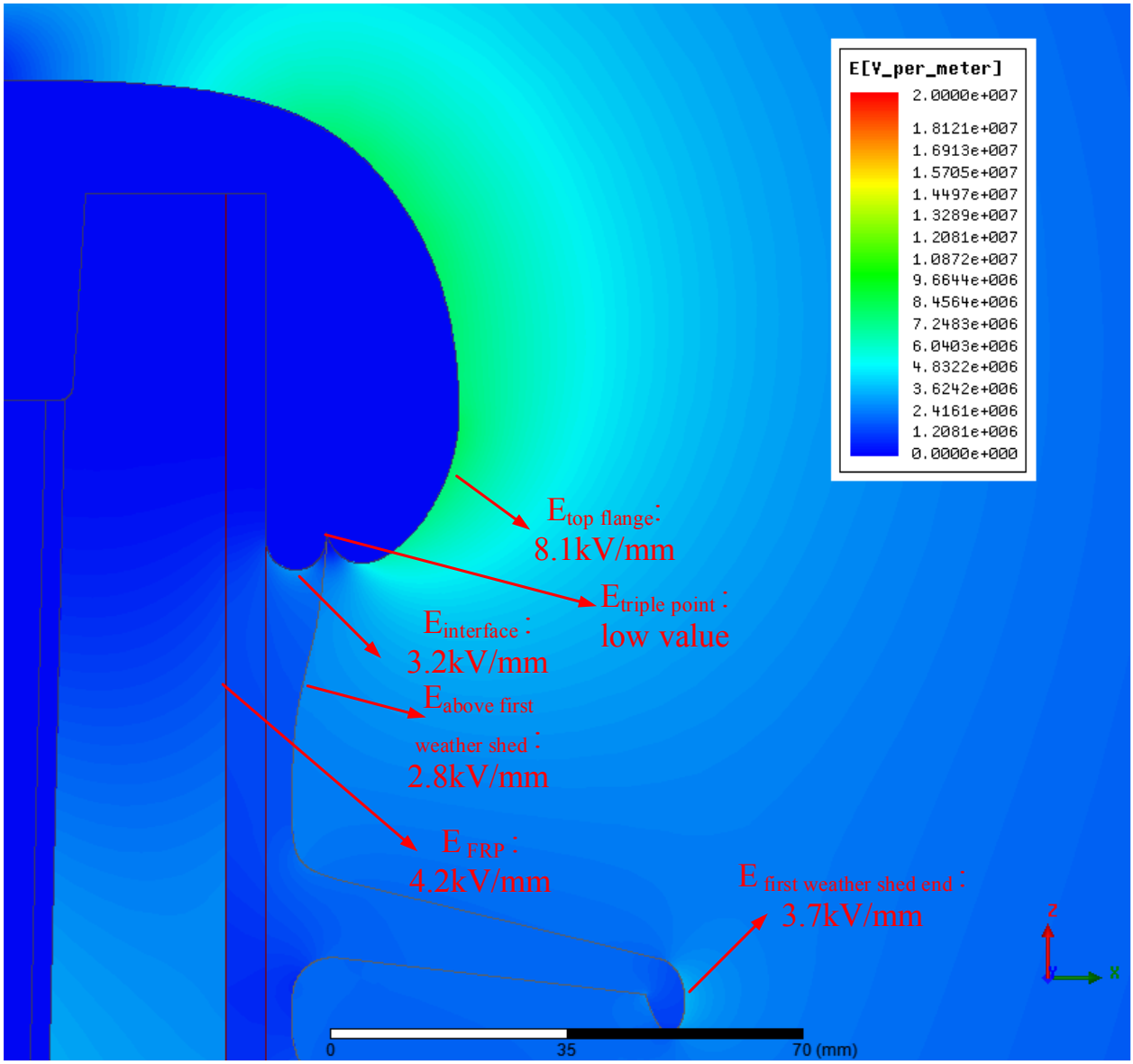


*Figure 128: Critical positions in the vicinity of top flange after the optimizations*

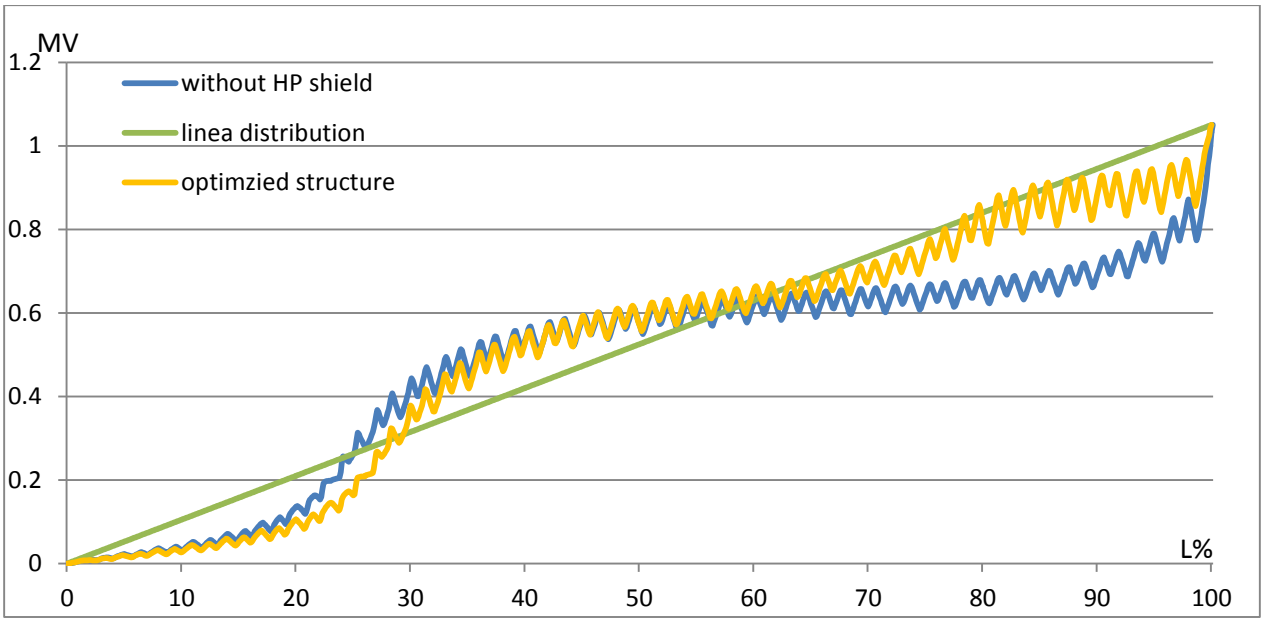


*Figure 129: Comparison of potential distribution along the silicon rubber weather sheds between linear, before and after optimizations*

# 6 Conclusions and further work

## 6.1 Conclusions

From the theoretical aspect the break-down mechanisms of a $SF_6$ bushing can be explained by three theories. The break-down between the conductor bar and ground electrode can be interpreted by the α process and streamer theory. The $E_{peak}$ at top flange mainly depends on the design of top flange periphery and triple points between the air, top flange and silicon rubber insulator. Flash-over along the surface of the silicon rubber insulator was discussed in 3.3. It attributes to the non-uniform potential distribution along the surface of silicon rubber insulator.

From the practical aspect the electrical characteristics of $SF_6$ bushings mainly depends upon the contour designs. In the optimization the bushing is separated into several components. The contours of every component are re-designed and optimized by the proposed genetic algorithm with preliminary investigation. The objective of preliminary investigation is to decide proper ranges and initial values for the chromosomes and accelerate the process of optimization. By combing the preliminary investigation, the genetic algorithm has been proven to enhance significantly the efficiency of the optimization. The results in chapter 5 and following table show that the electric field strength on critical points and the potential deviation along the silicon rubber sheds of optimized bushing decrease greatly compared with an original bushing. However, the optimal design yields to a little negative influence on the electric field strength along the fiber reinforced plastic (FRP) tube inside. (See first and second line of Table. 23) Besides that, compared with original dimensions the height, the diameter and volume of the optimized structure is reduced by 3%, 10% and 20% respectively. (See Table. 24 and Figure 130) Therefore, by the optimization it is possible to design a bushing with less weight, smaller dimension and more compactness. The optimal design has high probabilities to be free from partial discharges and flashovers. Furthermore, from the comparisons of $E_{max}$ on the critical points between the original and optimal design the genetic algorithm is proven to be effective in optimizing different materials and components of $SF_6$ bushing.

| $E_{max}$ (kV/mm) / Positions | Original (assumed) | Optimized | Percentages change (%) |
|---|---|---|---|
| Inside of fiber-reinforced plastic (FRP) | 4 | 4.16 | +4 |
| FRP inside (close to ground electrode) | 2.5 | 3.28 | +31.2 |
| Above first weather shed | 9.4 | 2.8 | -70.2 |
| End of first weather shed | 4.2 | 3.65 | -13 |
| Top flange | 18 | 8.13 | -54.1 |
| Shield at top flange | | 17.1 | |
| Conductor bar | 33.7 | 31.3 | -7.1 |
| Ground electrode | 27.1 | 26.2 | -3.3 |
| Max potential deviation (%) | 27 | 17.5 | -35.2 |

*Table. 23: Comparison of $E_{max}$ on the critical points between the original and optimal design under LIV 1050kV*

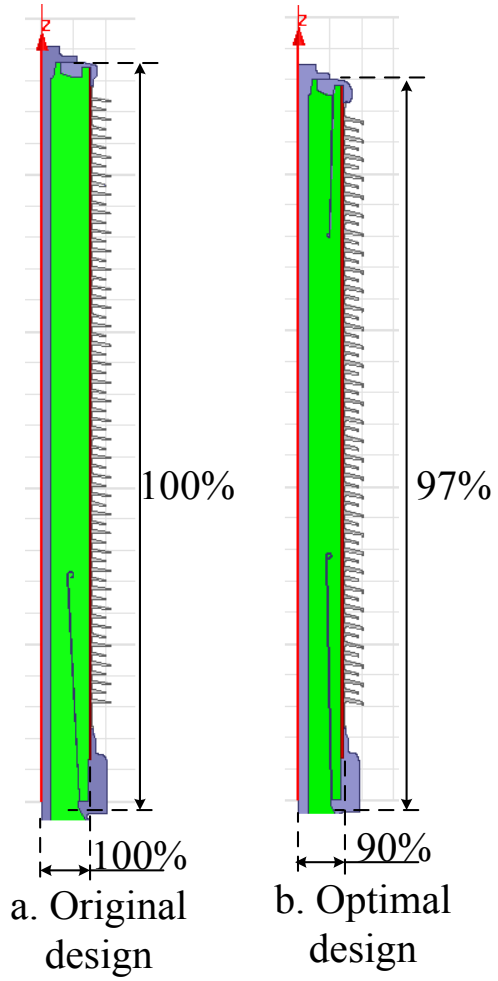


*Figure 130: Comparison of original and optimal design*

| | Height (%) | Diameter (%) | Volume (%) |
|---|---|---|---|
| Original | 100 | 100 | 100 |
| Optimal | 97 | 90 | 79 |

*Table. 24: Comparison of original and optimal design*

## 6.2 Recommendations for further work

From the optimal results of a $SF_6$ bushing the great advantages by using genetic algorithm and finite element method (FEM) are demonstrated. Apparently, it can be applied to optimize the contour of other electrical power apparatuses. Other optimization methods and simulation methods are not included in the discussion.

For the further research the following areas are worthy of being recommended:

- The other optimizations e.g. Quasi-Newton, artificial neural network (ANN) etc. or other simulation methods e.g. finite integration technique (FIT), charge simulation method (CSM), can be considered to optimize the contour design.
- Considering the structure of the ground electrode variant.9 (see 5.1.5) 3D simulation can also be applied to improve the accuracy of simulation results.
- Improve the performance of $SF_6$ bushing by the investigations of material characteristics e.g. conductivity, dielectric constant, micro-fillers in silicon rubber sheds etc. or of coating material e.g. nonlinear resistive coating.
- To validate the optimal contour design by type tests.
- Apply the genetic algorithm for the contour optimization of other electrical apparatuses

# 7 List of figures

# 8 List of tables

# 9 List of abbreviations

| | |
|---|---|
| SF6 | Sulfur hexafluoride |
| WS | Weather sheds |
| RA FWS | Region above first weather shed |
| FRP | fiber-reinforced plastic |
| RTV | Room temperature vulcanized |
| HTV | High temperature vulcanized |
| HTM | High temperature polymer electrolyte membrane |
| LSR | Liquid silicone rubbers |
| LMW | Low molecular weight |
| ANN | Artificial neutral network |
| CSM | Charge simulation method |
| CAD | Computer aided design |
| AC | Alternating current |
| LIV | Lightning impulse voltage |
| AM | Ansoft Maxwell |
| FEM | Finite element method |
| FIT | Finite integration technique |
| E | Electric field strength |
| $E_{peak}$ | Peak value of electric field strength |

| | |
|---|---|
| $E_{max}$ | Maximum value of electric field strength |
| $E_{tan}$ | Tangential component of electric field strength |
| $E_{tan,\ max}$ | Maximum tangential component of electric field strength |
| $E_{normal}$ | Normal component of electric field strength |
| GA | Genetic algorithm |
| $N_p$ | The population size of genetic algorithm |
| $G_{max}$ | Maximum iterations/generations of genetic algorithm |
| $E_{max,\ FRPG}$ | Maximum electric field strength at the inside of fiber-reinforced plastic tube close to the ground electrode |
| $E_{tangential,\ FRPG}$ | Absolute tangential component of $E_{max,\ FRPG}$ |
| HP | High potential |
| $U_{dev}$ | Potential deviation |
| USCD | Unified specific creepage distance |
| SPS | Site pollution severity |

# 10 Appendix

## 10.1 Specification of optimized ground electrode (V.1C)

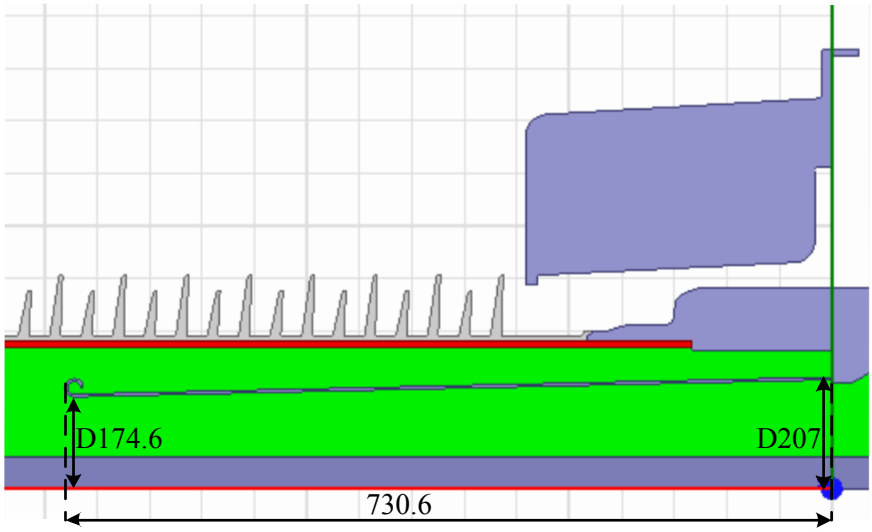


*Figure 131: Dimension drawing of variant.1C (mm)*

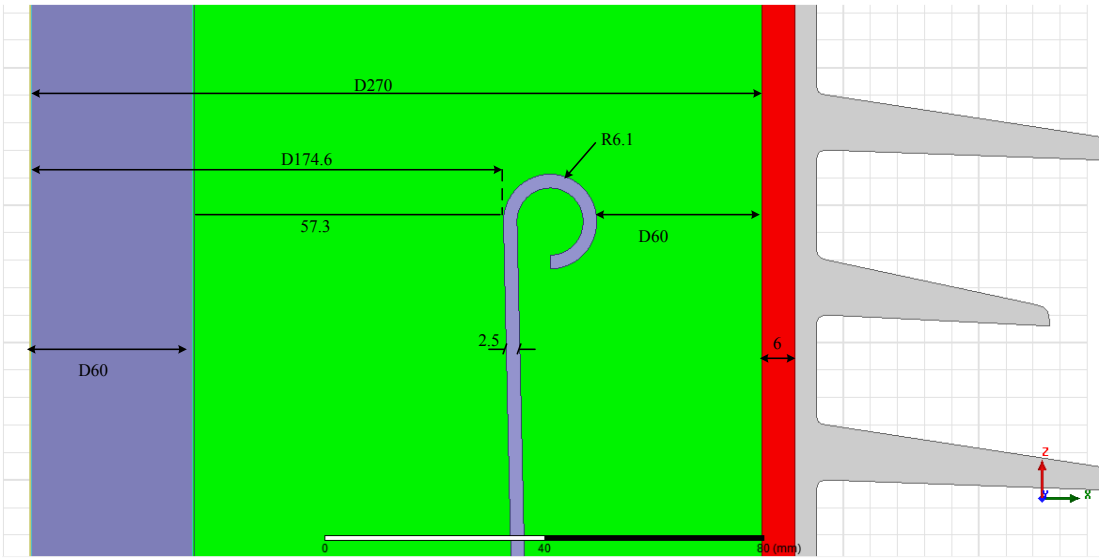


*Figure 132: Dimension drawing of variant.1C (detail with enlarged scale, mm)*

## 10.2 Specification of optimized top flange

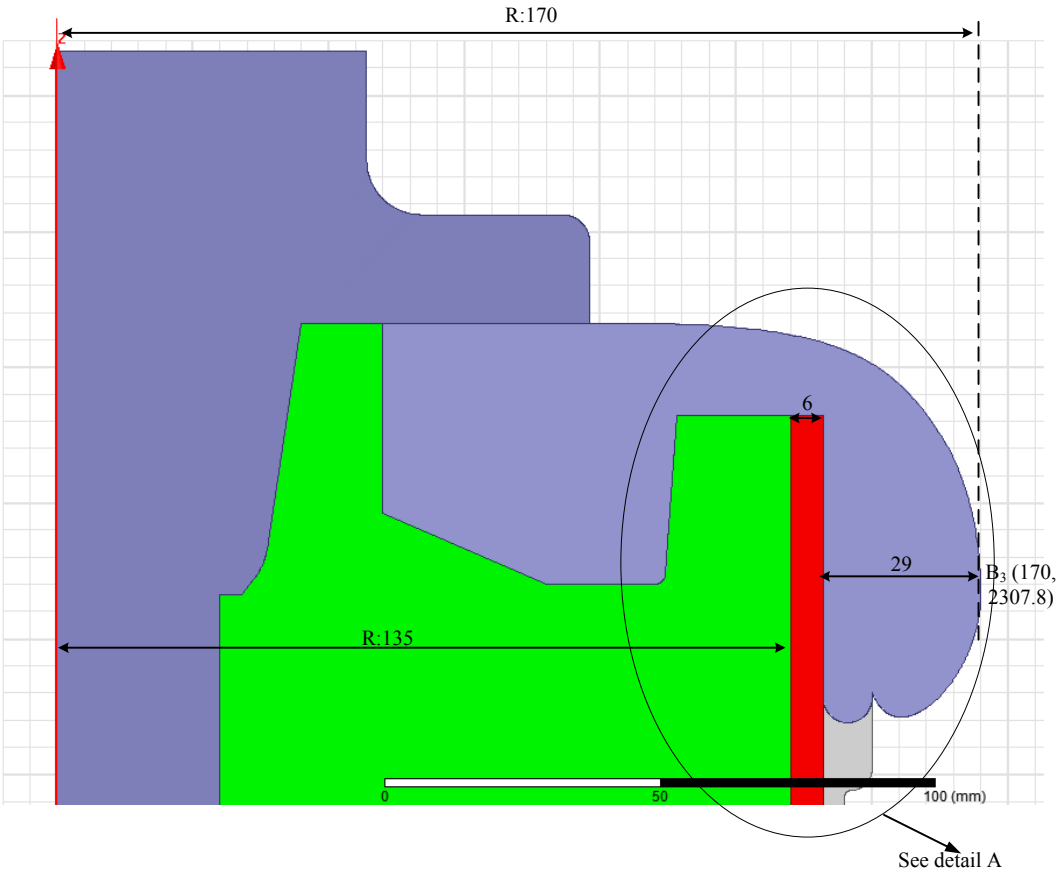


*Figure 133: Dimension drawing of optimized top flange (mm)*

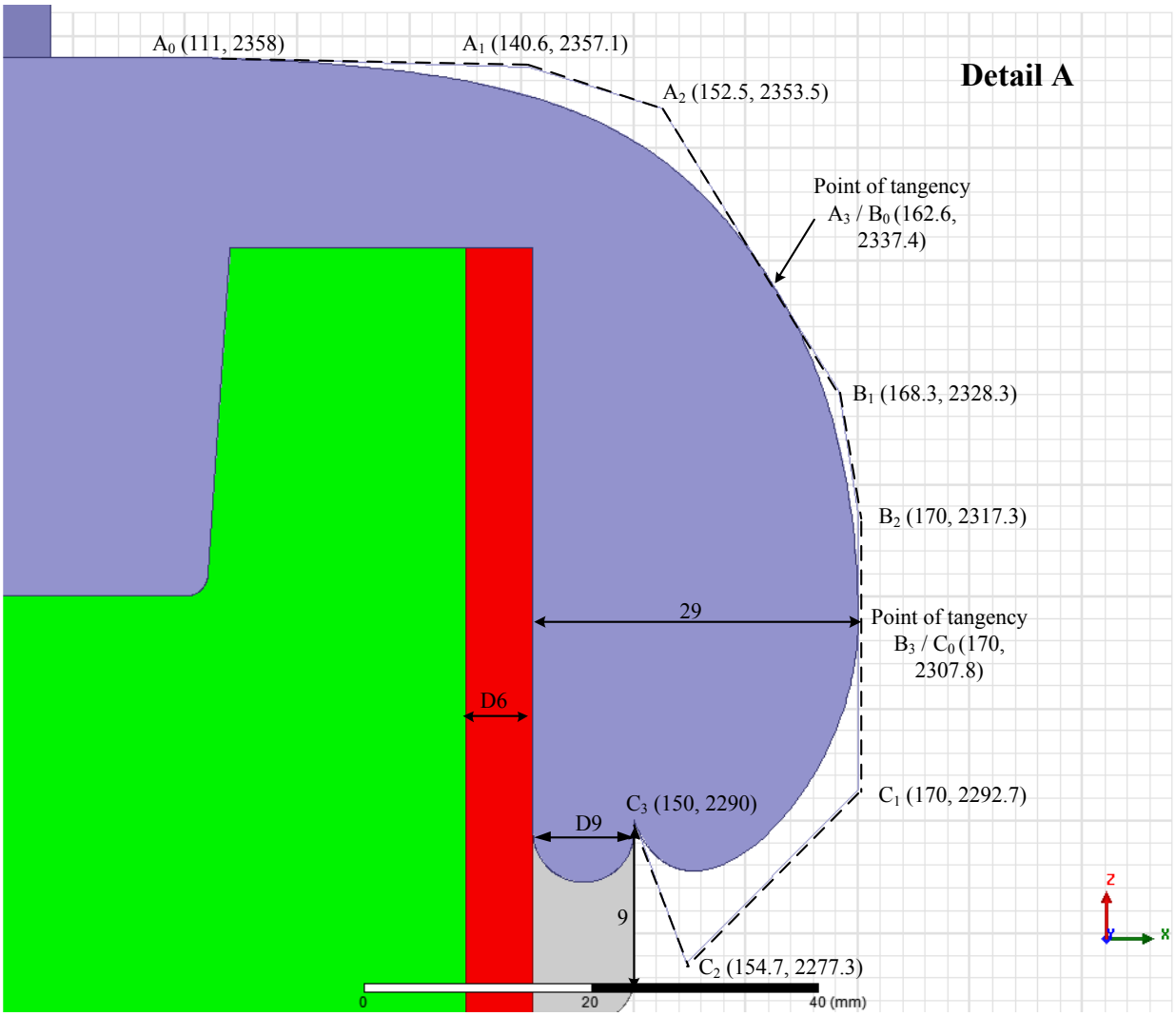


(a)

*Figure 134: Dimension drawing of optimized top flange (detail A, mm)*

## 10.3 Specification of optimized structure of region above first weather shed

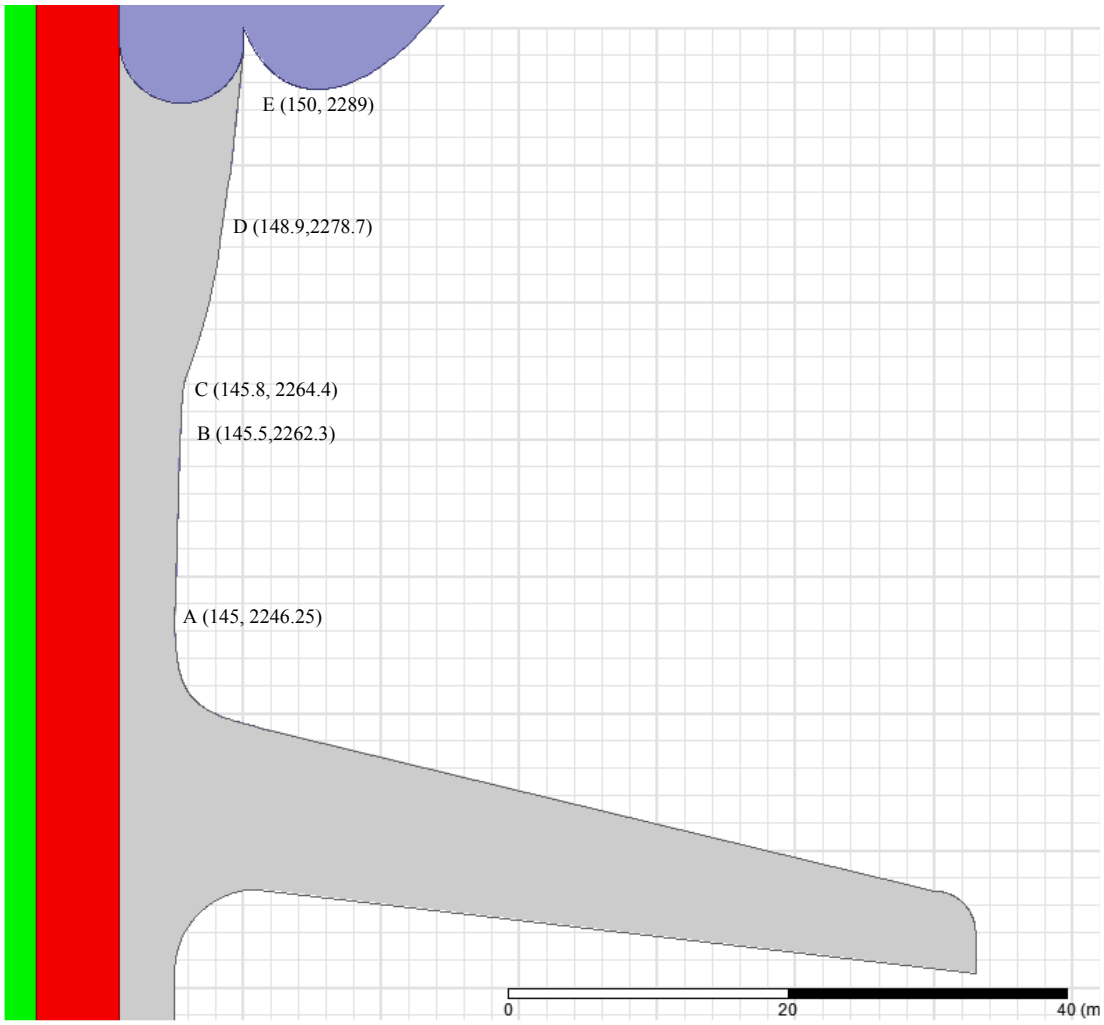


*Figure 135: Dimension drawing of optimized region above first weather shed (mm)*

$$S(x)=\begin{cases} -31.375x^3+13648.125x^2-1978938.18125x+95647063.78125 & x\in[145,145.5] \\ 52.29167x^3-22872.375x^2+3334794.56874987x-162068974.593744 & x\in[145.5,145.8] \\ 0.182439828641714x^3-79.7991810478856x^2+11637.5802532543x-563599.95891729 & x\in[145.8,148.9] \\ -1.51358463236493x^3+681.113084564219x^2-102155.767610864x+5108957.87316632 & x\in[148.9,150] \end{cases}$$

## 10.4 Specification of optimized structure of shield with HP

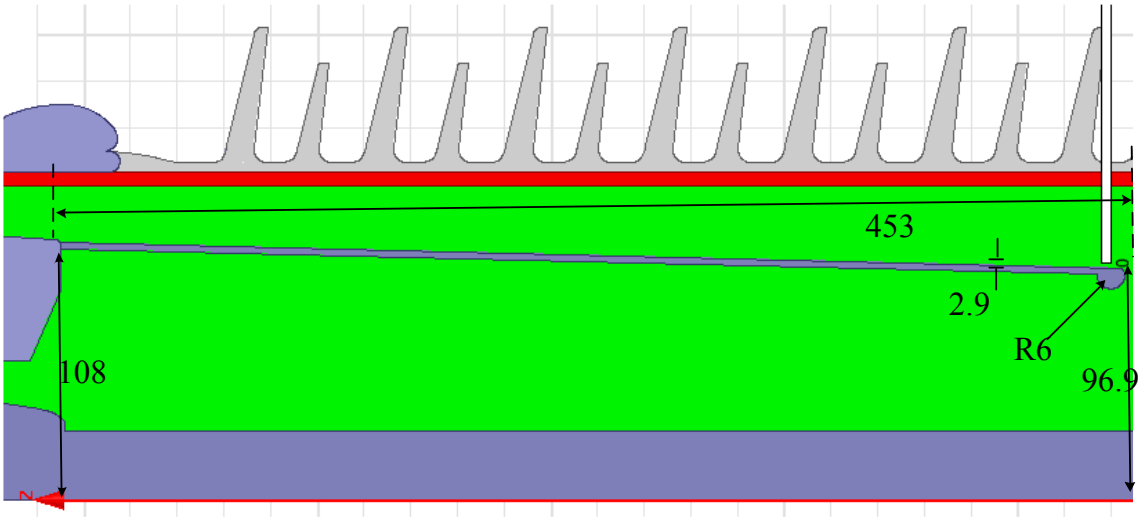


(b)

*Figure 136: Dimension drawing of optimized shield with HP (structure b, mm)*

## 10.5 Specification of optimized weather sheds

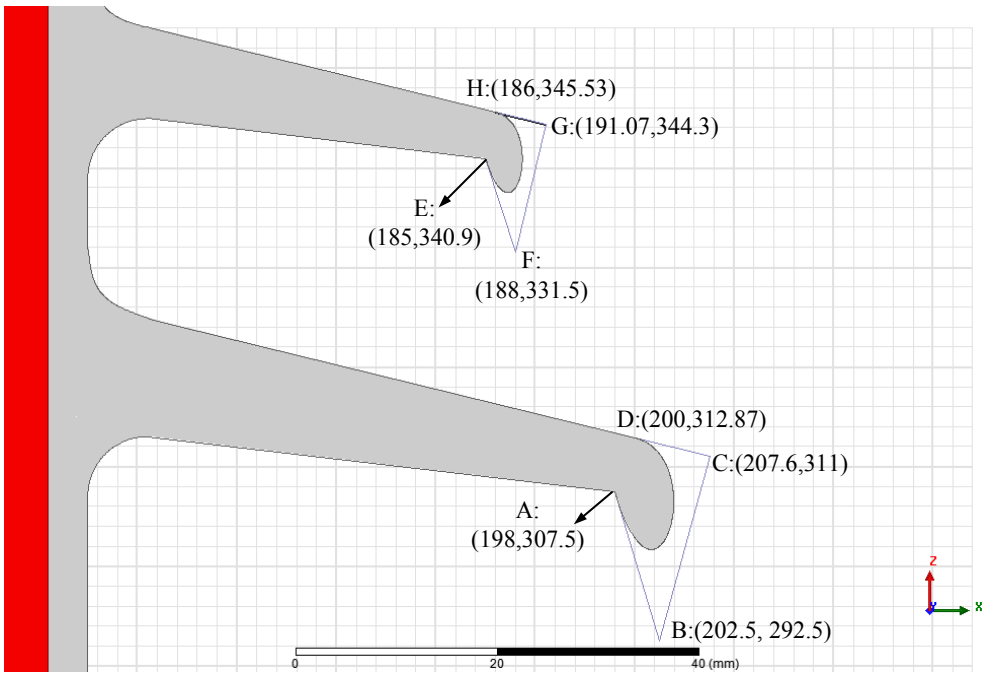


*Figure 137: Dimension drawing of optimized weather sheds*

## 10.6 Specification of optimized creepage distance

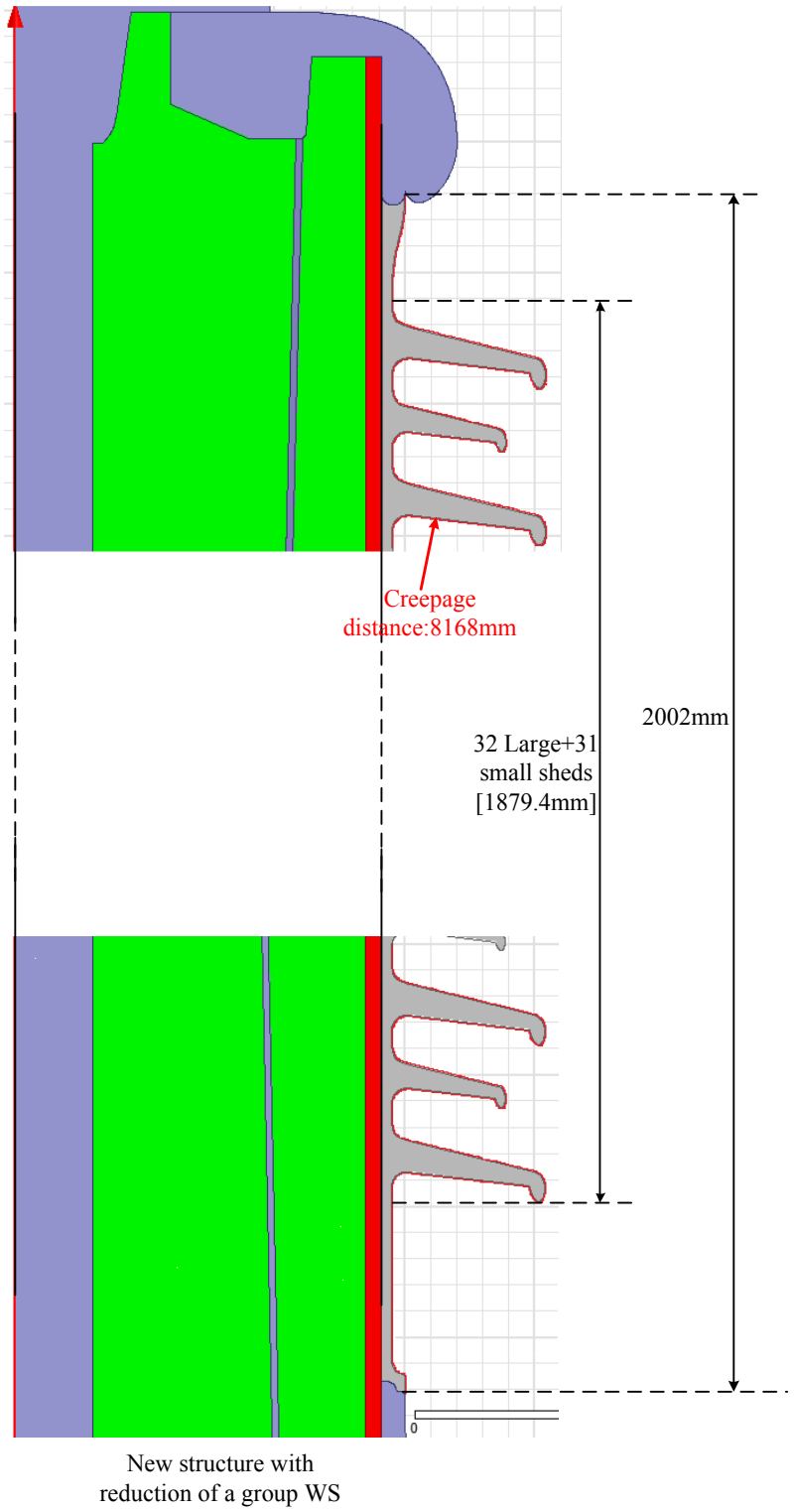


*Figure 138: Dimension drawing of optimized creepage distance*

# 11 Reference


*[1] Kitak, P.; Pihler, J.; Ticar, I., "Optimisation algorithm for the design of bushing for indoor SF6 switchgear applications,"Generation, Transmission and Distribution, IEE Proceedings-, vol.152, no.5, pp.691,696, 9 Sept. 2005*

*[2] Toshiaki Rokunohe, Tatsuro Kato, Makoto Hirose, Tetsu Ishigur, Development of Insulation Technology in Compact SF6 Gas-Filled Bushings, Wiley, Jan. 2010,*

*[3] Xiaoming Liu, Mingxue Zhao, Numerical calculation of electric field and analyses of insulation performance for bushings of extra high voltage $SF_6$ circuit breaker, Journal of Shenyang University of Technology, May.2008*

*[4] Ye Zhou, Junmei Wei, Optimization of Insulation Structure of 1100 kV Silicone Bushings 1100 kV, Annual symposium of Transmission and Distribution, 2010*

*[5] JOZE PIHLER, IGOR TICAR, JOZE VORSIC, OSZKAR BIRO, KURT PREIS, Design of SF6 Switchgear Components by Means of Electric Field Calculations, Power Engineering Maribor, IGTE TU Graz*

*[6] Ravindra Arora, Wolfgang Mosch, High Voltage and Electrical Insulation Engineering, ISBN: 978-0-470-60961-3, Wiley-IEEE Press, September 2011*

*[7] Mackevich, J.; Shah, M., "Polymer outdoor insulating materials. Part I: Comparison of porcelain and polymer electrical insulation,"Electrical Insulation Magazine, IEEE, vol.13, no.3, pp.5,12, May-June 1997*

*[8] Simmons, S.; Shah, M.; Mackevich, J.; Chang, R. J., "Polymer outdoor insulating materials. Part III-Silicone elastomer considerations,"Electrical Insulation Magazine, IEEE, vol.13, no.5, pp.25,32, Sept.-Oct. 1997*

*[9] Cherney, E.A., "Non-Ceramic insulators-a simple design that requires careful analysis,"Electrical Insulation Magazine, IEEE, vol.12, no.3, pp.7,15, May-June 1996*

*[10] Niemeyer, L.; Ullrich, L.; Wiegart, N., "The mechanism of leader breakdown in electronegative gases," Electrical Insulation, IEEE Transactions on , vol.24, no.2, pp.309,324, Apr 1989*

*[11] M Seeger, L Niemeyer and M Bujotzek, Leader propagation in uniform background fields in SF6 2009 J. Phys. D: Appl. Phys 42 185205*

*[12] Guoqing Chen,Qiaogen Zhang,Feng Wang. Discharge Characteristic Parameters and Mechanism in SF6 Gas. High voltage technologies, 2000,26(6):7-9,45.DOI:10.3969/j.issn.1003-6520.2000.06.003.*

*[13] Karady, G.G.; Shah, M.; Brown, R. L., "Flashover mechanism of silicone rubber insulators used for outdoor insulation-I,"Power Delivery, IEEE Transactions on, vol.10, no.4, pp.1965,1971, Oct 1995*

*[14] Shah, M.; Karady, G.G.; Brown, R. L., "Flashover mechanism of silicone rubber insulators used for outdoor insulation-II,"Power Delivery, IEEE Transactions on, vol.10, no.4, pp.1972,1978, Oct 1995*

*[15] Allen, N.L.; Mikropoulos, P.N., "Streamer propagation along insulating surfaces,"Dielectrics and Electrical Insulation, IEEE Transactions on , vol.6, no.3, pp.357,362, Jun 1999*

*[16] Allen, N.L.; Hashem, A.; Rodrigo, H.; Tan, B. H., "Streamer development on silicone-rubber insulator surfaces,"Science, Measurement and Technology, IEE Proceedings - , vol.151, no.1, pp.31,38, 5 Jan. 2004*

*[17] MENG Xiaobo, MEI Hongwei, CHEN Changlong, WANG Liming, GUAN Zhicheng, ZHOU Jun, Research on Characteristics of Streamer Propagation Along Insulation Surfaces [J]. Proceedings of the CSEE ,2013,(22):155-165.*

*[18] Rokunohe, T., Kato, T., Hirose, M. and Ishiguro, T. (2010), Development of insulation technology in compact SF6 gas-filled bushingss: Development of compact 800-kV SF6 gas-filled bushingss. Elect. Eng. Jpn., 171: 19–27. doi: 10.1002/eej.20898*

*[19] Murugan, N.; Sharmila, G.; Kannayeram, G., "Design optimization of high voltage composite insulator using Electric field computations,"Circuits, Power and Computing Technologies (ICCPCT), 2013 International Conference on , vol., no., pp.315,320, 20-21 March 2013*

*[20] Monga, S.; Gorur, R.S.; Hansen, P.; Massey, W., "Design optimization of high voltage bushings using electric field computations," Dielectrics and Electrical Insulation, IEEE Transactions on, vol.13, no.6, pp.1217,1224, December 2006*

*[21] Bhattacharya, K.; Chakravorti, S.; Mukherjee, P.K., "Insulator contour optimization by a neural network," Dielectrics and Electrical Insulation, IEEE Transactions on, vol.8, no.2, pp.157,161, Apr 2001*

*[22] Wen-Shiush Chen; Hong-Tzer Yang; Hong-Yu Huang, "Contour Optimization of Suspension Insulators Using Dynamically Adjustable Genetic Algorithms,"Power Delivery, IEEE Transactions on, vol.25, no.3, pp.1220,1228, July 2010*

*[23] Siemens AG, Power engineering guide, 6th edition, 2011*

*[24] The application of Ansoft 12 in the engineering electromagnetics, Bo Zhang, Hongliang Zhang, China Waterpower Press*

*[25] Ansoft Maxwell v11 User guide*

*[26] Bin LIV, Design for $SF_6$ High Voltage Apparatus, Third edition, China Machine Press*

*[27] Biscontini, B.; Russer, P., "A Novel Planar Multilayered Ultra Wide Band (UWB) Cylindrical Reflector Antenna,"Microwave Conference, 2007. APMC 2007. Asia-Pacific , vol., no., pp.1,4, 11-14 Dec. 2007*

*[28] S. Jarchi1, J. Rashed-Mohassel1, M. H. Neshati2, and C. Lucas3, A Dual Resonance Three Segment Rectangular Dielectric Resonator Antenna, PIERS Proceedings, August 27-30, Prague, Czech Republic, 2007*

*[29] Díaz-Morcillo, A., J. Monzó-Cabrera, et al. (2007). Application of Genetic Algorithms in the Determination of Dielectric Properties of Materials at Microwave Frequencies. Nature Inspired Problem-Solving Methods in Knowledge Engineering. J. Mira and J. Álvarez, Springer Berlin Heidelberg. 4528: 608-616.*

*[30] Wen-Shiush Chen; Hong-Tzer Yang; Hong-Yu Huang, "Contour Optimization of Suspension Insulators Using Dynamically Adjustable Genetic Algorithms,"Power Delivery, IEEE Transactions on , vol.25, no.3, pp.1220,1228, July 2010*

*[31] Farin, Gerald, Curves and surfaces for computer-aided geometric design (4 ed.). Elsevier Science & Technology Books. ISBN 978-0-12-249054-5, 1997*

*[32] IEC 60815-3 "Selection and dimensioning of high-voltage insulators intended for use in polluted conditions - Part 3: Polymer insulators for a.c. systems," VDE Verlag, Oct 2008*

*[33] Field calculation and tests of air/SF6 bushings, A.Axhausen, A. Grund and E.Kynast, Siemens AG, Berlin, Germany*

*[34] Classical Electrodynamics. J. D. Jackson. Wiley, 1975.*

*[35] The discussion of metal permittivity, Xiangjun Kuang, Journal of Sichuan University of Science and Engineering, Apr.2006*

*[36] Dielectric Physics, Zhiwen Ying, Science Press, Peking, 2000*